

CHARACTERIZATION AND LEACHING STUDIES ON DEEP-SEA MANGANESE NODULES AND THE SYNTHETIC ANALOGS

A Thesis Submitted
In Partial Fulfilment of the Requirements
for the Degree of
DOCTOR OF PHILOSOPHY

By
RAKESH KUMAR

to the

cg
**DEPARTMENT OF METALLURGICAL ENGINEERING
INDIAN INSTITUTE OF TECHNOLOGY, KANPUR**

November, 1988

Dedicated to my parents

CERTIFICATE

Certified that the work reported in this thesis entitled "Characterization and Leaching Studies on Deep-Sea Manganese Nodules and the Synthetic Analogs" by Rakesh Kumar has been carried out under our supervision and has not been submitted elsewhere for the award of degree.



R. K. Ray
Professor
Dept. of Metallurgical Engg.
Indian Institute of Technology
Kanpur

A. K. Biswas
Professor
Dept. of Metallurgical Engg.
Indian Institute of Technology
Kanpur

ACKNOWLEDGEMENTS

First and foremost, I wish to express my deep gratitude and lasting indebtedness to my supervisors, Professor A.K. Biswas and Professor R.K. Ray, for their all-round guidance and help rendered in preparing the final draft.

To all my other professors, who gave willing help at all time, I offer my sincere thanks. I would especially like to thank Dr. B.C. Raymahashay, who introduced me to the subject of 'Rock and Water Chemistry' and helped me to appreciate the multifaceted problems associated with manganese nodules, and Dr. T.R. Ramachandran for his help in electron microscopy work.

Late Dr. H.N. Siddiquie (former Director, National Institute of Oceanography, Goa) had been a source of inspiration during the inception of this work. The manganese nodule samples used in this work were kindly supplied by Dr. Siddiquie.

Dr. M.G. Hall (Department of Metallurgy and Materials, University of Birmingham, UK) and Dr. H.J. Klar (Gemeinschaftslabor für Elektronenmikroskopie, der Rheinisch-Westf. Technischen Hochschule, Aachen, W. Germany) deserve warmest thanks for their kind help in SEM work.

Professor Rudolf Giovanoli (University of Berne, Switzerland) provided valuable literatures on the oxyhydroxides of manganese and iron, particularly some older papers by late Professor W. Buser.

I express my deep appreciation for the help extended to me by the staff of Metallurgical Engineering and Materials Science departments.

I sincerely thank my friends for their assistance at various stages of this work.

I thank Mr. R.N. Srivastava for his meticulous typing and Mr. V.P. Gupta for his graphic skills.

The benediction, inspiration and constant encouragement of my parents have led to the completion of this work. My profoundest debts therefore must remain, as debts to parents always are, silent and unacknowledged.

Lastly, I must not fail to appreciate my dear wife Umi, who has tolerated all the hardships with patience and rare humour.

RAKESH KUMAR

CONTENTS

<u>Chapter</u>		<u>Page</u>
	LIST OF TABLES	viii
	LIST OF FIGURES	xi
	SYNOPSIS	xviii
I	INTRODUCTION	1
II	REVIEW OF THE LITERATURE	4
	2.1 Preamble	4
	2.2 Distribution and Chemical Composition	6
	2.3 Morphology	9
	2.4 Mineralogy	10
	2.4.1 Nature of Mineral Assemblage	10
	2.4.2 Oxyhydroxide Minerals of Manganese and Iron	10
	2.4.3 Accessory Minerals	29
	2.5 Genesis	30
	2.5.1 Source of Metals and Transportation Mechanisms	30
	2.5.2 Growth Processes	31
	2.5.3 Growth Rate	37
	2.6 Internal Microfeatures	37
	2.7 Occurrence of Nickel, Cobalt and Copper	39
	2.8 Metal Extraction	50
	2.9 Miscellaneous Aspects	55
	2.9.1 Technoeconomic Considerations	55
	2.9.2 Indian Efforts and Future Plan	56
	2.9.3 Legal and Environmental Problems	56
III	FORMULATION AND STATEMENT OF THE PROBLEM	58
	3.1 Missing Links: Mineralogy and Nodule Processing	58
	3.2 Research Strategies	59
	3.3 Key Objectives	63
IV	MATERIALS AND METHODS	64
	4.1 Materials	64
	4.1.1 Manganese Nodule Samples	64
	4.1.2 Synthetic Samples	65
	4.2 Characterization of Samples	69
	4.2.1 Analytical Methods	69
	4.2.2 Surface Area Measurements	76
	4.2.3 X-ray Diffraction	77
	4.2.4 Transmission Electron Microscopy	81
	4.2.5 Scanning Electron Microscopy	84
	4.2.6 Sequential Extraction	90
	4.3 Leaching Experiments on Synthetic Samples	90

<u>Chapter</u>		<u>Page</u>
V	PHASE IDENTIFICATION IN NODULES	94
	5.1 X-ray Diffraction	94
	5.2 Transmission Electron Microscopy	100
VI	INTERNAL STRUCTURE - SCANNING ELECTRON MICROSCOPIC STUDIES	123
	6.1 SEM/SE-Mode/EDAX Studies	123
	6.1.1 Chemical Composition	123
	6.1.2 Elemental Correlations	128
	6.1.3 Genesis and Factor Analysis	138
	6.2 SEM/BSE-Mode/EDAX Studies	154
	6.2.1 BSE vs. SE Mode	154
	6.2.2 Microfeatures and Chemical Characteristics	154
	6.2.3 Factor Analysis	172
	6.2.4 Internal Structure, Chemical Composition and Genesis	178
VII	PHYSICO-CHEMICAL NATURE AND LEACHING BEHAVIOUR OF PURE AND Ni, Co AND Cu BEARING MANGANESE(IV) OXYHYDROXIDES	186
	7.1 Characterization of Samples	187
	7.1.1 Chemical Composition and Surface Area	187
	7.1.2 Phase Constituents, Structure and Crystallinity	194
	7.1.3 Summary of Characterization Studies	208
	7.2 Leaching Studies	211
	7.2.1 General Considerations and Review	211
	7.2.2 Sulfuric Acid Leaching	215
	7.2.3 Sulfurous Acid Leaching	228
VIII	PHYSICO-CHEMICAL NATURE OF PURE AND Ni, Co AND Cu BEARING GOETHITES	235
	8.1 Characterization of Samples	235
	8.1.1 Chemical Composition and Surface Area	235
	8.1.2 XRD Studies	237
	8.1.3 Transmission Electron Microscopy	243
	8.2 Leaching Studies	248
	8.2.1 General Considerations	248
	8.2.2 Dissolution Behaviour of Iron	250
	8.2.3 Dissolution Behaviour of Minor Elements	256
IX	CHARACTERIZATION AND LEACHING RESULTS ON SYNTHETIC PHASES - CRITICAL DISCUSSION	263
	9.1 Effect of Method of Doping on Mode of Occurrence	263
	9.2 Leaching Behaviour of the Synthetic Phases	265
	9.2.1 Sulfuric Acid Leaching	265
	9.2.2 Sulfurous Acid Leaching	267

<u>Chapter</u>	<u>Page</u>
9.3 Implications in Manganese Nodule Genesis and Processing	268
9.3.1 Mode of Occurrence and Leaching Behaviour of Nodules	268
9.3.2 Significance of Internal Structure in Leachability of Nodules	274
9.3.3 Other Considerations	275
X CONCLUSIONS AND RECOMMENDATIONS	277
REFERENCES	283
APPENDIX	
A CHEMICAL COMPOSITIONS OF MANGANESE NODULES FROM SOME SELECTED REGIONS IN PACIFIC AND INDIAN OCEAN	310
B THE ANALYTICAL TECHNIQUES - CALIBRATION CURVE	312
C AVERAGE OXIDATION STATE (O/Mn RATIO) IN SYNTHETIC OXYHYDROXIDES OF MANGANESE	314
D SURFACE AREA ESTIMATION BY EGMME RETENTION METHOD	315
E QUANTITATIVE ESTIMATION OF MICROCRYSTALLINE DIMENSIONS IN GOETHITES	316
F FORTRAN IV COMPUTER PROGRAM FOR INDEXING OF SAED SPOT PATTERN	319
G NOTE ON THE OPERATION OF SEM IN SECONDARY ELECTRON (SE) AND BACK-SCATTERED ELECTRON (BSE) MODES	324
H FORTRAN-IV COMPUTER PROGRAM USED FOR FACTOR ANALYSIS AND CALCULATION OF CORRELATION COEFFICIENTS	327
I FORTRAN-IV PROGRAM FOR MULTIPLE REGRESSION ANALYSIS	337
J LIST OF MULTIPLY INDEXED SELECTED AREA ELECTRON DIFFRACTION PATTERNS	340
K ELEMENTAL COMPOSITION OF NODULES FROM DIFFERENT REGIONS IN CENTRAL INDIAN BASIN	341
L INTERACTION OF HYDROUS MANGANESE(IV) OXIDES WITH Ni, Co AND Cu IONS IN SOLUTION	342
M CRYSTAL FIELD THEORY	347
N FREE ENERGY DATA	354
O LEACHING DATA FOR OXYHYDROXIDES OF MANGANESE	356
P LEACHING DATA FOR GOETHITES	361

LIST OF TABLES

<u>Number</u>	<u>Title</u>	<u>Page</u>
II.1	The average composition of polymetallic nodules from different world oceans	8
II.2	Morphological characteristics of manganese nodules	9
II.3	Ratio of ionic radii of manganese and iron in different valency states to that of O^{2-}	11
II.4	Nomenclature of Mn(IV) oxide structure	14
II.5	Structure of oxide and oxyhydroxides of iron(III)	15
II.6	Manganese and iron oxide minerals	18
II.7	Summary of various nomenclatures used for manganese minerals in nodules	22
II.8	Phase identification techniques - limitations	29
II.9	Comparison of few promising hydrometallurgical processes	53
IV.1	Reagents used in different sequential extraction (SEQ) treatments	91
IV.2	Description of leaching conditions used for different samples	92
V.1	List of unambiguously solved selected area electron diffraction (SAED) patterns	101
V.2	Statistical occurrence of minerals in manganese nodules	103
V.3	Electron diffraction data on iron-bearing minerals compared with standard 'd' values from literature	107
VI.1(a)	Elemental composition of locations shown in Figure VI.1(a) (top-bottom)	126
VI.1(b)	Elemental composition of locations shown in Figure VI.1(b) (right-left)	127
VI.2	Correlation coefficients of inter-element relationship (total 49 spots considered)	131
VI.3	The correlation coefficients matrix for bulk chemical composition data of nodules from	

<u>Number</u>	<u>Title</u>	<u>Page</u>
	different regions in the Central Indian Ocean basin (37 compositions considered)	132
VI.4	Partial chemical analysis of manganese nodule leach liquours after different sequential extraction treatments listed in Table IV.1	134
VI.5(a)	Factor loading and communality at each observation point. Number of observations and elements considered are 45 and 12 respectively	140
VI.5(b)	Varimax factor scores for the factors listed in Table VI.5(a)	141
VI.6	Elemental composition of areas shown in Figure VI.7 (line X-O in Figure IV.1(b))	146
VI.7(a)	Factor loadings and communality at each observation point (Table VI.6). Number of observations and elements considered are 31 and 11 respectively	147
VI.7(b)	Varimax factor scores for the factors listed in Table VI.7(a)	148
VI.8	X-ray microanalysis of selected regions in different textural patterns (Figure VI.13). ZAF corrections were not applied, so the results are only semiquantitative	158
VI.9	X-ray microanalysis data of distinct regions in different morphologies	173
VI.10(a)	Factor loadings and communality for distinct regions in different morphologies (Figure VI.13(a-c), Table VI.9)	174
VI.10(b)	Varimax factor scores for the factors listed in Table VI.10(a)	175
VII.1	Chemical composition and specific surface area of birnessite samples	188
VII.2	Chemical equivalent balance in birnessites	191
VII.3	Crystal field stabilization energies and ionic radii of selected ions in an octahedral field	193
VII.4	Indexing of selected area electron diffraction (SAED) patterns (synthetic birnessite samples)	204

<u>Number</u>	<u>Title</u>	<u>Page</u>
VII.5	Standard free energy change ($\Delta G_{r,298}^{\circ}$) for the dissolution reactions listed in the text	213
VII.6	Fraction of manganese and minor elements reacted in sulfuric and sulfurous acid leaching of birnessite samples at different time intervals	218
VIII.1	Chemical composition and surface area of different goethite (α -FeOOH) samples	236
VIII.2	[I_{110}/I_{111}] and lattice parameter values for goethite samples	239
VIII.3	Microcrystalline dimensions (in nm) for G-O and G-Cu(C)	240
VIII.4	Mean crystalline dimension (MCD) along the a, b and c axes and MCD_{110} and MCD_{111} as calculated from XRD data	242
VIII.5	Summary of TEM observations and comparison of average length and width of goethite particles as measured from XRD and TEM	247
VIII.6	Fraction of iron and minor elements reacted in sulfuric and sulfurous acid leaching at different times	253
VIII.7	Linear and multilinear correlations between fractions of iron reacted (at $t = 5$) and physical characteristics of the samples	254

LIST OF FIGURES

<u>Number</u>	<u>Title</u>	<u>Page</u>
II.1	Distribution of nodules in the world oceans (hatched) with areas of significance (cross-hatched). Dotted line show limits of sedimentation rate of 30 mm/1000 years (49)	7
II.2	Typical arrangements of octahedra $[\text{Mn}(\text{O}, \text{OH}, \text{H}_2\text{O})_6]^{2+}$ sharing in manganese(IV) oxide minerals (a) layer structure-edge sharing, after Giovanoli (22), (b) tunnel structure-edge and corner sharing, after Burns and Burns (18)	13
II.3	Orientation relationship between structures of oxyhydroxides and oxide of trivalent iron (78)	16
II.4	Tetrametric unit resulting by cutting down the structure in Figure II.2(b), after Giovanoli (22)	26
II.5	Mineralogy and geochemistry of nodules forming in different marine environment, adopted from Lyle (26)	33
II.6	Three component diagram illustrating relationship between (Mn/Fe) ratio, (Ni + Cu + Co) content and different genetic type of nodules from Pacific ocean, after Halbach et al. (25)	35
II.7	Tunnel structure of T(3,3) todorokite, after Burns et al. (20)	42
II.8	Layered structure of birnessite, Giovanoli et al. (107)	44
II.9	Hybrid layered structure of asbolane illustrating possible sites for the occurrence of Ni, Co and Cu, after Chukhrov et al. (209)	45
IV.1	Schematic diagram of reaction vessel used in the synthesis of birnessite samples	66
IV.2	Schematic diagram of (a) nodule showing section used (hatched) for detailed SEM work (b) polished nodule section	86
V.1	XRD pattern of (a) as received sample (b), (c) 10 Å ^o phase from periphery and core of a nodule and (d), (e) material in (b) and (c) respectively, heated at 120°C, 10 hrs	95
V.2	XRD patterns after intercalation with dodecylammonium chloride (a), (b) 10 Å ^o phase from periphery and core of a nodule (c) synthetic Na-buserite and (d) synthetic Ni-buserite	97

<u>Number</u>	<u>Title</u>	<u>Page</u>
V.3	XRD patterns of nodule residues after sequential extraction: (a) residue 1 (Fe and silicate fraction) and (b) residue 2 (silicate fraction)	99
V.4	(a) Typical electron micrograph of Na-birnessite observed in Mn-nodule sample, (b) SAED pattern corresponding to (a)	104
V.5	(a) Electron micrograph and (b) SAED pattern from synthetic Na-birnessite	104
V.6	(a), (b) Electron micrograph and SAED pattern from a todorokite crystal with faulted structure	105
V.7	(a), (c) and (b), (d), Electron micrographs and corresponding SAED patterns showing variation in the crystallinity of goethite	109
V.8	(a), (b) Electron micrograph and SAED pattern of akaganeite (β -FeOOH) and/or lepidocrocite (γ -FeOOH) (c), (d) micrograph and SAED pattern indicating simultaneous occurrence of goethite (α -FeOOH) and akaganeite (β -FeOOH) or lepidocrocite (γ -FeOOH)	110
V.9	(a), (b) Electron micrograph and SAED pattern of synthetic intermediate phase formed during synthesis of goethite coprecipitated with cobalt	111
V.10	(a), (b) Electron micrograph and SAED pattern of mineral ferrihydrite	111
V.11	(a) Electron micrograph showing morphology similar to ferroxhyte (δ' -FeOOH) and vernadite (δ -MnO ₂) (b) and (c) typical SAED patterns from morphology similar to (a)	113
V.12	(a), (c) Electron micrographs of α -quartz in Mn-nodule sample and residue 2; (b), (d) SAED patterns corresponding to (a) and (c) respectively	116
V.13	(a), (c) Electron micrographs of labradorite in Mn-nodule sample and residue 2; (b), (d) SAED patterns corresponding to (a) and (c) respectively	117
V.14	Electron micrographs and SAED patterns from other accessory minerals (a), (b) kaolinite; (c), (d) montmorillonite-chlorite	118
V.15	(a) Electron micrograph and (b) EDAX spectra of a montmorillonite-chlorite particle	120
V.16	(a) Electron micrograph and (b) EDAX spectra of calcite particle	121

<u>Number</u>	<u>Title</u>	<u>Page</u>
VI.1(a)	SEM/SE micrograph of nodule section, top-bottom (vide Figure IV.1(b))	124
VI.1(b)	SEM/SE micrograph of nodule section, right-left (vide Figure IV.1(b))	125
VI.2(a)	Spatial distribution of Mn, Fe, Si, Ni, Co, Cu and Ti concentrations with respect to discrete sample locations (Figure VI.1(a), top-bottom)	129
VI.2(b)	Spatial distribution of Mn, Fe, Si, Ni, Co, Cu and Ti concentrations with respect to discrete sample locations (Figure VI.1(b), right-left)	130
VI.3	TEM micrographs of nodule samples after (a) SEQ I, (b) SEQ I, II, (c) SEQ I-III and (d) SEQ I-IV. Corresponding EDAX spectra are given in Figure VI.4. SEQ means sequential extraction. I, II, III and IV refers to the removal of exch- angeable ions, Mn-fraction, organic matter and Fe-fraction respectively	135
VI.4	EDAX spectra of Mn-nodule samples after (a) SEQ I, (b) SEQ I, II, (c) SEQ I-III and (d) SEQ I-IV	136
VI.5	Three component diagram illustrating relation- ship between major (Mn, Fe) and minor (Ni, Co, Cu, Ti) element/s and genetic constituents or Mn/Fe ratio	139
VI.6	Three co-ordinate plot of the normalized varimax factor loadings of locations shown in SEM/SE micrographs (Figure VI.1)	143
VI.7	SEM/SE micrograph of nodule section illustrating areas of analysis along the line X-0 (vide Figure IV.1(b))	145
VI.8	Three co-ordinate plot of normalized varimax factor loadings of areas shown in Figure VI.7. The diagram illustrate the reproducibility of factor model	150
VI.9	Three co-ordinate discrimination diagram for different locations in the nodule section with corresponding Mn/Fe ratio superimposed	151
VI.10	Three co-ordinate diagram of normalized varimax factor loadings of nodules from different loca- tions in Pacific ocean, the corresponding Mn/Fe	

<u>Number</u>	<u>Title</u>	<u>Page</u>
	ratio are superimposed. Bulk composition of nodules used in factor analysis (after Calvert and Price (160))	153
VI. 11	SEM micrographs illustrating the superiority of Z-contrast BSE images (a), (c)) over corresponding SE images ((b), (d))	155
VI. 12	BSE micrographs illustrating the overall view of internal features in nodule internal structure	156
VI. 13	BSE micrographs of typical morphological features (a) columnar and radial pattern, (b) dendritic segregation, (c) compact type of morphology and (d) detrital fragment embedded in nodule matrix. The distinct regions in different morphologies are marked	157
VI. 14	X-ray maps for BSE micrograph in (a), (b) Mn, (c) Fe, (d) Ni, (e) Co and (f) Cu	160
VI. 15	Concentration profiles of major (Mn, Fe) and minor (Ni, Co and Cu) elements superimposed on a typical region in columnar and radial pattern to illustrate the elemental association	161
VI. 16(a)	X-ray spectra from bright regions (C/B) in columnar and radial pattern. The diagram illustrate the relationship between Mn/Fe ratio and minor elements concentration	162
VI. 16(b)	X-ray spectra from grey regions (C/G1) and (D/G) in columnar and radial pattern and dendritic segregation	163
VI. 17	X-ray spectra from bright regions (D/B) in dendritic segregation	164
VI. 18	BSE micrograph of (CT/B) material present in cracks	166
VI. 19	X-ray maps for BSE micrograph in (a), (b) Mn, (c) Fe, (d) Ni and (e) Cu	167
VI. 20	Concentration profiles of Mn and minor elements (Ni, Co, Cu) superimposed on a typical region in compact type of morphology to illustrate the elemental association	168
VI. 21	X-ray spectra of bright regions (CT/B) in compact type of morphology illustrating negative correlation of Ni and Cu with Mn/Fe ratio	169

<u>Number</u>	<u>Title</u>	<u>Page</u>
VI. 22	(a) X-ray spectra of grey regions (CT/G) in compact type of morphology, (b) the diagram illustrating positive correlation between Fe concentration and concentration of other elements (Si, Al, K, Ti) in CT/G regions	170
VI. 23	X-ray spectra of dark and very dark regions in different morphologies	171
VI. 24	Classification of distinct regions in different morphologies in terms of factor loadings and Mn/Fe ratio	177
VI. 25	BSE micrographs illustrating increasing influence of hydrogenetic factor	179
VI. 26	BSE micrograph illustrating diffuse boundary between bright region (CT/B) and grey region (CT/G) in compact type of morphology	182
VII. 1	XRD patterns of busserites (a) Bu-O, (b) Bu-Ni(C), (c) Bu-Co(C), (d) Bu-Cu(C), (e) Bu-Ni(I), (f) Bu-Co(I) and (g) Bu-Cu(I)	195
VII. 2	XRD patterns of busserites (Bu) intercalated with dodecylammonium chloride (a) Bu-O, (b) Bu-Ni(C), (c) Bu-Co(C), (d) Bu-Cu(C), (e) Bu-Ni(I), (f) Bu-Co(I) and (g) Bu-Cu(I)	196
VII. 3	XRD patterns of birnessite samples (a) B-O, (b) B-Ni(I), (c) B-Co(I), (d) B-Cu(I), (e) B-Ni(C), (f) B-Co(C) and (g) B-Cu(C)	197
VII. 4	XRD patterns of birnessites (B-R(C)) intercalated with dodecylammonium chloride (a) B-Ni(C), (b) B-Co(C) and (c) B-Cu(C)	198
VII. 5 (a)-(d)	Some typical electron micrographs and SAED patterns from birnessite samples (a), (b) B-O, (c), (d) B-Co(C) (similar features observed for B-Ni(C) and B-Cu(C))	202
VII. 5 (e)-(h)	Electron micrographs and SAED patterns (e), (f) B-Ni(I) and (g), (h) B-Co(I)	203
VII. 6	Electron micrographs (a), (c) and corresponding SAED patterns (b), (d) from V-O	209
VII. 7	Dissolution of manganese(II) from different birnessite samples in sulfuric acid	216
VII. 8	Dissolution of doped Ni, Co and Cu in sulfuric acid (a) sorption mode (V-R(S) samples) and (b) coprecipitation and ion exchange mode (B-R(C) and B-R(I) samples)	217

<u>Number</u>	<u>Title</u>	<u>Page</u>
VII.9	XRD patterns of leach residues obtained after sulfuric acid leaching of birnessites (a) B-O, (b) B-Ni(C), (c) B-Co(C), (d) B-Cu(C), (e) B-Ni(I), (f) B-Co(I) and (g) B-Cu(I). B - Birnessite	220
VII.10	(a) Reaction mechanism for octahedrally coordinated metal ion in solid oxyhydroxide structure (adopted from references (63, 302)), (b) relationship between electronic configuration, crystal field stabilization energy (CFSE) and ionic radius of some selected metal ions (63,69)	226
VII.11	Dissolution behaviour of birnessites doped with Ni, Co or Cu in coprecipitation mode compared with pure birnessite (leaching medium - sulfurous acid)	229
VII.12	Dissolution behaviour of birnessites doped with Ni, Co or Cu in ion exchange mode compared with pure birnessite (leaching medium - sulfurous acid)	230
VII.13	Dissolution behaviour of V-O and V-R(S) samples in sulfurous acid	231
VIII.1	XRD patterns of goethite samples (a) G-O, (b) G-Ni(C), (c) G-Co(C), (d) G-Cu(C), (e) G-Ni(S), (f) G-Co(S) and (g) G-Cu(S)	238
VIII.2	MCD _a vs. MCD _b values for selected goethite lines (a) for G-O and (b) G-Cu(C)	241
VIII.3 (a)-(d)	Typical electron micrographs and SAED patterns (a), (b) G-O, (c), (d) G-Ni(C)	244
VIII.3 (e)-(h)	Electron micrographs and SAED patterns (e), (f) poorly crystalline goethite in G-Ni(C) and (g), (h) goethite outgrowth on hematite in G-Cu(C)	245
VIII.4	Electron micrographs (a) extinction contours in G-Ni(C) and (b) star shaped twins in G-Cu(C)	249
VIII.5	Dissolution of iron from different goethite samples in sulfuric acid	251
VIII.6	Dissolution of iron from different goethite samples in sulfurous acid	252
VIII.7	Effect of mode of doping on the dissolution of Ni, Co and Cu from doped goethite samples in sulfuric acid	257

<u>Number</u>	<u>Title</u>	<u>Page</u>
VIII.8	Effect of mode of doping on the dissolution of Ni, Co and Cu from doped goethite samples in sulfurous acid. The similarity in the dissolution behaviour of Ni in sorption and coprecipitation mode is illustrated	258
IX.1	Dissolution behaviour of Ni, Co and Cu from manganese nodule in sulfuric acid. Adopted from (a) Itoh et al. (225) and (b) Fuerstenau et al. (15)	270

CHARACTERIZATION AND LEACHING STUDIES ON DEEP-SEA
MANGANESE NODULES AND THE SYNTHETIC ANALOGS

A Thesis Submitted
In Partial Fulfilment of the Requirements
for the degree of
DOCTOR OF PHILOSOPHY

by
RAKESH KUMAR

to the
DEPARTMENT OF METALLURGICAL ENGINEERING
INDIAN INSTITUTE OF TECHNOLOGY KANPUR
November 1988

SYNOPSIS

The major interest in manganese nodules centres on the oxyhydroxides of manganese and iron because all the elements of potential economic interest are found associated with these phases. The mode of occurrence (e.g. substitution, sorption, coprecipitation etc.) of Ni, Co and Cu in oxyhydroxide phases of nodules is a poorly understood subject. The understanding of the manner in which minor elements occur in manganese nodules and its implications in nodule processing are of vital importance.

A brief introduction on manganese nodules (Chapter-I) is followed up by a detailed and critical review on manganese nodules with particular emphasis on the mineralogy of oxyhydroxide phases of manganese and iron and mode of occurrence of Ni, Co and Cu (Chapter-II).

The basic goal of this investigation was to enhance our understanding of nodule mineralogy and internal structure in general and occurrence of Ni, Co and Cu in oxyhydroxides of manganese and iron and its implications in manganese nodule processing in particular. The research strategy (Chapter-III) which was adopted has two major facets (a) characterization of nodules from

promising areas in Central Indian Ocean Basin region to elucidate the nature and identity of phase constituents, internal structure, elemental associations and mineral assemblages using X-ray diffraction (XRD), transmission electron microscopy (TEM) and scanning electron microscopy (SEM) with EDAX and (b) synthesis, characterization and leaching studies on pure and doped oxyhydroxides of manganese and iron with particular emphasis on the manganese mineral birnessite and the iron mineral goethite. The elements Ni, Co and Cu were doped in several modes viz. coprecipitation, ion exchange and sorption.

In any investigation, complete description of materials and techniques employed is of paramount importance. Detailed description of materials, synthesis methods, characterization techniques, leaching experiments and mathematical techniques employed in this investigation is presented in Chapter-IV.

The X-ray diffraction technique has limited utility for phase identification in manganese nodules for two reasons (i) the crystallite size of minerals in nodules is often less than $1\text{ }\mu\text{m} \times 1\text{ }\mu\text{m} \times 1\text{ }\mu\text{m}$ and (ii) the phases in amount less than 5% cannot be detected. TEM offers possibly the only means to study different crystalline constituents present in nodules because of its ability to examine very small sized particles of reasonable degree of crystallinity when operated in imaging mode coupled with selected area electron diffraction (SAED) mode. The multi-mineralic nature of nodules makes the indexing of SAED spot patterns a herculean task. To overcome this problem a FORTRAN-IV computer program was developed for the indexing purpose. The microfeatures observed in the electron micrographs of minerals often helps in phase

identification. TEM studies on nodule residues obtained after selective sequential extraction of Mn- and Fe-fraction and synthetic oxyhydroxide phases of manganese and iron have often helped in the unambiguous identification of minerals in nodules. Based on XRD and TEM studies (Chapter V) the presence of following phases was confirmed - Manganese minerals: Birnessite, Todorokite and $\delta\text{-MnO}_2$ (vernadite); Iron minerals: Goethite, Ferrihydrite and Ferroxhyte; Silicates: α -quartz, Feldspars, Montmorillonite and Kaolinite; Biogenics: Calcite.

The crystallinity of $\delta\text{-MnO}_2$ and iron bearing minerals was so poor that it was found impossible to record single crystal spot SAED pattern because of geometrical limitation of the microscope i.e. the selected area was much larger than the crystallite size. XRD studies on 10 \AA phase intercalated with dodecylammonium chloride indicated that the 10 \AA phase is likely to be predominantly todorokite or disordered busserite-todorokite assemblage. The mineral birnessite shows preferred orientation in $\langle 001 \rangle$ direction.

Scanning electron microscopy with X-ray micro-analysis (EDAX) was used in conjunction with statistical analysis (regression and Q-mode factor analysis) to study the elemental associations, internal structure and mineral assemblages present in nodules (Chapter-VI).

SEM/SE/EDAX analysis for the elements Mn, Fe, Ni, Co, Cu, Ti, Si, Al, Mg, K, Ca, Na, Cl and S was carried out on a polished section of a nodule at various points. Linear regression analysis of chemical composition data confirmed the correlations established by earlier workers e.g. positive correlation of Ni, Cu and Mg with Mn, Ti with Fe and Si with Al. Generally observed negative

correlation of Fe with Mn was not observed. This was explained in terms of multiple associations of Fe with Mn and Si. Cl and S did not show any significant correlation with other elements.

Dissolution behavior of elements in sequential extraction (i.e. selective sequential removal of exchangeable ions, Mn-fraction, organic matter, and Fe-fraction) was used to verify the elemental correlation observed in linear regression analysis. A very small amount of minor elements was found to be present in easily exchangeable form. The positive association of Ni and Mg with Mn, and Ti with Fe was corroborated by the results of sequential extraction. The dissolution behavior of Ni, Mg and Ti showed close correspondence with the dissolution behavior of respective major element. The positive correlation of Cu with Mn is not supported by its dissolution behavior in sequential extraction. The multiple association of Cu, as suggested by the sequential extraction data seems quite apparent because of the complex behavior of cuprous ion formed during reductive dissolution of manganese bearing phases. The sequential extraction data for Co suggested its multiple association with Mn- and Fe-fraction and perhaps organic matter.

Q-mode factor analysis of SEM/SE/EDAX data resulted in four significant factors. The factors with their elemental associations and genetic significance are listed below:

Factor 1 : Mn - Ni - Cu - Mg - Co -; diagenetic
Factor 2A : Si - Fe - Al - K - Ti -; siliceous ooze
Factor 2B : Si - Al - K - Na - Ca -; detrital
Factor 3 : Fe - Ti - Co - Ca - Mn -; hydrogenetic

The association of Fe with Si suggests that biological silica has a role to play in the fractionation of manganese and iron.

The atomic number (Z) contrast in back-scattered electron (BSE) mode in SEM allows distinction to be made among the different textural patterns present in the polished nodule section. X-ray mapping of different textural patterns, line and point scans provide valuable insight into the distribution of major (Mn, Fe and Si) and minor elements (Ni, Co, Cu, K, Mg etc.) and their associations vis-a-vis distinct morphologies and regions therein. SEM/BSE/Z-contrast micrographs revealed four distinct kinds of internal features for the polished section (i) dendritic segregation, (ii) radial and columnar pattern, (iii) compact type of morphology and (iv) detrital fragment embedded in the nodule matrix.

Statistical analysis of X-ray microanalysis data vis-a-vis regions in growth morphologies (detrital fragments excluded) by Q-mode factor analysis results in factors based on elemental associations which are typical of major phases observed in XRD and TEM investigation. Factor loadings for different regions enable finding correlations among textural patterns, chemical compositions and mineral assemblages. The characteristics of different internal features can be summarized as follows:

- (i) Dendritic Segregation - 10 A° phase (diagenetic substance) and $(\delta\text{-MnO}_2 + \text{FeOOH} \cdot \text{XH}_2\text{O})$ assemblage. The 10 A° phase is richest in Ni and Cu and shows small variation in composition. The 10 A° phase is predominantly todorokite.
- (ii) Columnar and Radial Pattern - characterized by intimate association (epitaxial growth) of $\delta\text{-MnO}_2$ and $\text{FeOOH} \cdot \text{XH}_2\text{O}$.

Ni and Cu correlate positively with Mn/Fe ratio. Co associates with Fe.

- (iii) Compact Type of Morphology - consisting of $10 A^{\circ}$ phase and iron rich silicate material. The phase boundary between $10 A^{\circ}$ phase and silicate material is often diffused. The $10 A^{\circ}$ phase shows variable composition. Ni, Co and Cu are found associated with manganese rich phase. Ni and Cu correlate negatively with Mn/Fe ratio. Fe rich silicate material is characterized by elemental assemblage Si-Fe-Al-Ti (Factor 2A). The $10 A^{\circ}$ phase appears to be disordered buserite or buserite-todorokite assemblage.

Simultaneous occurrence of the $10 A^{\circ}$ phase (diagenetic substance) with Fe-rich silicate material in compact type of morphology indicated that siliceous ooze play a role not only in the fractionation of Mn and Fe but also in the enrichment of Ni, Co and Cu in the diagenetic substance.

TEM and SEM investigations on manganese nodules provide valuable insight into nodules mineralogy, internal structure and elemental associations. However, these techniques are inadequate to throw any light on the precise mode of occurrence viz. coprecipitation, sorption, ion exchange, of minor elements. The phases in nodules are so intimately intermixed that it is difficult to extract a significant amount of a phase for systematic characterization and leaching studies. These handicaps impart a special status to the studies on synthetic analogs of phases present in nodules in elucidating the implication of mode of occurrence of minor elements in manganese nodule processing. The results of

characterization and leaching studies on the synthetic analogs are presented in Chapters VII and VIII.

The manganese(IV) oxides which were investigated include (i) pure birnessite and $\delta\text{-MnO}_2$ (randomly stacked birnessite) and (ii) Mn-R (R = Ni, Co, Cu) type binary hydrous manganese oxides with following sub-categories (a) birnessite - doped in coprecipitation and ion exchange mode and (b) $\delta\text{-MnO}_2$ - doped in sorption mode.

The characterization work shows that irrespective of the method of doping the elements get incorporated in structure of host manganese oxide phases. The incorporation of Ni(II), Co(II) and Cu(II) in the host phases takes place via simple ion exchange reaction/s involving Mn^{2+} , K^+ , Na^+ , H^+ and structural vacancies and exchange reaction with electron transfer step. The exchange reactions can be partly understood in terms of crystal field stabilization energies (CFSE) and the radii of ions involved. The exchange reactions which take place deep inside the structure of bulk phases are accompanied by structural breakdown and disorder and/or rearrangements leading to the formation of new phases. It is revealed by the surface area, XRD and TEM data that in terms of structural complexities the doped phases may be arranged as follows: sorption > ion exchange > coprecipitation mode. The synthetic phases show marked similarities with the phases in manganese nodules.

Leaching of birnessites in sulfuric acid is associated with the collapse of structure leading to the formation of new phases like nsutite and cryptomelane. Two significant observations were made regarding the dissolution of Ni, Co and Cu from doped manganese

oxide samples (i) for the same element in different mode of doping the degree of leachability is observed in the following order: sorption < ion exchange < coprecipitation and (ii) for the same mode of doping leachability of doped elements increases in the following order: Cu > Ni > Co. The leaching data of Mn(II) and doped elements can be adequately explained in terms of structural complexities and CFSE. All the birnessites and δ -MnO₂ samples are almost completely dissolved in SO₂ concentration as small as 0.2 wt %, in less than ten minutes.

Goethite (α -FeOOH) samples which were studied include (i) pure goethite and (ii) goethite doped with Ni/Co/Cu in coprecipitation and sorption mode. In the case of coprecipitation, the presence of Ni, Co and Cu during synthesis modifies the crystallization conditions and thus the crystal growth rate and in turn crystal morphology and degree of structural order. All the goethite samples were characterized in terms of chemical composition, surface area, phase constituents, crystallinity and structural disorder (by XRD) and crystal size and morphology (by TEM). It was found that the surface area data or microcrystalline dimension alone were not enough to explain the different dissolution behavior of iron from different samples in sulfuric acid leaching. The amount of Fe dissolved showed very strong correlation with surface area and structural disorder or microcrystalline dimension and structural disorder. The correlations observed were inferior in the case of sulfurous acid leaching indicating interference of doped elements on iron dissolution.

In contrast with δ -MnO₂ samples doped in sorption mode, the doped elements sorbed on the surface of goethite were easily

leachable in sulfuric acid leaching. The leachability of elements sorbed on goethite surface was better compared with elements doped in coprecipitation mode. In the latter case they may be present as part of goethite structure and/or occluded oxyhydroxide.

Leachability data for synthetic manganese nodules in sulfuric and sulfurous acid leaching showed marked similarities (in terms of leachability of elements, nature of dissolution curve) with dissolution behavior of actual nodules in similar media as reported in the literature. The characterization results on the synthetic manganese oxyhydroxides indicated that structure of phases plays a very important role in the uptake of Ni, Co and Cu in actual manganese nodules. The predominant mode of occurrence of Ni, Co and Cu is proposed to be structural substitution in oxyhydroxide phases of manganese. The implications of results on structure and leachability of synthetic manganese and iron oxyhydroxide phases are discussed for nodules of varying mineralogy and internal structure (Chapter-IX). The slow nature of sulfuric acid leaching may be partly attributed to the structural collapse during leaching which leads to the formation of poorly leachable phases.

The concluding remarks and scope for the future work are presented in the last chapter (Chapter-X).

CHAPTER - I

INTRODUCTION

Deep-sea manganese nodules, which have fascinated marine geologists since their discovery between the years 1872-1876 [HMS Challenger Expedition (1)], have come to be reckoned as the multi-element ore of the future in the last two to three decades. The commercially important metals in nodules are nickel, cobalt, copper and manganese (2-6). Zinc and molybdenum could also be recovered as byproducts (4, 7).

In 1973, total world consumption of Ni, Co and Cu was 6.5×10^5 tonnes, 2.5×10^4 tonnes and 8.0×10^6 tonnes respectively (6). The consumption of these metals has been increasing steadily since then, at an annual rate of 4-6% (6, 8). It is expected that by the turn of this century the demand for these metals might double and the remaining years of this century would witness a sharp depletion in these metal resources on land (6, 9). Thus production of these metals in future from land-based mineral deposits alone will not be quite adequate. Hence, there is a justifiable need and urgency for manganese nodules exploration with a view to eventually exploiting the important elements contained therein.

The ocean floors all over the world, especially the Pacific and the Indian ocean, are covered with ferromanganese nodules. The total reserve of sea-bed manganese nodules is estimated at 1.7 trillion tonnes, which may contain 25-49 billion tonnes nickel, 20-30 billion tonnes copper, 3-5 billion tonnes cobalt and

500-800 billion tonnes manganese (1, 10). On a global scale while the land based copper reserves may last another 40 years, reserves in sea-bed may be adequate for as long as 6000 years. The supply of nickel from ocean may last 50,000 years. There may be optimistic exaggeration in these estimates (11) because only a small proportion of the total tonnage of polymetallic nodules has economic value (5); but what is of special interest to the Indian scientific community is that one fifth of all the sea areas containing nodules are located in the Indian ocean.

It is known that India is not richly endowed with the minerals of copper, nickel and cobalt. India's entire need for nickel and cobalt and about 50% of that of Cu (1987-88, Cu production 48,500 tonnes) are met by imports (10). The existing geo-political necessity and price-supply structure of world market have led the country to explore the nodules in the Indian ocean (9).

The mineralogical and chemical character of the nodules vary from location to location in the ocean-bed and changes in these characteristics do affect the processing of the nodules (12). The gaps in our knowledge concerning the type of bonding of elements in manganese nodules have proved to be great handicap in the development of metallurgical processes for obtaining different metal values from the multi-element ore manganese nodules (4). Mineralogy, mode of occurrence of Ni, Co and Cu in nodules and their implications in nodules processing constitute the central theme of this thesis.

A brief and critical review (Chapter-II), on nodules mineralogy, mode of occurrence of minor elements, genesis and extractive metallurgy, follows as a prelude to Chapter-III which defines

precise scope and statement of present research problem. The general details regarding materials used and experimental techniques employed are presented in Chapter-IV. The main emphasis in the subsequent two chapters (Chapters V and VI), which focus on mineralogy, chemical composition, internal structure and genesis of typical nodules from Central Indian Ocean Basin, is on occurrence of Ni, Co and Cu. The characterization and leaching studies (Chapters VII-IX) on synthetic analog of oxyhydroxide phases of manganese and iron are aimed to enhance our understanding of manganese nodules process mineralogy. The final conclusions of this investigation and scope for the future work are highlighted in the last chapter (Chapter-X).

CHAPTER - II

REVIEW OF THE LITERATURE

2.1 Preamble

The inner structure of nodules consists of concentric zones around a nucleus, usually a stone fragment, fossil bone material or a fragment of an older manganese nodule. The chemical compositions of concentric growth zones around the nucleus show that they are built up of hydrated manganese and iron oxides. The major interest in manganese nodules centres on the oxide constituents of manganese and iron because inter-element correlations have demonstrated that all the elements of potential economic interest (e.g. Ni, Co and Cu) are associated with these phases (13).

The BET surface area of nodules is approximately $200 \text{ m}^2/\text{g}$, indicating the cryptocrystalline nature of mineral constituents in nodules (14, 15). Although mineralogy of deep-sea manganese nodules has been the subject of many papers, considerable disagreement exists in literature regarding the nomenclature of constituent minerals, particularly the manganese minerals. This is attributed to the cryptocrystalline nature of minerals present which often makes them apparently amorphous to X-ray. Besides, comparison of the observed d-spacings in the X-ray diffraction patterns from nodules with those of the synthetically produced and terrestrial manganese and iron oxides have led to further ambiguities. The problem of nomenclature has been discussed by several authors on different occasions (16-23). The major source of confusion concerns

the phases: 10 A⁰-manganite-todorokite, todorokite-buserite, δ -MnO₂ birnessite, δ -MnO₂-vernadite, birnessite-7 A⁰-manganite.

Use of transmission electron microscopy (TEM) with selective area electron diffraction (SAED) and EDAX, high resolution transmission electron microscopy (HRTEM), IR and Mossbauer spectroscopy, in the recent past, have been of great help in solving many identification problems related with nodule mineralogy. Mineraloid (minerals with particle size less than 30-40 A⁰) are amorphous even to electron microscopy.

Occurrence of minor elements in manganese nodules is closely linked with the genesis or growth environments of the nodules (24-26). Typically, nodules forming in seamount regions are, in general, rich in Fe, Co, Pb and Ti and nodules in abyssal plane with thick sediment cover, low sedimentation rate and high biological productivity are enriched in Mn, Ni, Cu and Mg.

Almost complete association of Cu and Ni with manganese, and Co with either manganese or iron has been established with microprobe studies. However, uncertainties persist about the exact mode of occurrence of these elements. So far no single phase of these elements has been detected (27). Insufficient information is available regarding valency state of these elements (18, 28). Several theories on the manner in which these elements occur in nodules lie in the broad domain of crystal chemistry, surface chemistry and geochemistry. These include substitution (e.g. substitution of Fe³⁺ or Mn⁴⁺ in iron oxide phase or δ -MnO₂ by Co³⁺), occurrence as an essential part of crystal structure (e.g. Ni and Cu in todorokite), surface adsorption and solid solution (e.g. coprecipitation, redox processes at the surfaces).

The various aspects of manganese nodules have been reviewed in many excellent books, monographs and review articles (1, 4-6, 24-49). However, it is difficult to find a review which deals with extensive characterization of nodules and its relevance to subsequent chemical processing to recover the strategic elements like Ni, Co and Cu from them. In the following pages a review on manganese nodules is presented with particular emphasis on mineralogy, genesis, mode of occurrence of Ni, Co and Cu as well as the chemical processing of nodules and their inter-relationships.

2.2 Distribution and Chemical Composition

Ore grade nodules are generally found to occur 1,500 to 2,500 km from the land, under water at 4,000 to 6,000 m depth, in area of low sedimentation rate. The majority of them are located on the sediment surface so that the upper side is in contact with the sea-water and lower side in nearly liquid mud of the sediment water interface.

Figure II.1 shows the distribution of manganese nodules and of sedimentation rate in world oceans. The abundance of nodules in Indian ocean is intermediate between Pacific ocean (lowest sedimentation rate) and Atlantic ocean (highest sedimentation rate) (4). According to Archer (11), in 60% of areas in which nodules are present (i.e. $33 \times 10^6 \text{ km}^2$) the nodule density may be of the order of 15 kg/m^2 .

One of the key factors which determines the economic grade of the nodules is their chemical composition. It has been estimated that first generation nodule mining operation will be economically viable for nodules containing (Ni + Co + Cu) greater than 2.5% (5).

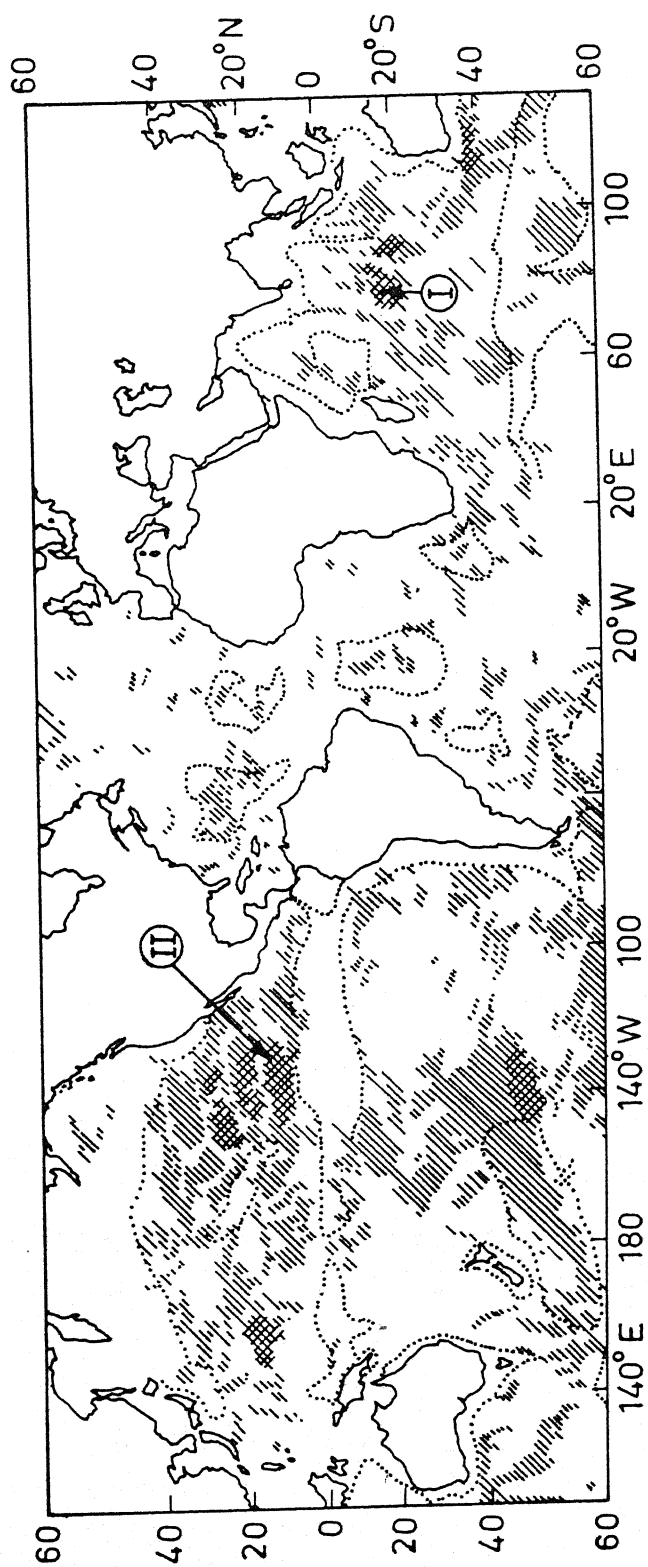


Fig. II.1. Distribution of ferromanganese nodules in the world oceans (hatched) with areas of significance (cross-hatched). Dotted line show limits of sedimentation rate 30 mm/1,000 years (49).

- (I) Central Indian basin.
- (II) Clarion Clipperton fracture zones.

Table II.1 gives the average composition of nodules from different oceans. The Indian ocean has an intermediate average composition between the Pacific and the Atlantic ocean. The average composition has only limited meaning because large scale regional variations in nodule compositions are often observed. It is now established that even the Pacific ocean can be divided into four regions namely of high iron, high manganese, high nickel and copper and high cobalt (vide Appendix-A, for details) (37, 52). The richest yet known manganese nodule field, where first nodule mining operation is likely to start, is situated in North Central Pacific between the Clarion Clipperton Fracture Zone, about $10-20^{\circ}\text{N}$ and $120-160^{\circ}\text{W}$ (4). The nodules in this region have average composition 1.16% Cu, 1.28% Ni, 0.23% Co, 24.6% Mn and an average abundance of 9 kg/m^2 in 6 million km^2 area (4, 12). The central Indian ocean basin is the most promising area in the Indian ocean (vide Appendix-A) (37). The most

Table II.1: The average composition of polymetallic nodules from different world oceans (50, 51)

Metal	Percent, dry weight basis			
	Pacific ocean	Indian ocean	Atlantic ocean	World average
Manganese	19.27	15.25	15.46	16.17
Iron	11.79	13.35	23.01	16.60
Nickel	0.846	0.534	0.308	0.49
Copper	0.706	0.290	0.141	0.25
Cobalt	0.290	0.241	0.234	0.30
Combined nickel and copper	1.552	0.824	0.449	0.74

enriched Mn, Ni and Cu values are reported from nodules associated with siliceous sediment in the central part of this basin between 10-15°S and 75-80°E in water depth of 5,000 m of about 0.7 million km² (49). On an average the nodule composition is 26.1% Mn, 1.20% Ni, 1.16% Cu and 0.12% Co (5). Average abundance of nodules in Central Indian ocean basin appears to be less than the best known region in Pacific ocean (5).

2.3 Morphology

Table II.2 provides an abbreviated summary of the nature and variability of the morphological characteristics of manganese

Table II.2: Morphological characteristics of manganese nodules (27)

<u>Characteristics</u>	<u>Nature and extent of variability</u>
Size	Size can vary from 0.5 to greater than 20 cm. Normal size 2-5 cm.
External shape	Various shapes observed e.g. spherical, ellipsoidal, discoidal or tabular, botryoidal, flat faced.
Surface texture	Surfaces are usually mammilated. Two types (i) smooth and (ii) gritty.
Color	Reddish brown to black with variation of black as most common.
Nucleus	can be any solid object, often influences shape of nodule. Example - rock, nodule fragment, volcanic glass, biological fragment - tooth, fossil, bone, sponges etc. Some time no apparent foreign nucleus.
Internal fracture	Generally filled with clay minerals, also clay free fractures lined with overgrowth of ferromanganese oxides. Two types - radial and concentric.
Interior zoning	Common feature of all nodules. Three types - (i) continuous varied band, (ii) continuous uniform band and (iii) discontinuous band.

nodules. The term 'morphology' is used in its broad sense to include not only external size and shape but also the macroscopic features present in nodule interior.

2.4 Mineralogy

2.4.1 Nature of Mineral Assemblage:

The phases in the nodules are fine-grained and intimately intergrown giving rise to complex internal structures (16, 17, 24). BET surface area measurement, Mössbauer spectroscopy, X-ray diffraction, transmission electron microscopy (TEM) and scanning electron microscopy (SEM) studies have revealed that particle size of crystallites in nodules may vary from 1000 \AA to less than 100 \AA (14-19, 53). The minerals are usually characterized by numerous structural defects, essential vacancies that might not be ordered, domain intergrowth, extensive solid solution and cation exchange properties that lead to non-stoichiometry and detract from long range ordering of the crystals (27, 54, 55). They appear to be amorphous or exhibit broad diffuse X-ray diffraction patterns. Particles less than $30\text{-}40 \text{ \AA}$ are amorphous even to electron microscopy (27). Even under TEM large number of particles either do not give any reflection or give one or two diffuse rings.

2.4.2 Oxyhydroxide Minerals of Manganese and Iron:

Crystal Structure:

Electron spin resonance (ESR) (56, 57), X-ray photoelectron spectroscopy (XPS or ESCA) (28, 58, 59) spectra and chemical methods (e.g. iodimetry and oxalate methods) (60, 61) have revealed that tetravalent manganese dominates in manganese nodules.

Presence of only small amount of divalent manganese has been indicated in ESR spectra of some nodules (57). However no trivalent manganese has been detected (28, 62) which is relatively unstable. Burns (63) points out that trivalent manganese may be stabilized in very distorted octahedral sites. Thus the presence of trivalent manganese may only be inferred from crystallographic considerations.

Mössbauer spectra of manganese nodules show the presence of trivalent iron (53, 64-68). Negligible amount of divalent iron (<2% FeO) has been found (65, 66). The presence of trivalent iron has also been confirmed by XPS or ESCA (28, 59).

Table II.3 compares the ratio of the radii of manganese and iron ions in different valency states to that of O^{2-} with ideal ratio for octahedral coordination.

Table II.3: Ratio of ionic radii of manganese and iron in different valency states to that of O^{2-}

Ion M^{z+}	Radius*	Ratio	Ideal ratio for octahedral coordination
	$r_{M^{z+}}$ or $r_{O^{2-}}$	$[r_{M^{z+}}/r_{O^{2-}}]$	
Mn^{2+}	0.83	0.593	
Mn^{3+}	0.645	0.461	
Mn^{4+}	0.53	0.3785	0.414 - 0.732
Fe^{2+}	0.78	0.557	
Fe^{3+}	0.645	0.4607	
O^{2-}	1.40	-	-

* Ref. (69, 70).

From Table II.3, it is clear that manganese in oxidation state II, III and IV and iron in oxidation state II and III almost exclusively prefer an octahedral coordination albeit in a more or less distorted manner. Depending on electron configuration, manganese atom will be egg-shaped in coordination polyhedral (Jahn-Teller effect) (22). Due to same coordination number, certain iron(III) oxide and manganese(IV) oxide are isostructural and they show epitaxial intergrowth in manganese nodules (18). The larger ionic radius of Fe^{3+} compared with Mn^{4+} results in larger spacings for the $(10\bar{1}0)$ and $(11\bar{2}0)$ planes of the hexagonal close packed systems (approximately 2.50 to 2.56 \AA and 1.48 to 1.54 \AA ; corresponding distance for Mn^{4+} are 0.06-0.10 \AA less) and Fe-Fe interatomic distance across edge-shared $(\text{Fe}(\text{O},\text{OH})_6)$ octahedra ranges from 2.95 to 3.05 \AA (Mn-Mn distance approximately 2.87 \AA) (27, 71).

By appropriate edge and/or corner sharing of the basic octahedron unit (i.e. $\text{M}(\text{O}, \text{OH}, \text{H}_2\text{O})_6^{z+}$ octahedron, $\text{M} = \text{Mn}^{4+}, \text{Fe}^{3+}$ etc.) a unified lattice geometry can be displayed for various groups of manganese and iron oxyhydroxides (e.g. chain, ring and layer structure). Typical arrangements of octahedra sharing relevant to manganese minerals are shown in Figure II.2(a) (layer structure, edge sharing in two dimensions) and Figure II.2(b) (tunnel structure, edge and corner sharing). More detailed discussion on the structural aspects of manganese and iron oxide-hydroxides may be found in several papers (22, 36, 73-75).

Recently Turner and Buseck (76) proposed a nomenclature scheme for the structure of manganese(IV) oxides. In this, the families of oxides are designated by the symbolism $\text{T}(\text{m},\text{n})$, where

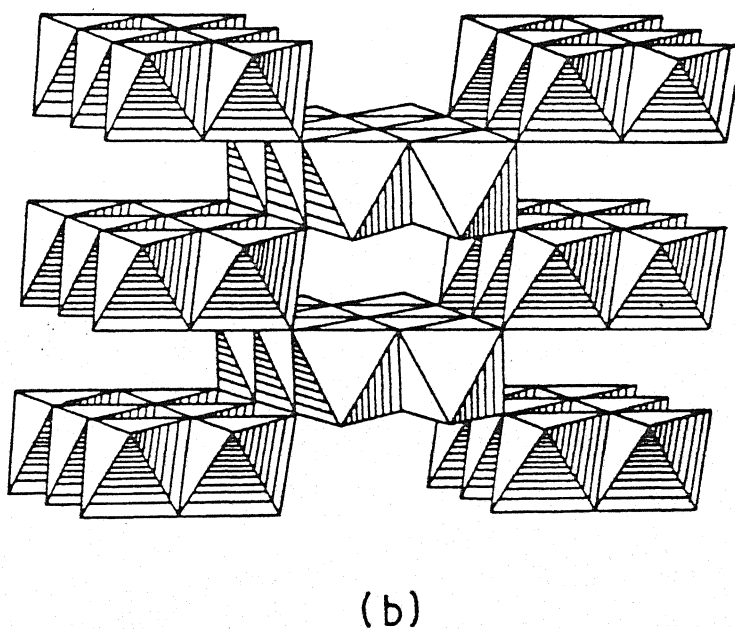
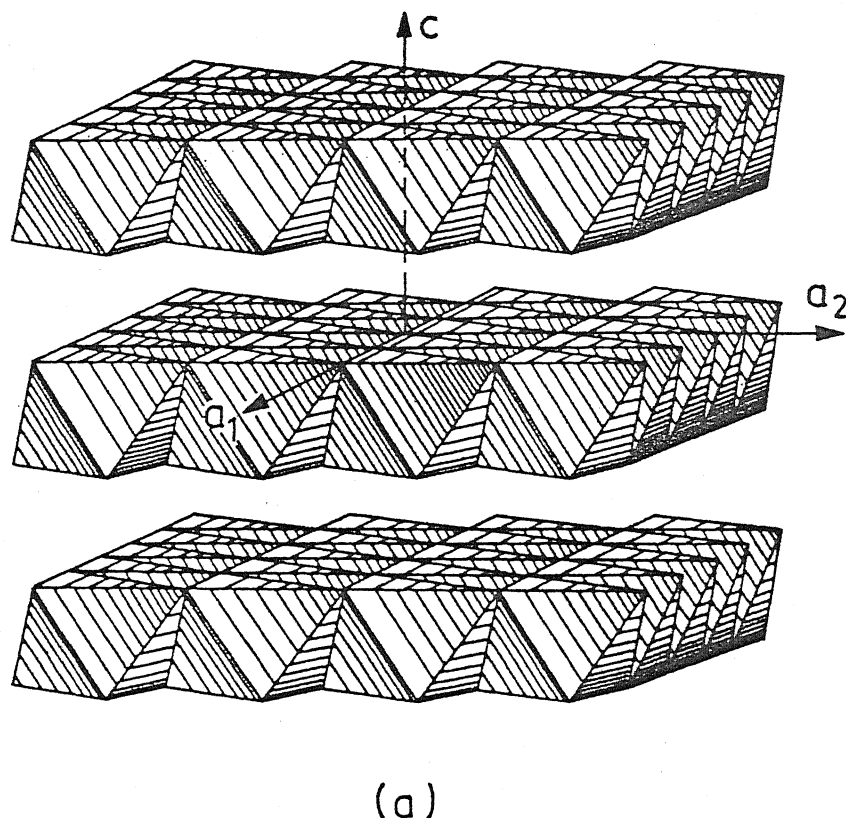


Fig. II.2. Typical arrangements of octahedra $[\text{Mn}(\text{O}, \text{OH}, \text{H}_2\text{O})_6]^{2+}$ sharing in manganese (IV) oxide minerals (a) layer structure-edge sharing, after Giovanoli (22), (b) tunnel structure-edge and corner sharing, after Burns and Burns (18).

T denotes the tunnel structure and m and n are width of infinite chain (in units of octahedra) forming walls of tunnel (see Table II.4).

Table II.4: Nomenclature of Mn(IV) oxide structure (76)

Family name	Common dimension m	Variable n				Sheeted end member n \rightarrow ∞
		1	2	3	4	
Nsutite	1	T(1, 1)	T(1, 2)	T(1, 3)	T(1, 4)	
Hollandite-romanechite	2	T(2, 1)	T(2, 2)	T(2, 3)	T(2, 4)	Birnessite
Todorokites	3	T(3, 1)	T(3, 2)	T(3, 3)	T(3, 4)	Buserite

According to this scheme, the structure shown in Figure II.2(a) and Figure II.2(b) may be represented as $T(m, \infty)$ and $T(1, 2)$. The relationship between todorokite $T(3, n)$ and buserite $T(3, \infty)$ may be noted. Birnessite has a $T(2, \infty)$ structure. The mineral referred to as δ - MnO_2 in literature is randomly stacked birnessite (23). The nomenclature scheme of Turner and Buseck (76) adequately differentiates among the manganese(IV) oxides in terms of $Mn(IV)O_6$ octahedra arrangement, however, it fails to elucidate the presence of other ions in the structure. Asbolanes are hybrid layer manganese(IV) oxides consisting of alternations of the layers of Mn^{4+} octahedra and Co-Ni octahedra (77). It is not possible to represent the structure of asbolanes in terms of $T(m, n)$ nomenclature.

Goethite (α -FeOOH) has an alternating double chain structure such as shown in Figure II.2(b). The structural differences among the oxyhydroxide of Fe(III) can be understood by defining

the close packed oxide or oxide-hydroxide lattice and placing iron into tetrahedral or octahedral sites. Table II.5 illustrates the structural differences among iron(III) oxides and oxide-hydroxides. 80% of Fe in δ -FeOOH is present in octahedral position (78).

Table II.5: Structure of oxide and oxyhydroxides of iron(III) (74, 75, 79)

Compound	Oxide lattice structure*	Fe(III) site/s	Stacking sequence of closed-packed oxygen layer	Stacking direction
α -FeOOH	H.C.P.	Octahedral	-AB-AB-AB-	$\langle 001 \rangle$
δ -FeOOH	H.C.P.	Octahedral and tetrahedral	-	$\langle 001 \rangle$
α -Fe ₂ O ₃	H.C.P.	Octahedral	-AB-AB-AB-	$\langle 001 \rangle$
γ -FeOOH	C.C.P.	Octahedral	-ABC-ABC-	$\langle 051 \rangle$
β -FeOOH	B.C.C.	Octahedral	-	-

* H.C.P. - Hexagonal close packed, C.C.P. - Cubic close packed, B.C.C. - Body centered cubic.

Because of structural similarities, topotactic transformation of δ - and γ -FeOOH to α -FeOOH are possible. Also α -FeOOH itself can transform into α -Fe₂O₃ topotactically (74, 78). The crystallographic and orientation relationships among δ -FeOOH, α -FeOOH and α -Fe₂O₃ are illustrated in Figure II.3. The mineral β -FeOOH which has hollandite type tunnel structure does not have any structural analog and can transform to mineral like α -Fe₂O₃ non-topotactically (74).

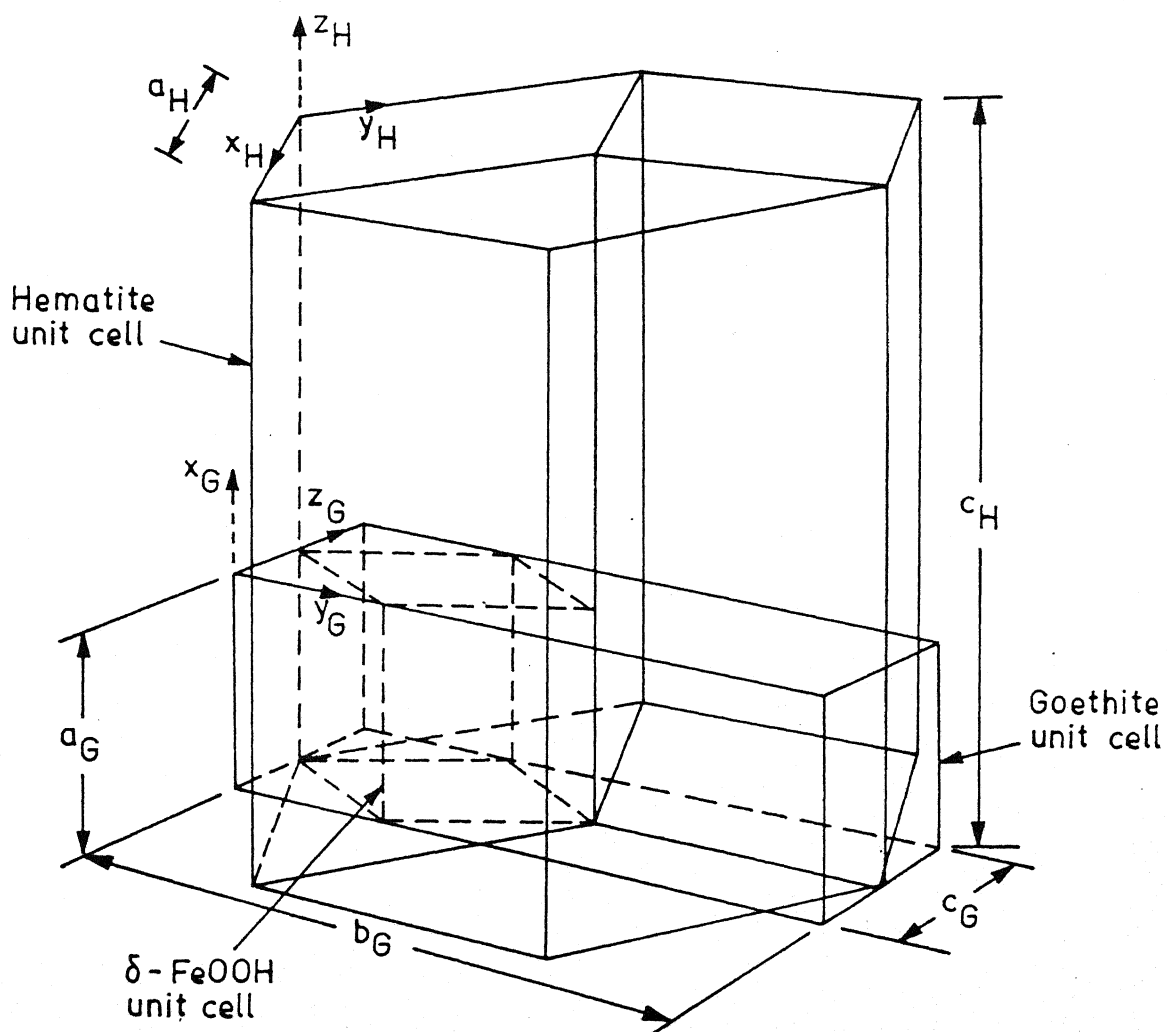


Fig. II.3. Orientation relationship between structures of oxyhydroxides and oxide of trivalent iron (78).

Minerals:

A large number of manganese and iron oxide minerals have been identified or tentatively suggested to occur in manganese nodules (36, 80-83). Todorokite, birnessite and vernadite (or $\delta\text{-MnO}_2$) are the predominant manganese oxide minerals occurring in manganese nodules. Goethite is the most frequently observed iron oxide mineral. Available crystallographic data and information on chemical composition and crystal structure together with X-ray diffraction data are listed in Table II.6 for the predominant manganese and iron oxide minerals and few other minerals relevant to our discussion.

Manganese oxide mineral characterized by X-ray diffraction lines at 9.5 to 9.8 \AA and 4.8 to 4.9 \AA is one of the most common phases observed in the manganese nodules. This phase, a hydrated Mn-Mg-Ca-Na-Ni-Cu oxide, often with significant concentration of Ni and Cu, was characterized as todorokite or buserite (10 \AA manganite) (Table II.6) due to its disordered nature, confusing X-ray pattern and difficulty in determining the structure type by X-ray diffraction measurements (20, 21, 76, 85, 86). TEM and HRTEM studies on the nodules have confirmed the occurrence of todorokite in the nodules and its tunnel structure (76, 87, 88). Buserite has a layered structure (90, 91). Todorokite shows both fibrous and platy morphology (76). Chukhrov et al. (83, 87) have indicated that as many as five todorokite polymorphs might exist, all having the same 'b' (2.85 \AA) and 'c' (9.59 \AA) parameters and 'a' parameter as multiple of 4.88 \AA (i.e. having structure such as T(3,2), T(3,3), T(3,4) etc.) (76, 87, 88).

Table II.6: Manganese and iron oxide minerals (27, 36, 81-84)

Mineral	Approximate formula	Crystal system	Cell parameters, Å ^o a b c	Prominent four X-ray lines (d-Å ^o)
<u>Mn-oxide</u>				
Todorokite	(Ca, Na, K, Ba) (Mg, Mn ²⁺ , Zn) Mn ₅ O ₁₂ ·xH ₂ O	Pseudo-orthorhombic	9.75 2.85 9.59	9.68, 4.80, 2.39, 1.33
Buserite	Na Mn oxide hydrate	Hexagonal	8.41 - 10.01	10.00, 7.28, 5.06, 1.47
Synthetic Na-birnessite	Na ₄ Mn ₁₄ O ₂₇ ·9H ₂ O	Orthorhombic	8.54 15.39 14.26	7.09, 3.56, 2.51, 2.42
Synthetic Na free birnessite	Mn ₇ O ₁₃ ·5H ₂ O	Hexagonal	2.84 - 7.27	7.21, 3.61, 2.46, 2.33
Birnessite	(Na, Ca, K) (Mg, Mn) Mn ₆ O ₁₄ ·5H ₂ O	Hexagonal	2.85 - 7.1	7.27, 3.60, 2.44, 1.41
Vernadite (or δ-MnO ₂)	MnO ₂ ·m(R' ₂ O, RO, R ₂ O ₃)·nH ₂ O	Hexagonal	2.86 - 4.7	2.46, 2.20, 1.42
Co-Ni asbolane	[Mn ⁴⁺ O _{2-x} (OH) _x] _x + [R' ₂ ²⁺ (OH) _{2-2y+x}] _{1-y}	Hexagonal	2.823 - 9.34 3.04 - 9.34	9.60, 4.82, 2.45, 1.42
<u>Fe-oxide</u>				
Goethite (α-FeOOH)	FeOOH	Orthorhombic	4.65 10.02 3.04	4.18, 2.69, 2.45, 2.19
Akaganeite (β-FeOOH)	(OH, Cl, H ₂ O) Fe ₈ (O, OH) ₁₆	Tetragonal	10.48 10.48 3.02	7.40, 3.31, 2.54, 1.64
Lepidocrocite (γ-FeOOH)	FeOOH	Orthorhombic	3.88 12.54 3.07	6.26, 3.29, 2.47, 1.94
Ferroxyhyte (δ'-FeOOH)	FeOOH	Hexagonal	2.93 - 4.60	2.54, 2.22, 1.69, 1.47
Ferrihydrite	5Fe ₂ O ₃ ·9H ₂ O	Hexagonal	5.08 - 9.40	2.50, 2.21, 1.96, 1.48

R = Ca, Co, Fe, Mn etc.; R' = Na, K.

Birnessite in manganese nodules is characterized by X-ray diffraction lines at 7.0 to 7.3 \AA and 3.5 to 3.6 \AA . It has been suggested that both the sets of lines must be present to establish the presence of birnessite because hollandite, cryptomelane and zeolites such as phillipsite, clay and mica show the 7 \AA line (27, 80). Birnessite has a layered structure ($T(2,\infty)$ type) and a surface area of 30-75 m^2/g (27, 92, 93).

The phase in nodules giving two X-ray diffraction lines at 2.40-2.45 \AA and 1.41-1.42 \AA is designated as vernadite or $\delta\text{-MnO}_2$. This phase is characterized by poor crystallinity, very high surface area (300 m^2/g !) and variable composition (27, 92). This phase is often found associated with iron. It is believed (94) that iron present may be intimately associated with or may be found as an epitaxial growth of ferroxhyte ($\delta'\text{-FeOOH}$) rather than be a part of vernadite structure. Cobalt is found to be associated with vernadite (95).

Other manganese minerals that have been reported in manganese nodules include pyrolusite, ramsdellite, nsutite, hollandite, psilomelane etc. A good discussion of these minerals and others is found in a review by Burns and Burns (54) and recent review by Giovanoli (73).

Poor understanding of oxyhydroxide minerals of iron present in manganese nodules stems from two factors: the fine grain size (or cryptocrystallinity) and the fact that iron is present in octahedrally coordinated high spin ferric state. As a result of the fine grain size, X-ray diffraction patterns have rarely been recorded for these minerals. Because of symmetry of d^5 electron shell in ferric ion, it has been quite difficult to identify the minerals using Mössbauer spectroscopy (96). The lack of our

understanding of iron mineralogy in nodules is significant not only from the geochemistry point of view but from the processing point of view also; this is on account of iron bearing minerals constituting important gangue material in nodules and the reported positive association of Co with Fe. In spite of difficulties, Mössbauer spectroscopy and electron diffraction techniques have been frequently used for their identification (19, 53, 64-68, 96, 97). These efforts are reviewed by different workers (27, 71, 96).

Based on Mössbauer effect studies of iron in manganese nodules and associated sediments in five areas in equatorial and south-west Pacific, Thijs et al. (97) concluded that the form of iron in deep-sea manganese nodules is identical and independent of the environment of deposition. According to these workers (97), iron occurs in deep-sea nodules as a mixture of goethite (α -FeOOH), akaganeite (β -FeOOH), lepidocrocite (γ -FeOOH) or poorly crystallized Fe-oxides. Iron oxyhydroxide minerals in nodules have particle size less than 200 \AA (19, 53).

Goethite (α -FeOOH) is the polymorph to which most other FeOOH phases revert on aging through topotactic transformations. High concentration of Cl^- inhibits the formation of goethite. Thus the widely reported occurrence of goethite in nodules is probably secondary and may result from the fact that it is the end product of hydrolysis and oxidation in FeOOH phases such as ferroxhyte, lepidocrocite etc. (71).

Nomenclature Problems:

Confusion in the manganese nodule mineralogy is attributed to the cryptocrystalline nature of minerals present and the difference of observed d-spacings in X-ray diffraction work with those

of synthetically produced and terrestrial manganese and iron oxide phases. The major source of confusion surrounds manganese oxide minerals since iron oxide minerals have most often been missed in X-ray diffraction studies. In Table II.7 are summarized different names assigned to different d-spacings found in nodules on the basis of comparison with synthetic or terrestrial minerals.

The synthetic 10 \AA° manganite phase (or 10 \AA° manganate (21)) (Na-Mn oxide hydrate) was given the name buserite in honor of W. Buser (14) by Giovanoli (22, 111). Due to poorly crystalline nature of phases in manganese nodules and closeness of 'd' value of buserite and todorokite (Table II.7), the phase in nodules showing 10 \AA° and 5 \AA° lines was often cited as todorokite, buserite (or 10 \AA° manganate) (20, 21, 85, 112). Nomenclature problem was further complicated by the proposition of Giovanoli et al. (22, 102) that todorokite is not a valid mineral and it is a mixture of buserite, birnessite and manganite ($\gamma\text{-MnOOH}$). Validity of todorokite as the mineral species, its occurrence in manganese nodules and its tunnel structure (tektomanganate group) has been established by XRD, TEM and HRTEM (20, 55, 76, 85, 87, 88, 113).

Giovanoli (21, 89) has accepted todorokite as a valid mineral species, however the mineral has been put in the phyllomanganate category (73, 103, 104). Most authors do not distinguish between 10 \AA° manganate or buserite and todorokite (24, 25, 39, 49, 73, 86, 100-104, 114).

It has been observed that the 10 \AA° phase in nodules on heating gets converted to either birnessite (7 \AA° , 3.6 \AA°) or $\delta\text{-MnO}_2$ (2.4 \AA° , 1.4 \AA°) (25, 115). Buserite is known to change into birnessite on drying or heating (90, 107). Occurrence of

Table II.7: Summary of various nomenclatures used for manganese minerals in nodules

Observed d-spacings, (approx.)	Name assigned	References
10, 5 Å ^o	10 Å ^o manganite (s)	(<u>14</u> , <u>24</u> , <u>72</u> , <u>98-101</u>)
	10 Å ^o manganate (s)	(<u>4</u> , <u>22</u>)
	Buserite (s)	(<u>22</u> , <u>102-104</u>)
	Todorokite (t)	(<u>25-27</u> , <u>33</u> , <u>61</u> , <u>86</u> , <u>105</u> , <u>106</u>)
7, 3.6, 2.4, 1.4 Å ^o	7 Å ^o manganite (s)	(<u>24</u> , <u>72</u> , <u>98-101</u>)
	Manganous manganite (s)	(<u>19</u>)
	Sodium manganese(II,III) manganate(IV) (s)	(<u>107</u>)
	Birnessite (s/t)	(<u>17</u> , <u>19</u> , <u>27</u> , <u>33</u> , <u>105</u> , <u>108</u>)
	δ-MnO ₂ (s/t)	(<u>14</u> , <u>107</u>)
2.4, 1.4 Å ^o	Birnessite (2 lines)	(<u>109</u>)
	δ-MnO ₂ (s/t)	(<u>14</u> , <u>27</u> , <u>99</u> , <u>100</u> , <u>110</u>)
	Vernadite (t)	(<u>83</u>)
	z-disordered birnessite	(<u>23</u> , <u>103</u> , <u>104</u>)

(s) - Synthetic; (t) - Terrestrial.

buserite (layered structure) has been reported in some recent studies (112, 116). The phase referred to as todorokite by Perseil and Giovanoli (103) has layered structure. Chukhrov et al. (84) have suggested that mixed-layer asbolane (hybrid layered structure manganese oxide)-buserite assemblages occur in oceanic ferromanganese concretions. X-ray diffraction patterns containing lines at 9.8, 4.8 and 2.4 Å⁰ can correspond to any one of the four phases viz. buserite, asbolane, mixed layer asbolane-buserite and todorokite (84).

The analogy between synthetic Na-birnessite, Na free birnessite (22, 107), terrestrial birnessite (117) and the phase (7.0 Å⁰, 3.6 Å⁰) in manganese nodules is well established (118, 119). 7 Å⁰ manganite, manganous manganite, sodium manganese(II,III) manganate(IV), birnessite and marine birnessite represent the same phase having layered structure of the type T(2,∞). The name birnessite has been recommended for this phase (19, 54).

The phase in manganese nodules with d-spacings 2.40-2.45 Å⁰ and 1.40-1.42 Å⁰ has been designated as δ-MnO₂ or disordered birnessite (Table II.7). The main point of debate about this phase is that whether it should be considered a separate phase at all. Giovanoli et al. (23, 120) have reported that this phase is a randomly stacked birnessite and δ-MnO₂ does not correspond to the stoichiometry of the phase. Giovanoli (23) has suggested that the name δ-MnO₂ be abandoned. Burns and Burns (18) recommend that δ-MnO₂ and birnessite be considered as two distinct phases. Burns and Burns's recommendations are based on the observation of Chukhrov et al. (83, 87) (i.e. Mn²⁺ rich todorokite is oxidized to δ-MnO₂) and the finding of Brown (18, 121) (i.e. δ-MnO₂ under pressure

rehydrate to show two additional lines at 9.6 \AA^0 and 4.8 \AA^0). Birnessite does not rehydrate under pressure to give any additional lines (18, 121). There are ample evidence to suggest similarity between this phase in nodules ($d = 2.4$ and 1.4 \AA^0) and the synthetic disordered variety of birnessite (23, 92, 102, 122). Depending upon crystallinity the same phase may behave differently with respect to pressure-induced rehydration. Besides, ions like Mg, Ni and Cu sorbed on the surface of natural marine phase may alter the course of rehydration reaction significantly. This is because the 10 \AA^0 phases (both todorokite and busserite) are known to be stabilized by these ions (20, 90, 101).

$\delta\text{-MnO}_2$ or disordered phase has been named as vernadite (83, 123, 124) in the Russian literature. Giovanoli and Chukhrov agree with each other that $\delta\text{-MnO}_2$ or vernadite refers to the same phase with d-spacings 2.40 \AA^0 and 1.41 \AA^0 (23). Haynes et al. (27) point out that vernadite is distinguished from structurally disordered birnessite by its high specific surface area. This perhaps is not true because the surface area of the so-called disordered birnessite was found to be of the order of $300 \text{ m}^2/\text{g}$ by BET determination (92). Although $\delta\text{-MnO}_2$, vernadite and randomly stacked birnessite represent the same disordered variety of birnessite, however the name $\delta\text{-MnO}_2$ or vernadite may be used for this phase because of its high surface area which may impart unique surface properties.

Identification Techniques and Their Limitations:

The principal method for the identification of the minerals in manganese nodules has been X-ray powder diffraction technique both with diffractogram and photographic methods. X-ray method is a very powerful tool for the crystals of usual size

($\geq 1 \mu\text{m} \times 1 \mu\text{m} \times 1 \mu\text{m}$). Minerals in manganese nodules have complex assemblages and vary in size from 1000 \AA to less than 100 \AA . X-ray techniques have severe limitations for this kind of material and often result in amorphous or broad diffuse peaks (16, 35). X-ray diffraction, if not used carefully, may lead to grave error of interpretation. Uncritical use of X-ray techniques in the past have led to erroneous reports of minerals in manganese nodules.

It may be noted here that by cutting the respective edifice in Figure II.2(b) bit by bit we end up at some stage with tetrametric pieces shown in Figure II.4. This unit may be responsible for the interatomic vectors reflected in X-ray powder patterns of extremely finely divided varieties of quite different phases. They will produce in the observed range of powder pattern two reflections only. It will obviously be most difficult, if not impossible, to attribute such a phase to one particular structure type from X-ray diffraction evidence alone. Reported evidence of $\gamma\text{-MnO}_2$ (4 lines pattern, $d=2.4$ and 1.41 \AA strong lines) was probably due to this reason (22). Dehydration and oxidation of nodules when removed from the sea (121, 125) and presence of preferred orientation (126) may result in further complexities in X-ray diffraction patterns. Burns and Burns (18) have recommended the use of $\text{Fe}(K_\alpha)$ radiation (with Mn-filter). This source not only provides the simplest method of reducing acute fluorescence when Co and Cu radiations are used, but it also increases the precision of lines at large d-spacings ($9.5\text{-}10.0 \text{ \AA}$). $\text{Mo}(K_\alpha)$ radiation with Guinier-De-Wolf X-ray camera gives good result for finely crystalline material in order to resolve smaller d-spacings (22).

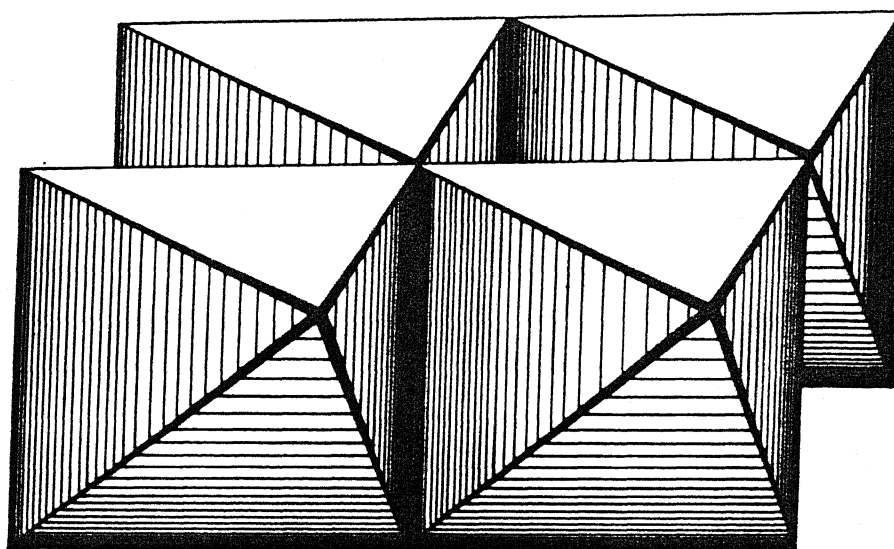


Fig. II.4. Tetrametric unit resulting by cutting down the structure in fig. II.2(b), after Giovanoli (22).

The complex assemblage of particles smaller than 1 μm found in the manganese nodules is best suited to studies by TEM. The morphology of manganese and iron oxide minerals as revealed by transmission electron microscopy is not specific but some distinctive features can occasionally be used as an aid in identification. Selected area electron diffraction (SAED) technique (in TEM) serves as an important technique for phase identification in manganese nodules (22, 83, 124, 127, 128). Chukhrov et al. (124) have pointed out that although SAED with TEM can be very useful on its own, combination with microanalysis arrangement (EDAX/WDS) can add appreciably to its value for unambiguous identification. Phase identification by TEM provides valuable insight into the nature of phases present in nodules e.g. crystallinity, disorder in the structure etc.

Smaller particles with sizes less than 30-40 \AA (named as mineraloids (27)) are amorphous even to the electron microscope. So far no definite phases of nickel, cobalt and copper have been identified in manganese nodules although these elements are known to be present in them. This remains a mystery whether it is due to the small particle size or an altogether different mode of occurrence. The high vacuum and high energy of electron beam in an electron microscope may destroy the sample even. These problems can be minimized using cold stage and HVTEM. Structure imaging by high resolution transmission electron microscopy (HRTEM) and simultaneous microanalysis have been used to identify and reveal the structure of phases and establish the nature of defects and intergrowth in manganese nodules (55, 76, 88).

Some of the problems of structure identification in tetravalent manganese oxide have been addressed through IR spectroscopy by Potter and Rossman (129). They demonstrated that it is possible to distinguish between different (MnO_6) structural profiles in the mid IR region. Using this technique the layered structure of birnessite was established. Todorokite and buserite were established as distinct phases; however the exact nature of todorokite structure could not be determined. IR can probably be used as a secondary tool for identification.

Mössbauer spectroscopy offers a powerful method for studying the mode of incorporation of iron in nodules and marine sediments. This technique is specific to this element and reveals information on the chemical environment of Fe in the lattice. As pointed out earlier, its main disadvantage lies in the difficulty in distinguishing the spectra of octahedrally coordinated high spin ferric iron surrounded by oxygen ligands because of high symmetry of this arrangement. Limited attempts to study the iron mineralogy in nodules by Mössbauer spectroscopy have been reviewed by Johnston and Glasby (96) and Thijs et al. (97). Precision and reproducibility aspects in Mössbauer spectroscopy are discussed by Dyar (130). Precise Mössbauer parameters of iron oxide and oxyhydroxide minerals are available in recent papers (131, 132). Based on Mössbauer spectroscopy data (133) it has now become clear that ferrihydrite and goethite are two distinct minerals. The hyperfine field (H_i) of ferrihydrite (470-500 kOe, 4.2°K) is different from that of goethite (505 kOe, 4.2°K). Efforts to distinguish between α - and β -polymorphs of FeOOH in nodules by Mössbauer spectroscopy have not been successful (97).

The limitations of the various identification techniques have been summarized in Table II.8.

Table II.8: Phase identification techniques - limitations

Technique	Limitations
X-ray diffraction	Many nodule minerals are too fine-grained or amorphous making X-ray diffraction technique inapplicable. Not useful for phase concentration <5 wt %
SEM, TEM, HRTEM and electron probe	Sample must be small enough to fit inside sample chamber. Less than about 6 mm ² area is viewed by SEM, less than 1.5 mm ² for TEM and about 50 mm ² for an electron probe. Some of the minerals are amorphous even to TEM
IR spectroscopy	Medium sensitivity down to 1-2%. Broad absorption of OH group may overlap other spectral features in application to nodules
Mössbauer spectroscopy	Difficulty in distinguishing the spectra of octahedrally coordinated high spin ferric iron
Thermal analysis (TGA and DTA)	Information is often empirical and complementary analytical methods are needed to interpret data.

2.4.3 Accessory Minerals:

The accessory minerals in nodules include silicates and biogenic minerals. Detailed accounts of these are presented by Bischoff, Piper and Leong (134), Glasby and Thijssen (135) and Haynes et al. (27, 80, 81). The most commonly observed minerals include α -quartz, feldspars, montmorillonite, phillipsite and calcite. Mohapatra and Sahoo (136) have identified the zeolite mineral merlinoite in Indian ocean nodules for the first time.

2.5 Genesis

The important aspects of nodule genesis are the source of metals, mechanisms of transportation to the site of nodule growth and the growth processes leading to the accretion of oxyhydroxide phases in nodules (33, 37, 137). The growth processes and growth features are of particular importance to understand the macroscopic mechanisms leading to the incorporation of Ni, Co, Cu etc. in nodules (25, 26, 37, 49, 100, 138, 139).

2.5.1 Source of Metals and Transportation Mechanisms:

There are three hypotheses concerning the primary source of manganese and other elements: (a) terrigenous, (b) volcanic and (c) cosmogenic (4, 37, 137). There is no general consensus regarding source of metals for nodule growth (37). Most of the deposits derive their metals from more than one possible source (37).

Irrespective of the source of metals some mechanism is required to transport them to reaction sites where they can be extracted into the forming of ferromanganese oxides. The mechanisms by which manganese and associated elements can be transported to the sediment-water interface are: (i) normal processes of oceanic circulation, (ii) biological removal and transportation by planktons and (iii) post sedimentary remobilization (4, 37). Planktons live in great quantity in surface layer of the sea depending on UV radiation. The predominant part of the plankton is composed of either calcium carbonate or opaline SiO_2 . After death planktons sink down to sea-bottom. Pressure dependent dissolution of calcium carbonate test at about 4000 m water depth (calcium carbonate compensation depth (CCD)) and dissolution of opaline test

from sea-surface to the bottom and within the sediment can serve as the mode of transport and source of element for nodule growth (4, 37). The parallel increase in Ni and Cu accumulation rate, depth and productivity support the hypothesis that much of Ni and Cu is transported by rains of biogenic debris (26, 140). Based on material balance calculations Marchig and Gundlach (141) contended that for nodules in north central Pacific, which lie on porous siliceous ooze, more than 96% of metal content is received by diagenetic mobilization in sediment.

2.5.2 Growth Processes:

The genesis of ferromanganese nodules on deep-sea bottom of most oceans has been the object of chemical (24, 105, 142-144) as well microbiological speculations (143-149). Since nearly all nodules contain nuclei of minerals, clays, remnants of bones, teeth and various other components, these nuclei are thought to be the starting point for Mn-Fe precipitation and accumulation processes (33, 105, 142, 147). The precipitation as well as continuous accretion of the Mn(IV) and Fe(III) oxides may have been caused by chemical oxidation and/or by the activity of manganese oxidizing micro-organisms (143, 144).

Basically two different growth processes are responsible for nodule formation: (a) diagenetic growth from the pore water and (b) hydrogenetic growth from the near bottom sea-water. Evidence for the two distinct modes of precipitation of metals in abyssal nodule was first presented by Raab (150). He noted that nodules from abyssal northern equatorial Pacific had compositionally distinct upper and lower surfaces; the upper surfaces were

enriched in Fe, Co and Pb while lower surfaces contained more Mn, Ni, Cu and Mo. Ku and Broecker (151) and Lalou and Brichet (152) also noted that upper and lower surfaces of nodules often have distinctly different α -activities. Usui suggested that the asymmetry and discontinuity of individual thin layers in the nodule internal structure indicate the possibility of intermittent overturn and/or rotation (100). The major source of overturn and rotation are unknown (153, 154), however implication of this is that the distinction between top and bottom is apparent and it is not always possible to assign the elements in nodule to either source.

Significant advances in the understanding of nodule genesis have emerged from the detailed investigations on inter-relationships of nodule composition, mineralogy and internal structure with growth environment i.e. sediment type, sedimentation rate, submarine topography, bottom sea currents, biological productivity, sea and pore water composition etc. (4, 24-26, 100, 115, 139, 155-163).

Marine diagenesis is well documented in literature (26, 105). Depending upon the extent and nature (oxic or reducing) of diagenesis, the mineralogy and metal uptake of nodules vary (26). Figure II.5 presents a summary of observations on mineralogy and geochemistry of nodules growing in different marine environment.

Hydrogenetic growth dominates in area of low productivity, high sedimentation rate and seamount regions, where sediment covers are thin or absent (25, 26, 156-158). The hydrogenetic nodules (or substance) consist of mixture of intimately intergrown δ -MnO₂ and FeOOH.XH₂O. These are characterized by a low Mn/Fe ratio and

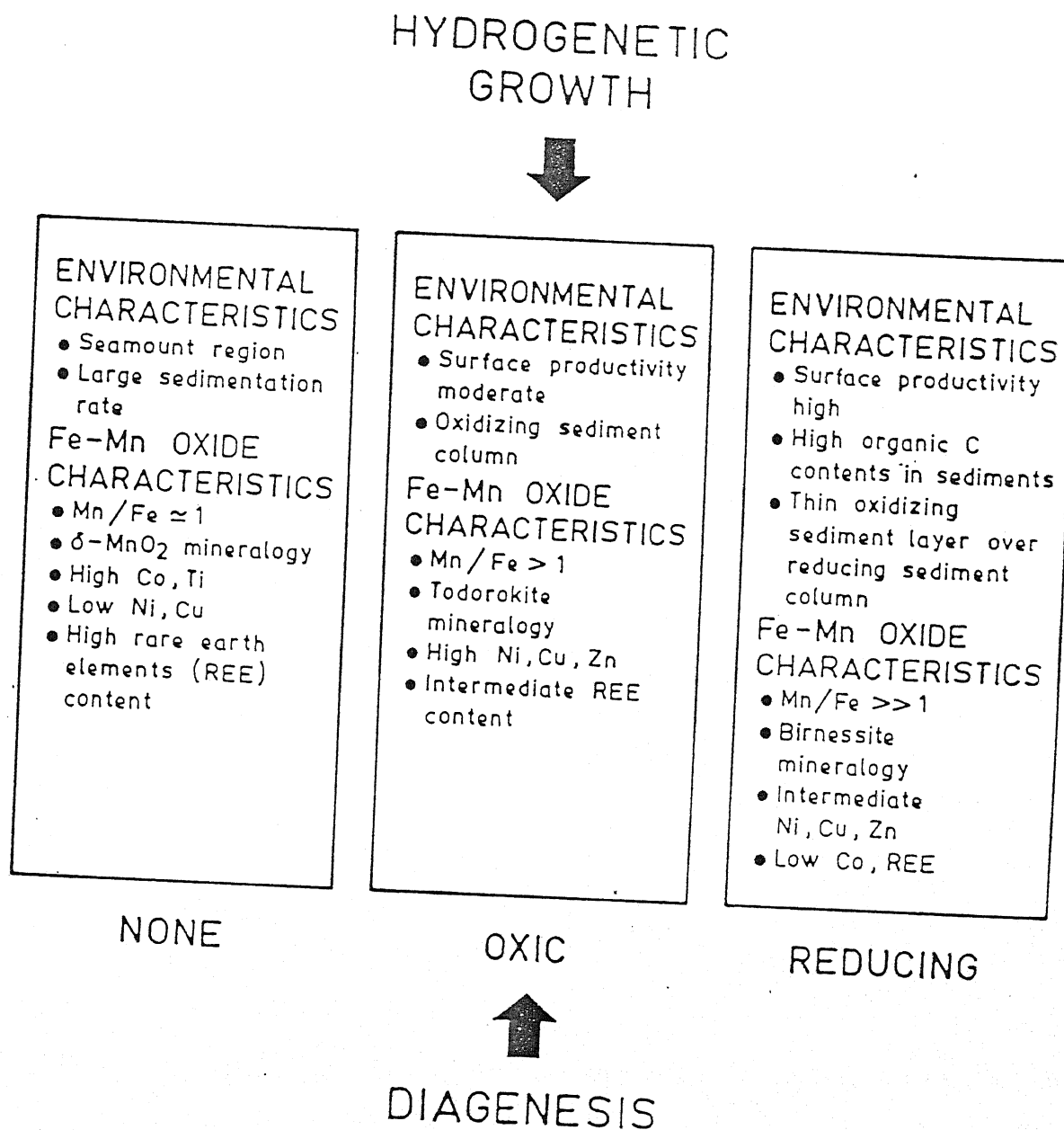


Fig. II.5. Mineralogy and geochemistry of nodules forming in different marine environment, adopted from Lyle (26).

enrichment of minor elements such as Co, Ti and Pb and very poor crystallinity (grain size $<300 \text{ \AA}$) (25, 26, 100, 138, 139, 156-158).

Diagenetic growth predominates in the area of high biological productivity, low sedimentation rate and thick sediment cover (found in abyssal plane). Diagenetic nodules are characterized by high concentration of Ni, Cu, Mg etc. and high Mn/Fe ratio. The major phase in diagenetic substance is the 10 \AA -phase (todorokite/buserite). The crystallinity of diagenetic substance is better compared with hydrogenetic substance (grain size $>700 \text{ \AA}$) (25, 26, 100, 138, 158).

Mn/Fe ratio provides a measure of relative importance of sea-water and diagenetic source of material in nodule growth (157, 159). The negative correlation of Mn and Fe is caused by differing mixture of Fe-rich hydrogenetic material and Mn-rich diagenetic substance. Due to enrichment of Ni and Cu in diagenetic substance these elements show a positive correlation with Mn/Fe ratio. Several attempts (25, 26, 100, 138, 157, 164) have been made to discriminate among different genetic type of nodules using Mn/Fe ratio and total Ni, Co and Cu content (Figure II.6). Hydrogenetic (type-B), diagenetic (type-A) and mixed-type (type-AB) show Mn/Fe ratio as less than 2.5, between 2.5-4.0 and greater than 4.0 respectively (25, 26, 157). Another A_c type of nodules are noted, in regions of very high biological productivity, which are characterized by high Mn/Fe ratio (>5.0) and lower Ni and Cu contents compared to type-A nodules (25). Nodules also contain differing proportions of Fe-rich silicate phases. This additional content of Fe results in a change in Mn/Fe ratio and correlations between different genetic type of nodules and Mn/Fe ratio (157).

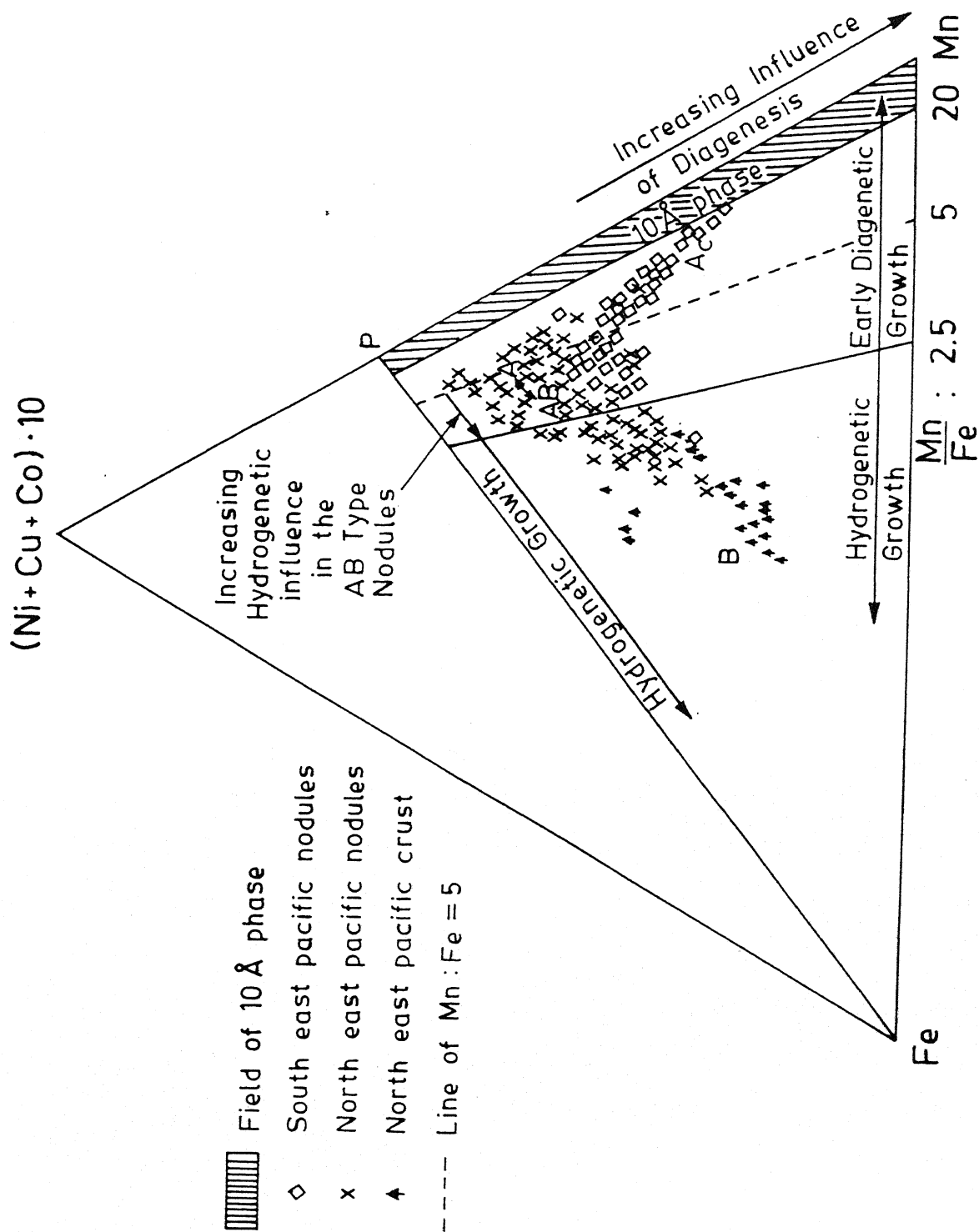


Fig. II.6. Three component diagram illustrating relationship between (Mn/Fe) ratio, (Ni+Cu+Co) content and different genetic type of nodules from Pacific ocean, after Halbach et al. (25).

The separation of Mn and Fe during diagenetic reactions in recent sediment and enrichment of Mn relative to Fe in the surface oxide formed from migrating pore water have been extensively documented (26, 105, 144, 159, 165-168). However the mechanism of fractionation is still not well understood. Krauskopf (165) and Ehrlich (147) proposed that the separation is facilitated by selective enzymatic oxidation of non-biologically adsorbed Mn(II) on negatively charged oxides. Some workers have explained the fractionation on the basis of thermodynamic considerations (4, 25, 105). In contrast with manganese, the concentration of ferric complexes $\text{Fe}(\text{OH})_3^0$ and $\text{Fe}(\text{OH})_4^-$ in the sediment environment are relatively less sensitive to Eh and pH found in the environment; Fe is therefore not as readily recycled as Mn (4, 25, 105). Alternatively, the fractionation has also been explained in terms of interaction of opaline SiO_2 with oxyhydroxides of manganese and iron (26, 166-171). Lyle et al. (26, 171) have proposed that interaction of biogenic silica (which contain trace elements like Ni, Cu etc.) with oxyhydroxides of manganese and iron results in the formation of Fe-rich semectite and well crystallized todorokite. Halbach et al. (25) contradicted these views and propose that the only pre-requisite to the formation of todorokite is the mobilization of Ni and Cu in the sediment. Too high remobilization of Mn in the sediment result in the ^{formation of} Mn rich birnessite phase (A_c type of nodule) (25). Lyle (26) has contended that reducing diagenesis to form manganese nodules occur only in small area of world ocean. Bischoff et al. (172) have shown that the formation of Fe-semectite in marine environments is thermodynamically feasible. Oxygen isotopes data on semectite from Central Pacific ocean show that semectite has been formed at sea-floor temperature (166).

What thickness of sediment is involved in nodule formation is open to question (26, 37, 159, 173, 174). Piper and Williamson (173) contend that diagenetic reactions as they influence the fractionation of elements between nodule and sediment phase are restricted to the very surface sediment. According to Lyle (26), the thickness involved is related with oxic or anoxic environment.

2.5.3 Growth Rate:

The growth of nodules is not a continuous process. It has been found (radiometric and other studies) that exceptionally high Mn zone (diagenetic substance) may have growth rate in excess of 50 mm/million years whereas Fe-rich zone represent period of extremely slow growth rate (<5 mm/million years) (49, 139, 175-177). The average growth rate of nodules may vary between 4-10 mm/million years (49).

The growth rate of nodules is significantly smaller than the sedimentation rate (10-30 mm/1000 years) (4). In spite of large discrepancy in sedimentation rate and nodule growth rate, nodules are not buried. It is believed that nodules are kept on the sediment surface by bioturbation and sediment erosion (4).

2.6 Internal Microfeatures

Concentric growth structure of manganese nodules was first recognized by Murray and Renard about a century back (177). However, major efforts to unveil the complexities associated with nodule structures and relate them to chemical composition and nodule genesis have taken place only in past two to three decades after recognition of nodules as the multielement ore of the future (16, 17, 24, 25, 35, 37, 100, 110, 115, 128, 138, 139, 179-191)

Cameron (179) and Arrhenius (180) were the first to show the complexity of layering in nodules by means of photomicrography. Layer-wise chemical heterogeneity was noted by Burns and Fuerstenaue (110) in microprobe studies on nodules. Friedrich et al. (181, 182) showed that differing reflectivity of micro-layers was due to differing contents of manganese and iron. Lighter layers were generally rich in manganese and poor in iron (182). Dunham and Glasby (185) investigated the growth features in nodules by SEM-BSE mode and EDAX and noted that banding characteristics in manganese nodules persist down to the finest size resolvable by existing techniques. Margolis and Glasby (186) suggested that microfine laminae observed by them during SEM investigation indicated the discontinuity in nodule growth.

The most commonly observed textural growth pattern of manganese nodules is collomorphic globular segregation (137). Often the segregation becomes linked into polygons and cusps (24, 37). Andrushenko and Skornyakova have additionally noted concentrically banded, parallel and shelly laminar structures in Pacific ocean nodules (183). Based on chemical compositions, mineralogy and optical properties Sorem, Foster and Fewkes classified the various textural patterns found in nodules as mottled, massive, columnar, laminated and compact (35, 188).

Sorem and Fewkes (188) contended that assuming an average growth rate of 10 mm/million year, a layer or shell of 1 μm thickness may record sea floor history for over 100 years. There have been some attempts to correlate the internal structure of nodules with genesis or growth history (25, 100, 139). The diagenetic and hydrogenetic substance in nodules can be often identified

by their diagnostic appearance in the photomicrograph. The diagenetic substance in nodules which consist of 10 A⁰-phase shows variable textures such as compact conformable thin layers, dendritic segregation, fracture filling veinlets, network and massive aggregates (25, 100). Hydrogenetic substance which is characterized by intimate association of δ -MnO₂ and FeOOH.XH₂O shows simple texture, stratification with radial or columnar pattern (25, 100). Cobalt is often found enriched in hydrogenetic substance (25, 100).

Besides the growth features, other important features of the internal structure of nodules include the nodule core, biogenous material and cracks and fissures. SEM-SE mode-EDAX studies have been particularly useful to elucidate these features. Details of these have been noted and reviewed (27, 37, 102, 193).

2.7 Occurrence of Nickel, Cobalt and Copper

Statistical Correlations:

Statistical analyses of bulk elemental compositions data show that certain group of elements vary coherently from nodule to nodule (24, 33, 37). The positive correlation of Ni and Cu with Mn, and of Co with Mn or Fe is well established (4, 24, 25, 33, 37, 52, 150-160, 194-199). Halbach et al. (25, 157) have found out that for Mn/Fe ratio greater than 5, Ni and Cu correlates negatively with the Mn/Fe ratio.

Positive correlation of nickel and copper with manganese has also been established by microprobe analysis, however, Co shows positive correlation with either Mn or Fe (100, 110, 182, 200, 201).

Valency States:

Valency states of iron and manganese in the nodules are well established through spectroscopy and other chemical methods. However, the hypothesis regarding the valency state of nickel, cobalt and copper enriched in nodules have been based primarily on metal associations, statistical correlations and geographic variations. Goldberg (194) indicated that cobalt/nickel ratios are an indicator of oxidation environment at the surface of ferromanganese nodules because the oxidation of Co(II) to Co(III) is thermodynamically more favourable than the oxidation of Ni(II) to Ni(III). Burns and Burns (18) have used the inter-element relationship derived from microprobe analysis to deduce the valency state of Ni, Cu and Co. Since Ni and Cu show strong correlations with Mn, so Ni^{2+} and Cu^{2+} may substitute for Mn^{2+} (18). Positive correlation of Co with Mn or Fe has been used to infer the substitution of Mn^{4+} and Fe^{3+} by Co^{3+} (18, 101).

Electron spin resonance (ESR) spectroscopy has been applied to determine the valency state of the minor transition elements in nodules (24, 56, 58). Comparison of the nodule spectra with those of transition metal salts indicated some similarity in the spectra of deep-sea nodules with those of trivalent cobalt oxide, but did not show any similarity with oxides of copper and nickel (24).

X-ray photoelectron spectroscopy XPS or ESCA is an experimental method of analysing the surface of materials and of distinguishing among various possible oxidation states (202 - 204). Dilard et al. (28) have established the valency state of Fe, Mn, Co, Ti and Pb in Pacific ocean nodules using XPS. Cobalt and titanium are reported to be present in trivalent and tetravalent

state respectively (28). Kanungo and Sahoo (205) have reported (from XPS measurements) the occurrence of Co(II), Co(III) and Ni(II) in manganese nodule from Indian ocean. Varnetsov et al. have used the XPS technique to find out the oxidation state of Mn, Fe, Ni and Co on γ -FeOOH sorbent (206).

Substitution Mode:

Enrichment of Ni, Co and Cu in manganese nodules is often explained in terms of substitution by the atoms of these elements in the crystal structure of the host manganese and iron oxide minerals. The foundation of the theory of substitution mode of occurrence rests on the valency state deduced from inter-element correlations, phase type and chemical composition relationship observed in some cases and proposed structure of the host phases (18, 20, 22, 36, 72, 76, 84, 85).

Tunnel structure of a T(3,3) type polymorph of todorokite is shown in Figure II.7. Burns et al. proposed that three types of atomic substitution in tunnel structure may occur (20, 85): (1) substitution of Mn^{2+} (radius 0.81 \AA) and/or Mn^{3+} (0.65 \AA) by other divalent cations e.g. Ni^{2+} (0.70 \AA) and Cu^{2+} (0.73 \AA) in the walls formed by chains of edge shared (MnO_6) octahedra (characteristically three octahedra), (2) replacement of Mn^{4+} (0.54 \AA) by cation like Co^{3+} (0.53 \AA) in the 'ceilings' or 'floor' typically three (as shown in figure) but as many as seven or more (MnO_6) octahedra wide, (3) in the tunnels' interiors adjacent to Mn^{4+} vacancies in the ceilings where a variety of large cations (e.g. Ba^{2+} (1.36 \AA), Na^+ , K^+), H_2O molecules and hydrated transition metal cations can be accommodated (20). It has been found that substitution of Mn^{2+} by divalent ions like Na^{2+} , Co^{2+} , Ca^{2+} ,

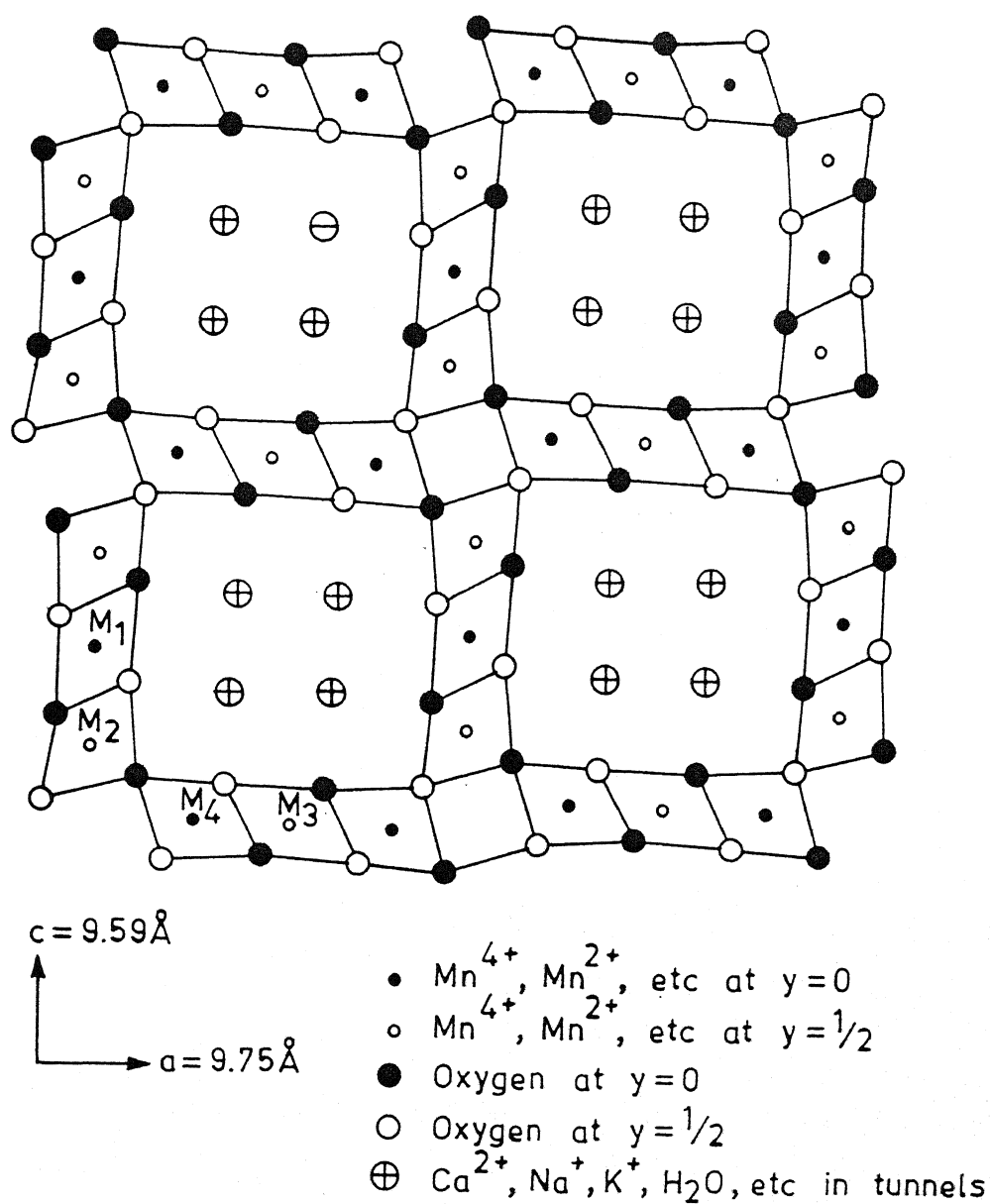


Fig. II.7. Tunnel structure of T(3,3) todorokite, after Burns et al. (20).

Mg^{2+} etc. and incorporation of water molecules are essential to the stabilisation of todorokite in marine environment (20).

Birnessite is postulated to contain layers of edge shared (MnO_6) octahedra separated by about 7.2 \AA along the C-axis which encloses sheets of H_2O molecules (Figure II.8). In the birnessite structure one out of six octahedral sites in the layer of linked (MnO_6) octahedra remains unoccupied. The vacant Mn^{4+} sites are distributed according to different patterns to the adjacent (MnO_6) octahedral layers resulting in a two-layered orthorhombic cell (Figure II.8). The Mn^{2+} and Mn^{3+} ions are arranged above and below the vacancies and are bonded with oxygen in both the (MnO_6) layer and the sheet of H_2O molecules. Divalent cations e.g. Cu (0.73 \AA), and Ni (0.70 \AA) may be located directly above and below the vacancies in the edge-shared (MnO_6) octahedral sheets bound in the birnessite structure rather than be randomly adsorbed on the external surface of microcrystallites (18, 22, 27, 80, 120).

The Co-Ni asbolane structure (77, 84, 207) can be considered as hybrid with alternation of layers of Mn^{4+} octahedra and Co-Ni octahedra; these layers form two sublattices, distinguished by the unit cell parameters (Figure II.9). In contrast to the continuous Mn^{4+} layers, the Co-Ni layers are discontinuous and could be called island-like. The octahedral position of Co-Ni layer could be occupied not only by Ni^{2+} or Co^{2+} , but also by other divalent or trivalent cations with radius about $0.65\text{--}0.75 \text{ \AA}$, among them are Cu^{2+} (0.73 \AA), Zn^{2+} (0.74 \AA), Mg^{2+} (0.72 \AA), Fe^{3+} (0.645 \AA), Mn^{3+} (0.65 \AA) and may be Co^{3+} (0.61 \AA , high spin) (69, 70, 207-209).

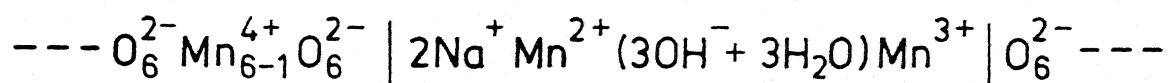
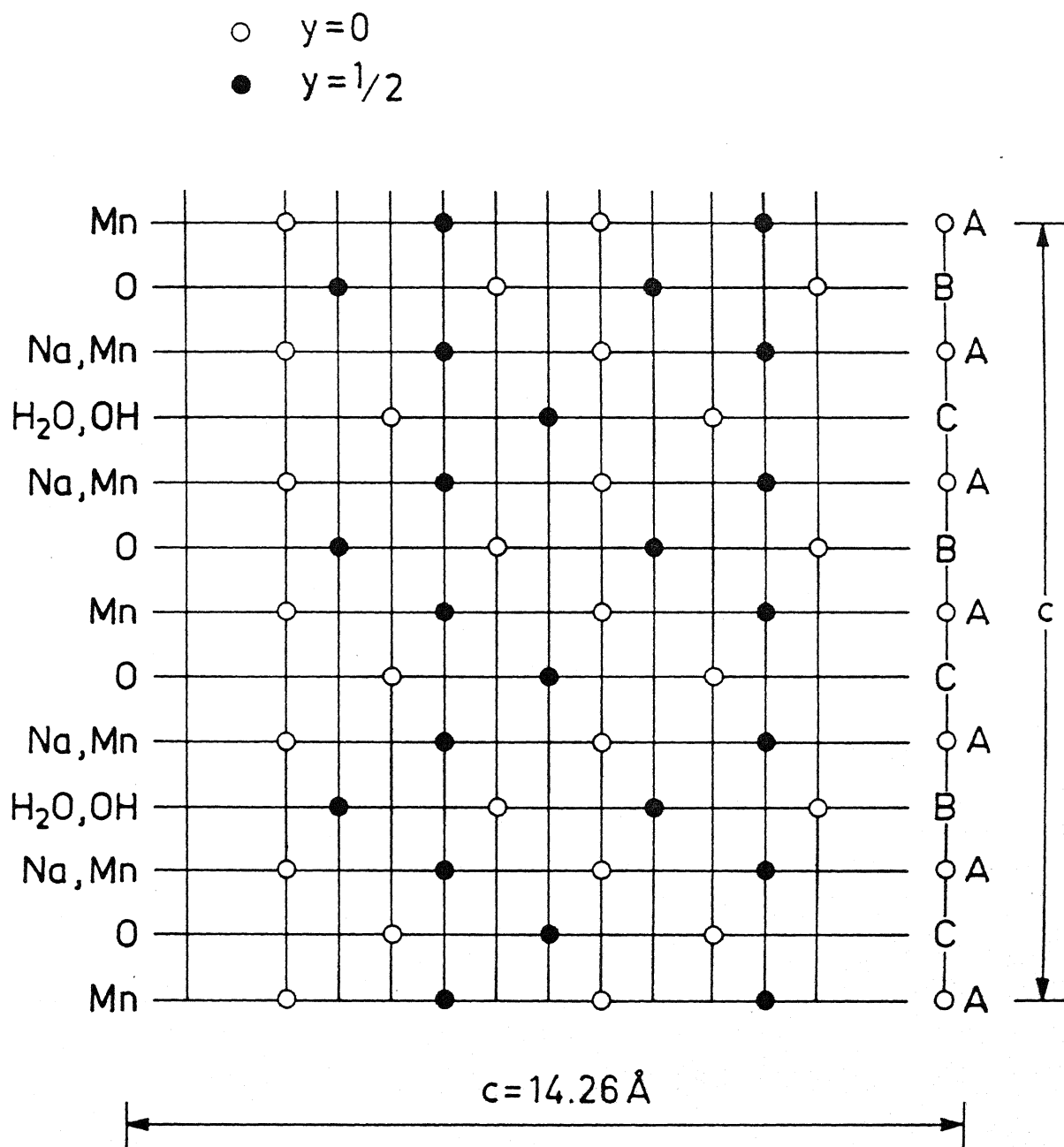


Fig. II.8. Layered structure of birnessite, Giovanoli et al. (107).

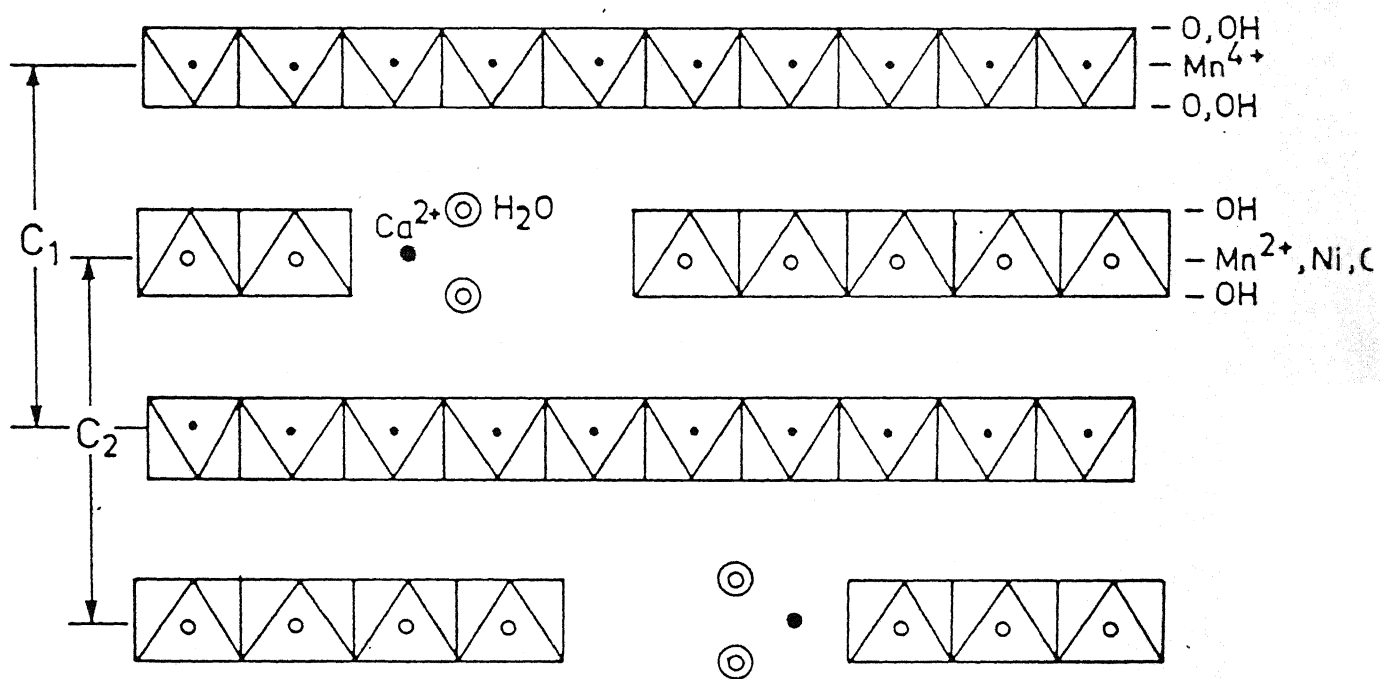


Fig. II.9. Hybrid layered structure of asbolane illustrating possible sites for the occurrence of Ni, Co and Cu, after Chukhrov et al. (209).

The ionic radius of low spin Co^{3+} (0.53 \AA°) is nearly identical to Fe^{3+} (0.55 \AA° , low spin) and Mn^{4+} (0.54 \AA°). It has been suggested that this can allow Co^{3+} to substitute for Mn^{4+} and Fe^{3+} in $\delta\text{-MnO}_2$ and Fe oxide minerals and explain why cobalt associates with iron and manganese phases in nodules (80, 101). There is no experimental evidence available regarding occurrence of low spin Fe^{3+} (octahedral coordination) in manganese nodules. Henderson (69) has noted that in all minerals, at pressure existing in earth crust, the octahedral crystal field stabilization energy (CFSE) is never sufficiently large to produce the low spin state for all 3d configurations.

Adsorption Mode:

Attempts have been made to explain the enrichment of trace elements in nodules by adsorption model (210). Crerar and Barnes (105) and Glasby (211) have concluded that adsorption may be a dominant means of extracting Mn, Fe and other trace elements from sea water into ferromanganese nodules. On the basis of inter-element relationship in nodules, Goldberg (194) proposed that adsorption onto particulate Fe and Mn species accounts for the co-vari-
 ance of Ni and Cu with Mn, and of Co with Fe. Adsorption onto iron and manganese oxide was invoked by Sevast'yanov and Volkov (212) to explain the correlation of Ni, Co and Cu with manganese. Halbach et al. (169) have proposed that enrichment of Co in hydrogenetic substance is attributed to specific surface adsorption and subsequent oxidation of Co^{2+} to Co^{3+} in strong electric field of Si^{4+} . Robust complexes of Co(III) and $\equiv \text{FeH}_2\text{SiO}_4^-$ prevent most of cobalt from being available for 10 \AA° -phase precipitation.

Although circumstantial evidence to support the adsorption mode of occurrence of Ni, Co and Cu in nodules is abundant, till date there is no experimental proof. Several proposed models (e.g. Goldberg (194), Goldberg and Arrhenius (213)) have been based on little or no experimental evidence.

Research on surface chemistry of hydrous manganese dioxide and iron oxide has been carried out by several workers (210). However it is difficult to extrapolate these data to explain the phenomena in the marine environment. Li (214) has attempted to explain the removal of transition elements (e.g. Ni, Co, Cu etc.) by hydrous manganese dioxide and iron oxide in marine environment with the help of surface characteristics of these oxides, Gibbs free energy of adsorption and fundamental parameters like electronegativity.

Adsorption mechanism does not preclude subsequent incorporation or migration of the atoms into the lattice sites and interstitial spaces.

Solid Solution Mode:

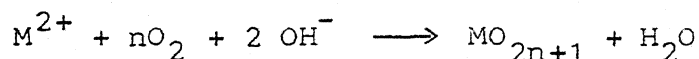
Occurrence of nickel, cobalt and copper as solid solution with oxide of manganese and iron is closely linked with the precipitation of manganese and iron oxides in marine environment. Hem (215) points out that the co-precipitation process in which accessory ions are included in the growing crystal lattice is more realistic than simple adsorption or ion exchange. The hypothesis is mainly based on thermodynamic calculations, results of metal extraction and crystal field theory. Thermodynamic calculations involve many simplified assumptions regarding solid and liquid species present in the marine environment. In the complex marine

environment, bacteria may play an important role, however, the role of bacteria is yet to be elucidated (210, 216).

Arrhenius and Bonatti (217) suggested that manganese dioxide formed by rapid precipitation under comparatively reducing circumstances may offer a favourable condition for solid solution of Co^{2+} . The possibility of oxidation of Co^{2+} to Co^{3+} in the marine environment, when the concentration of Co^{2+} exceeds 10^{-8} M, was suggested by Burns (218). The reaction is assumed to be catalysed by $\text{Fe}(\text{OH})_3$ and is also favoured by $\text{Co}(\text{OH})_3$ forming solid solution with $\text{Fe}(\text{OH})_3$.

On the basis of crystal field theory, nickel in $\delta\text{-MnO}_2$ in manganese nodule was proposed to be present due to oxidation of Ni^{2+} to Ni^{4+} (63).

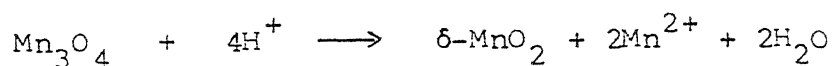
From thermodynamic calculations, Han (219) proposed that metal ions of nickel, cobalt and copper are more stable as ionic species rather than as oxides at the ocean bottom. He used the following reaction for his calculations:



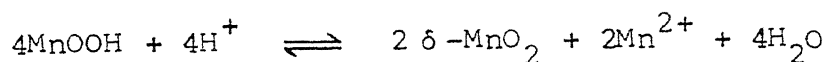
The species assumed by him were Mn^{2+} , Fe^{2+} , Co^{2+} , Cu^{2+} , Ni^{2+} (in aqueous phase) and MnO_2 , Fe_2O_3 , Co_3O_4 , CuO , Ni_3O_4 (solid species). It may be noted that his calculations involved very simplified assumptions. So far, no separate phase of nickel, cobalt and copper has been detected (27). Perhaps nickel, cobalt and copper occur in the aqueous marine environment as organic complexes (220).

Crerar and Barnes (105) proposed that the oxidation of manganese occurs by adsorption and catalytic oxidation at the nucleating surfaces such as sea floor silicates.

Hem (215) proposed that the disproportionation of hausmannite (Mn_3O_4) and manganite (MnOOH) i.e. the reactions



and



may be catalysed, if half the electron transfers in the disproportionation reactions are diverted to the formation of Co_3O_4 from Co^{2+} , Ni_3O_4 or $4\text{Ni}(\text{OH})_2 \cdot \text{NiOOH}$ from Ni^{2+} , or CuO from CuCl_3^{2-} .

Murray et al. (221) point out that these reactions are based on the hypothesis that Mn(III) is present. This is inconsistent with the XPS measurements made so far (221).

Leaching Behaviour:

There have been attempts to infer the mode of occurrence of minor elements on the basis of dissolution behaviour of nodules (39, 222-224). According to Han and Fuerstenau (223), if the lattice substitution mechanism is valid, one may expect ion exchange phenomena to control the way the minor elements are leached from the nodules. However, if the metals occur in nodules due to adsorption mechanism, the corresponding behaviour of the minor elements will be determined by conditions that promote desorption. On the other hand, if metals occur only as occluded oxides, conditions for solubilizing the oxide should provide a basis for extraction.

The close correlation between manganese solubilization and nickel and cobalt release in bacterial reduction of manganese nodules led Ehrlich et al. (222) to suggest that nickel and cobalt are more tightly bound to manganese than is copper. Some workers

(39, 223, 225) have reported that in acid leaching of manganese nodules, the bulk of copper and nickel can be dissolved without attacking the manganese phase appreciably, while only a portion of cobalt can be dissolved. In the leaching of these elements in reducing agents e.g. hydroxylamine hydrochloride or sulfurous acid, behaviour of nickel and cobalt followed that of manganese closely (223, 224). In the same investigation (223, 224) different behaviour of copper has been reported in sulfurous acid leaching (bulk of copper solubilized) and hydroxylamine hydrochloride (partial dissolution). Even in the sulfurous acid leaching, different behaviour of copper has been reported by different workers (223, 226).

Since minor elements in manganese nodules behave independently of major elements, Han and Fuerstenau (223) contend that that occurrence of these elements in substitution mode is unlikely. This inference is in contrast with the reported occurrence of todorokite in manganese nodules. Under this situation substitution within the mineral lattice as well as adsorption are likely (37).

The multimineralic nature of nodules coupled with specific chemical and/or kinetic effects resulting from the nature of leaching medium make it difficult to deduce information regarding mode of occurrence of minor elements from leaching data.

2.8 Metal Extraction

The physical and chemical nature of nodules make this material a unique ore. Nodules are highly porous and carry 15-20% water which is held tenaciously in pores of different size and mineral structures. Intimate mineral assemblage and fine dissemination of valuable metals (Ni, Co and Cu) make the physical upgrading

methods like gravity concentration, electromagnetic and electrostatic separation ineffective (17, 39, 40, 227). Therefore, chemical and metallurgical processing of large quantities of nodules are required for the recovery of moderate quantities of valuable metals. In developing suitable metallurgical processes for nodules, the gaps in our knowledge concerning the type of bonding of elements in nodules are a great handicap (4). Besides, the simultaneous presence of a number of metals makes the separation and purification of leach liquour a highly complicated task (39).

In spite of many difficulties several methods for recovering the valuable metals from nodules, using pyrometallurgical, hydrometallurgical or combination of the two processes, have been worked out on a laboratory or pilot plant level. Fuerstenau and Han (39) and Hubred (40) have reviewed various processing technique developed for manganese nodules. Updated flowsheets for a large number of promising metal extraction processes are available in U.S. Bureau of Mines reports (41). The extraction processes are generally based on smelting/reduction and/or leaching, solvent extraction, precipitation and electrowinning. The pyrometallurgical and pyro-cum-hydrometallurgical techniques include chlorination (7, 228-230), segregation roasting (231, 232), high temperature gaseous/solid reduction and subsequent leaching in ammonical medium (e.g. Caron process) (41, 233), reduction and HCl leach, smelting and H_2SO_4 leach etc. (39-41). Large quantities of moisture and complex nature of nodule gives an upper hand to hydrometallurgical processes over pyrometallurgical or pyro-cum-hydrometallurgical routes.

CENTRAL LIBRARY

LIBRARY

106231

LIBRARY

The hydrometallurgical processes involve an attack on the nodule material by aqueous solution of a suitable reagent to dissolve the metal values. There are two important variations of this, namely, three metal processes [high pressure, high temperature sulfuric acid leaching (Mao Bay Process (10)), leaching in ammonical medium in the presence of cuprous ions (Cuprion process (234-236))] and four metal process (e.g. leaching in reducing medium like aqueous SO_2 (226, 237)).

Metal recoveries in some typical leaching processes are compared in Table II.9.

As a three metal process, sulfuric acid pressure leaching and Cuprion processes are quite attractive (41). However, when the recovery of manganese is also desired, aqueous SO_2 leaching is more attractive due to its simplicity and rapid nature as compared to other processes (226). Khalafalla and Pahlman (226) have suggested a combination of dilute sulfuric acid leaching (for Cu extraction) with aqueous SO_2 leaching (for Mn, Ni, Co extraction).

The recovery of the various metals in the nodule leach liquor poses many problems (39). The key one being that the leach solution contains metals which have very similar complexing properties and hence do not offer much selectivity to a process. Hence a combination of different processes is essential to treat the leach solution, the combination depending on various factors such as acid or ammonia leach (249, 250), if acid whether a hydrochloric or sulfuric leach (39, 225, 251-255), principal impurities etc. (39, 255). Combination of various techniques such as cementation with aluminium, middle and high carbon ferromanganese, iron

Table II.9: Comparison of few promising hydrometallurgical processes

S. No.	Name of leaching process	Source ⁺ of nodule used	Experimental conditions					Metal recovery, %					Comments	Ref.
			Temp °C	Time	Reagent concentration	Pulp density wt %	Other	Ni	Co	Cu	Mn	Fe		
1	2	3	4	5	6	7	8	9	10	11	12	13	14	15
I	SULFURIC ACID LEACHING	P	90	10 hr	0.5 N	2.5	-	89	10	93	6	30	Nickel extraction more time dependent	(225)
		P	25	168 hr	0.2 N	2	pH-0.5	80	45	93	2.5	60		(238)
		P	45	12 hr	-	2	pH-2	50	8	70	-	-		(15)
		I	94	6 hr	0.1 N	-	-	100	9	91	12	14	Significant effect of temperature on nickel recovery	(227)
		-	30	10 min	1 M	6	1M FeSO ₄	85	90	83	100	-	Fe ⁺⁺ ions significant effect	(239)
II	SULFUROUS ACID LEACHING	-	30	2 min	1 M	6	FeSO ₄	-	-	-	92	-		(239)
		I	100	4 hr	0.7 N	-	0.5% C	100	80	100	50	-	C reducing agent	(240)
		P	25	10 min	5 wt %	10	R=0.8	60	30	5	70	5	Selectivity function of R*	(237)
		P	25	10 min	9 wt %	10	R=1.4	95	95	90	95	70		(237)
		I	25	30 min	5.4 wt %	6	R=0.9	68	29	6	91	52	Four metal process	(241)
III	AMMONIUM SULFITE LEACHING	I	25	30 min	5.4 wt %	3	R=1.7	94	98	55	96	53		(241)
		I	31	20 min	3.6 wt %	10	-	81	86	72	88	2		(248)
		-	60	1 hr	1 M	2	-	90	94	93	0.7	-	Selective for Ni, Co and Cu	(242)
		-	60	1 hr	8 M	2	-	64	79	74	1.7	-		(242)
		I	60	2.5 hr	1 M	1	-	73	89	65	0.8	1.0		(241)
IV	HYDROXYLAMINE HYDROCHLORIDE LEACHING	I	60	2.5 hr	1 M	1	Cu ⁺ ion 0.5 g	96	98	89	2	35		(241)
		P	25	2 hr	1 wt %	-	pH-5.5	95	95	20-80	100	5-40		(224)
		I	25	2 hr	1 wt %	1	pH-5.5	100	100	45	100	2		(241)

contd....

Table II.9 (continued)

1	2	3	4	5	6	7	8	9	10	11	12	13	14	15
V	HIGH TEMPERATURE HIGH PRESSURE SULFURIC ACID LEACHING	- P I	200- 250 200 150	1 hr 1 hr 3 hr	0.5-2 N - 0.5 N	3.5 - 5	- 300* psi 100 psi	75- 88 80 100	83- 90 30 90	86- 92 90 100	7- 26 5 <5	11- 82 2 -	11- Three metal processes; Under O ₂ pressure Fe and Mn decreases	(243) (244) (245)
VIA	CUPRION PROCESS	P	60	2 hr	102 g NH ₄ ⁺ /L	2-20	8.2 g Cu ⁺ /L	94	88	90	-	-	Three metal process, CO bubbling to gener- ate Cu ⁺	(246)
VIB	OTHER VARIATIONS OF AMMONIA LEACHING	- I	60 80	4 hr 4 hr	100 g/L NH ₃ 30 g/l NH ₃	- - -	1M NH ₄ ⁺ 0.5M Mn 1.75M NH ₄ ⁺ 0.7M Mn ⁺⁺	88 96	92 90	89 94	- 20	- 2	Mn ²⁺ reducing agent	(247) (248)
P		P	170	1 hr	34 g/l NH ₃	-	2M NH ₄ ⁺ 600 psi	80	20	100	-	-	High pressure	(39)
I		I	80	4 hr	42 g/l NH ₃	-	0.37M NH ₄ ⁺ 0.2 g glucose/g nodule	90	60	100	<5	-	Glucose reducing agent	(248)

+ - means unknown, P and I stand for Pacific and Indian ocean respectively.

Mole of SO₂ in solution* R = $\frac{\text{weight of nodules, g}}{\text{weight of SO}_2 \text{ in solution}} \times 100$, ** Partial pressure of oxygen.

etc. (225, 253); precipitation (H_2S) (39, 40, 253), reduction with H_2 (40) and solvent extraction using LIX63, LIX64, LIX70 (General Mills Inc., U.S.A.) and Kelex 100 (Ashland Chemical Co., U.S.A.) solvents, have been used to selectively separate the metals from leach liquor (39, 40, 225, 250-252, 256).

2.9 Miscellaneous Aspects

2.9.1 Technoeconomic Considerations:

Manganese nodules will be an extremely rich ore if positioned on the earth surface (4). However mining of nodules from a depth of 4000-6000 m is estimated to raise the cost exorbitantly (5). By 1980 fairly detailed cost estimates had been prepared based on engineering design for commercial operation in the best known areas (6). The first generation commercial mining operation is expected to start in areas with an average nodule density $\sim 10 \text{ kg/m}^2$ and grade % (Ni + Cu + Co) greater than 2.25 (5, 11). The optimum scale for an operation would be 3 million tons of nodule/year (5, 257). It is estimated (1979) that the capital cost of such an operation would be 15×10^8 \$ and the operating cost about \$ 70/tonne of nodules excluding depreciation (6).

In the world market, metals like copper and nickel have not shown increase in price over the past 7-8 years. In fact copper price which was 1.3 \$/lb came down to 0.7-0.8 \$/lb in 1984. Cobalt for which the price soared to an all time high in 1979 (\$ 40/lb) came down to \$ 12/lb in 1984 (10). The U.S. nickel price (\$ 3.4/lb) was an all time high in 1980. It is estimated that the nickel price (in terms of 1979 money value) will have to cross about \$ 5/lb for an attractive return from nodule venture (6).

The price of metals indicates an oversupply of nickel, cobalt and copper in world market or fall in production cost due to technological development. This being the situation for land based resources, large scale investment in nodule mining may meet strong resistance at least in the near future (10). However, there is no doubt that one day (may be after 10-30 years) nodules could become a major source of supply of nickel, cobalt, copper and manganese (6).

2.9.2 Indian Efforts and Future Plan:

Realising the future importance of the polymetallic nodules from sea bed, the Government of India towards late 1970s took up an ambitious programme for survey, mining and extracting nickel, cobalt and copper from nodules of Indian ocean. Sustained survey and exploration work of the National Institute of Oceanography (Goa) in Central Indian Ocean Basin over the last six years have revealed that the nodules available in Central Indian Ocean basin are comparable in grade and abundance to those of the Pacific Ocean. Two candidate mining sites have also been demarcated, where the total value of nickel, copper and cobalt is around 2.5 wt % and manganese around 20% on dry basis. The country has formulated a time bound programme to undertake commercial mining of nodules around 2005.

2.9.3 Legal and Environmental Problems:

The legal problems associated with deep sea mining, which will usually be done out of 200 mile national zone, are three fold: (i) who will develop them, (ii) under what legislation and terms and conditions and (iii) who will benefit or suffer from

their development (6). The 'Moratorium' resolution of 1969 and the U.N. resolution of 1970 proclaim the principles of sea as a heritage of the whole human race (4-6). Thus the nations having the technological possibilities should exploit the seas and share the profit with underdeveloped nations. The legal problem of deep-sea mining are not yet solved (5, 6, 32). Moncrieff (6) suggest that the time gained due to lower metal price in world market should not be wasted and it should be utilized to settle the legal problem associated with nodule mining.

Besides legal problems, the future mining of nodules is associated with unforeseen ecological and environmental problems which need to be kept in mind (258, 259).

CHAPTER - III

FORMULATION AND STATEMENT OF THE PROBLEM

3.1 Missing Links: Mineralogy and Nodule Processing

Review of literature on the extractive metallurgy of nodules (Chapter-II) has indicated the superiority of the hydro-metallurgical routes of metal extraction from manganese nodules over the pyrometallurgical routes. Prosser (260) has highlighted the influence of mineralogical factors on the dissolution behaviour of minerals.

There are four important aspects of nodule mineralogy which are relevant to their processing viz. (i) assemblages of minerals, (ii) physico-chemical nature of oxyhydroxide minerals of manganese and iron present in nodules, (iii) mode of occurrence of economically important elements in host oxyhydroxides of manganese and iron and (iv) nature of siliceous/calcareous gangue minerals.

Han and Fuerstenau (261) have elucidated the role of nodule porosity in sulfuric acid leaching. The intimate association of minerals in nodules is well appreciated in the context of applicability of beneficiation processes for nodules (17, 39, 142, 227). Technological aspect of nature of siliceous or calcareous gangue in leaching of ore and minerals is also well documented (226, 262). However, implication of physico-chemical characteristics of oxyhydroxides of manganese and iron and mode of occurrence of Ni, Co and Cu are poorly understood and least investigated.

The intimate association of poorly crystalline minerals in manganese nodules is physically similar to nickel-laterite ores

and manganese wads. However, the identity of minerals, elemental associations and perhaps mode of occurrence of Ni, Co and Cu are quite different in manganese nodules and land-based laterites and manganese wads. This distinction between the mineralogy of nodules and land based reserves has been almost always ignored during development of metal extraction processes (e.g. Caron process, Cuprion process, Moa Bay process etc.) from manganese nodules (41). In spite of the fact that a large number of processes have been developed and patented for metal extraction from manganese nodules, the variations in process parameters vis-a-vis nodules mineralogy and internal structure stand in the way of their universal application. Research data on nodule mineralogy and internal structure vis-a-vis growth environment have been extensively used by marine geologists to elucidate the genesis of nodules (e.g. 25, 100). Unfortunately, it seems that the relevance of such data has not been properly appreciated and co-related while designing the processing strategy for the recovery of useful elements from nodules.

The broad objective of this investigation is to reduce the gap in our understanding of the mineralogy of oxyhydroxide phases of manganese and iron, mode/s of occurrence of Ni, Co and Cu in host phases, the internal structure of the nodules vis-a-vis their leaching characteristics.

3.2 Research Strategies

Central Indian ocean basin holds the maximum promise for future mining of nodules in the Indian ocean (5, 49). Nodules in Central Indian ocean basin have been reported to have mineralogical

and chemical similarities with nodules in the Pacific ocean. Published work on the mineralogy and internal structure of nodules in Central Indian ocean is meagre and has been confined to results obtained by using techniques (e.g. X-ray diffraction, optical microscopy) which are of limited utility for nodule characterization (3, 37). In order to enhance our understanding of the nature and identity of phase constituents, internal structure, elemental association and mineral assemblages in nodules from the Central Indian ocean, detailed characterization work has been contemplated using diverse techniques viz. X-ray diffraction (XRD), transmission electron microscopy (selected area electron diffraction (SAED) and imaging mode), scanning electron microscopy (secondary electron (SE) and back scattered electron (BSE) mode with EDAX) and sequential extraction. To enhance the usefulness of TEM and SEM/EDAX techniques for nodule characterization, development and/or use of computer programs for indexing of SAED spot patterns and relevant statistical evaluation techniques (regression and Q-mode factor analysis) were envisaged. It has also been planned to present the genetic interpretation of nodule internal structure using factor model. Investigations into the occurrence of nickel, cobalt and copper vis-a-vis internal structure, location of major elements and minerals have been so planned as to form the core of the characterization work.

There are as yet no published data available on the mechanism/s of incorporation (viz. lattice substitution, sorption and coprecipitation etc.) of Ni, Co and Cu in host oxyhydroxides of manganese and iron in manganese nodules. Attempts to identify the exact mode of incorporation from leaching data have not been

very successful due to the multi-mineralic nature of nodules (39, 222-224). Although very limited amount of spectroscopic and high resolution transmission electron microscopic (HRTEM) studies on nodules has been attempted in this direction, it has been found that, in general, these methods are complicated by several factors as follows: ESR - due to the presence of large number of paramagnetic ions; IR - due to large water content; ESCA - continuous outgassing by nodules makes the attainment of vacuum needed quite difficult; and HRTEM - structural collapse takes place in high vacuum. The intimate associations of minerals in manganese nodules make it difficult to extract a significant amount of a particular phase to carry out systematic characterization and leaching studies. All these factors invariably point to the necessity to carry out leaching studies on well characterized synthetic analog of phases present in actual nodules.

Investigations into the characterization and leaching behaviour of pure and doped oxyhydroxides of manganese and iron have been planned with a view to enriching our knowledge on (i) role of physico-chemical characteristics of host phases on their dissolution behaviour, (ii) influence of doped element on precipitation/dissolution behaviour of host phases and (iii) effect of method of doping on the occurrence and dissolution behaviour of doped element.

Synthetic oxyhydroxide phases of manganese and iron which have been included for study in the research plan are listed below:

(A) Manganese minerals (i) pure birnessite and $\delta\text{-MnO}_2$, (ii) Mn-R (R = Ni, Co, Cu) type binary hydrous manganese oxide minerals with following subcategories (a) birnessite doped in

coprecipitation and ion exchange mode and (b) δ - MnO_2 -doped in sorption mode.

(B) Iron mineral (i) pure goethite (α - FeOOH), (ii) goethite doped with Ni/Co/Cu in coprecipitation and sorption mode.

Selection of minerals was primarily based on the availability of synthesis method. Todorokite has not been included because of nonavailability of synthesis method. It may be mentioned here that synthetic metal busserites have been erroneously named todorokites by Mckenzie (93, 129). Birnessite is a representative member of sheet structure phyllomanganates (73). δ - MnO_2 is included because of its very high specific surface area which may impart unique surface properties (263). Goethite samples doped with Ni, Co and Cu in ion exchange mode are not included in this investigation because significant amount of element cannot be doped in this mode. The physico-chemical characteristics for which samples were intended to be characterized include chemical composition, oxidation state, phase constituent/s, crystallinity, structural disorder, structure type etc. Leaching media selected were sulfuric acid (non-reducing) and sulfurous acid (reducing). The technological importance of sulfuric and sulfurous acid as leaching media has been highlighted in the literature(225, 226).

Lastly, it has been intended to compare the leaching results on synthetic phases with the leaching data on actual manganese nodules in similar leaching media (i.e. sulfuric and sulfurous acid) and highlight the significance of physico-chemical characteristics and leaching behaviour of synthetic phases to explain the behaviour of nodules of different mineralogy and internal structures.

3.3 Key Objectives

It was hoped that research targets as enumerated above would help us in obtaining new insight into the following specific areas related with manganese nodules:

- (i) Mineralogy and internal structure of manganese nodules.
- (ii) Occurrence of Ni, Co and Cu in nodules.
- (iii) Dissolution behaviour of host oxyhydroxides of manganese and iron with doped element (Ni, Co and Cu) vis-a-vis physico-chemical characteristics and method of doping viz. sorption, ion exchange and coprecipitation.
- (iv) Significance of mineralogy, internal structure and mode of occurrence of Ni, Co and Cu in manganese nodule processing.

CHAPTER - IV

MATERIALS AND METHODS

4.1 Materials

This section deals with the materials used in this investigation. The sources of materials used or prepared and the methods of preparation are presented here.

4.1.1 Manganese Nodule Samples:

Manganese nodule samples which were collected on the cruise of M.V. Skandi Surveyor in 1983 from Central Indian Ocean Basin, were received from National Institute of Oceanography (Goa) in powder, broken and unbroken conditions. The average chemical composition of nodules in Central Indian Ocean Basin has been reported (5) as follows: Mn 26.1%, Fe 7.6%, Ni 1.2%, Co 0.12%, Cu 1.16% (wt %). The nodule powder (dried at 110°C) composition as determined in the laboratories of I.I.T. Kanpur is given below: Mn - 21.6%, Fe - 13.2%, Ni - 0.7%, Co - 0.08%, Cu - 0.48%, SiO₂ - 16.6%, Weight loss at 110°C - 19.9% and weight loss at 900°C - 33.5%.

Unbroken nodules were ellipsoidal in shape and their size (major dimension) varied between 2-2.5 cm. Nodules represented mixed AB type. Top (smooth surface) and bottom (gritty surface) of nodules could be easily recognized by the criterion of Raab (264).

Besides the as received samples, nodule residues after selective sequential removal (vide Section 4.2.6 on sequential extraction) of exchangeable ions, Mn-fraction, organic matter and Fe-fraction were also investigated.

4.1.2 Synthetic Samples:

(A) Manganese Oxhydroxides:

The samples which were synthesized fall in two broad categories:

- (a) Birnessite samples: (i) Pure Na-birnessite, (ii) Birnessite with Ni/Co/Cu-coprecipitation mode and (iii) Birnessite with Ni/Co/Cu ion exchange mode.
- (b) δ -MnO₂ samples: (i) Pure δ -MnO₂ and (ii) δ -MnO₂ with Ni/Co/Cu-sorption mode.

The above samples will be referred to as B-O, V-O, B-R(C), B-R(I) and V-R(S). B- and V-stand for birnessite and δ -MnO₂ (or vernadite) respectively. R is the doped element (Ni, Co or Cu) and O, C, I and S refer to pure sample, coprecipitation, ion exchange and sorption mode.

It may be recalled (vide Table II.4) that birnessite has a layered structure (T(2, ∞) type) δ -MnO₂ is a randomly stacked variety of birnessite. The name δ -MnO₂ is used in this investigation just to highlight the high specific surface area of structurally disordered variety of birnessite.

Preparation of Birnessites: The birnessite samples were prepared by dehydration of respective buserite samples.

Na-birnessite was prepared by a method similar to that used by Giovanoli et al. (107). 200 ml of 0.5 M Mn(NO₃).4H₂O solution is poured in a 1000 ml thermostatically controlled ($\approx 30^\circ\text{C}$) double walled cylinder fitted with a 30 mm, G-1 glass frit at the bottom (vide Figure IV.1). Oxygen is bubbled through the solution at a rate of 2.5 L/min and a solution of 55 g NaOH ($\approx 30^\circ\text{C}$) in 200 ml H₂O

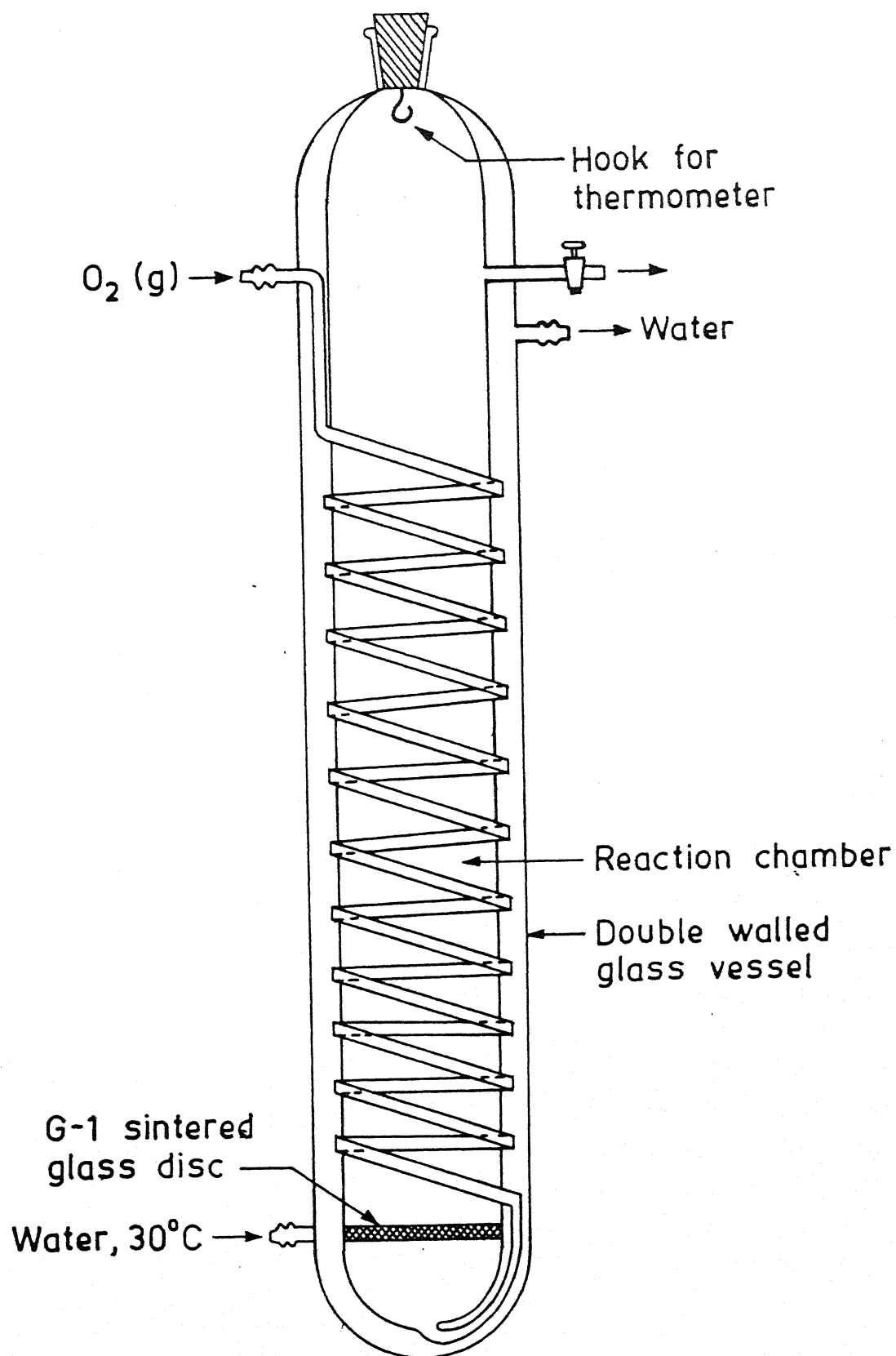


Fig. IV.1. Schematic diagram of reaction vessel used in the synthesis of birnessite samples.

is added to the nitrate solution. After 4-5 hrs the oxygenation is stopped. The black precipitate (Na-buserite) is isolated in a centrifuge and thoroughly washed 6-7 times with triple distilled water. The above product (Na-buserite) is isolated and dried in oven at 120°C for 24 hrs to get Na-birnessite.

The method adopted for synthesis of B-R(C) samples was similar to B-O. In this case same amount of NaOH solution was added to 200 ml solution containing both $\text{Mn}(\text{NO}_3)_2 \cdot 4\text{H}_2\text{O}$ and $\text{R}(\text{NO}_3)_2 \cdot \text{XH}_2\text{O}$. The Mn/R mole ratio in the solution was approximately 20.

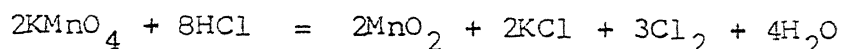
B-R(I) samples were prepared from thoroughly washed Na-buserite (Bu) samples. Na-buserite equivalent to one synthesis (yield ≈ 10 g Na-birnessite on drying) was equilibrated with 750 ml of 0.67 M respective metal nitrate solution for one week at room temperature. The pH was measured at the beginning and intermediate time intervals during progress of ion exchange reaction. The initial and final pH's were as follows:

Sample	Initial pH	Final pH
Bu-Ni(I)	5.3	4.4
Bu-Co(I)	5.1	4.6
Bu-Cu(I)	3.7	3.5

(Decrease in pH means release of H^+ ions during exchange). The Bu-R(I) samples were isolated and washed NO_3^- free (diphenylamine test). B-R(I) samples were obtained from Bu-R(I) samples by drying at 120°C as before.

Dried birnessite samples were ground and sieved to get -210 +149 μm and -63 + 53 μm size fractions.

Preparation of δ -MnO₂ Samples: δ -MnO₂ was prepared by the following reaction but with an excess of KMnO₄ to ensure oxidizing condition (122),



The actual procedure adopted was the one used by Buser et al. (122) to get the highly disordered variety of birnessite (referred to as δ -MnO₂ in this investigation and by Buser et al. (122) also).

18 ml of concentrated HCl (sp. gr. 1.181) was added to 250 ml of 0.4 M boiling KMnO₄ solution. The product obtained was thoroughly washed, dried at 120°C and ground -53 μ m size before storing.

V-R(S) samples were prepared from undried V-O. Undried and washed V-O (7.5 g on drying) was equilibrated with 4500 ml of 3.5×10^{-4} M R(NO₃)₂.XH₂O solution at pH 8.2 ± 0.2 and temperature $25 \pm 1^\circ\text{C}$ for 36 hrs. No base electrolyte was used. The solid samples were isolated by centrifuging and treated further by methods as adopted for V-O.

(b) Iron Oxyhydroxides:

Three kinds of sample were prepared: (i) Goethite without any minor element addition, (ii) Goethite^{with}/Ni/Co/Cu-coprecipitation mode and (iii) Goethite with Ni/Co/Cu-sorption mode.

These samples will be referred to as G-O, G-R(C) and G-R(S). G-refers to goethite.

Preparation of Goethite: G-O used in this investigation was prepared by the method of Atkinson et al. (265) and reported by Schenck et al. (266). Two hundred ml of 2.5M KOH was added to 50 g of Fe(NO₃)₂.9H₂O in 825 ml triple distilled water. The rust coloured

precipitate was aged for 24 hrs at 60°C under reflux. The precipitate turned golden yellow after aging. This was centrifuged, thoroughly washed and dried at 120°C.

G-R(C) samples were prepared by method similar to that for G-O. In this case 200 ml of KOH was added to 50 g of $\text{Fe}(\text{NO}_3)_3 \cdot 9\text{H}_2\text{O}$ and 5×10^{-2} mole of divalent Ni/Co/Cu (as nitrate salt) in 825 ml of water. The Fe/R mole ratio in the solution was 25. This ratio was selected so as to avoid any detectable separate phase formation for the minor elements (267-269).

G-R(S) samples were prepared from undried G-O. Undried and washed G-O (equivalent to one synthesis, ≈ 10 g on drying) was equilibrated with 6000 ml of $\text{R}(\text{NO}_3)_2 \cdot \text{XH}_2\text{O}$ solution (3.5×10^{-4} M) at $\text{pH } 8.2 \pm 0.2$ and temperature $25 \pm 1^\circ\text{C}$ for 36 hrs. Goethite suspension has a tendency to coat the electrodes which causes pH drift. In order to avoid this problem, the electrode was frequently cleaned and calibrated. The minor element concentration in the sorption experiment was selected with the following consideration: (i) to have adequate amount in the solid for chemical analysis and (ii) to minimize hydrolytical effects (266, 270).

4.2 Characterization of Samples

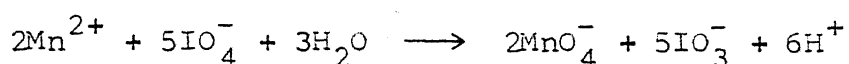
4.2.1 Analytical Methods:

The different chemical analysis methods used in this investigation include: Mn (permanganate method (271)); Fe (1, 10 phenanthroline method (272)); Ni/Co/Cu (Na-DDTC method (273, 274)) (all by colorimetric method); dissolved SO_2 (iodimetry (275)) and oxidation state of manganese (oxalate method (60, 61)).

The colorimetric measurements were made on a Bausch and Lomb Spectronic-20 colorimeter. The standard for different elements were prepared by dissolving 0.1 g pure metal (99.999%) in 15 ml (1:1) HNO_3 . The volume was made upto 100 ml to get a concentration of 1000 $\mu\text{g/ml}$.

The details of estimation procedure, calibration curve determination and interference problems faced are given below.

Estimation of Manganese: The estimation of manganese by permanganate method is based on the following oxidation reaction of manganous ions by periodate (271)



This reaction proceeds fairly rapidly in hot solution containing nitric or sulfuric acid.

15-20 ml nitric acid (12N) and 5-10 ml orthophosphoric acid (85%) are added to the solution containing (0.1-1.0 mg) manganese. This was followed with the addition of 0.3 g potassium metaperiodate. The solution is heated to boiling with stirring and kept at or slightly below the boiling point for 15-20 minutes. The solution is cooled to room temperature, diluted to 100 ml and absorbance of purple colored solution measured in 1 x 1 cm quartz tube at 525 nm against a reagent blank. The following relationship was found between amount of Mn and absorbance, by linear regression

$$X_{\text{Mn}} = 2.205 \cdot A_{\text{X}(525)}$$

where X_{Mn} is amount of manganese (mg) in 100 ml and $A_{\text{X}(525)}$ is corresponding absorbance at 525 nm. The accuracy and reproducibility of the method were better than $\pm 2\%$ (vide Appendix-B).

Cl^- and H_2SO_3 interfere in the estimation of manganese by this method. Cl^- was removed by heating with HNO_3 (till near dryness) and fuming off with H_2SO_4 . The sulfite was oxidized to sulfate by boiling off the solution with HNO_3 before analysis.

Large quantities of Ni, Co and Cu interfere in the estimation. However the range of Ni, Co and Cu concentrations encountered were significantly small and did not cause any appreciable interference.

Estimation of Iron: Ferrous ion forms colored complex with 1, 10 phenanthroline which has maximum absorbance between 510-520 nm. Beer's law holds for iron concentration between 0 to 2.5 μg (in 100 ml) when excess of reagent is present (272).

To a suitable aliquote of sample, containing 0-2.5 μg Fe, 5 ml of freshly prepared hydroxylamine hydrochloride solution is added to reduce the ferric iron into ferrous iron. After 5 minutes, the volume is increased to 80-85 ml and pH adjusted to 3.0 ± 0.1 using nitric acid or ammonia. 8 ml of 1, 10-phenanthroline solution (0.2 g/100 ml water) are added for complexation reaction and volume is made upto 100 ml. Color is allowed to develop for 20 minutes and measured at 520 nm against a reagent blank. The following relationship was found between concentration of Fe and absorbance (vide Appendix-B)

$$X_{\text{Fe}} = 4.494 A_{X(520)}$$

X_{Fe} is amount of iron in μg and $A_{X(520)}$ is corresponding absorbance. The accuracy of method was better than $\pm 3\%$. No significant interference of Ni, Co and Cu was observed for the range of these elements encountered.

Estimation of Ni, Co and Cu: Ni, Co and Cu were estimated by sodium diethyl-di-thio-carbamate (Na-DDTC) method (273, 274). The method is based on color complex formation between Ni, Co and Cu and Na-DDTC. Mn and Fe interfere in the estimation. The interference is prevented by masking these elements with sodium tetrapyro-phosphate and citric acid (for Ni and Co estimation) or citric acid and EDTA (for Cu estimation). To enhance the sensitivity of the method and reduce the effect of interfering elements, the colored complex is extracted in chloroform (273, 274).

An aliquot of the sample containing 5 to 25 μg copper/4-20 μg Co/2-12.5 μg Ni, in a volume of 5-30 ml, is transferred to a 100 ml beaker. A similar amount of water is placed in another beaker to be used for a blank determination of reagents employed.

The solution is made basic by adding ammonium hydroxide. To the sample and blank are added 4 ml of sodium tetrapyrophosphate solution (4 g/100 ml water) (Ni and Co estimation). In the case of Cu, sodium tetrapyrophosphate addition is omitted and 10 ml of EDTA solution (10 g disodium salt of EDTA/100 ml) is added instead.

5 ml of citric acid solution (35 g/100 ml H_2O) is added and the solution pH readjusted to 8.2-8.8. 2 ml of 0.1% (by weight in water) of Na-DDTC solution are added and mixed after the pH readjustment and color is allowed to develop for 10 minutes.

The color complex is extracted with chloroform in a 125 ml separating funnel. The extraction is made three times with 10, 8 and 4 ml of chloroform for 2, 2 and 1 minute respectively and organic layer collected in a 25 ml volumetric flask.

The content of volumetric flask is made upto volume (25 ml) with chloroform. The absorbance/transmittance of sample is read

against reagents blank at 435 nm, 370 nm and 325 nm for Cu, Co and Ni respectively.

It was found necessary to remove traces of Ni, Co and Cu from the citric acid solution (prior to its use) to get reproducible results. These elements were removed by adding Na-DDTC solution and extracting with chloroform. The excess organic solvent was boiled off.

The amount of Ni, Co and Cu are related with absorbance or transmittance by the following relationships (vide Appendix-B)

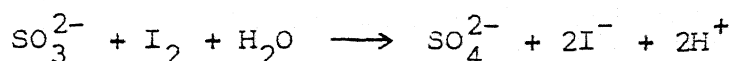
$$X_{\text{Ni}} (\mu\text{g}) = 75.429 A_{\text{X}(325)}$$

$$X_{\text{Co}} (\mu\text{g}) = 0.5998 (100 - T_{\text{X}(370)})$$

$$X_{\text{Cu}} (\mu\text{g}) = 6.80 A_{\text{X}(435)}$$

For Ni and Cu the accuracy and reproducibility of this method was better than $\pm 2\%$. However the method was less sensitive for cobalt for which accuracy and reproducibility was better than $\pm 3\%$. No interference of Mn, Fe and dissolved SO_2 was observed.

Estimation of Dissolved SO_2 : The iodimetric method (275) for determination of dissolved SO_2 is the most used and reliable method for macro-amounts. The chemical reaction is



A potential source of error is partial oxidation of sulfite by atmospheric oxygen. In order to minimize it, the sample was added to excess I_2 and unreacted I_2 back titrated with thiosulfate.

Reagents Preparation:

1. Standard I_2 solution - 12.691 g of resublimed I_2 was

- dissolved in 150 ml H_2O containing 20 g KI and diluted to one litre. The H_2O was boiled and cooled just before use.
2. Thiosulfate solution - 25 g of $\text{Na}_2\text{S}_2\text{O}_3$ was dissolved in one litre H_2O . 0.1 g Na_2CO_3 and 0.4 ml CHCl_3 was added to the solution for its stabilization. The solution was stored in amber colored bottle.
 3. Starch solution (indicator) - 2 g of starch was mixed with little water and the slurry poured into about 200 ml of boiling distilled water. The solution was boiled till it became colorless. The solution was cooled to room temperature and diluted to one litre.

Procedure:

Thiosulfate Standardization - 25 ml of I_2 was titrated with thiosulfate solution until the I_2 color became pale yellow. The solution was diluted to about 200 ml, 2 ml starch solution added and titration continued until the color became blue to colorless.

SO_2 Estimation - Dissolved SO_2 was estimated in sulfurous acid leaching experiments, before and after the experiment. 40-60 ml standard I_2 solution of appropriate strength was pipetted out into a 250 ml conical flask. The sample (5 ml) was added and mixed. The excess I_2 was titrated with standard thiosulfate using starch near the end point.

Fe(II) Interferes in SO_2 Estimation - To determine SO_2 in the presence of Fe(II), one aliquot is titrated normally. The titre corresponds to all the existing reducing species. In the second aliquot, SO_2 is masked with formaldehyde (15 ml) before titration. The I_2 consumed corresponds to the reducing species other than SO_2 .

The difference in the two titres corresponds to the sulfite ion content present.

In the leaching experiments with goethites, the maximum change in SO_2 concentration during leaching was 5%. The dissolved SO_2 (0.4 g/0.25 g manganese oxide) was almost completely consumed in the leaching of manganese oxyhydroxide.

Oxidation State of Manganese: The oxidation state of manganese (O/Mn ratio) in synthetic oxyhydroxide phases of manganese was estimated by oxalate method (60, 61).

The O/Mn ratio as MnO_x was calculated using the following formula (60)

$$x = 1 + \frac{1}{2} \frac{[\text{Total oxidized equivalents } \text{O}_x]}{[\text{Total moles of manganese } \text{Mn}_T]}$$

where $[\text{O}_x] = 2[\text{Mn(IV)}] + [\text{Mn(III)}]$

and $[\text{Mn}_T] = [\text{Mn(IV)}] + [\text{Mn(III)}] + [\text{Mn(II)}]$.

The oxalate method and other analytical methods (60) cannot distinguish between Mn(III) and a combination Mn(II) and Mn(IV). The oxalate method involves reduction of manganese in valency state +(III) and +(IV) to +(II) state by excess oxalic acid and back titration of unreacted oxalic acid by KMnO_4 solution.

Reagents Preparation:

1. Sodium oxalate standard - 0.6710 g of sodium oxalate ($\text{Na}_2\text{C}_2\text{O}_4$) was dissolved in 100 ml distilled water to get an oxalate concentration of 0.05 M.
2. Potassium permanganate solution - 1.5884 g of KMnO_4 was dissolved in one litre water and stored in amber colored bottle. The solution was standardized against standard

sodium oxalate in the presence of 10 ml, 1N H_2SO_4 at 70°C . The strength was found to be 0.00996 M.

3. Oxalic acid solution - 2.5274 g of oxalic acid was dissolved in 500 ml of distilled water. This was standardized against standardized KMnO_4 (0.00996 M) at 70°C in the presence of sulfuric acid. The strength was found to be 0.0394 M.

Procedure:

50 mg of synthetic manganese oxide was reacted with 25 ml of 0.0394 M oxalic acid solution in a 250 ml conical flask. After completion of reaction, 10 ml of 1N H_2SO_4 is added and solution heated to 70°C before titration with 0.00996 M KMnO_4 . The amount of KMnO_4 used is equivalent to unreacted oxalic acid. The details of results are presented in Appendix-C and summarized in Chapter-VII.

Presence of oxidized cobalt in the samples results in over estimation of oxidized equivalents and $[\text{O}/\text{Mn}]$ ratio (60).

4.2.2 Surface Area Measurements:

Ethylene glycol and its derivatives (e.g. ethylene glycol monoethyl ether (EGMEE)) retention methods have been used by different workers for estimation of surface area of soils and minerals (276-278). In this investigation ethylene glycol monomethyl ether (EGMME) retention method is used for estimation of surface area of synthetic manganese and iron oxyhydroxide samples.

0.3-0.5 g solid was dried in aluminum cup (2.5 cm dia, 3 mm height) at 120°C and equilibrated at 25°C over CaCl_2 (-40 + 65 mesh) in vacuum desiccator (vacuum 10^{-2} torr) to get a constant

weight. 2 ml of EGMME is added to the cup and the cup is again kept back in the desiccator under vacuum (10^{-2} torr). The desiccator is evacuated at frequent intervals to maintain the vacuum. When the cup has been in the vacuum for 24 hrs, the vacuum is released and the cup weighed quickly to prevent any moisture pick up from the atmosphere. The cup is again returned to the desiccator and same vacuum (10^{-2} torr) is maintained. The weighing operation is repeated at 8-16 hrs until two successive weight agreed within a few tenth of a mg. 4-6 cups containing samples and a blank can be used in this procedure at a time.

Surface area is calculated by the following equation:

$$SA = W_g/W_s \times 2.9 \times 10^{-3}$$

where SA = specific surface area m^2/g ; W_s = initial weight of sample in gram (before EGMME addition); W_g = weight (in grams) of EGMME retained by the sample; constant 2.9×10^{-3} refers to the grams of EGMME required to form a monolayer on one m^2 surface (this value corresponds to a molecular coverage of 42 \AA^2 per molecule).

The surface area measurements were done on birnessites, $\delta\text{-MnO}_2$ and goethites samples. The details for different samples are presented in Appendix-D and later chapters (vide Sections 7.1.1 and 8.1.1). The reproducibility of this method was better than $\pm 1 m^2/g$.

4.2.3 X-ray Diffraction:

X-ray diffraction has been used for the characterization of manganese nodule samples and synthetic oxyhydroxides of

manganese and iron. XRD is a useful technique for identification of crystalline constituent/s present in amount greater than 5-10%. Crystallinity is generally defined by the XRD line widths. XRD can give information on two aspects: structural order and particle size or, more exactly, coherently diffracting domain size (278-281). Due to orientation effects, ratio of XRD intensities can give qualitative information on the shape of particles and their dimensions e.g. I_{110}/I_{111} ratio in goethite (vide Section 8.1.2). XRD in conjunction with intercalation of phyllomanganate with dodecylammonium chloride have been used in the recent past to distinguish between layer or more complex structure present (89, 91, 112, 282).

XRD traces were recorded on a Rich Seifert Iso-Debyeflex 2002 D diffractometer using Cr- K_α radiation (wave length ' λ ' = 2.2902 Å) and graphite monochromator. The samples were scanned under following conditions: Scanning speed - 1.2/3.0° 2 θ /min, tube voltage - 40 kV and tube current - 25 mA. The scanning speed of 1.2° 2 θ /min has been used for manganese nodule samples and quantitative estimation of crystallinity in synthetic goethite samples. Quartz has been used as an external standard. XRD line intensities were taken as the product of height and width at half peak height. Synthetic buserite samples were examined under XRD, in wet conditions; drying of sample results in collapse of structure to 7 Å⁰-phase.

Phase Constituents: The inter-planar spacings ('d' values) were calculated using the Bragg's law i.e. $\lambda = 2 d \sin\theta$. The observed 'd' spacings were compared with values reported in JCPDS X-ray data files for expected minerals (18, 27).

Crystallinity: Crystallinity or coherently scattering domain size was estimated for synthetic samples. Domain boundaries represent high energy regions and are preferentially attacked during leaching of samples.

Micro-crystalline dimension (MCD_{hkl}) was calculated using the Scherrer equation (281), i.e.

$$MCD_{hkl} = \frac{0.92}{\beta_{1/2} \cdot \cos \theta_{hkl}}$$

(where $\beta_{1/2}$ is width (in radians) at half height ($\Delta\theta$, not $\Delta 2\theta$) corrected for instrumental effects, θ_{hkl} is Bragg angle corresponding to reflection hkl and ' λ ' is wave length of radiation used).

For qualitative comparison, in a group of samples belonging to the same category, uncorrected line width can be used (281).

Specific surface area of a material is inversely proportional to particle size i.e. the smallest dimension will influence the specific surface area to the maximum extent. Birnessite and goethite particles are flake and lath shaped respectively. Smallest dimensions MCD_{001} (for birnessite) and MCD_a (or MCD_{100} , for goethite) and expected to have maximum influence on the surface area of birnessite and goethite respectively.

Only qualitative comparison of crystallinity (in terms of line width) was made among birnessite samples because doping of Ni, Co and Cu was accompanied by phase changes. Quantitative estimation of crystallinity was made for goethite samples, the details of the procedure adopted are as follows.

$\beta_{1/2}$ values for the first nine reflections (namely 020, 110, 120, 130, 021, 101, 040, 111 and 140) from goethite XRD patterns were measured and corrected for instrumental effects using quartz

(5-20 μm) as an external standard (vide Appendix-E, for details). The corrected values of $\beta_{1/2}$ were used to calculate MCD_{hkl} . The MCD_{hkl} values were resolved in a-, b- and c-direction of the goethite unit cell by multiplying with cosine of angle (Ψ) between perpendicular to the plane (hkl) and crystal axis (Appendix-E). The details of average MCD_a , MCD_b and minimum MCD_c calculations are presented by Schulze and Schwertmann (278). Average MCD_a was computed using MCD_a calculated from 110, 120, 130, 111 and 140 lines. MCD_b was taken as an average of MCD_b calculated from 021 and 020 line, and minimum value of MCD_c was taken as the value calculated from 021 reflection (Appendix-E). Theoretically speaking, if line broadening occurs due to crystallite size alone, MCD_a value calculated from different reflections will be more or less same in the experimental error limits. Assuming experimental error to be a common factor for all the samples, the standard deviation in MCD_a calculation may be treated as the relative measure of structural disorder for different samples. Standard deviation (in average MCD_a) calculations were done for all the goethite samples studied (Appendix-E).

Intercalation and XRD: XRD studies on intercalated natural 10 \AA^0 -phase and synthetic buserites and corresponding birnessites were made to distinguish between simple layer structure or more complex structure present in them. Intercalation of layered structure phyllomanganates results in the lattice expansion i.e. basal spacing to be precise. This is exhibited by a series of diffraction lines at 25.5, 12.8, 8.56, ..., \AA^0 corresponding to 001, 002, 003, ..., reflections of intercalated complex (91).

The samples were intercalated with 0.1 M dodecylammonium chloride solutions for 48 hrs. A few drops of suspension placed on a glass slide were examined by X-ray in wet condition. It was found difficult to record the line at 25.5 \AA^0 (001 reflection) due to limitation of diffractometer used. Occurrence of 002, 003,... reflections in the XRD pattern of intercalated samples was taken as measure of positive response to intercalation.

Unit Cell Dimensions in Synthetic Samples: The unit cell dimensions for goethite samples were calculated from X-ray powder diffraction data using 110/130 and 110/140 line pairs and 111 line (279). For birnessite samples the change in the position of 001 reflection (i.e. c-dimension of unit cell) is treated as a measure of structural change on doping since the other dimensions remains more or less unchanged (90).

4.2.4 Transmission Electron Microscopy:

TEM, in imaging and selected area electron diffraction (SAED) mode, was used as a major technique for phase identification in manganese nodules. Transmission electron microscopic studies were carried out using a 100 kV electron microscope (Philips EM-301). Besides the as received nodule powder sample, samples from distinct locations in broken pieces and nodule residues after removal of manganese and manganese plus iron fraction by sequential extraction (vide Section 4.2.6) were investigated to minimize possibility of missing any phase. Some of the nodule particles and residue (after sequential extraction) samples were also examined under a TEM-EDAX system (Philips EM-400 transmission electron microscope).

The purpose of TEM studies on synthetic oxyhydroxide samples was to compliment the XRD results in terms of particles size, shape, structural disorder and mineral assemblages. Besides, the technique was also used to detect any separate phase formation for the Ni, Co and Cu in the doped samples.

For sample preparation dilute and uniform suspension of solid was made in acetone medium using an ultrasonic vibrator. One or two drops of this suspension was placed on a carbon film supported by copper grid. For each sample at least three grids were prepared. Gold was used as a standard for calibration of the camera constant ($L\lambda$, L = camera length, cm, λ = wavelength, \AA) of the microscope. The mean value of $L\lambda$ calculated ($R_d = L\lambda$) from the strong (111) and (311) Debye-Scherrer rings of gold was used. $L\lambda$ values were cross checked with pure α -quartz sample and a good match was obtained in less than 1% deviation.

In the microscope, d spacings corresponding to Bragg condition for reflecting planes can be measured from observed diffraction spots or rings in diffraction patterns by using the camera constant ($L\lambda$).

The multimineralic nature of nodules makes the indexing of SAED spot patterns a very difficult task. The indexing is further complicated due to large variations observed in the lattice parameters of oxyhydroxides of manganese and iron. In order to overcome this problem, a FORTRAN IV computer program was developed for the indexing of SAED spot patterns. The program, together with formulae and conditions employed in its development, is presented as an appendix (Appendix-F). Briefly the program works in the following steps: (i) READ (a) Number of diffraction patterns to be

analysed and number of minerals to be considered, (b) Name of minerals and their crystallographic data, (c) Interplanar spacings DE1, DE2 and DE3 (DE3 refers to the diagonal of parallelogram formed by reciprocal lattice vectors \vec{R}_1 and \vec{R}_2 corresponding to DE1 and DE2) and interplanar angles PE1 ($\vec{R}_1 \wedge \vec{R}_2$) and PE2 ($\vec{R}_1 \wedge \vec{R}_3$) (PE1 and PE2 are represented by φ_1 and φ_2 in Table V.1), (ii) Pick up crystallographic data for a specific mineral, generate 'd' values and SCAN through each diffraction pattern for a possible match of DE1, DE2 and DE3 and PE1 and PE2 for the same zone axis in the specified error limits, and (iii) In case a match is found (a) CALCULATE beam direction, (b) WRITE (HKL)'s, theoretical value of 'd', interplanar angles, beam direction, mineral name and its crystallographic data. The program can handle 20 diffraction patterns and any number of minerals depending upon the memory space available. H, K and L values in the limit -10 to +10 are used. A limit of $|H| + |K| + |L|$ equal to 12 is used to avoid generation of large number of 'd' values. In general, this limit is found to be sufficient.

All the minerals listed in U.S. Bureau of Mines report (27, 81) and recent literatures (77, 83, 283) were used in indexing of SAED patterns. Minerals for which crystallographic data are not well defined, were not used in indexing of SAED spot patterns. $\pm 4\%$ and $\pm 2^\circ$ error limits were used for interplanar spacings and interplanar angles respectively. These limits were chosen keeping in view the complex nature of minerals in nodules. The minerals in nodules can at best be considered as the analog of terrestrial or synthetic minerals. Large variations in unit cell dimensions and compositions are observed even for synthetic and terrestrial

minerals (83, 91). Higher error limit often leads to the coincidence ambiguity problem in indexing and results in multiple indexing of the same pattern. One way to solve this problem is to take more than one pattern from the same region, which should lead to the same end result (127). In general, it was found difficult to record indexable pattern in more than one orientation due to the poorly crystalline nature of manganese nodule samples used. Data obtained from actual nodules, residue samples and synthetic minerals, wherever possible, were used for unambiguous identification.

4.2.5 Scanning Electron Microscopy:

SEM studies on polished nodule sections were carried out using a Cambridge Stereoscan scanning electron microscope (SEM)* coupled with an EDAX system for X-ray microanalysis. The microscope was used both in secondary electron (SE) and back scattered electron (BSE) modes (A note on the working of SEM in SE and BSE modes is presented in Appendix-G).

Sample Preparation: Since the purpose of this work was to obtain chemical analysis data together with microstructural features, a smooth scratch free surface was desired.

The preparation of samples for SEM work involved (a) nodule impregnation with adhesive, (b) sample cutting and (c) polishing. The merits and demerits of different impregnation techniques and resin used have been reviewed (201, 284). In the present investigation, the method of Sorem and Fewkes (35) which is supposed to

* Some microstructural features were also recorded on a 35 CF JEOL SEM, accelerating voltage 15 kV (indicated on electron micrographs).

give the best results, has been followed. Araldite was used instead of castolite resin. Araldite was diluted with acetone for easy impregnation in vacuum. Impregnated nodules were mounted on a glass slide with Araldite and dried. Mounted samples were cut into slices of 5-8 mm thickness (Figure IV.2a) from top to bottom using a diamond cutter with 0.3 mm blade and working at a slow speed. No coolant was used. The samples were polished on 001 to 004 grade emery papers. Glycerin was used as a lubricant during polishing. Final polishing was done on a nylon lap using diamond paste. Sample polishing down to 0.25 μm diamond paste has been found to be adequate. The samples were cleaned in an ultrasonic cleaner after final polishing.

SEM-SE Mode-EDAX Studies: The SEM was operated in SE mode under following conditions:

accelerating voltage - 20 kV, tilt angle - 30° , Elev. - 45.0° and azim. - 0.0° .

X-ray microanalysis data were obtained from 49 point areas (25 point areas from top to bottom and 24 point areas from right to left (Figure IV.2b)) for 14 elements namely, Mn, Fe, Si, Al, Ni, Co, Cu, Na, K, Mg, Ca, Ti, Cl and S. Besides, 10 point areas across the line X-0 (Figure IV.2(b)) were analysed in detail (three or more observations around each point) for 11 elements (Na, Cl and S omitted). The resolution of X-ray microanalysis was 2-4 μm . All the X-ray microanalysis data were corrected using a ZAF correction program.

SEM-BSE Mode-EDAX Studies: Z-contrast images are the easiest SEM, BSE images to obtain (285). Compared to optical microscope, the

give the best results, has been followed. Araldite was used instead of castolite resin. Araldite was diluted with acetone for easy impregnation in vacuum. Impregnated nodules were mounted on a glass slide with Araldite and dried. Mounted samples were cut into slices of 5-8 mm thickness (Figure IV.2a) from top to bottom using a diamond cutter with 0.3 mm blade and working at a slow speed. No coolant was used. The samples were polished on 001 to 004 grade emery papers. Glycerin was used as a lubricant during polishing. Final polishing was done on a nylon lap using diamond paste. Sample polishing down to 0.25 μm diamond paste has been found to be adequate. The samples were cleaned in an ultrasonic cleaner after final polishing.

SEM-SE Mode-EDAX Studies: The SEM was operated in SE mode under following conditions:

accelerating voltage - 20 kV, tilt angle - 30° , Elev. - 45.0° and azim. - 0.0° .

X-ray microanalysis data were obtained from 49 point areas (25 point areas from top to bottom and 24 point areas from right to left (Figure IV.2b)) for 14 elements namely, Mn, Fe, Si, Al, Ni, Co, Cu, Na, K, Mg, Ca, Ti, Cl and S. Besides, 10 point areas across the line X-O (Figure IV.2(b)) were analysed in detail (three or more observations around each point) for 11 elements (Na, Cl and S omitted). The resolution of X-ray microanalysis was 2-4 μm . All the X-ray microanalysis data were corrected using a ZAF correction program.

SEM-BSE Mode-EDAX Studies: Z-contrast images are the easiest SEM, BSE images to obtain (285). Compared to optical microscope, the

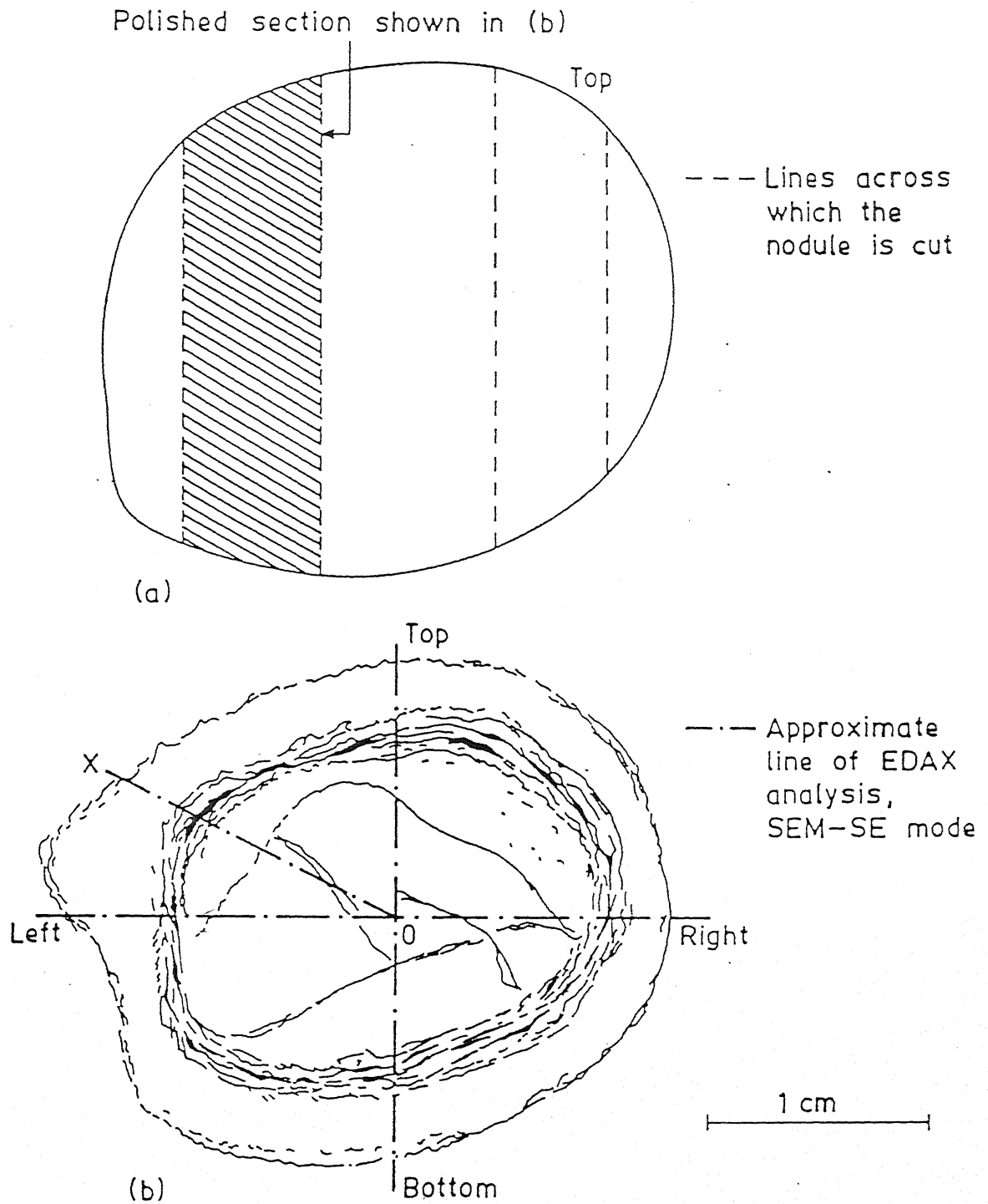


Fig. IV.2. Schematic diagram of (a) nodule showing section used (hatched) for detailed SEM work (b) polished nodule section.

SEM offers considerable advantage of immediate X-ray microanalysis of Z-contrast images. The contrast in BSE Z-contrast images (from polished surfaces) is better compared to SEM-SE images.

SEM backscattered electron micrographs were recorded from a large number of interesting regions. The distinct regions from typical electron micrographs were analysed for nine elements (Mn, Fe, Si, Al, Ni, Cu, Ti, K and Ca) to correlate the morphological features with chemical analysis. Co was not included in the X-ray microanalysis because of its low concentration and interference due to FeK_β line. The microanalysis data were not corrected for ZAF. Other means of chemical analysis which were employed to see the elemental distribution vis-a-vis morphology included X-ray mapping, line and point scans for individual elements.

Statistical Analysis: X-ray microanalysis data were analysed using linear regression analysis and Q-mode factor analysis. The details of these techniques are given below.

(a) Linear regression: The metal contents of the nodules at discrete points obtained by SEM/EDAX analysis were correlated using linear regression. Linear regression coefficient (r) between a set of X, Y data is defined as

$$r = \frac{C_{XY}}{\sqrt{S_X \cdot S_Y}}$$

where C_{XY} is covariance and S_X and S_Y are variance of X and Y.

Mathematically

$$C_{XY} = \frac{1}{n-1} \sum_{i=1}^n X_i Y_i - \left(\frac{\sum_{i=1}^n X_i}{n} \cdot \frac{\sum_{i=1}^n Y_i}{n} \right) / n$$

$$S_X = \frac{1}{n-1} \sum_{i=1}^n x_i^2 - \left(\frac{\sum_{i=1}^n x_i}{n} \right)^2$$

$$S_Y = \frac{1}{n-1} \sum_{i=1}^n y_i^2 - \left(\frac{\sum_{i=1}^n y_i}{n} \right)^2$$

Significance level of 99% was defined using null hypothesis (286).

(b) Factor analysis: Factor analysis is a multivariate data analysis technique which describes most of the variance in a complex data set in terms of a few statistically independent linear combination of original variables, known as factors. A detailed discussion on 'factor analysis' is beyond the scope of this thesis and may be found in reference (287). A brief description of the technique follows which shall be adequate to understand the contents of later chapters.

In factor analysis, the relationship within a set of m variables is regarded as reflecting the correlations of each of the variables with p mutually uncorrelated underlying factors. The usual assumption is that $p < m$. Variance in m variables is therefore derived from variance in the p factors, but in addition a contribution is made by unique sources which independently affect the m original variables. Factor analysis refers to the p underlying factors as common factors and summarizes the independent contribution as a unique factor. The factor model may be mathematically expressed as

$$X_j = \sum_{r=1}^p l_{jr} \cdot f_r + \epsilon_j$$

where f_r is the r^{th} common factor, p is the specified number of

factors and ϵ_j is random variation unique to the original variables X_j . Because there are m original variables X_j , there are m random variables ϵ_j , taken together these constitute the unique factor. The coefficient l_{jr} is loading of the j^{th} variate on r^{th} factor.

The sum of square of f_r for j^{th} variable is known as communality

$$h_j^2 = \sum_{r=1}^p f_r^2$$

The value of h_j^2 refers to the total explained variance for j^{th} variable. The magnitude of h_j^2 is function of p , if the number of factors is equal to the number of variables (i.e. $p = m$) then $h_j^2 = 1$. For p factors the remaining $(1.0 - h_j^2)$ variance of variable j is unique component associated with that variable.

Number of factors (p) to be extracted needs to be judiciously selected. Some analysts recommend retaining all those factors which have eigen-values greater than 1. The number of factors (p) also depends on whether they can be assigned any physical significance.

There are two modes in which factor analysis can be performed i.e. R-mode and Q-mode. For R-mode factor analysis, the name comes from the symbol for multiple correlation because it investigates interrelationships in a matrix of correlations between variables. The factors which are generated are new variables, having the form of linear combinations of original variables. In the Q-mode factor analysis, the role of samples and variables is reversed i.e. the factor analysis is concerned with interrelationship between samples.

In this investigation Q-mode factor analysis model with VARIMAX orthogonal rotation (factors are assumed to be uncorrelated) was used. The necessary FORTRAN IV computer program (Appendix-H) for computation has been reported by Davis and Sampson (287).

4.2.6 Sequential Extraction:

The technique involved the selective sequential removal of exchangeable ions, Mn-fraction, organic matter and Fe-fraction from manganese nodules by chemical treatments. This technique is normally used in geochemical studies (288). The objective of using this technique was two-fold: (i) to provide an independent check on elemental correlations established in SEM-EDAX studies on nodule sections and (ii) to use the technique as a concentration method for different phase constituents, so that the residues can be used for phase identification by conventional XRD and TEM.

The experimental procedure employed was similar to that of Robinson (288). The experimental conditions and reagents used in different sequential extraction steps are listed in Table IV.1.

The experiment was started with six dried nodule powder samples of ~0.2 g each. After each treatment, one thoroughly washed solid sample and three leach liquors were retained. Leach liquors were analysed by analytical techniques as described before. The residues were examined by XRD, TEM and TEM-EDAX.

4.3 Leaching Experiments on Synthetic Samples

Leaching behaviour of all the samples listed in Section 4.1.2 was investigated.

Table IV.1: Reagents used in different sequential extraction (SEQ) treatments (288)

Treatment	Purpose	Experimental conditions
SEQ-I	Removal of exchangeable ions	0.1M ammonium citrate adjusted to pH 8.4 with NH_4OH ; 20 min at 25°C
SEQ-II	Removal of Mn-fraction	0.1M $\text{NH}_2\text{OH}\cdot\text{HCl}$ in 0.01M HNO_3 , 0.5 hr at 25°C
SEQ-III	Removal of organic matter	50% H_2O_2 - 0.025M HNO_3 (3:2 mixture); heated to dryness, repeated once; residue extracted in 1M $\text{NH}_4\text{C}_2\text{H}_3\text{O}_2$ in 6% HNO_3 ; 0.5 hr at 25°C
SEQ-IV	Removal of Fe-fraction	0.7M $\text{NH}_2\cdot\text{NH}_2\cdot\text{H}_2\text{O}$ adjusted to pH 2.1 with HCl (hydrazine hydrochloride), 6 hrs at 90°C

Leaching experiments were carried out in a multineck, cylindrical glass reaction vessel immersed in a thermostatically controlled water bath. Sulfuric acid and sulfurous acid were used as leaching media. Sulfurous acid solutions of desired concentration were prepared by dissolving SO_2 gas generated by reaction of sulfuric acid on sodium metabisulfite. Stirring speed of 900 r.p.m. was constant in all the leaching experiments. Solution samples (5 ml) were withdrawn at selected time intervals and filtered.

The leaching conditions used for different samples are summarized in Table IV.2.

Table IV.2: Description of leaching conditions used for different samples

S. No.	Sample	Leaching medium	Leaching conditions				
			Temp. °K	Conc. M	pH	Pulp density	Size µm
1	Birnessites	H ₂ SO ₄	323	0.5	-	0.2	-63+53
2	All δ-MnO ₂ samples	H ₂ SO ₄	323	0.5	-	0.2	-53
3	Goethites	H ₂ SO ₄	323	0.5	-	0.2	-53
4	Birnessites	H ₂ SO ₃	293	0.03*	1.8	0.1	-210 +149
5	All δ-MnO ₂ samples	H ₂ SO ₃	293	0.03	1.8	0.1	-53
6	Goethites	H ₂ SO ₃	293	0.23	1.5	0.1	-53

* Molar concentration in terms of SO₂.

For leaching of goethites in sulfurous acid, the concentration of SO₂ and pH were measured at the beginning and end of the leaching experiments. Concentration and pH remained almost constant during leaching. Almost all the dissolved SO₂ was consumed during leaching of manganese oxyhydroxides.

Presentation of Leaching Data: Leaching data (for S. No. 1-6, Table IV.2) are presented in terms of mole/cm², 'fraction reacted' (F_i) or 'leachability parameter' (NF_i). Leachability parameter (NF_i) for an element i is defined as follows:

$$NF_i = \frac{F_i}{SA} \text{ (g m}^{-2}\text{)}$$

where

SA = Initial specific surface area of sample m^2/g).

The use of normalized fraction reacted (NF_i) was found to be essential in order to have a coherent basis for leaching data comparison among the different samples, eliminating the ever-present factor of the magnitude of surface area.

The reproducibility of leaching experiments is of the same order as that of analytical methods used. The chemical analysis was often repeated to check the reproducibility.

The mathematical techniques which are used in processing of leaching data include linear and multilinear regression (Appendix-I).

CHAPTER - V

PHASE IDENTIFICATION IN NODULES

The results of phase identification studies on nodules are presented and discussed in this chapter. The contents are divided into two subsections; while the first subsection deals with the results of X-ray diffraction studies, the transmission electron microscopy results are covered in the second subsection.

5.1 X-ray Diffraction:

General Features:

The XRD patterns given in Figure V.1 illustrate some salient features of minerals present in manganese nodules. Most often nodule powder samples yield XRD patterns similar to Figure V.1(a). This pattern depicts the X-ray amorphous nature of nodule material and also shows the limitation of this technique in the identification of minerals present in nodules having crystallite size much less than $1\text{ }\mu\text{m} \times 1\text{ }\mu\text{m} \times 1\text{ }\mu\text{m}$ in dimension (22).

The XRD patterns in Figure V.1(b) and V.1(c) correspond to the $10\text{ }\text{\AA}$ -phase rich material collected from the periphery and centre of a manganese nodule sample. Marked change in the position of $10\text{ }\text{\AA}$ line might have resulted due to dehydration of this phase. Samples having XRD patterns shown in Figure V.1(b) and V.1(c) when heated at 120°C for 10 hrs yielded XRD patterns (Figure V.1(d) and V.1(e)) which appear to be quite identical.

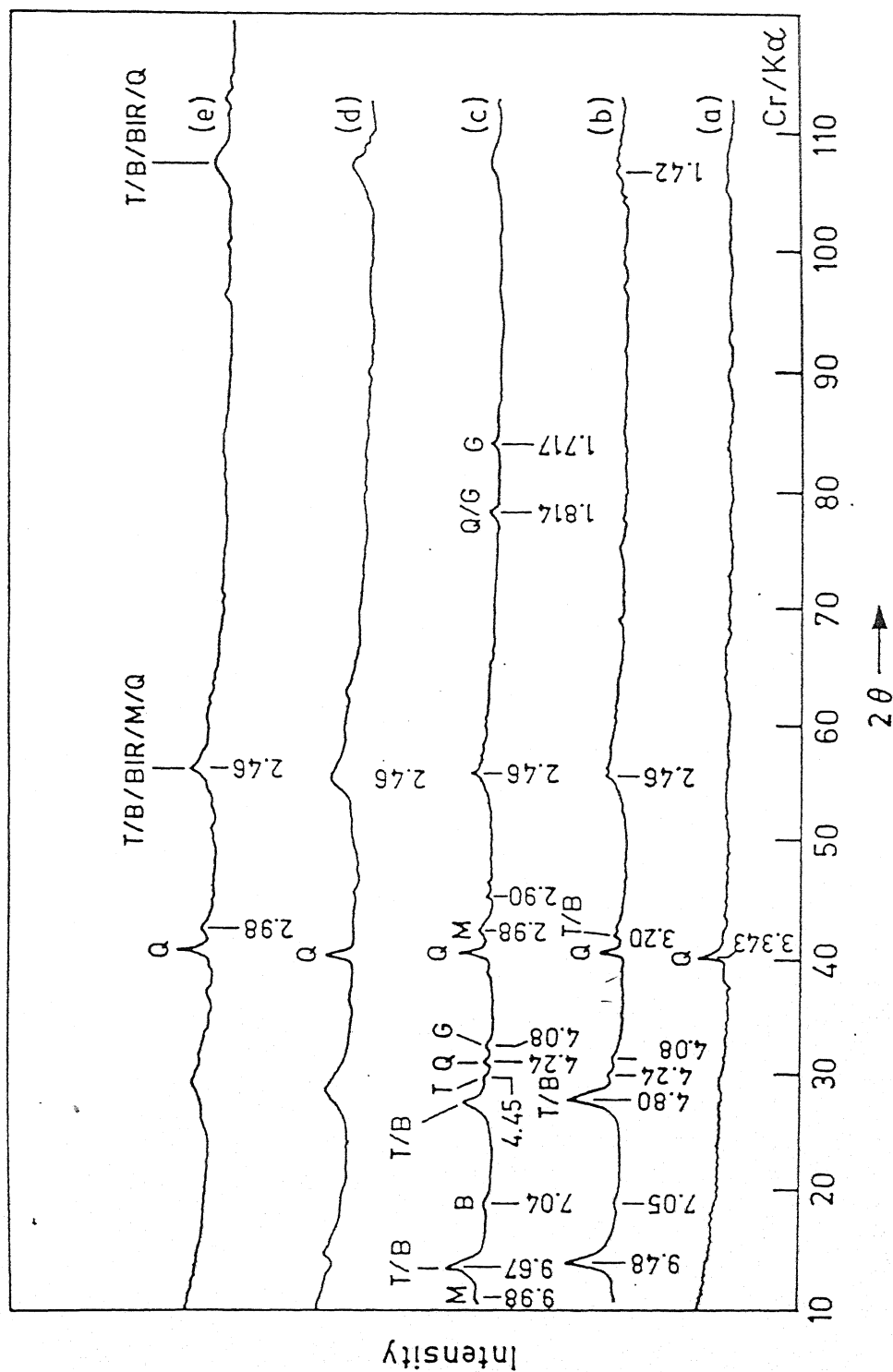


Fig. V.1. XRD pattern of (a) as received sample (b), (c) 10- \AA phase rich material from periphery and core of a nodule and (d), (e) material in (b) and (c) respectively heated at 120 $^\circ\text{C}$, 10 hrs.
 T- Todorokite, B- Buserite, BIR- Birnessite, Q- α -quartz
 G- Goethite, M- Montmorillonite-chlorite.

Structure of 10 \AA° -Phase:

The XRD patterns for 10 \AA° -phase in Figure V.1(b) and V.1(c) do not throw any light on the nature of this phase in terms of buserite (layered structure) or todorokite (tunnel structure). Synthetic metal-buserites yield birnessite ($7.0, 3.6 \text{ \AA}^{\circ}$) on heating or dehydration. Absence of XRD lines at 7 and 3.6 \AA° in Figure V.1(d) and V.1(e) indicates that the 10 \AA° phase may be either todorokite or disordered variety of buserite (73).

Attempts were made to ascertain the structure of 10 \AA° -phase by intercalation with dodecylammonium chloride. The XRD patterns of intercalated natural samples are presented in Figure V.2(a) and V.2(b) together with XRD patterns of intercalated synthetic Na-buserite and Ni-buserite (Figure V.2(c) and V.2(d)). Figure V.2(a) and V.2(b) indicate that the structure of natural 10 \AA° -phase is not simple layered structure similar to Na-buserite. These results are in contrast with the findings of Ostwald and Dubrawski (112). These workers (112) have shown that the marine 10 \AA° -phase has a layered structure similar to Na-buserite. Although the structure of synthetic Ni-buserite itself is open to question, R. Giovanoli (Personal Communication, May 1988) has contended that insertion of Cu(II) and Ni(II) in the interlayer of buserite increases the interlayer bridging forces to such an extent that intercalation with dodecylammonium chloride does not occur. Increased interlayer bridging forces represent only one of the possibilities because sample with tunnel structure will also respond negatively to intercalation. It is interesting to note that the intensity of line at 9.67 \AA° in the XRD pattern of phase from the core of the nodule

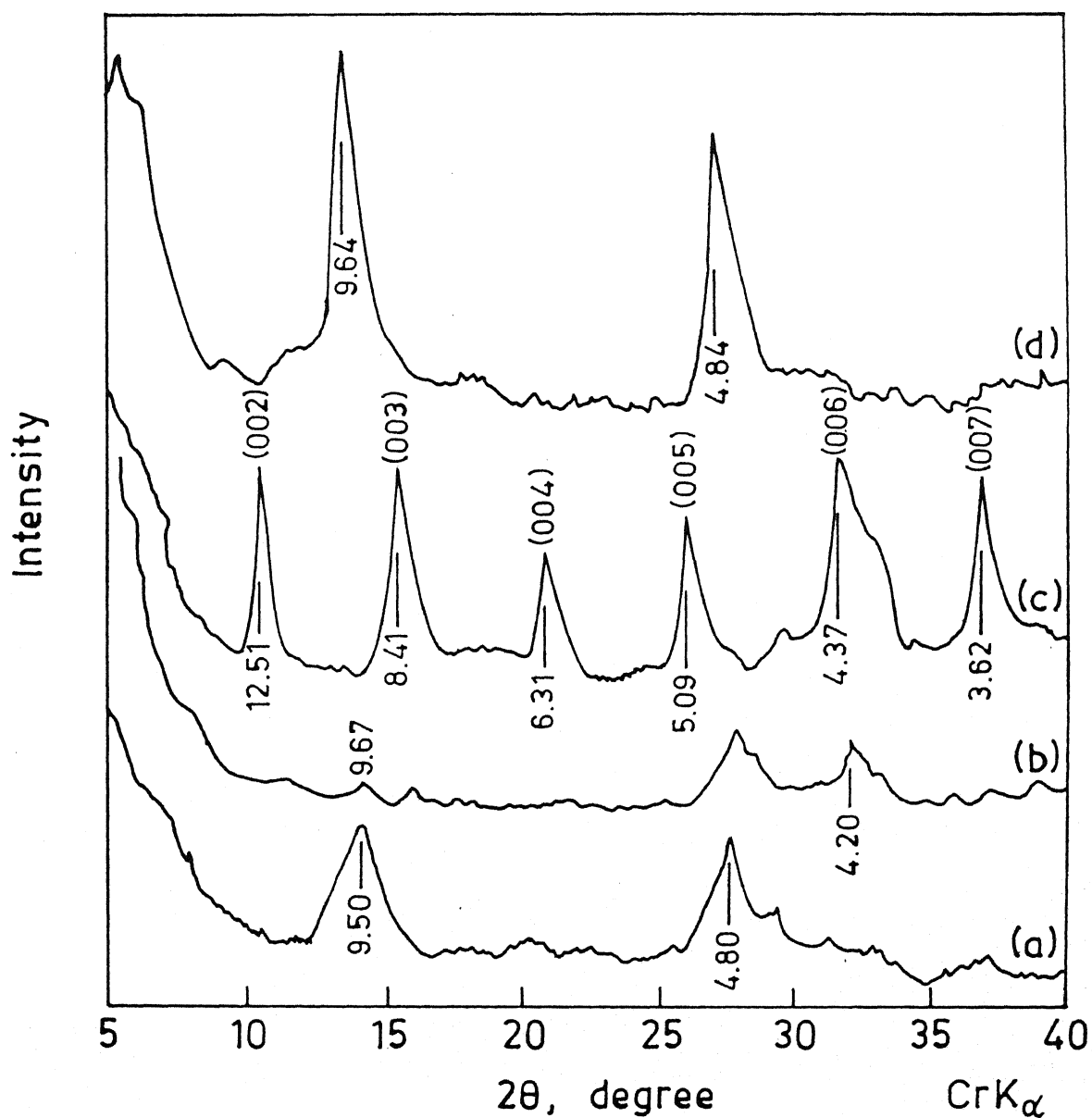


Fig. V.2. XRD patterns after intercalation with dodecylammonium chloride (a), (b) 10 Å phase from periphery and core of a nodule (c) synthetic Na-buserite and (d) synthetic Ni-buserite.

(Figure V.1(c)) decreases after intercalation (Figure V.2(b)). The results for 10 A° -phase from periphery of nodule are quite different (Figure V.1(b) and V.2(a)) i.e. the intensity of peak (9.48 A°) remains unaffected. These results suggest that the stability of 10 A° -phase from core of nodule is poorer compared to the phase from the periphery of nodule and negative intercalation response of core material results due to its disordered layered structure. It is suggested that the 10 A° phase from the periphery is todorokite (more stable) and from the centre is disordered busserite or busserite-todorokite assemblage (less stable).

XRD of Nodule Residues:

Figure V.3 shows the XRD patterns from nodule residues obtained after sequential extraction experiments (Section 4.2.6) on nodule powder sample. The XRD pattern of corresponding original nodule powder sample has been reported before in Figure V.1(a). Figure V.3(a) and V.3(b) correspond to the residue 1 containing Fe-fraction plus silicate material (obtained after sequential extraction treatments, 1-3) and residue 2 (silicate material obtained after sequential extraction treatments, 1-4) respectively.

Almost all the peaks which are assigned for Fe-bearing minerals in the XRD pattern of residue 1 (Figure V.3(a)) remain unaltered or increase in intensity in the XRD pattern of residue 2 (siliceous material) (Figure V.3(b)). This means that the peaks in Figure V.3(a) correspond to silicate phases. The technique of X-ray diffraction is not at all helpful in elucidating the nature of iron bearing minerals.

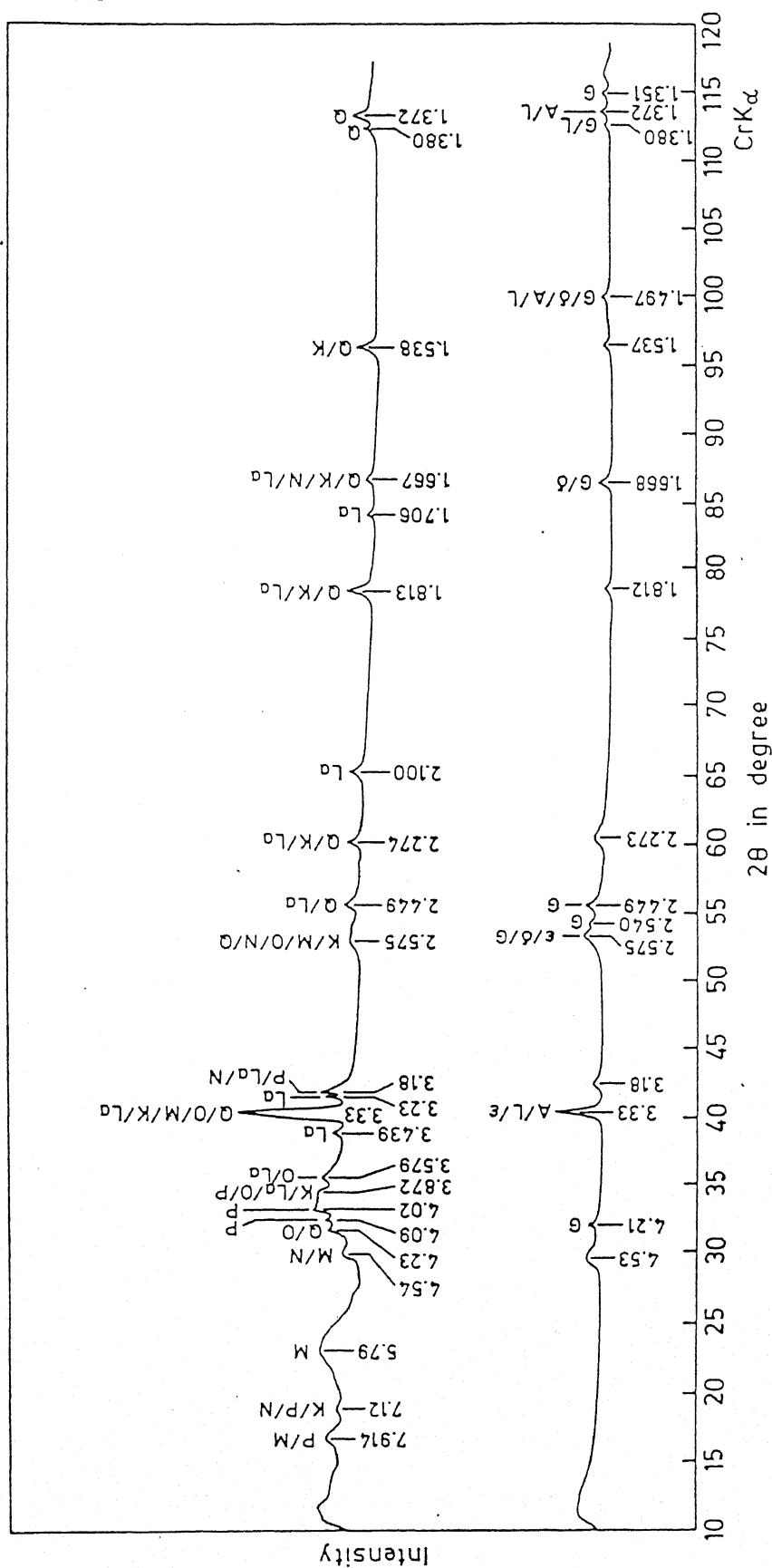


Fig. V.3. XRD patterns of nodule residues after sequential extraction (a) residue 1 (Fe+silicate fraction) and (b) residue 2 (silicate fraction).

G-Goethite, A-Akaganeite, L-Lepidocrocite, ε-ε-FeOOH, δ-δ-FeOOH, P-Phillipsite, O-Orthoclase, La-Labradorite, K-Kaolinite, N-Nontronite, M-Montmorillonite-Chlorite, Q-α-quartz.

The silicate minerals, particularly the ones which are of detrital origin, are not detected by X-ray because of their very small amount (<5%). The concentration of siliceous fraction, by sequential extraction, does help in elucidating the XRD features of siliceous fraction in a better way (Figure V.3). Most of the silicate minerals except perhaps zeolites remain unaffected by the chemical treatments employed in sequential extraction (134, 135, 288). The silicate minerals which can be inferred from XRD patterns (Figure V.3) are as follows:

α -quartz (SiO_2), orthoclase (KAlSi_3O_8), labradorite ($\text{Ca}_{0.7}\text{Na}_{0.3}\text{Al}_{1.7}\text{Si}_{2.3}\text{O}_8$), kaolinite ($\text{Al}_2(\text{OH})_4\text{Si}_2\text{O}_5$), montmorillonite-chlorite ($(\text{Na}, \text{K}, \text{Ca}/2)_{0.34}\text{Mg}_{0.8}\text{Al}_{2.58}(\text{Si}_{3.32}\text{Al}_{0.68})\text{O}_{10}(\text{OH})_5 \cdot 2\text{H}_2\text{O}$ (semectite), montronite (Fe-semectite), phillipsite ($\text{Na}_2\text{O} \cdot \text{Al}_2\text{O}_3 \cdot 3.3\text{--}5.3 \text{SiO}_2 \cdot 4.3\text{--}5.7 \text{H}_2\text{O}$) etc.

5.2 Transmission Electron Microscopy

TEM offers possibly the only means of studying the poorly crystalline constituents present in the nodules because of its ability to examine very small sized particles of reasonable degree of crystallinity when operated in imaging mode coupled with selected area electron diffraction.

Large number of particles were examined under the microscope. At least fifty percent of particles yielded no diffraction pattern or mixed patterns difficult to analyse. Selected area electron diffraction (SAED) patterns from more than one hundred particles were recorded and further processed for indexing. SAED spot patterns which could be indexed unambiguously are listed in Table V.1. A

Table V.1: List of unambiguously solved selected area electron diffraction (SAED) patterns

Mineral name	Ref. ASTM	Experimental					(hkl) _i			Theoretical					Beam dire- ction	Remark Sample/ Figure
		d ₁ A°	d ₂ A°	d ₃ A°	φ ₁ deg- ree	φ ₂ deg- ree	i=1	i=2	i=3	d ₁ A°	d ₂ A°	d ₃ A°	φ ₁ deg- ree	φ ₂ deg- ree		
MANGANESE MINERALS																
Na-Birnessite	23-1046	4.42	4.42	2.59	61.0	30.5	130	130	060	4.40	4.40	2.57	62.0	31.0	001	0*
		4.27	4.21	2.43	60.0	31.0	200	131	331	4.27	4.21	2.43	60.5	30.6	013	0/V.4
		2.22	2.26	3.24	138.0	71.0	063	260	203	2.26	2.19	3.18	138.9	71.6	312	0
		7.63	3.39	2.84	78.5	56.5	020	014	034	7.70	3.47	2.93	77.0	55.2	100	0
Todorokite	13-164	2.38	2.38	1.38	58.0	29.0	211	211	022	2.39	2.39	1.39	58.5	29.2	011	0
		2.11	2.07	1.97	114.5	59.0	310	173	403	2.14	2.08	1.94	114.1	58.4	394	0/V.6
SILICATES																
α-quartz	5-490	5.41	4.26	3.34	90.0	51.5	001	100	101	5.41	4.26	3.24	90.0	51.8	010	0/V.12
		3.39	3.36	2.30	86.5	42.0	011	101	112	3.34	3.34	2.28	85.8	42.8	111	2*/V.12
		4.23	2.29	1.80	74.5	50.0	100	012	112	4.26	2.28	1.82	74.5	50.1	021	1*
		3.34	1.99	1.61	81.5	53.0	011	201	210	3.34	1.98	1.61	82.0	53.5	122	0
Montmorillonite -chlorite	12-237	4.49	4.53	4.49	120.0	60.0	110	110	020	4.51	4.51	4.53	120.2	60.1	001	0, 1, 2/ V.14
Kaolinite	14-164	2.60	2.97	1.96	90.5	41.5	200	0010	2010	2.60	2.98	1.95	90.0	41.1	010	1
		3.72	4.34	4.03	122.0	54.5	112	021	111	3.75	4.32	4.13	122.4	53.8	112	1/V.14
Labradorite	18-1202	2.49	3.66	1.75	63.5	26.0	241	130	171	2.51	3.63	1.75	64.6	25.8	3110	0
		4.44	5.85	3.72	95.5	38.5	021	111	130	4.36	5.83	3.63	94.5	38.4	312	0/V.13
		1.80	3.31	1.65	94.5	30.0	171	112	263	1.78	3.37	1.62	94.1	28.8	1518	2
		5.90	5.71	6.50	127.5	65.5	111	111	020	5.83	5.66	6.42	126.9	65.2	101	2/V.13

* Observed in: 0 - as received sample; 1 - residue after removal of only Mn; 2 - siliceous residue.

significant number of patterns, particularly from the original nodule samples suffered from multiple indexing (vide Appendix-J). The statistical occurrence of minerals is summarized in Table V.2.

The manganese mineral Na-birnessite ($a = 8.54 \text{ \AA}$, $b = 15.39 \text{ \AA}$, $c = 14.26 \text{ \AA}$, orthorhombic) was identified four times unambiguously and observed four times with other minerals (Tables V.1 and V.2). Quite often the particles corresponding to Na-birnessite showed preferred orientation perpendicular to $\langle 001 \rangle$ direction (Table V.1). A typical electron micrograph of Na-birnessite is given in Figure V.4(a) along with its SAED pattern (Figure V.4(b)). This mineral shows flake like morphology (107) and this feature is apparent in the micrograph. The diffraction pattern in Figure V.4(b) can also be indexed for α -quartz. But keeping in view the similarity in the morphology and spot intensities between the natural and the synthetic mineral (Figure V.5(a) and V.5(b)) it was concluded that birnessite is the one which is more probable.

Todorokite ($a = 9.75 \text{ \AA}$, $b = 2.849 \text{ \AA}$, $c = 9.59 \text{ \AA}$; pseudo-orthorhombic, $\beta \simeq 90$) is the other manganese mineral which has been identified (Tables V.1 and V.2). SAED patterns of todorokite often get mixed up with those for cryptomelane (ASTM 20-908) and vernadite (ASTM 15-604). This is not surprising because crystallographic data of all these minerals are quite similar. Cryptomelane has been observed in manganese nodules very rarely (83). Giovanoli (23) has categorically pointed out that the X-ray data in ASTM file under No. 15-604 have been erroneously entered for the mineral vernadite and actually corresponds to cryptomelane. The occurrence of todorokite in the sample studied is in accordance with XRD data and metal association (Mn-Ni-Cu-Mg-Na) observed in the present

Table V.2: Statistical occurrence of minerals in manganese nodules

Mineral name and nature of pattern	No. of times observed	Reference	
		ASTM	Others
Birnessite (S)	9(4 [*])	23-1046	-
Todorokite (S)	4(2)	13-164	-
Nsutite (S)	1	17-510	-
δ -MnO ₂ (Vernadite) (R)	Many	-	(83, 124)
Goethite (R)	Many	17-536	-
Ferroxyhyte (R)	Many	-	(83, 124)
Ferrihydrite (R)	Many	-	(283)
Manganite	1	13-157	-
α -quartz (S)	6(4)	5-490	-
Montmorillonite (S)	Many	12-231	-
Orthoclase (S)	2	19-931	-
Labradorite (S)	10(4)	18-1202	-
Kaolinite (S)	3(1)	14-164	-
Sanidine (S)	3	19-1227	-
Prehnite (S)	2	7-333	-
Pyrophyllite (S)	2	12-203	-
Mordenite (S)	4	6-239	-
Phillipsite (S)	2	12-195	-

S - Spot pattern, R - Ring pattern.

* - Number of unambiguously solved diffraction patterns.

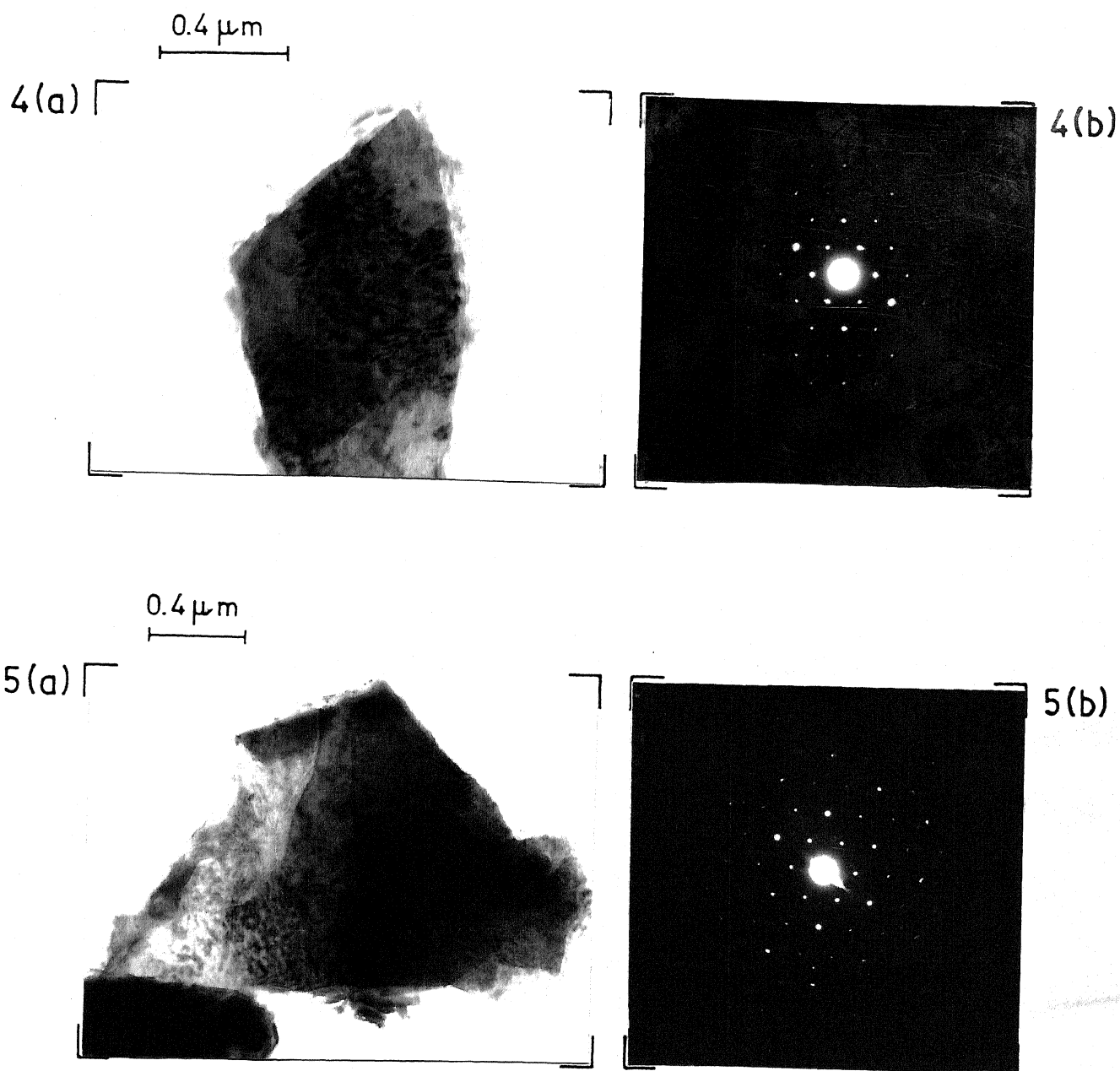


Fig. V.4. (a) Typical electron micrograph of Na-birnessite observed in Mn-nodule sample (b) SAED pattern corresponding to (a).

Fig. V.5. (a) Electron micrograph and (b) SAED pattern from synthetic Na-birnessite.

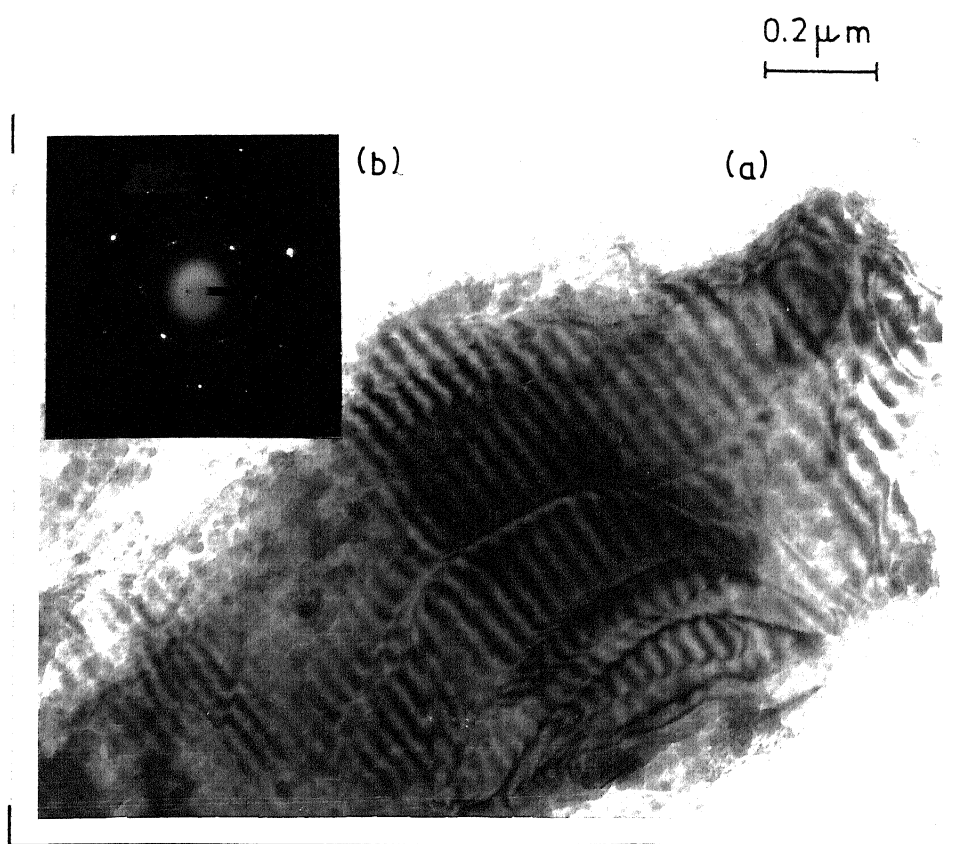


Fig. V.6. (a), (b) Electron micrograph and SAED pattern from a todorokite crystal with faulted structure.

investigation. Todorokite is known to show many types of structural disorder. Turner and Buseck (55, 88) have noted that differently sized tunnel structures in todorokite result in streaking of diffraction patterns; diffuse diffraction spots occur if one tunnel type is sufficiently prominent. Also the disordered intergrowth sequences are themselves not consistent over even small areas of crystal. This perhaps explains the observation of additional diffuse diffraction spots in the SAED pattern (Figure V.6(b)) of todorokite crystal shown in Figure V.6(a). The fringes in Figure V.6(a) may be the result of changing stacking sequence in the todorokite crystal.

Negative response of the 10 \AA^0 -phase detected by XRD to the intercalation treatment coupled with TEM observations (Table V.1, Figure V.6(a) and V.6(b)) indicate the more probable occurrence of todorokite in the samples investigated. The presence of layered structure busserite ($a = 2.86$, $c = 9.6\text{--}10.0 \text{ \AA}^0$; hexagonal) cannot be completely ruled out keeping in view the occurrence of birnessite. Detection of birnessite (only by TEM) indicates that the crystallinity of this mineral is very poor. It is likely that the mineral busserite gets converted into birnessite under high vacuum of TEM.

Electron diffraction data for the different iron bearing minerals observed in this investigation are listed in Table V.3 along with standard 'd' values obtained from literature. Attempts to record a single crystal SAED pattern from iron bearing minerals failed due to geometrical limitation of microscope i.e. the selected area for the diffraction was much larger than the individual iron bearing mineral crystals. The grain size turned out to be less than about 200 \AA^0 .

Table V.3: Electron diffraction data on iron-bearing minerals compared with standard 'd' values* from literature

GOETHITE ASTM (17-537) d, A° (hkl)	THIS WORK FIG. 7 d, A°	AKAGANEITE ASTM (13-157) d, A° (hkl)	LEPIDOCROCITE ASTM (8-98) d, A° (hkl)	THIS WORK FIG. 8 d, A°	FERRIHYDRITE (JONES and SALEH, 283) d, A° (hkl)	THIS WORK FIG. 10 d, A° (hkl)	FERROXYHYTE (CHUKHROV, 83, 124) d, A° (hkl)	THIS WORK FIG. 11 d, A°
4.18 110	4.25							
3.38 120	-	3.31 310	3.29 120	3.33				
2.52 101	2.52				2.53 110	2.53	2.54 100	2.52
2.25 121	2.28				2.23 112	2.22	2.23 101	
2.19 140	-	2.10 321	2.09 060	2.12	1.97 113	1.97		
1.69 240	1.69				1.72 114		1.69 102	
1.50 320	1.52				1.515 115	1.52	1.50 110	1.51
1.32 321	1.31				1.48 300			
1.26 331	1.26				-	1.27		
1.24 142	-				204			
			1.21 280	1.23				
					1.07 306/	1.11		
					118			
					0.965 119	0.95		
					0.881 1110			
					0.854 0011	0.86		
					0.844 330			

* Only relevant lines presented.

The mineral goethite (α -FeOOH) was observed with varying degree of crystallinity as shown in Figure V.7(a) and V.7(c). The corresponding SAED patterns are shown in Figure V.7(b) and V.7(d). Poor crystallinity of goethite may result from high concentration of Cl^- in sea water and poor crystallinity of primary iron bearing phases which convert into goethite due to air oxidation (71).

The SAED pattern in Figure V.8(b) which corresponds to the electron micrograph in Figure V.8(a) may be assigned to both akaganeite (β -FeOOH) or lepidocrocite (Table V.3). Johnston and Glasby (96) and Thijs et al. (97) contend that stabilization of β -FeOOH by the presence of Cl^- ions makes it the more preferred oxyhydroxide of iron present in nodules. Based on IR spectroscopy, Mossbauer spectroscopy and transmission electron microscopy (TEM) studies on ferric chloride hydrolysis products, Kauffman and Hazel (79) have observed that the initially formed amorphous ferric oxyhydroxide gel appears to be a structurally mixed phase with discrete microstructural clusters of phases similar to α -FeOOH and β -FeOOH. The present work on synthesis of goethites from nitrate solution yields intermediate products which have morphological and diffraction pattern similarities with the natural material (Figure V.9(a) and V.9(b)). It is likely that the synthetic material represent phases (δ - and γ -FeOOH) which can topotactically transform into goethite (Figure II.3). The mineral β -FeOOH can transform into goethite only non-topotactically. Morphological and SAED evidence (Figure V.8(c) and V.8(d)) for the natural material suggest that it indeed gets converted into α -FeOOH (lath shaped crystals). Lines at $d = 3.31$ and 3.38 \AA^0 are of strong and medium intensities in β or γ and α -FeOOH respectively (Figure V.8(b) and V.8(d)).

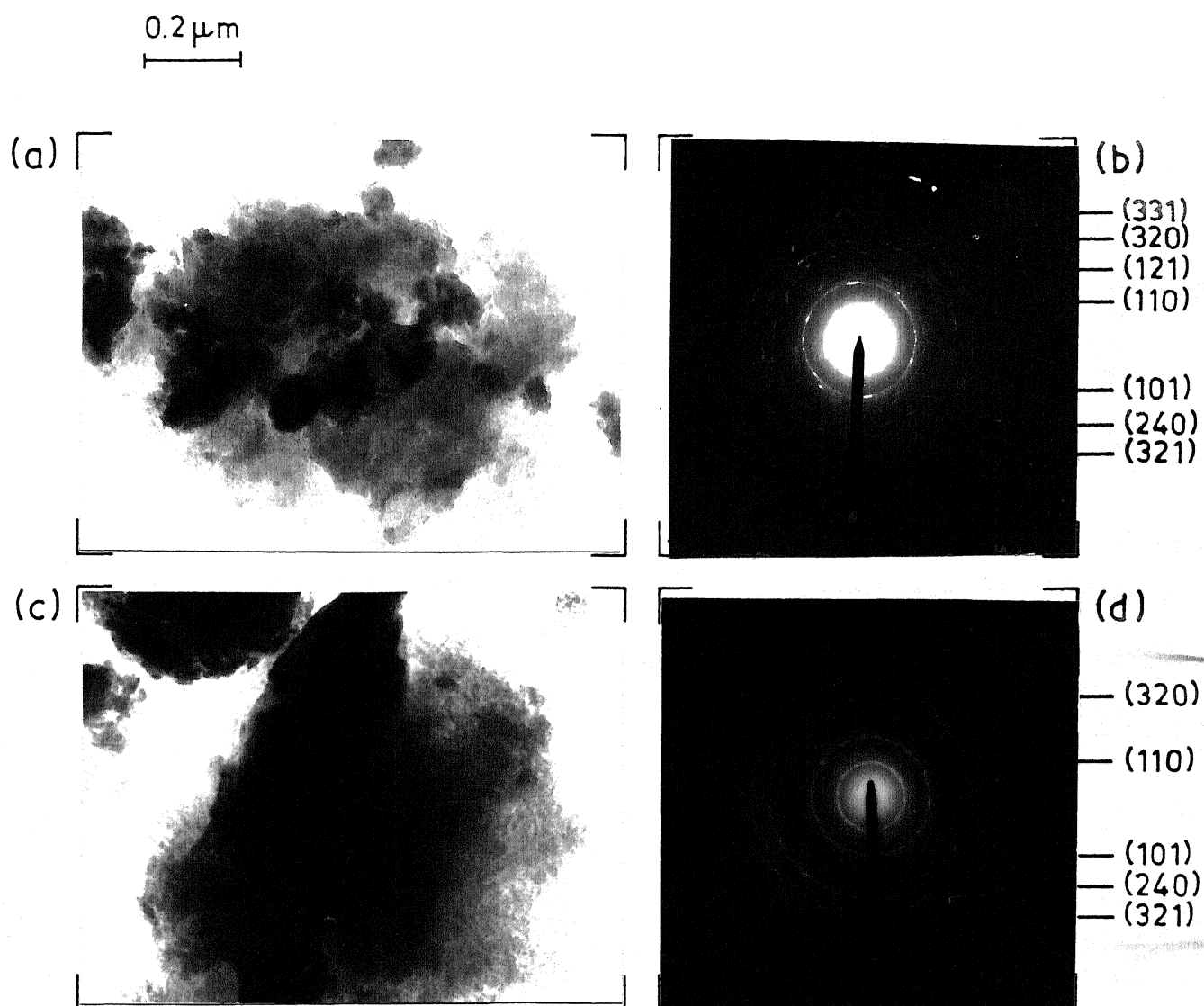


Fig. V.7. (a), (c) and (b), (d), electron micrographs and corresponding SAED patterns showing variation in the crystallinity of goethite.

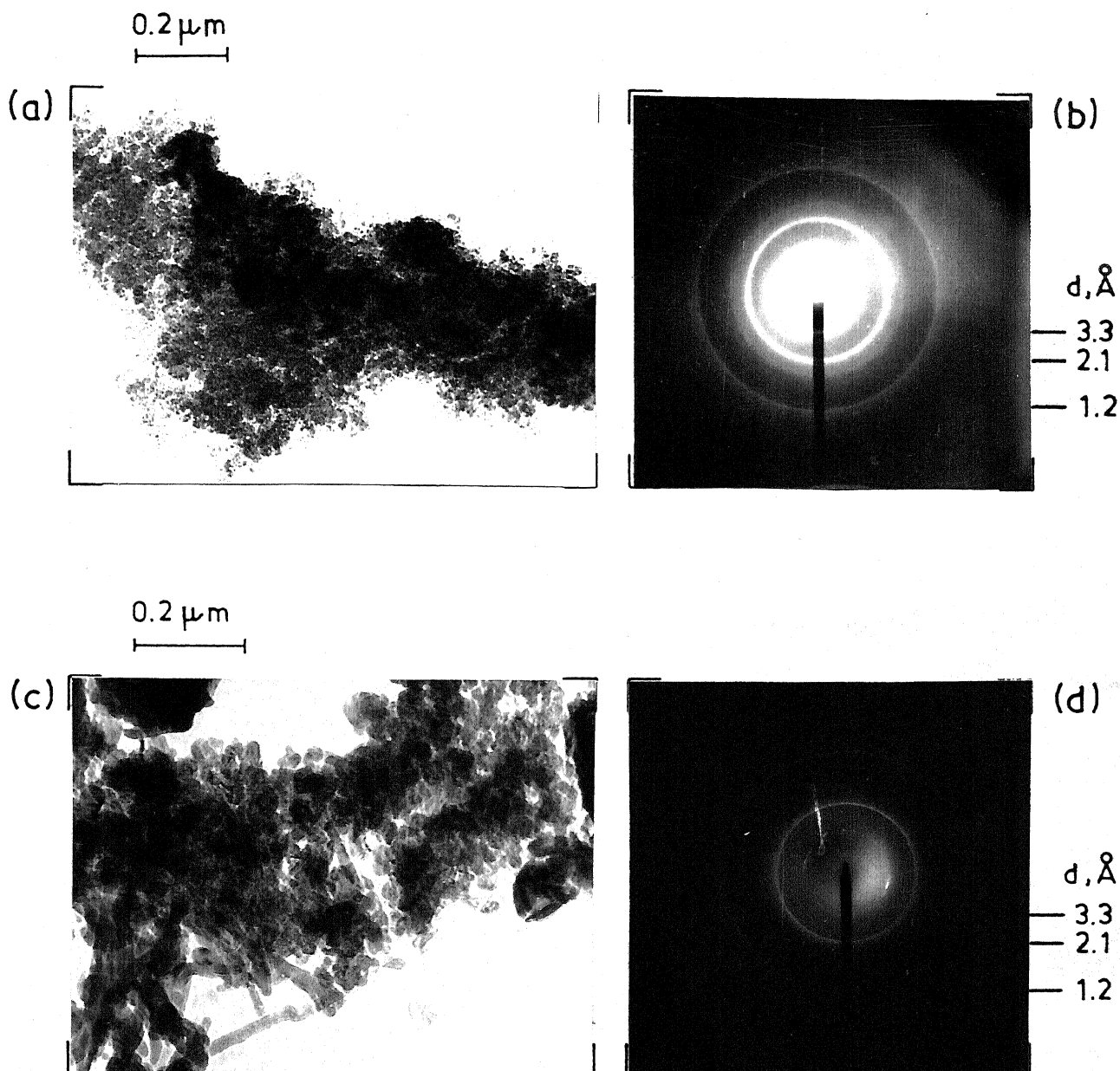


Fig. V.8. (a), (b) electron micrograph and SAED pattern of akaganeite (β -FeOOH) and/or lepidocrocite (γ -FeOOH) (c), (d) micrograph and SAED pattern indicating simultaneous occurrence of goethite (α -FeOOH) and akaganeite (β -FeOOH) or lepidocrocite (γ -FeOOH).

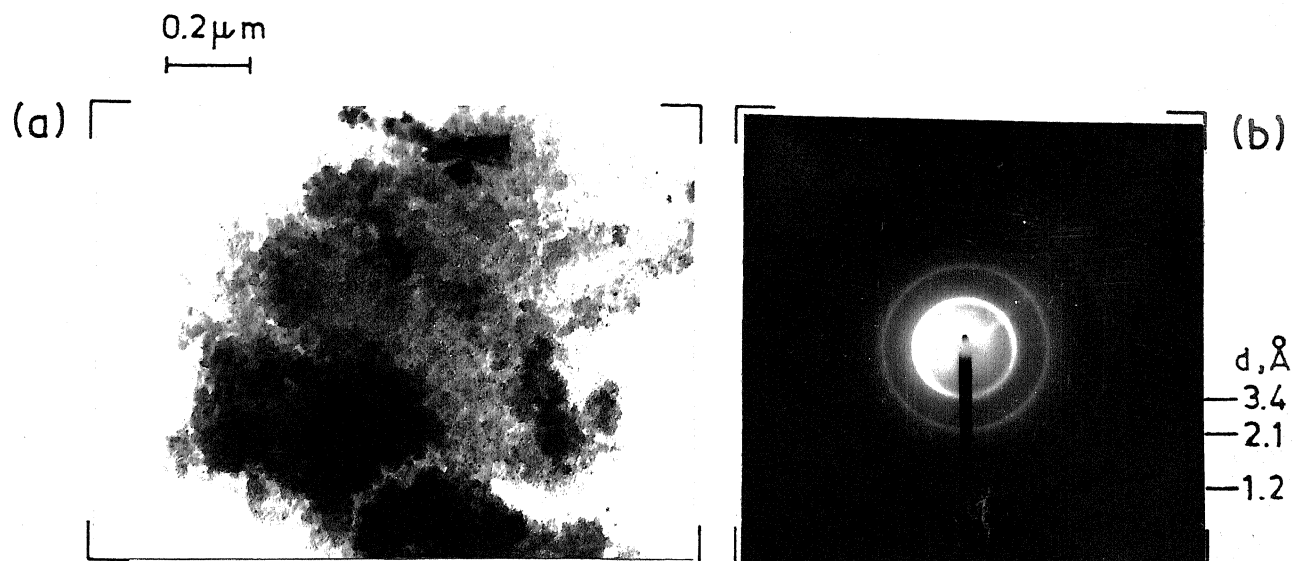


Fig. V.9. (a), (b) Electron micrograph and SAED pattern of synthetic intermediate phase formed during synthesis of goethite coprecipitated with cobalt.

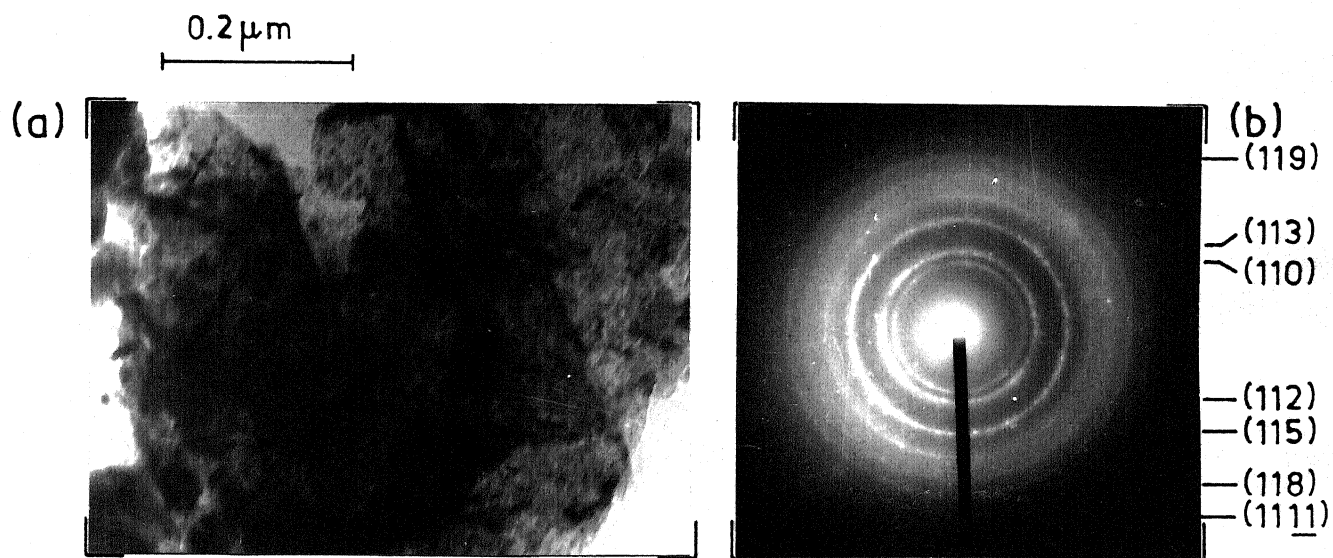


Fig. V.10. (a), (b) Electron micrograph and SAED pattern of mineral ferrihydrite.

Figures V.10(a) and V.10(b) show the electron micrograph and corresponding SAED from another area. All the lines in the diffraction pattern of Figure V.10(b) can be assigned to the mineral ferrihydrite ($5\text{Fe}_2\text{O}_3 \cdot 9\text{H}_2\text{O}$) (71, 124, 283, 289, 290). Presence of ferrihydrite in the Pacific ocean nodules has been reported in the TEM investigation of Heimendahl et al. (19). Ferrihydrite is an ill-defined phase in literature. Atkinson et al. (265) have suggested that the principal lines at $d = 2.52 \text{ \AA}$, 1.48 \AA and 1.27 \AA could arise from a combination of goethite $d(021) = 2.58 \text{ \AA}$ and $d(040) = 2.49 \text{ \AA}$; $d(002) = 1.51 \text{ \AA}$ and $d(061) = 1.45 \text{ \AA}$; and $d(042) = 1.29 \text{ \AA}$ and $d(080) = 1.25 \text{ \AA}$. Burns and Burns (18) propose that the mineral referred to as ferrihydrite is merely a poorly ordered arrangement of (FeO_6) octahedra. According to Murray (71), it is more likely that ferrihydrite serves as a source of dissolved iron for crystallization of goethite from solution phase. Recent Mossbauer studies (133) have shown that hyperfine field (H_i) for goethite (505 kOe , 4.2°K) is quite distinct from ferrihydrite ($470\text{--}500 \text{ kOe}$, 4.2°K). The 'd' spacings observed for ferrihydrite in this investigation are well in accordance with recently published electron diffraction data for this mineral by Jones and Saleh (283). It is worthwhile to note that (a) the line at $d = 4.2 \text{ \AA}$ observed for goethite (strongest line) is missing for ferrihydrite and (b) the line at $d = 1.96\text{--}1.97 \text{ \AA}$ which is supposed to be diagnostic for ferrihydrite (124) is present in the ferrihydrite observed in this work.

The morphology shown in Figure V.11(a) is typical of vernadite ($\delta\text{-MnO}_2$) or ferroxhyte ($\delta'\text{-FeOOH}$) (83, 124). Vernadite and ferroxhyte can be distinguished from each other by diagnostic

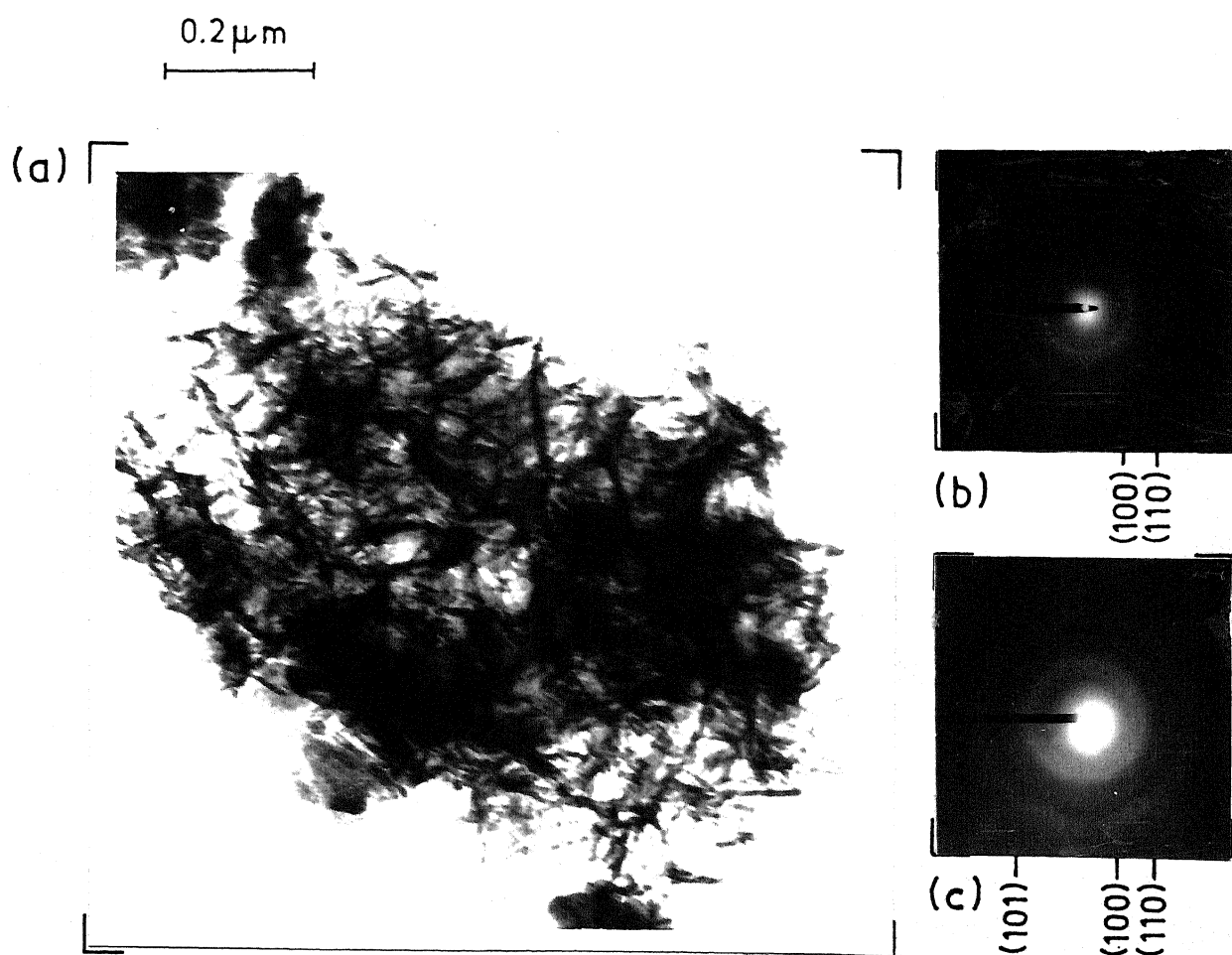


Fig. V.11. (a) Electron micrograph showing morphology similar to ferrosyhyte (δ' -FeOOH) and vernadite (δ -MnO₂), (b) and (c) typical SAED patterns from morphology similar to (a).

differences in their respective diffraction patterns. Whereas the electron diffraction pattern of ferroxhyte contains the reflections 2.50 \AA° (100), 2.21 \AA° (101), 1.69 \AA° (102) and 1.50 \AA° (110); that of vernadite shows only the reflections 2.4 \AA° (100), 2.2 \AA° (101) and 1.4 \AA° (110). In the latter, the reflection (101) is mostly very weak and the reflection (102) is absent (83). These diagnostic differences were not always clear in the several particles of this morphology observed in this work. Three distinct kinds of SAED patterns were recorded from particles of this morphology. Some particles did not yield any pattern at all and others either gave two rings at 2.52 \AA° and 1.5 \AA° (Figure V.11(b)) or three rings at 2.45 \AA° , 2.2 \AA° (diffuse) and 1.45 \AA° (Figure V.11(c)). Particles which gave two reflections at 2.52 \AA° and 1.5 \AA° were observed more frequently in the residue obtained after removal of Mn-fraction from original nodule powder sample (as compared to original sample), thus providing sufficient evidence for occurrence of ferroxhyte in the sample studied by us. Absence of the reflection at 1.69 \AA° in particles which gave three reflections at 2.45 \AA° , 2.2 \AA° and 1.45 \AA° indicates the presence of vernadite or $\delta\text{-MnO}_2$. Efforts to separate the two phases in the TEM-EDAX study were not successful in the sense that the EDAX spectra invariably consisted of mixture of iron and manganese. Ferroxhyte is known to show epitaxial intergrowth with $\delta\text{-MnO}_2$ in manganese nodule (18). Close association between Mn and Fe in particles of this morphology provides further evidence for the occurrence of vernadite in the sample studied in this investigation.

The accessory minerals definitely identified in nodule samples include α -quartz, feldspars, kaolinite, montmorillonite (Tables V.2 and V.3) and calcite. Studies on the residues helped in unambiguous identification of these minerals.

The mineral α -quartz ($a = 4.913 \text{ \AA}$, $c = 5.405 \text{ \AA}$; Hexagonal) was identified unambiguously two times in the original nodule samples and once each in residue 1 (Fe-fraction + silicates) and residue 2 (silicate material) (Table V.1). Some typical electron micrographs and their respective SAED patterns are presented in Figure V.12.

Diffraction pattern for feldspar minerals e.g. labradorite ($\text{Ca}_{0.7}\text{Na}_{0.3}\text{Al}_{1.7}\text{Si}_{2.3}\text{O}_8$; $a = 8.176 \text{ \AA}$, $b = 12.865 \text{ \AA}$, $c = 7.102 \text{ \AA}$; $\alpha = 93^\circ$, $27.1'$, $\beta = 116^\circ$, $2.9'$, $\gamma = 90^\circ$, $30.6'$) (Figure V.13) could be indexed only in large error limits compared to other minerals (Table V.1). This is perhaps related to the purity of minerals present in the nodule samples. Change in the proportion of Na and Ca and substitution of these elements by other elements is a common feature of feldspar minerals.

Sheet structure of kaolinite ($\text{Al}_2(\text{OH})_4\text{Si}_2\text{O}_5$; $a = 5.155$, $b = 8.959$, $c = 7.407 \text{ \AA}$; $\alpha = 91.68^\circ$, $\beta = 104.87^\circ$, $\gamma = 89.94^\circ$) is evident in the electron micrograph of Figure V.14(a). Figure V.14(b) shows the corresponding diffraction pattern. In the indexed pattern (Figure V.14(b)) different diffraction spots satisfy the extinction condition $3h^2 + k^2 = \text{odd}$, and this corresponds to the first ellipse in the texture pattern of this mineral (291). The streaking of the spots may be caused by deformation in the crystal which might have resulted during powdering or partial leaching in sequential extraction (291).

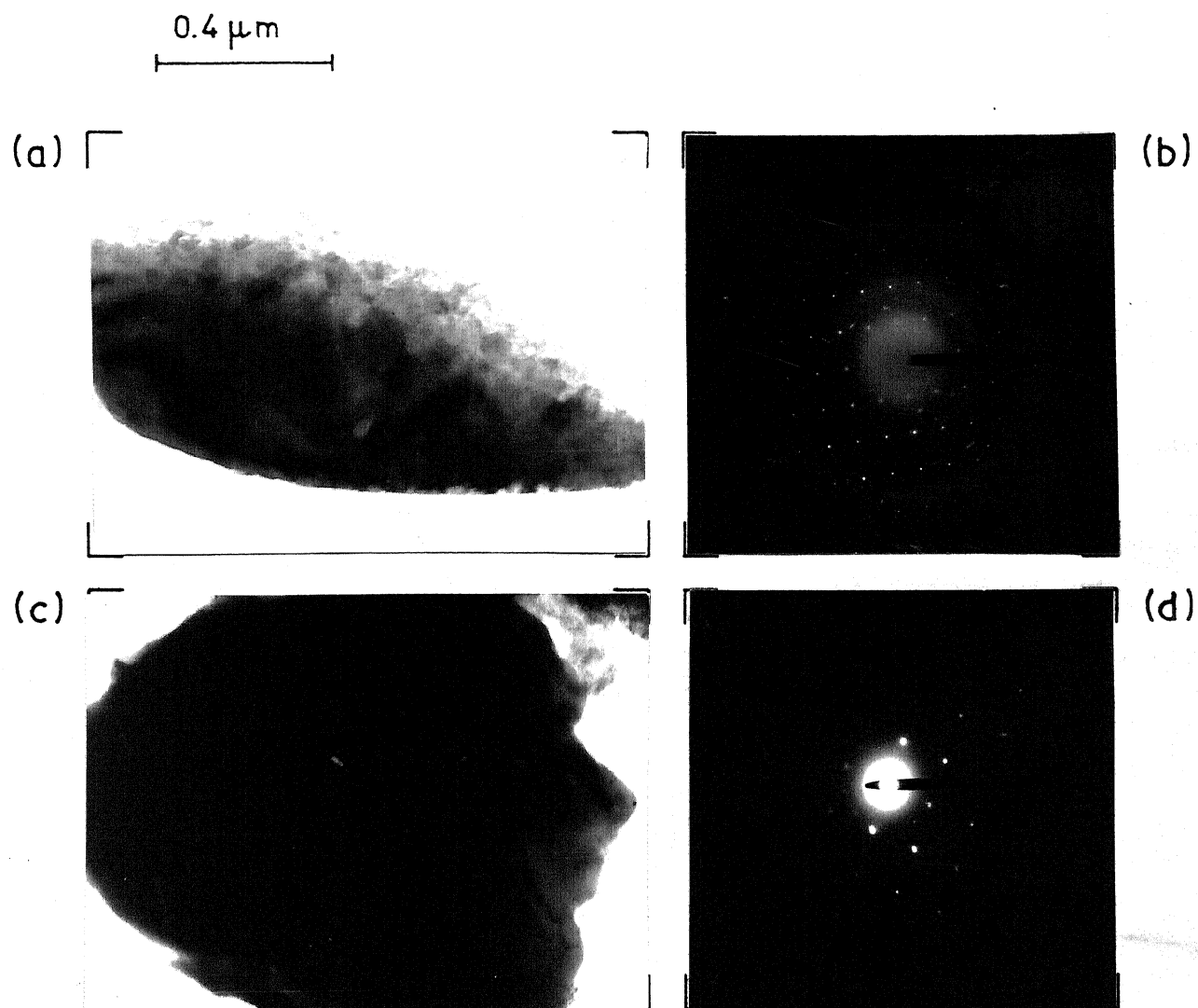


Fig. V.12. (a), (c) Electron micrographs of α -quartz in Mn-nodule sample and residue 2; (b), (d) SAED patterns corresponding to (a) and (c) respectively.

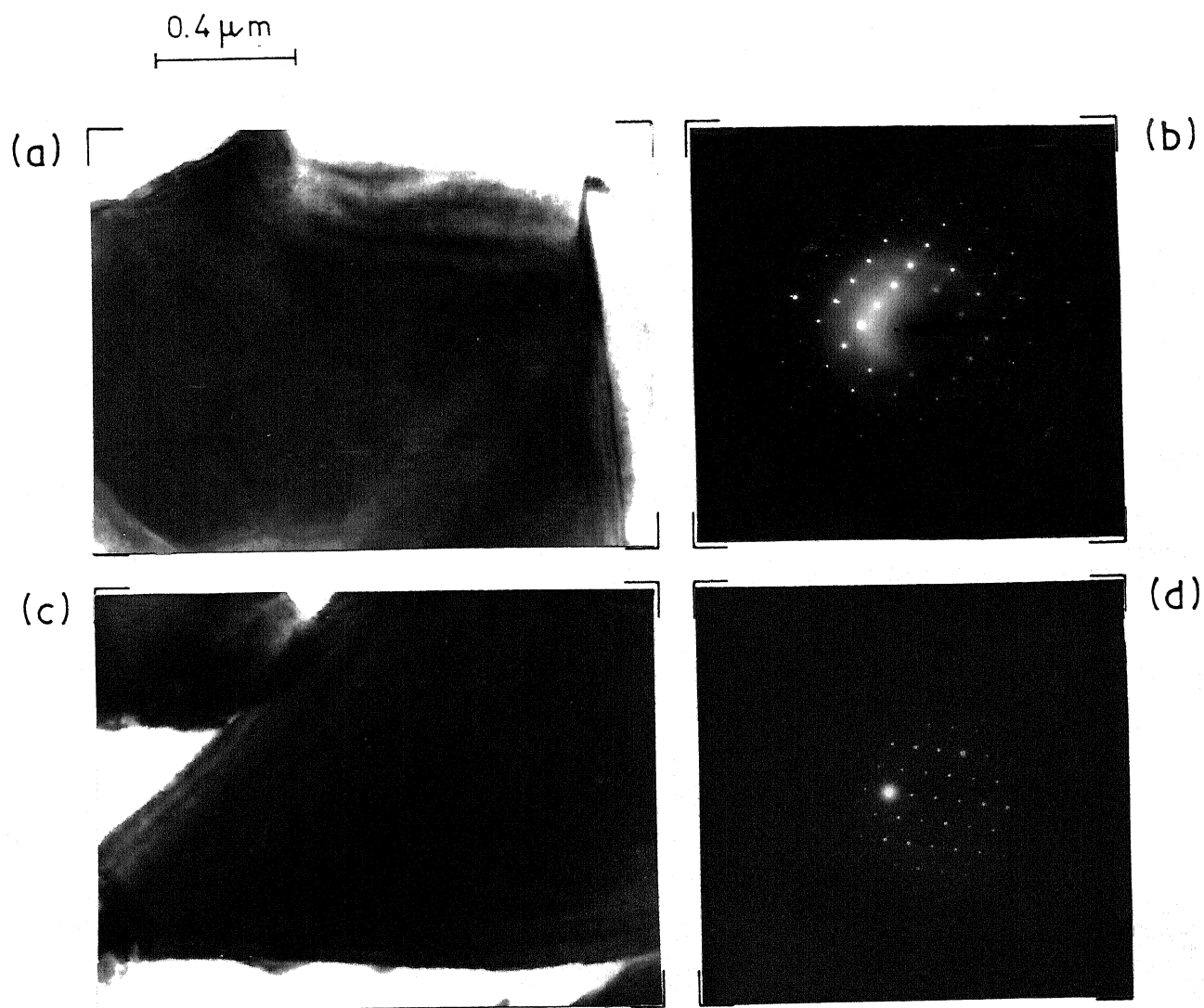


Fig. V.13. (a), (c) Electron micrographs of labradorite in Mn-nodule sample and residue 2; (b), (d) SAED patterns corresponding to (a) and (c) respectively.

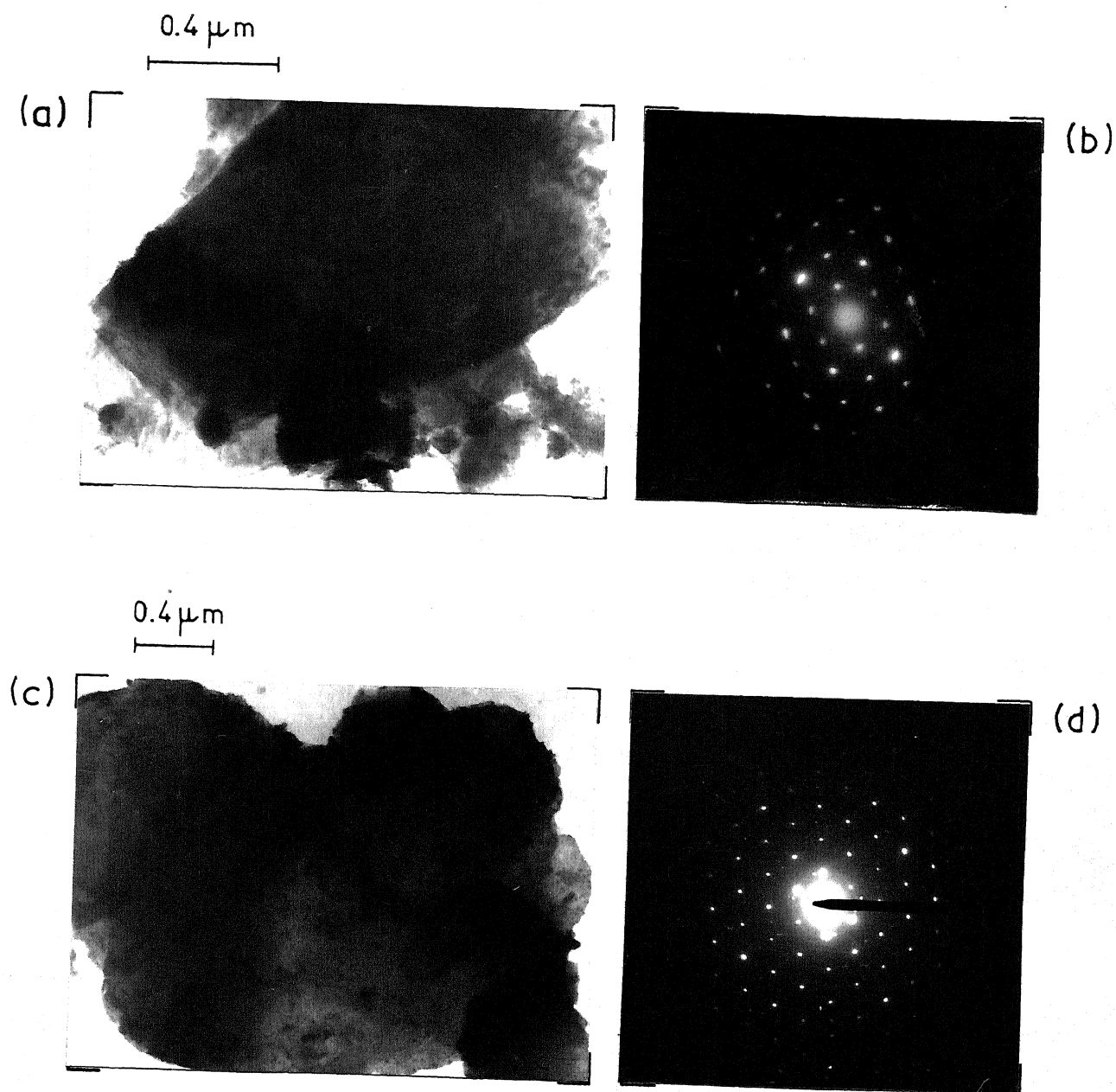


Fig. V.14. Electron micrographs and SAED patterns from other accessory minerals (a), (b) kaolinite; (c), (d) montmorillonite-chlorite.

Quite frequently the mineral montmorillonite-chlorite ($(\text{Na,K,Ca}/2)_{0.34}\text{Mg}_{0.8}\text{Al}_{2.55}(\text{Si}_{3.32}\text{Al}_{0.68})\text{O}_{10}\text{OH}_5$; $a = 5.2$, $b = 9.05$, $c = 29.8$; Orthorhombic) (Figure V.14(c) and V.14(d)) was identified during this investigation. The occurrence of this mineral is corroborated by TEM-EDAX spectra in Figure V.15. Montmorillonite represents a family of silicates which shows wide variations in chemical composition and crystallographic data (292). Some workers have suggested that the authigenic clay minerals e.g. montmorillonite (or semectite) may act as a sink for iron in marine sediments and nodules (26). Some percentage of iron may be associated with montmorillonite. This is indicated by (a) close correlation among Si-Fe-Al and Mg (vide Sections 6.1.3 and 6.2.3) and (b) iron content of siliceous residue (>10%) in which iron bearing oxyhydroxide minerals were not recorded. The iron bearing semectite is known as nontronite (292) for which the crystallographic data and composition are not well defined. The reflection at $\sim 4.5 \text{ \AA}^0$ which is observed too frequently for the mineral montmorillonite-chlorite is also the strongest reflection for nontronite. Simultaneous occurrence of both montmorillonite-chlorite and nontronite has been reported in marine environment (168).

The biogenic mineral calcite (CaCO_3) was detected only during TEM-EDAX study on nodule powder samples. The electron micrograph and EDAX spectra for this mineral are presented in Figure V.16.

Apart from the above, the presence of several other minerals can be tentatively suggested (Table V.2) on the basis of indexed diffraction patterns from a number of mineral aggregates such as

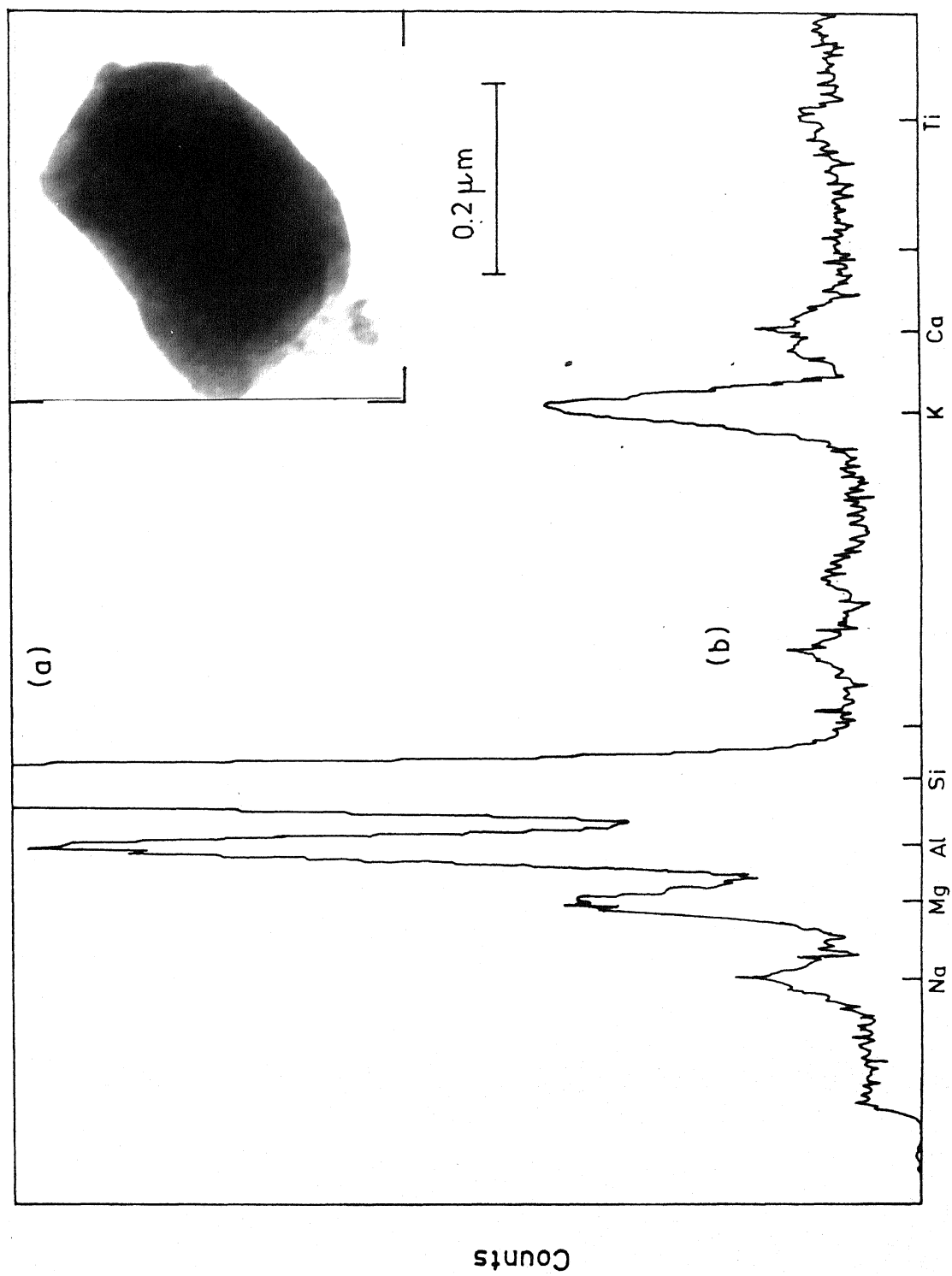


Fig. V.15. (a) Electron micrograph and (b) EDAX spectra of a montmorillonite-chlorite particle.

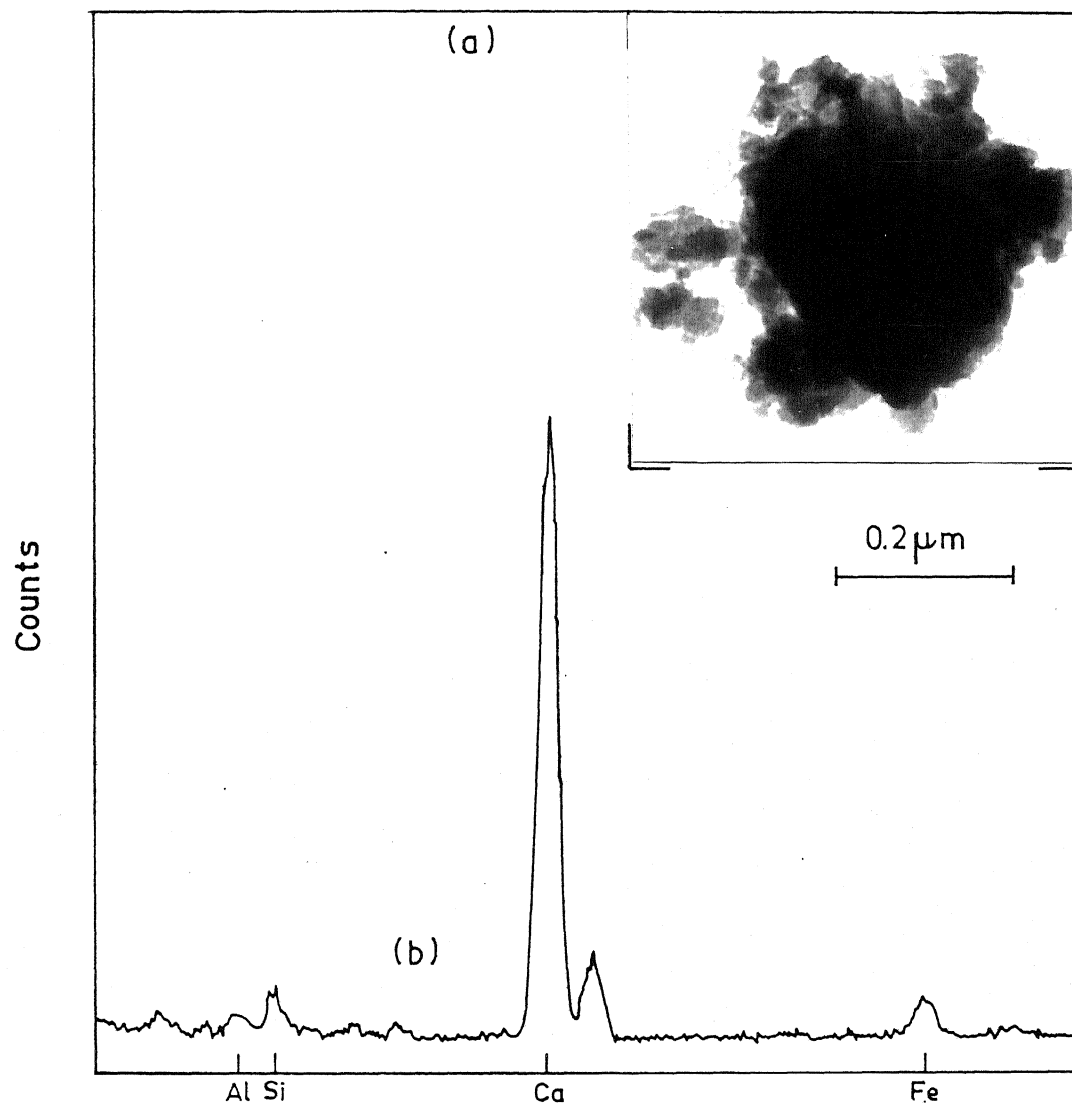


Fig. V.16. (a) Electron micrograph and (b) EDAX spectra of calcite particle.

mordenite, phillipsite, orthoclase, sanidine, prehnite, pyrophyllite and nsutite.

Summing Up:

Based on XRD and TEM studies on nodules from Central Indian Ocean basin it has been possible to identify the following minerals:
Mn mineral: 10 Å⁰-phase (todorokite/buserite), birnessite, δ -MnO₂ (or vernadite); Fe-minerals: goethite, ferrihydrite, ferroxhyte;
Silicates: α -quartz, feldspars, kaolinite, montmorillonites;
Biogenics: Calcite.

CHAPTER - VI

INTERNAL STRUCTURE - SCANNING ELECTRON MICROSCOPIC STUDIES

Characterization results of nodule internal structure are presented and discussed in this chapter. The term 'characterization' is used in its broadest sense to include not only chemical composition (major and minor elements), phase constituents and morphological features but also genetic factors. The major emphasis is on the occurrence of Ni, Co and Cu and growth features. An understanding of nodules growth features vis-a-vis genesis is important from geological point of view and in developing a scientific basis for metal extraction from nodules of different internal structure.

6.1 SEM/SE-Mode/EDAX Studies

6.1.1 Chemical Composition:

Figure VI.1(a) and VI.1(b) show the SEM/SE micrographs of a typical nodule section taken along two different lines (vide Figure IV.2(b)). The inserted numbers indicate the regions from which X-ray microanalysis data were collected. The result of SEM/EDAX analysis for 14 elements is listed in Table VI.1. The last column indicates the total weight accounted for. The rest of the mass represents the element like C, H, O etc. (not accounted for in the analysis). Too high a difference indicates analysis from a crack or organic matter alone. The chemical composition of nodule has been found to vary over an interval as small as 1 μm .

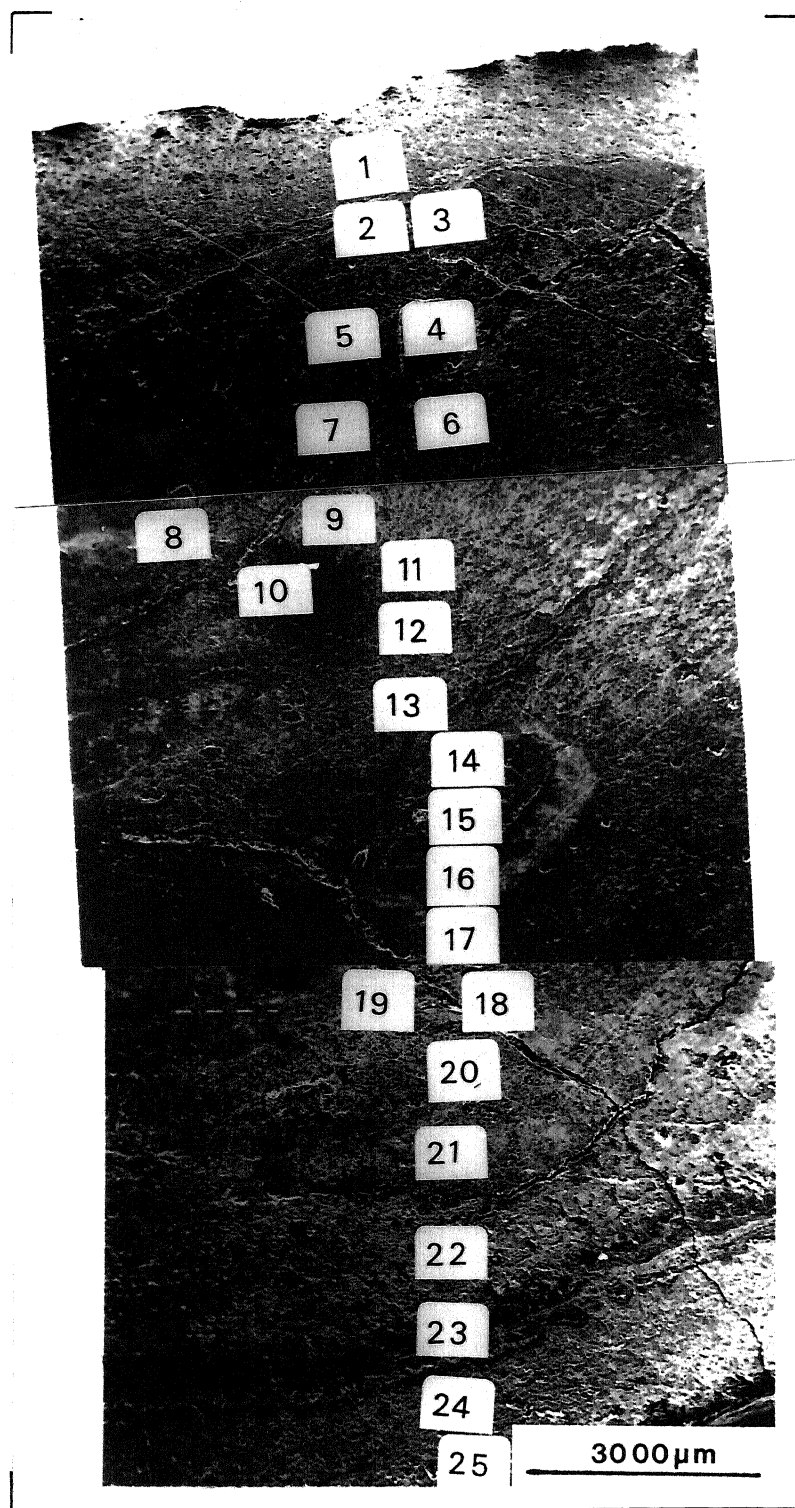


Fig. VI.1(a). SEM/SE micrograph of nodule section, top-bottom [vide Fig. IV.1(b)].

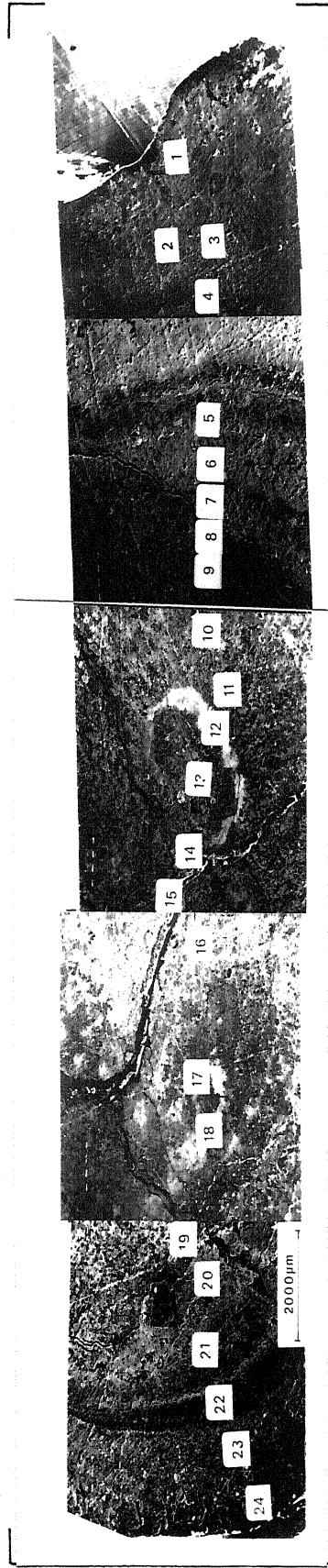


Fig. VI.1(b). SEM/SE micrograph of nodule section, right-left
[vide Fig. IV.1(b)].

Table VI.1(a): Elemental composition of locations shown in Figure VI.1(a) (top-bottom)

S.No./ Loca- tion	Element, wt %														Mn/Fe ratio	Total weight
	Mn	Fe	Ni	Co	Cu	Ti	Si	Al	Mg	K	Ca	Na	Cl	S		
1	22.37	12.19	0.72	0.18	0.26	0.50	6.88	1.82	0.39	0.57	1.47	1.08	0.36	0.17	1.8	48.9
2	35.00 ⁺	7.52	1.56	0.22	0.66	0.30	2.01	0.67	0.74	0.75	1.14	0.73	0.32	0.25	4.7	51.8
3	1.64	12.91	0.05	0.00	0.33	0.29	21.55	4.20	1.59	2.78	0.07	0.52	0.22	0.10	0.1	46.3
4	0.08	0.18	0.02	0.06	0.01	0.04	28.79	9.25	0.00	0.25	5.65	2.23	0.04	0.00	0.4	46.6
5	0.55	4.58	0.06	0.00	0.06	0.22	15.11	4.24	0.79	0.89	0.08	0.16	0.48	0.03	0.1	27.2
6	13.90	2.12	0.97	0.03	0.44	0.00	6.05	2.38	1.27	0.42	0.11	0.15	0.43	0.16	6.5	28.4
7	16.28	3.18	0.64	0.15	0.63	0.17	8.14	3.46	1.09	0.53	0.19	0.04	0.30	0.09	5.1	34.8
8	0.12	0.18	0.24	0.01	0.00	0.02	28.62	8.58	0.00	0.35	4.54	1.99	0.05	0.00	0.7	44.7
9	0.70	5.70	0.03	0.02	0.38	0.22	21.00	4.63	1.03	1.22	0.05	0.23	0.17	0.13	0.1	35.5
10*	0.20	0.12	0.07	0.02	0.02	0.00	0.15	0.04	0.03	0.34	0.15	0.00	0.70	0.75	1.7	2.59
11	6.62	1.98	0.22	0.01	0.40	0.04	17.23	4.55	0.67	2.95	0.25	0.96	0.09	0.08	3.3	36.1
12	0.37	6.34	0.05	0.06	0.17	0.30	20.66	5.53	1.34	1.37	0.07	0.24	0.18	0.11	0.1	36.8
13	25.00	1.82	1.62	0.08	0.87	0.10	5.32	2.78	1.71	0.82	0.51	0.98	0.07	0.36	13.7	42.0
14	5.24	8.43	0.30	0.02	0.14	0.14	13.71	3.86	1.22	1.05	0.30	0.54	0.15	0.10	0.6	35.2
15	13.91	19.46	0.36	0.16	0.77	0.80	28.32	9.45	1.90	2.42	0.68	0.71	0.55	0.23	0.7	79.7
16	15.92	12.41	0.49	0.22	0.80	0.42	18.59	6.22	2.20	1.08	0.88	0.43	0.61	0.25	0.8	60.5
17	3.60	15.07	0.03	0.03	0.30	0.37	14.89	2.93	1.25	1.41	0.43	0.48	0.18	0.02	0.2	40.9
18	20.24	2.52	1.18	0.00	0.88	0.02	9.04	3.50	2.20	0.80	0.44	0.80	0.16	0.22	8.0	42.0
19*	0.25	0.33	0.00	0.00	0.03	0.00	3.00	0.08	0.08	0.01	0.01	0.01	1.13	0.04	0.8	5.0
20	0.63	5.46	0.34	0.00	0.07	0.02	18.36	4.54	1.24	1.53	0.18	0.37	0.50	0.06	0.1	33.3
21	21.82	2.70	0.96	0.30	0.92	0.18	7.54	3.34	1.79	0.82	0.52	0.48	0.14	0.17	8.1	41.6
22	33.68	0.31	1.89	0.00	1.01	0.08	1.70	1.64	1.95	0.65	0.72	0.61	0.29	0.21	110.4	44.7
23	16.20	6.39	0.77	0.17	0.77	0.21	2.69	1.57	1.83	0.30	0.58	0.32	0.44	0.15	2.5	32.4
24	13.41	7.72	0.33	0.17	0.50	0.29	3.63	1.25	0.65	0.34	0.86	0.34	1.67	0.22	1.7	31.4
25	33.11	3.42	2.06	0.00	1.32	0.28	3.87	1.44	1.48	0.50	1.15	0.71	0.26	0.18	9.7	49.8

Table VI.1(b): Elemental composition of locations shown in Figure VI.1(b) (right-left)

S.No./ Loca- tion	Element, wt %														Mn/Fe ratio	Total weight
	Mn	Fe	Ni	Co	Cu	Ti	Si	Al	Mg	K	Ca	Na	Cl	S		
1	26.73	4.60	1.01	0.04	0.98	0.11	3.07	0.05	0.51	0.43	0.85	0.48	0.72	0.39	5.81	41.0
2	12.15	3.35	0.57	0.00	0.35	0.11	1.13	0.36	0.33	0.27	0.55	0.34	0.15	0.08	3.62	19.7
3	15.18	11.48	0.34	0.18	0.44	0.33	5.73	1.67	0.52	0.48	1.31	0.93	0.81	0.24	1.32	39.6
4	22.02	3.01	1.04	0.10	1.04	0.16	2.37	1.53	1.31	0.30	0.46	0.19	0.97	0.09	7.32	34.6
5	25.67	5.89	0.88	0.07	1.11	0.19	2.64	1.97	2.23	0.36	0.42	0.71	0.35	0.28	4.36	42.8
6	19.18	5.55	0.73	0.12	0.70	0.13	2.89	1.76	0.81	0.57	0.70	0.61	0.63	0.17	3.56	34.5
7	21.35	2.63	1.03	0.27	1.02	0.04	2.69	3.30	1.73	0.37	0.58	0.52	0.52	0.27	8.12	36.3
8	22.49	1.39	1.12	0.16	0.78	0.06	1.17	3.49	1.34	0.31	0.51	0.36	0.42	0.13	16.13	33.7
9	23.17	3.67	1.19	0.05	0.89	0.13	7.27	2.67	2.14	0.78	0.53	0.72	0.17	0.18	6.31	43.6
10	1.34	3.79	0.27	0.00	0.28	0.09	16.25	4.75	1.04	1.29	0.06	0.19	0.38	0.09	0.45	30.0
11	10.82	3.40	0.44	0.00	0.52	0.07	11.19	3.71	1.35	1.00	0.11	0.63	0.44	0.06	2.71	34.3
12	14.51	16.05	0.24	0.00	0.33	0.24	7.09	1.77	1.45	0.59	1.23	1.13	0.11	0.07	0.90	44.8
13	0.47	7.05	0.02	0.14	0.15	0.09	15.93	4.22	1.07	1.49	0.04	0.18	0.69	0.12	0.05	32.3
14	10.13	0.90	0.58	0.16	0.51	0.00	2.59	1.13	0.66	0.19	0.09	0.31	0.64	0.22	11.24	18.1
15*	0.12	2.68	0.00	0.00	0.31	0.00	0.51	0.11	0.01	0.03	0.07	0.03	0.57	0.08	0.14	4.5
16	10.13	1.68	0.47	0.09	0.49	0.05	10.89	3.58	1.30	1.12	0.13	0.71	0.33	0.10	6.03	31.1
17	0.71	3.89	0.05	0.09	0.15	0.06	16.12	6.08	0.90	1.26	0.35	0.28	0.52	0.14	0.18	30.6
18	0.39	8.11	0.00	0.00	0.12	0.11	15.17	3.26	1.04	1.27	0.07	0.44	0.41	0.17	0.04	30.5
19*	2.18	1.33	0.00	0.08	0.39	0.03	5.55	3.62	0.33	0.42	0.12	0.11	0.74	0.15	1.62	15.0
20	0.19	0.03	0.14	0.00	0.09	0.04	28.47	8.18	0.00	0.39	4.06	2.44	0.01	0.13	5.96	44.2
21	25.33	3.33	1.01	0.37	0.99	0.24	1.79	1.72	2.38	0.27	0.57	0.58	0.58	0.15	7.61	39.2
22	14.43	6.14	0.83	0.23	0.75	0.18	4.46	2.05	1.52	0.32	0.39	0.23	0.38	0.29	2.35	32.2
23	24.50	8.03	1.03	0.08	0.72	0.53	3.66	1.82	1.16	0.51	1.20	0.88	0.33	0.33	3.01	44.4
24	25.03	1.85	1.79	0.00	1.31	0.08	1.56	1.79	1.77	0.33	0.42	0.12	1.01	0.25	13.57	37.3

* - Not included in the calculation of Factor Model.

+ - Underline means highest concentration.

6.1.2 Elemental Correlations:

Regression Analysis:

Variations in the concentration of major (Mn, Fe and Si) and minor (Ni, Co, Cu and Ti) elements corresponding to the micrographs in Figure VI.1(a) and VI.1(b) are plotted in Figure VI.2(a) and VI.2(b). Positive correlation of Ni and Cu with Mn and of Ti with Fe may be noted in Figure VI.2. Fe shows an ill-defined correlation with Mn and a positive correlation with Si. Co also correlates with either manganese or iron (Figure VI.2).

Linear regression coefficients for the multivariate data set in Table VI.1 were calculated and are listed in Table VI.2. The Mn/Fe ratio is included in correlation coefficients matrix because of its geochemical significance (157). The coefficients with 99% level of significance are underlined. Based on the correlations observed in Table VI.2, the elements can be put into the following categories

- (a) Mn-Ni-Cu-Mg-Co
- (b) Fe-K-Ca-Ti-Co
- (c) Si-Al-K-Na-Ca-Fe
- (d) Cl-S.

The elements Cl and S do not show any significant correlation with other elements.

Correlation coefficients were also calculated for bulk chemical analysis data of nodules from 37 locations in Central Indian Ocean basin (Appendix-K). The triangular correlation coefficients matrix is given in Table VI.3. It is interesting to note that the correlation coefficients obtained from regional bulk

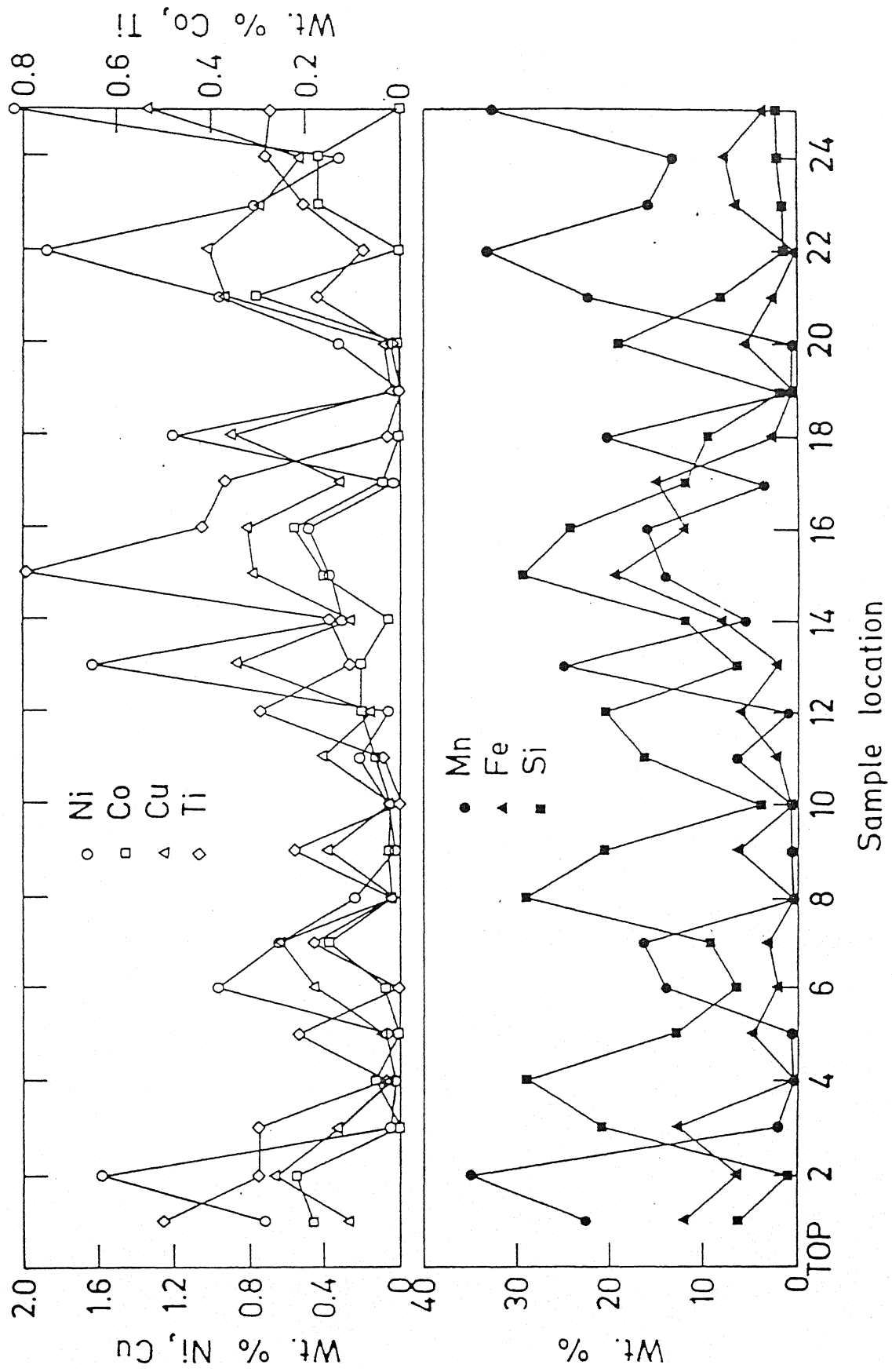


Fig. VI.2(a). Spatial distributions of Mn, Fe, Si, Ni, Co, Cu and Ti concentrations with respect to discrete sample locations. (Fig. VI.1(a), top to bottom).

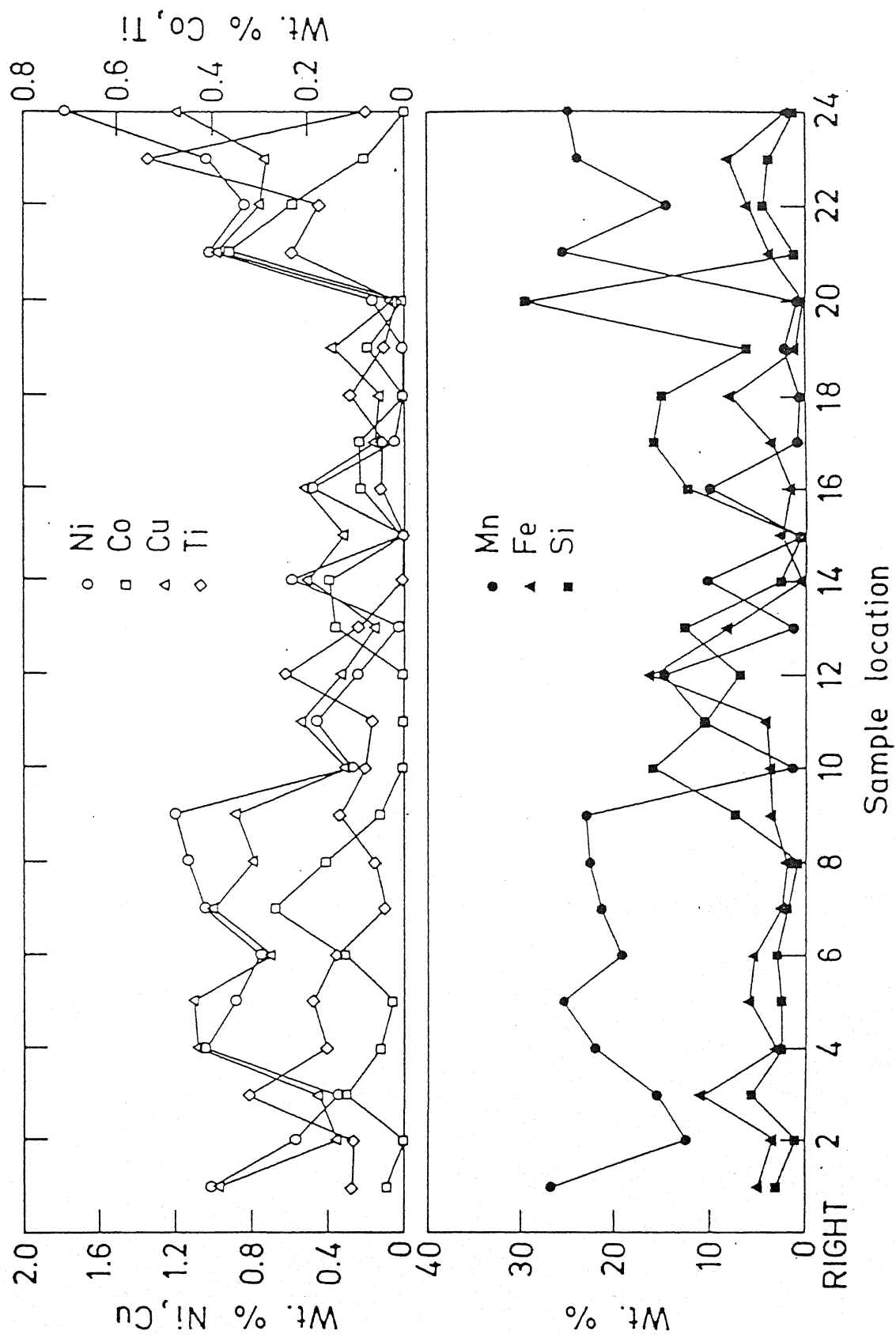


Fig. VI.2(b). Spatial distribution of Mn, Fe, Si, Ni, Co, Cu and Ti concentrations with respect to discrete sample locations (Fig. VI.1(b), right to left).

Table VI.2: Correlation coefficients of inter-element relationship (total 49 spots considered)

	Mn	Fe	Ni	Co	Cu	Al	Si	Cl	S	Mg	K	Na	Ca	Ti
Mn	1.000													
Fe	0.008	1.000												
Ni	<u>0.635</u>	-0.286	1.000											
Co	<u>0.404</u>	0.194	0.093	1.000										
Cu	<u>0.870</u>	-0.088	0.561	<u>0.367</u>	1.000									
Al	- <u>0.436</u>	0.067	- <u>0.44</u>	-0.080	- <u>0.405</u>	1.000								
Si	- <u>0.604</u>	0.149	- <u>0.554</u>	-0.259	- <u>0.527</u>	<u>0.919</u>	1.000							
Cl	0.034	0.160	-0.161	0.139	0.094	- <u>0.385</u>	- <u>0.430</u>	1.000						
S	0.060	-0.042	0.143	0.196	0.332	-0.362	-0.354	0.169	1.000					
Mg	<u>0.543</u>	0.276	0.260	0.299	<u>0.679</u>	-0.016	-0.131	-0.130	0.100	1.000				
K	-0.296	<u>0.448</u>	- <u>0.376</u>	-0.187	-0.188	<u>0.393</u>	<u>0.560</u>	-0.291	-0.192	0.215	1.000			
Na	0.011	0.005	-0.110	-0.336	-0.147	<u>0.523</u>	<u>0.484</u>	- <u>0.492</u>	-0.176	-0.203	-0.015	1.000		
Ca	-0.165	<u>0.466</u>	-0.104	-0.032	-0.199	<u>0.513</u>	<u>0.456</u>	-0.305	-0.113	-0.360	-0.251	0.886	1.000	
Ti	0.261	<u>0.810</u>	-0.057	0.312	0.184	0.127	0.161	0.011	0.085	0.282	0.321	0.047	-0.007	1.000
$\frac{Mn}{Fe}$	-	-	<u>0.439</u>	-0.237	<u>0.437</u>	-	-	-	-	-	-	-	-	-0.066

Table VI.3: The correlation coefficients matrix for bulk chemical composition data of nodules from different regions in the Central Indian Ocean basin (37 compositions considered*)

	Mn	Fe	Ni	Co	Cu
Mn	1.00				
Fe	-0.35	1.00			
Ni	0.40	-0.54	1.00		
Co	0.01	0.22	-0.05	1.00	
Cu	0.33	-0.48	0.49	-0.07	1.00
Mn/Fe	-	-	0.59	-0.08	0.46

* Vide Appendix-K.

analysis data (Table VI.3) are similar to the correlations observed for X-ray microanalysis data on the nodule section examined (Table VI.2). These results indicate that the coherent chemical composition variations on regional scale persist down to the micro-level in a single nodule. Thus detailed micro-level characterization studies on a single nodule are expected to provide deep insight into the geochemistry of nodules in the entire region.

Most of the correlations observed for SEM/EDAX data are well established (Section 2.7). Mn generally correlates negatively with Fe. Figure VI.2 shows that Mn does correlate negatively with Fe at certain discrete points. No observed correlation between Mn and Fe (Table VI.2) is likely to be due to multiple association of iron. This is reflected by weak positive correlations among Fe, Si and Al, which is an indication of the presence of iron bearing

alumino-silicates. Co correlates positively both with Mn and Fe; more significantly with Mn.

Sequential Extraction:

Sequential chemical extractions (i.e. selective sequential removal of exchangeable ions, Mn-fraction, organic matter and Fe-fraction, vide Section 4.2.6) were carried out to know the partitioning of minor elements in the different constituents of manganese nodules and compare the results with elemental correlations derived from SEM/EDAX data (Table VI.2).

The chemical analysis results for leach liquors and solid samples (TEM micrographs given in Figure VI.3) obtained in sequential extractions (SEQ) on manganese nodule powder samples are given in Table VI.4 and Figure VI.4.

Insignificant fractions of different minor elements are present as easily exchangeable ions. Weight change is less than 1% after the removal of exchangeable ions (Table VI.4). The dissolution behaviour of Ni, Mg and Ti shows close relationship with dissolution of Mn and Fe (Figure VI.4), corroborating the positive correlation of Ni and Mg with Mn and that of Ti with Fe.

Sequential extraction data in Table VI.4 indicate that a significant proportion of Cu may be associated with organic matter. The fraction of Cu dissolved in SEQ-II (removal of Mn-fraction) is quite disproportional to the Mn-fraction dissolved. This is in contrast with the observed positive correlation of Cu with Mn for SEM-EDAX data (Table VI.2). Stiff et al. (201) have explained that the discrepancy between statistical correlations (derived from microprobe data) and dissolution behaviour of Ni and Cu, vis-a-vis

Table VI.4: Partial chemical analysis of manganese nodule leach liquors after different sequential extraction treatments listed in Table IV.1

Chemical analysis* of nodule sample (wt %):
 Mn - 21.6
 Fe - 13.2
 Ni - 0.7
 Co - 0.08
 Cu - 0.48

Treatment	Purpose	wt % of element leached				wt % of nodule dissolved
		Mn	Fe	Cu	Co	
SEQ-I	Removal of exchangeable ions	0.48	0.9	<1	<1	<1
SEQ-II	Removal of Mn-fraction	80.4	7.9	12.9	55.9	40
SEQ-III	Removal of organic matter	4.6	5.0	63.4	29.4	20
SEQ-IV	Removal of Fe-fraction	13.0	77.8	13.9	13.2	30
Sum		98.1	91.6	90.2	98.5	90
Balance		1.6	8.4	9.8	1.5	10**

* Dried at 110°C

** Siliceous residue.

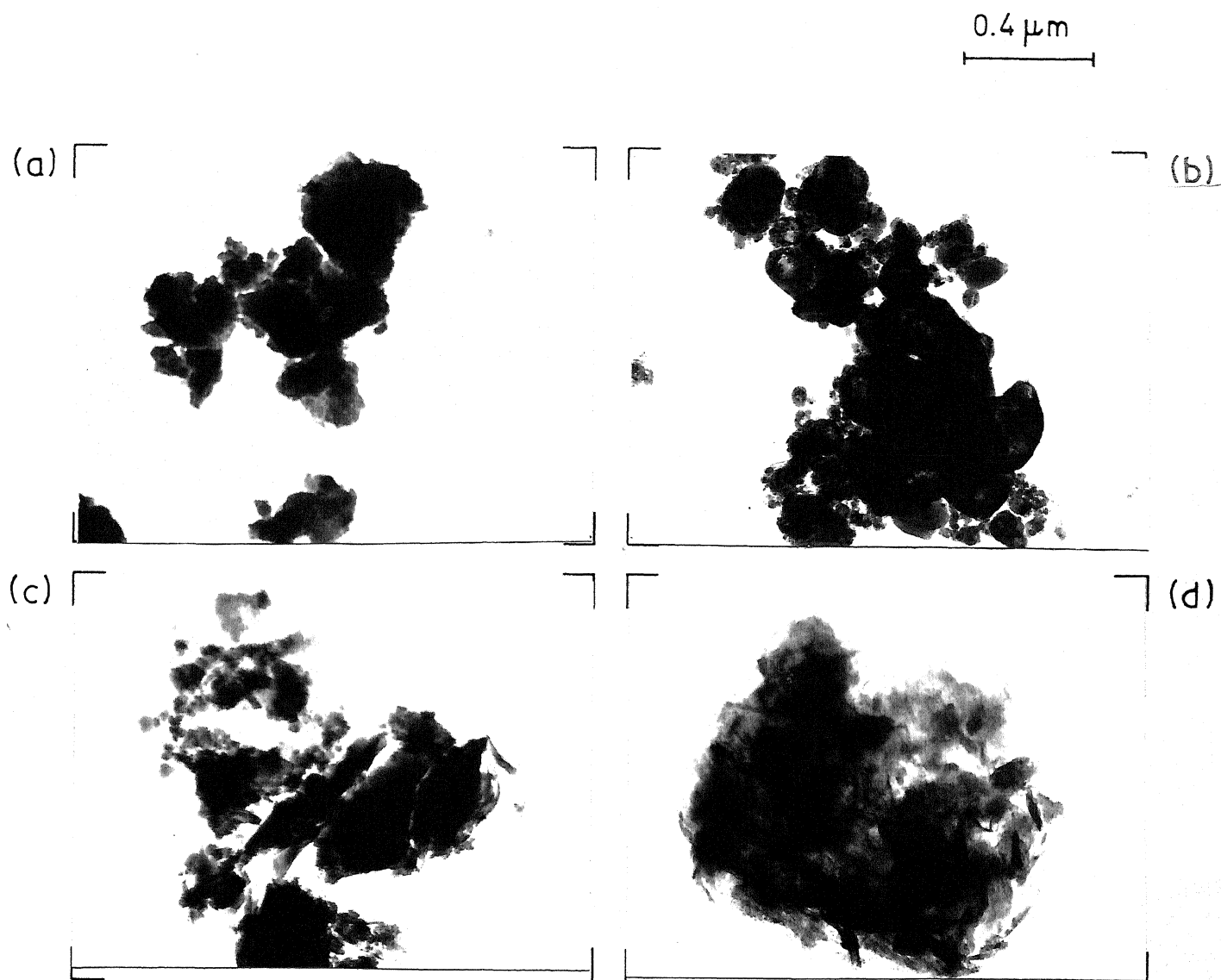


Fig. VI.3. TEM micrographs of nodule samples after (a) SEQ I, (b) SEQ I, II, (c) SEQ I-III and (d) SEQ I-IV. Corresponding EDAX spectra are given in Fig. VI.4. SEQ means sequential extraction. I, II, III and IV refers to the removal of exchangeable ions, Mn-fraction, organic matter and Fe-fraction respectively.

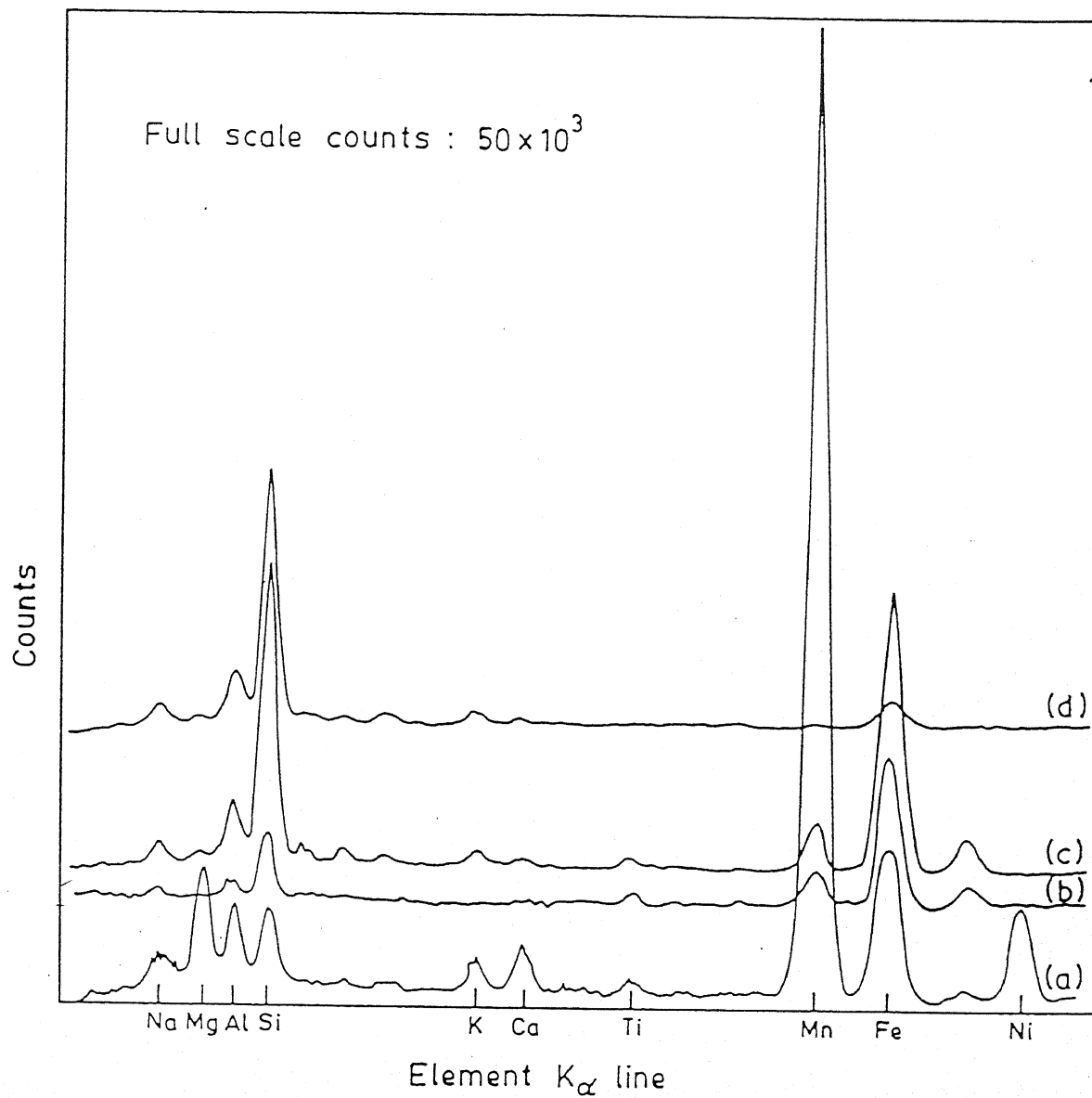


Fig. VI.4. EDAX spectra of Mn-nodule samples after (a) SEQ-I, (b) SEQ-I,II, (c) SEQ-I-III and (d) SEQ-I-IV.

Mn, occurs due to different mechanisms of incorporation of Ni and Cu in manganese nodules. It is expected that the dissolution behaviour of a minor element from manganese nodules will be governed by its association with the major element, mode of occurrence and chemistry in the leaching medium employed. Insufficient information is available regarding mode of occurrence of minor elements together with their leaching behaviour in different leaching media. Hydroxylamine hydrogen chloride ($\text{NH}_2\text{OH} \cdot \text{HCl}$) employed for solubilization of manganese in SEQ-II is a strong reducing agent. Research data (293-295) on the chemistry of copper in reducing environments, e.g. hydroxylamine hydrogen chloride, hydrazine etc., have indicated that small quantities of dissolved copper very markedly catalyse the auto-oxidation of the reducing agent. The order of catalytic activity ($\text{Cu(II)} \gg \text{Co(II)} > \text{Fe(II)} > \text{Mn(II)} > \text{Ni(II)} > \text{Zn(II)}$) highlights the much different catalytic activity of Cu(II) compared with Ni(II) and other ions (293-295). The Cu(II) ions are reduced to Cu(I) ions which form insoluble chlorocomplex or undergo reaction such as $2\text{Cu}^+ \rightarrow \text{Cu}^{2+} + \text{Cu}^0$ (295, 296). Thus it is likely that copper gets precipitated as chlorocomplex of cuprous ion and/or Cu^0 in the SEQ-II and redissolves in the dilute nitric acid employed in SEQ-III (Table IV.1). It is proposed that the discrepancy between positive correlation of Cu with Mn (Table VI.2) and sequential extraction data (Table VI.4) is nothing unusual and Cu is actually present with Mn-fraction together with Ni.

The sequential extraction data also corroborate the multiple association of Co with Mn and Fe (Table VI.4) and association of Na with silicate fraction (Figure VI.4).

6.1.3 Genesis and Factor Analysis:

Three Component Diagram:

An attempt was made to assign the minor elements like Ni, Co, Cu and Ti (Table VI.1, Figure VI.2) to the hydrogenetic and diagenetic substances in the nodule using a three component diagram (as shown earlier in Figure II.6 for the bulk chemical analysis data). $(Ni + Cu)/Co/Ti$ were plotted with Mn and Fe on a triangular graph (Figure VI.5). As is shown in the figure, it is difficult to assign the minor elements to different genetic substances very clearly as reported by other workers (25, 100, 157). In other words, the hydrogenetic and diagenetic factors alone are not sufficient to explain the chemical variations.

Factor Analysis:

The variation in the composition of nodule at discrete locations was examined by Q-mode factor analysis. For factor analysis only 45 observation and 12 elements were considered. Two elements, Cl and S, were left out because (i) they do not show any significant correlation with other elements (Table VI.2), (ii) they result in a separate minor factor if included and (iii) for the purpose of simplification, so that the data could be presented on a three co-ordinate diagram. Observations 10 and 19 (top-bottom) and 15 and 19 (right-left) were not included in the calculation of model because they seem to correspond to either the organic matter or cracks (total weight accounted for is small) and result in extraordinarily low communality. Factor loadings and factor scores results are presented in Table VI.5(a) and VI.5(b). Factor analysis results show that -

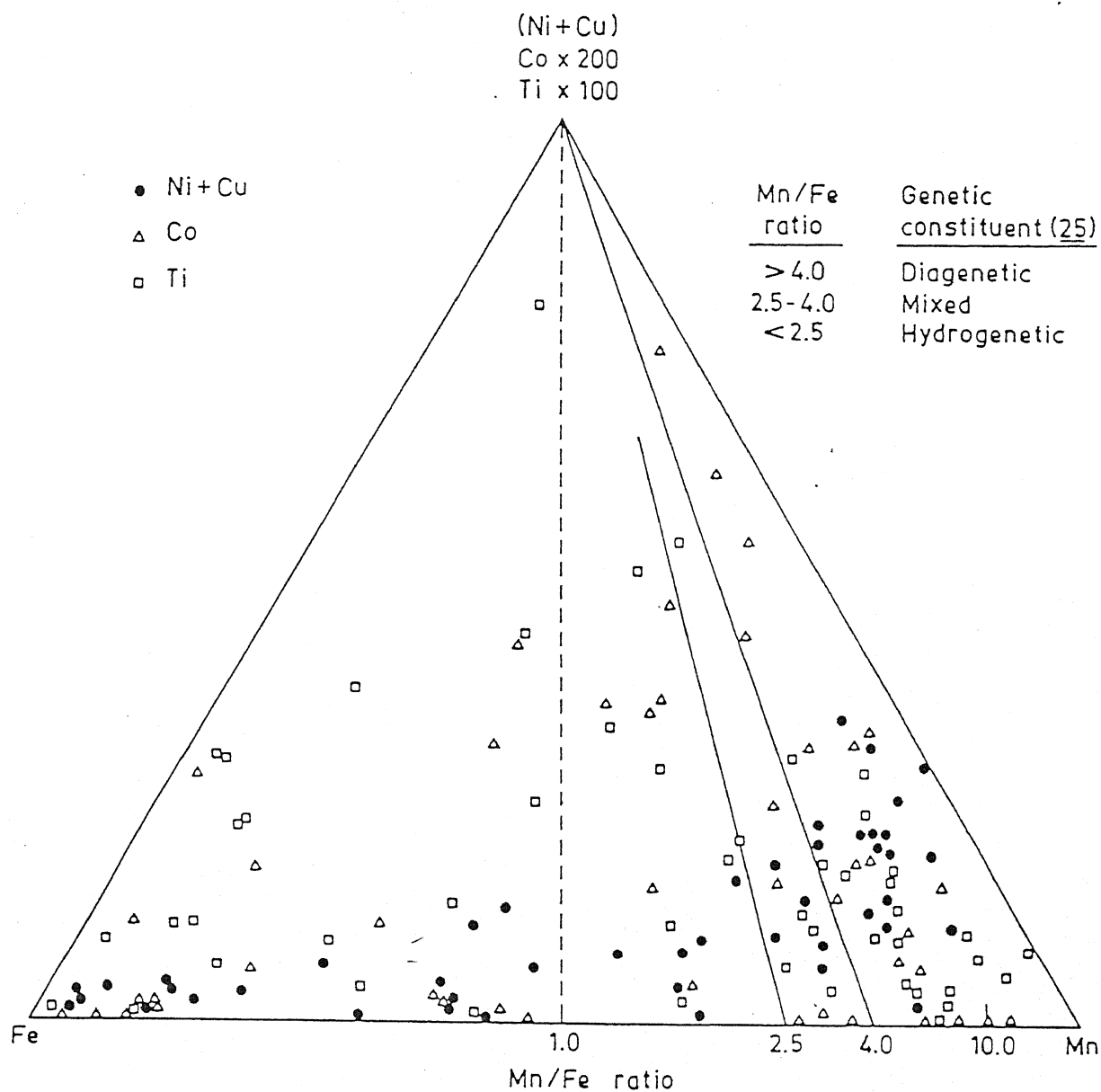


Fig. VI.5. Three component diagram illustrating relationship between major (Mn, Fe) and minor (Ni, Co, Cu, Ti) element/s and genetic constituents or Mn/Fe ratio.

Table VI.5(a): Factor loadings and communality at each observation point. Number of observations and elements considered are 45 and 12 respectively

S. No.	Loca- tion	Factor loadings, f_r				Communality (h_1^2) $h_j^2 = \sum_{r=1}^4 f_{jr}^2$
		1	2	3	4	
1	1T	0.5611	0.3203	-0.6903	-0.2063	0.9364
2	2T	0.8523	0.1163	-0.4222	-0.1161	0.9317
3	3T	0.2588	0.9269	-0.1842	0.0104	0.9602
4	4T	0.0072	0.5656	-0.2521	-0.7116	0.8899
5	5T	0.1989	0.9366	-0.1103	-0.1828	0.9624
6	6T	0.8716	0.4411	0.0624	-0.0644	0.9623
7	7T	0.8113	0.4645	-0.2192	-0.0812	0.9285
8	8T	0.0783	0.5927	0.0431	-0.7028	0.8532
9	9T	0.2371	0.7308	-0.2441	-0.4139	0.8212
10	11T	0.3249	0.7820	0.0470	-0.2522	0.7828
11	12T	0.2610	0.9283	-0.1596	-0.1335	0.9732
12	13T	0.9303	0.3179	-0.0174	-0.1087	0.9787
13	14T	0.4063	0.8632	-0.1951	-0.1422	0.9685
14	15T	0.4116	0.7956	-0.3902	-0.1017	0.9650
15	16T	0.6120	0.6831	-0.3490	-0.0644	0.9670
16	17T	0.3166	0.8278	-0.4185	0.0335	0.9617
17	18T	0.8559	0.4757	0.0802	-0.0860	0.9727
18	20T	0.2843	0.9292	0.0412	-0.1725	0.9758
19	21T	0.8437	0.3689	-0.2381	-0.0657	0.9089
20	22T	0.9501	0.2013	-0.0034	-0.0346	0.9443
21	23T	0.8539	0.3689	-0.2933	0.0867	0.9587
22	24T	0.6878	0.3471	-0.6249	-0.0455	0.9861
23	25T	0.9400	0.1666	-0.0859	-0.1019	0.9290
24	1R	0.9034	0.1213	-0.2062	-0.1634	0.9000
25	2R	0.8563	0.1937	-0.2824	-0.1340	0.8684
26	3R	0.5757	0.3775	-0.6909	-0.1743	0.9816
27	4R	0.9527	0.2223	-0.1491	-0.0021	0.9793
28	5R	0.9040	0.3389	-0.1444	0.0505	0.9556
29	6R	0.8755	0.2922	-0.3370	-0.1250	0.9811
30	7R	0.8987	0.2623	-0.1797	-0.0692	0.9135
31	8R	0.9394	0.2290	-0.1162	-0.1104	0.9606
32	9R	0.8908	0.4306	-0.0428	-0.0377	0.9822
33	10R	0.3540	0.9109	0.0432	-0.1786	0.9888
34	11R	0.6705	0.7140	0.0021	-0.1411	0.9793
35	12R	0.5103	0.5780	-0.4580	-0.0314	0.8051
36	13R	0.2264	0.7251	-0.3486	-0.3296	0.8072
37	14R	0.8835	0.1993	-0.1924	-0.1105	0.8695
38	16R	0.6215	0.6451	-0.2391	-0.0951	0.8686
39	17R	0.2608	0.8832	-0.0714	-0.2785	0.9308
40	18R	0.2279	0.9468	-0.1509	-0.0840	0.9782
41	20R	0.0838	0.5008	-0.0814	-0.8310	0.9551
42	21R	0.8618	0.2285	-0.3025	0.0355	0.8876
43	22R	0.8312	0.3613	-0.3271	0.0339	0.9296

contd...

Table VI.5(a) contd...

S. No.	Loca- tion	Factor loadings, f_r				Communality (h_j^2) $h_j^2 = \sum_{r=1}^4 f_r^2$
		1	2	3	4	
44	23R	0.7941	0.3179	-0.4351	-0.0799	0.9273
45	24R	0.9571	0.1842	0.0603	0.0073	0.9536
Variance		70.8	15.3	3.9	3.1	
Cumulative variance		70.8	86.1	90.0	93.2	

* T - means top-bottom (Figure VI.1(a))
 R - means right-left (Figure VI.1(b)).

Table VI.5(b): Varimax factor scores for the factors* listed in Table VI.5(a)

Element	Varimax factor scores (l_{jr}), Columns = Factors			
	1	2	3	4
Mn	0.7574	-0.2165	-0.1414	-0.0795
Fe	-0.0621	0.3949	-0.8405	0.2918
Ni	0.7064	-0.1651	0.2831	-0.1785
Co	0.2392	-0.0781	-0.6440	0.0035
Cu	0.7551	-0.0091	0.1184	0.0561
Ti	0.0453	0.2053	-0.6822	0.2277
Si	-0.1099	0.6260	-0.0144	-0.7468
Al	0.0611	0.4584	0.0804	-0.7542
Mg	0.6197	0.5746	0.2135	0.5666
K	0.0053	0.6161	0.0202	0.1968
Na	0.1673	0.0145	-0.1134	-0.7242
Ca	-0.0052	-0.0828	-0.3810	-0.8394

* Factor 2 and 4 are respectively referred as 2A and 2B in the text.

- (i) four significant factors (eigenvalue >1) explain 93% variance in the data set,
- (ii) the factors are based on the following metal associations

Factor	Metal association
1	Mn-Ni-Cu-Mg-Co-Na
2	Si-Al-Fe-Mg-K-Ti
3	Fe-Co-Ti-Ca-Na-Mn
4	Si-Al-Na-Ca

and (iii) in general the communality (h_j^2) at each observation point is high (~ 1).

It is interesting to note that metal association Si-Al-K-Na-Ca-Fe observed in linear regression analysis (vide Section 6.1.2) splits up into two factors i.e. Factor-2 and Factor-4 and positive correlation of Fe with Si shows up more clearly. We shall refer factor-2 and factor-4 as Factor 2A and 2B respectively in our remaining discussion.

Assuming the communality at each observation point to be equal to one (i.e. $h_j^2 = 1$) the factor loadings in Table VI.5(a) are plotted on a triangular graph (Figure VI.6) in terms of three variables: factor-1, factor-2 (sum of factor 2A and 2B i.e. $f_2^2 = f_{2A}^2 + f_{2B}^2$) and factor-3. Points on which loadings of factor-2B are high have been underlined in Figure VI.6. It may be noted that the three factors allow discrimination of all the points in the data set. Location 16 (top-bottom) and locations 11, 12 and 16 (right-left) show scatter in Figure VI.6. Mathematical analysis by factor analysis cannot distinguish between phase boundary between two distinct kinds of materials and intimate association of

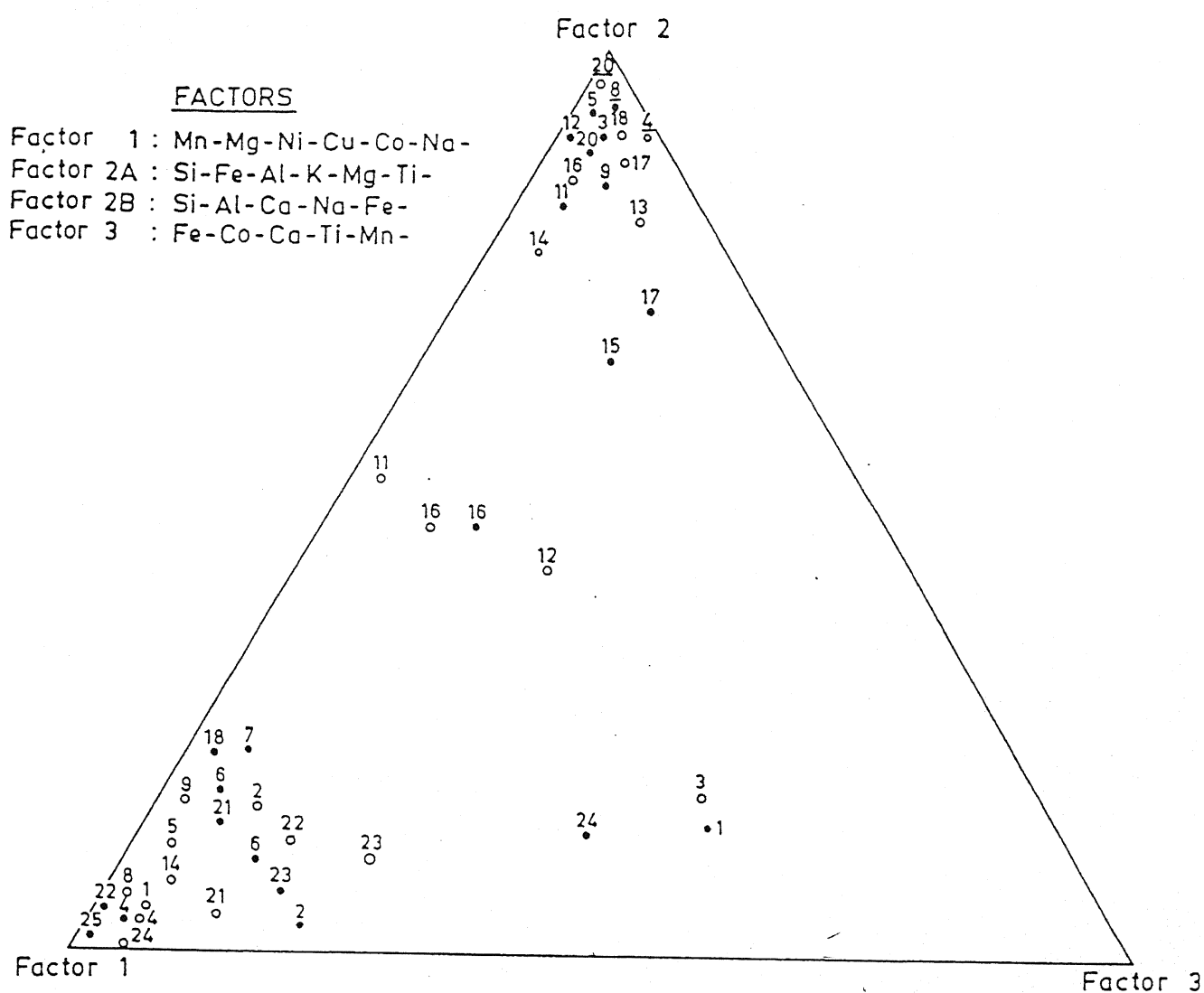


Fig. VI.6. Three co-ordinate plot of the normalized varimax factor loadings of locations shown in SEM/SE micrographs (Fig. VI.1).
 • top-bottom, o right to left.

two different kinds of material. As discussed in a later section (Section 6.2.3) this scatter arises due to accidental measurements on phase boundaries separating the materials represented by factor-1 or 3 and factor-2.

In order to check the reproducibility of the factor model just described, a separate set of X-ray microanalysis data (Table VI.6) collected across the line X-0 (Figure VI.7 also refer Figure IV.2(b)) was again processed by the Q-mode factor analysis model. In this case slight change in the X-ray microanalysis data collection technique was made. Three observations (except location 1, four observations) were made from areas around each location. Total 31 observations and 11 elements (Cl, S and Na not included) were considered. The factor loadings and factor scores are given in Table VI.7(a) and VI.7(b). The three significant factors which explain 95% variance in the data set are based on elemental association very similar to factor-1, factor-2A and factor-3 described before. Factor-2B does not appear as a separate factor. The factor loadings in Table VI.7(a) indicate that the communality for point 4C (S. No. 13) is very low. Close examination of composition on location 4C and locations 4T, 8T and 20R in Table VI.5(a) on which factor-2B shows significant loading indicates that the compositions are very similar in the two cases.

Since no other location has composition similar to 4C, in the data set given in Table VI.6, factor-2B constitutes a minor factor in this case. It is interesting to note that the non inclusion of Na (minor element) in the factor analysis does not alter the general nature of factors generated indicating the stability of factor model.



Fig. VI.7. SEM/SE micrograph of nodule section illustrating areas of analysis along the line X - O (vide Fig. IV.1(b)).

Table VI.6: Elemental composition of areas shown in Figure VI.7 (Line X-O in Figure IV.1(b))
(Three or four microanalyses are recorded from each area)

S. No.	Loca- tion	Element, wt %												Mn/Fe ratio
		Mn	Fe	Ni	Co	Cu	Ti	Si	Al	Mg	K	Ca	Na	
1	1	25.32	25.32	1.20	0.19	0.59	0.17	5.80	2.23	1.21	0.32	0.84	-	4.85
2	1A	20.22	11.36	0.37	0.36	0.47	0.50	4.28	1.34	0.41	0.13	1.47	-	1.78
3	1B	5.40	19.00*	0.16	0.18	0.00	0.40	5.95	1.93	0.68	0.57	0.89	-	0.28
4	1C	14.57	14.04	0.14	0.14	0.06	0.44	7.59	2.06	0.32	0.21	0.96	-	1.04
5	2A	20.88	4.02	0.76	0.00	0.65	0.20	8.80	5.10	0.86	0.29	0.46	-	5.19
6	2B	24.64	4.66	0.81	0.24	0.47	0.23	4.92	3.04	1.70	0.25	0.44	-	5.29
7	2C	24.77	7.20	1.31	0.20	0.36	0.32	4.15	2.21	1.25	0.18	0.42	-	3.44
8	3A	31.60	2.85	1.66	0.16	1.30	0.12	1.50	1.63	1.82	0.19	1.03	-	11.09
9	3B	30.00	1.60	1.96	0.23	1.18	0.14	3.65	2.85	1.87	0.33	0.65	-	18.75
10	3C	29.48	5.84	0.83	0.29	1.06	0.21	1.71	1.29	1.34	0.12	0.87	-	5.05
11	4A	17.46	13.67	0.53	0.24	0.06	0.31	5.02	1.49	0.58	0.19	0.85	-	1.28
12	4B	24.63	5.38	0.92	0.17	0.60	0.29	5.13	2.76	2.18	0.26	0.75	-	4.57
13	4C	1.29	2.08	0.00	0.08	0.00	0.00	28.60	8.82	0.11	2.79	0.16	-	0.62
14	5A	32.83	0.68	1.63	0.00	0.65	0.14	2.66	1.92	2.31	0.37	0.32	0.24	48.28
15	5B	34.54	0.94	1.79	0.09	0.70	0.09	1.73	1.51	1.38	0.25	0.63	0.23	36.74
16	5C	32.98	1.99	1.65	0.18	0.90	0.10	0.96	2.00	1.76	0.19	0.86	0.34	16.57
17	6A	26.30	3.89	1.33	0.05	0.45	0.11	4.31	2.60	2.35	0.28	0.73	0.19	6.76
18	6B	22.60	5.50	0.73	0.18	0.30	0.26	6.66	3.37	0.91	0.38	0.85	0.34	4.11
19	6C	35.11	1.23	1.50	0.07	0.85	0.13	1.28	1.25	1.62	0.30	0.56	0.24	28.54
20	7A	28.16	3.13	0.90	0.10	0.44	0.28	6.91	1.16	0.94	0.21	0.78	0.22	9.00
21	7B	34.13	1.62	1.57	0.01	1.03	0.10	1.33	1.85	1.26	0.33	0.74	0.20	21.10
22	7C	20.60	7.89	0.74	0.04	0.53	0.08	7.46	2.43	1.29	0.42	0.60	0.43	2.61
23	8A	2.28	11.53	0.00	0.18	0.00	0.13	15.04	4.02	1.47	1.13	0.23	0.07	0.20
24	8B	1.85	11.59	0.00	0.04	0.00	0.08	21.37	3.95	1.50	1.24	0.20	0.18	0.16
25	8C	31.01	1.47	2.01	0.00	0.65	0.00	3.65	2.11	2.04	0.37	0.55	0.28	21.10
26	9A	3.80	13.62	0.09	0.04	0.00	0.06	17.29	3.44	1.27	1.05	0.32	0.48	0.30
27	9B	7.67	13.83	0.19	0.23	0.11	0.16	13.27	3.15	1.11	0.68	0.58	0.40	0.55
28	9C	8.64	14.49	0.32	0.11	0.20	0.09	12.47	2.49	1.02	0.63	0.58	0.23	0.60
29	10A	12.32	10.20	0.58	0.106	0.00	0.36	13.61	5.50	1.55	0.55	0.39	0.21	1.21
30	10B	0.86	8.17	0.00	0.182	0.00	0.00	23.58	7.03	1.38	1.08	0.12	0.10	0.11
31	10C	2.59	13.50	0.00	0.00	0.00	0.14	18.57	3.96	1.30	1.14	0.24	0.32	0.19

* Underline means highest concentration in this table

- Na analysis was not performed.

Table VI.7(a): Factor loadings and communality at each observation point (Table VI.6). Number of observations and elements considered are 31 and 11 respectively

S. No.	Location	Factor loadings, f_r			Communality $\sum_{r=1}^3 f_r^2$
		1	2	3	
1	1	0.8236	-0.2663	-0.4829	0.9824
2	1A	0.4210	-0.1638	-0.8753	0.9702
3	1B	0.1844	-0.4709	-0.8396	0.9605
4	1C	0.2833	-0.3636	-0.8572	0.9472
5	2A	0.8365	-0.4001	-0.2550	0.9249
6	2B	0.7684	-0.3422	-0.4740	0.9321
7	2C	0.8122	-0.3040	-0.4070	0.9176
8	3A	0.9285	-0.1167	-0.2940	0.9622
9	3B	0.9238	-0.1749	-0.2594	0.9513
10	3C	0.7905	-0.1363	-0.5343	0.9289
11	4A	0.4208	-0.3291	-0.8344	0.9815
12	4B	0.7973	-0.3444	-0.4513	0.9580
13	4C	0.0612	-0.8353	0.0177	0.7017
14	5A	0.9494	-0.2255	-0.0700	0.9571
15	5B	0.9640	-0.1021	-0.2051	0.9818
16	5C	0.9379	-0.1332	-0.2946	0.9841
17	6A	0.8893	-0.3432	-0.2037	0.9501
18	6B	0.6826	-0.3522	-0.6087	0.9604
19	6C	0.9685	-0.1181	-0.1982	0.9913
20	7A	0.7969	-0.2032	-0.5117	0.9382
21	7B	0.9589	-0.0980	-0.1738	0.9592
22	7C	0.7965	-0.4642	-0.3306	0.9590
23	8A	0.2405	-0.9037	-0.3219	0.9781
24	8B	0.2046	-0.9496	-0.2014	0.9840
25	8C	0.9589	-0.2199	-0.0182	0.9681
26	9A	0.2301	-0.9065	-0.3035	0.9668
27	9B	0.3015	-0.6889	-0.6298	0.9621
28	9C	0.3695	-0.7178	-0.5351	0.9381
29	10A	0.4918	-0.6669	-0.4845	0.9213
30	10B	0.1952	-0.9096	-0.1744	0.8958
31	10C	0.1861	-0.9180	-0.2877	0.9601
Variance		72.7	15.7	6.3	
Cumulative variance		72.7	88.4	94.7	

Table VI.7(b): Varimax factor scores for the factors listed in Table VI.7(a)

Element	Varimax factor scores (l_{jr}), Columns = Factors		
	1	2	3
Mn	0.9384	0.2000	-0.1510
Fe	-0.1681	-0.4698	-0.7238
Ni	0.8651	0.1346	0.1817
Co	0.1105	0.0598	-0.7875
Cu	0.7114	0.1883	0.0696
Ti	0.0452	0.0864	-0.9084
Si	-0.0368	-0.8005	0.0851
Al	0.1488	-0.6388	0.1131
Mg	0.7450	-0.4689	0.2208
K	0.0241	-0.5522	0.1736
Ca	0.3134	0.1114	-0.6809

Factor loadings in Table VI.7(a) are presented on a triangular diagram in Figure VI.8. Similarity in the distribution of points highlights the reproducibility of the model.

Genetic Significance:

By comparison of elemental association observed in Factors 1, 3 and 2B with the chemical characteristics of different genetic type of substance (25, 26, 100, 138, 139) present in nodules, Factor-1, 3 and 2B can be assigned diagenetic, hydrogenetic and detrital origin.

Factor 2A is the result of interaction of biogenic silica with oxyhydroxide of manganese and iron of hydrogenetic and/or diagenetic origin as proposed by Lyle et al. (26, 171) and Hein et al. (166, 170) (vide p. 36). This factor will be referred as of siliceous ooze origin. Association of Fe in factor-2A makes it difficult to assign the minor elements to hydrogenetic and diagenetic substance in Figure VI.5.

Figures VI.6 and VI.8 are combined in Figure VI.9 and different points are superimposed with corresponding Mn/Fe ratio. There appears to be every gradation between factor-1 (diagenetic) and factor-3 (hydrogenetic). The increasing influence of factor-1 on factor-3 is associated with a gradual increase in Mn/Fe ratio. Locations with Mn/Fe ratio greater than 10 are very highly loaded with diagenetic factor. On the other hand, Mn/Fe ratio in the range 1-2 is associated with large influence of hydrogenetic factor. The points which are heavily loaded with factor-2 show a characteristic Mn/Fe ratio of less than 1.

FACTORS

Factor 1 : Mn-Mg-Ni-Cu-Co-

Factor 2 : Si-Fe-Al-K-Mg-Ti-

Factor 3 : Fe-Co-Ca-Ti-Mn-

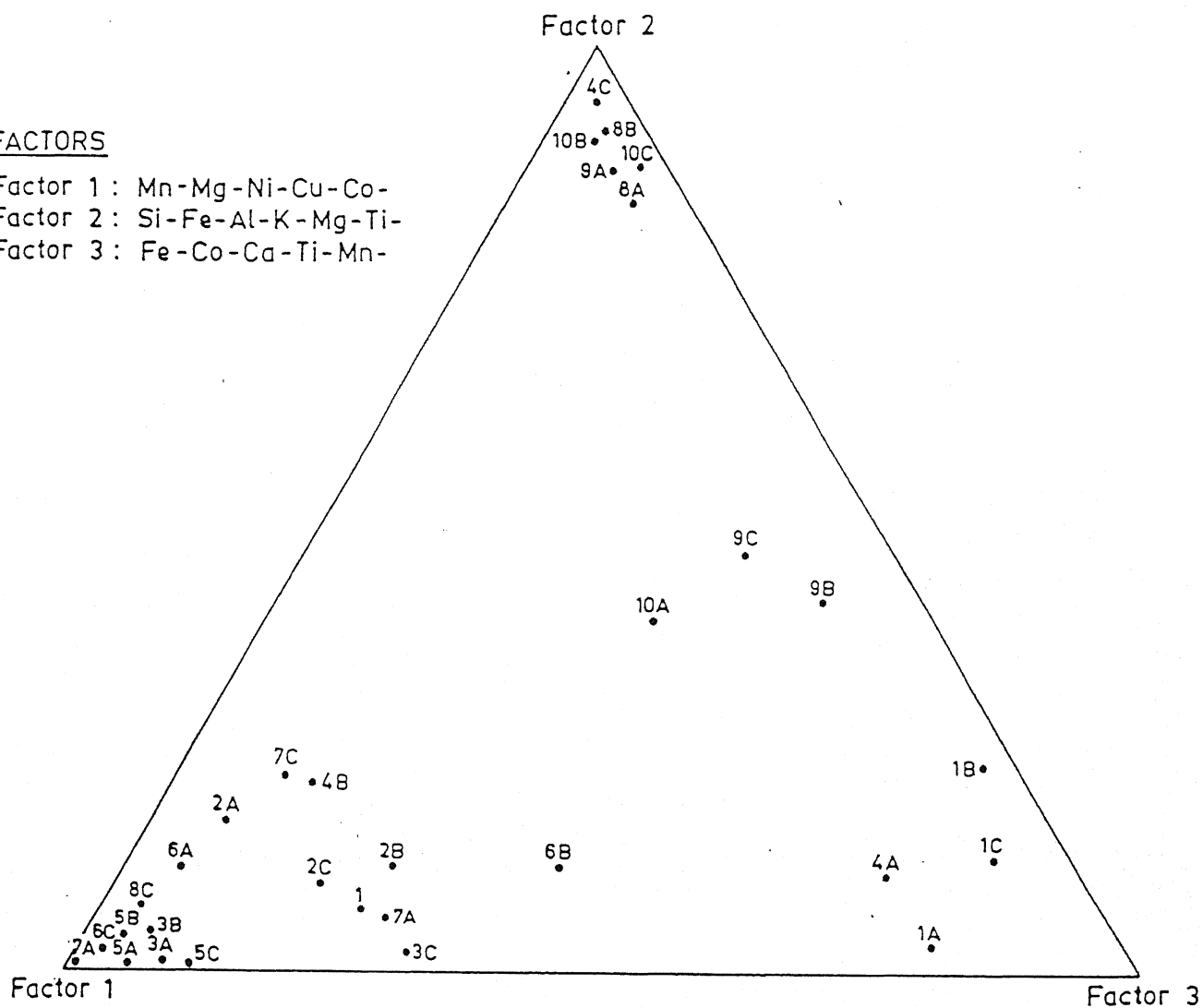


Fig. VI.8. Three co-ordinate plot of normalized varimax factor loadings of areas shown in Fig. VI.7. The diagram illustrate the reproducibility of factor model.

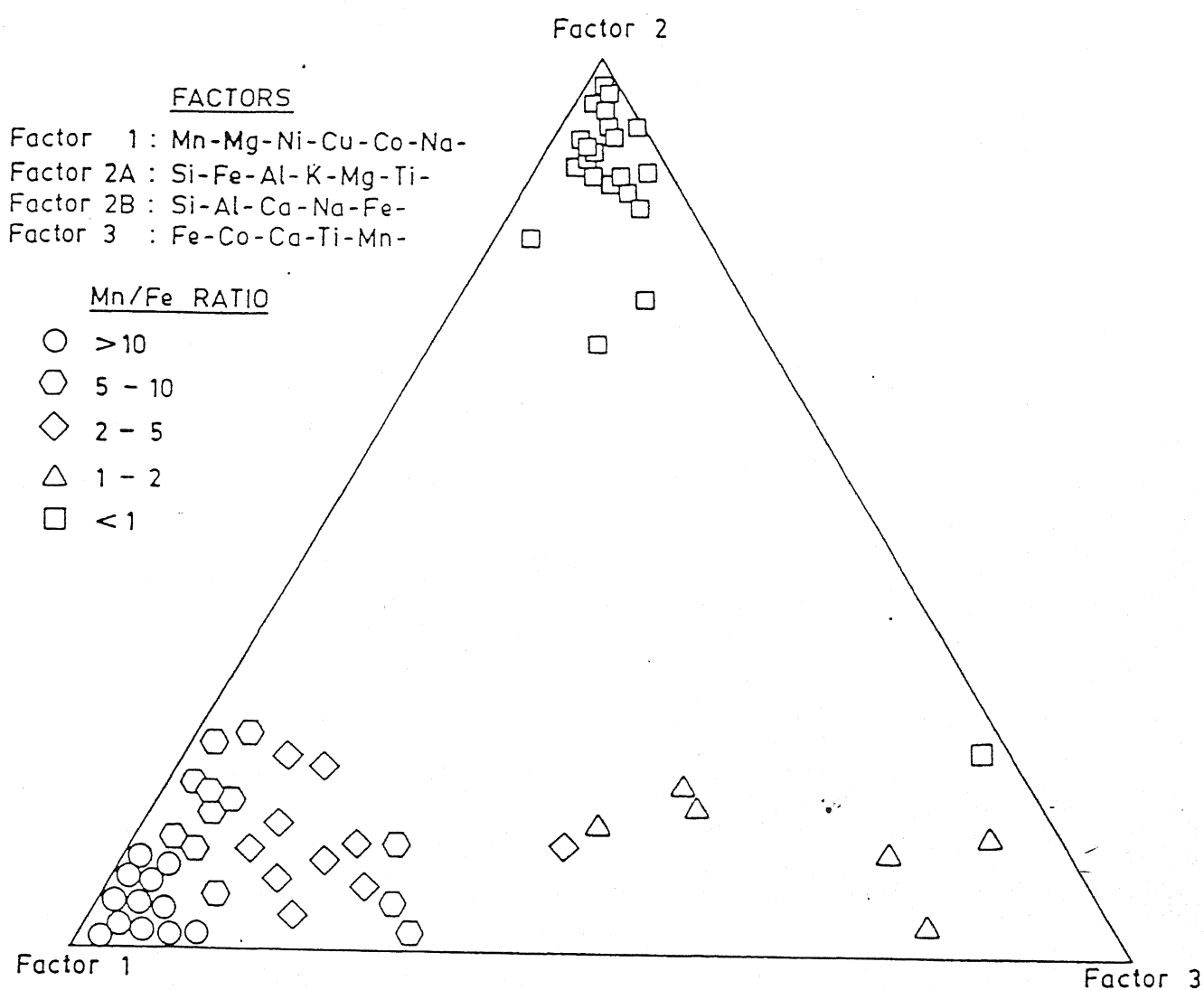


Fig. VI.9. Three co-ordinate discrimination diagram for different locations in the nodule section with corresponding Mn/Fe ratio superimposed.

Calvert and Price (160) used the Q-mode factor model for the analysis of bulk chemical analysis data of nodules from different regions in the Pacific ocean. The discrimination diagram (with little modification in the nomenclature of factors) is reproduced in Figure VI.10. The elemental associations described by Calvert and Price (160) are very similar to the one observed in the present work from the X-ray microanalysis data (Figures VI.6 and VI.8). Factor model based upon bulk chemical analysis is inadequate to split factor 2 as factor 2A (Fe-rich aluminosilicates and factor 2B (aluminosilicates of detrital origin) (Figure VI.6). As indicated in Figure VI.6, the model derived from SEM/EDAX data elucidate the nature of aluminosilicate fractions in nodules in a more comprehensive way because of the micro-level of analysis involved.

Since the bulk chemical analysis data deal with the average value of Mn/Fe ratio, the Mn/Fe ratios assigned to different points in Figure VI.10 (bulk data) are much smaller than those shown in Figure VI.6 (X-ray microanalysis data). However, the positive correlation observed between Mn/Fe ratio and factor-1 (Mn-Ni-Cu-Mg-) (for SEM/EDAX data) is evident for bulk data also (Figure VI.6).

Factor analysis of bulk composition data of nodules from different regions can discriminate among regions on the basis of predominant operating factor. However, it cannot provide any details insight into the genesis of nodules. As shown in this and subsequent sections, factor analysis of microanalysis data provides much deeper insight into the genesis of nodules in terms of both major and minor operating factors.

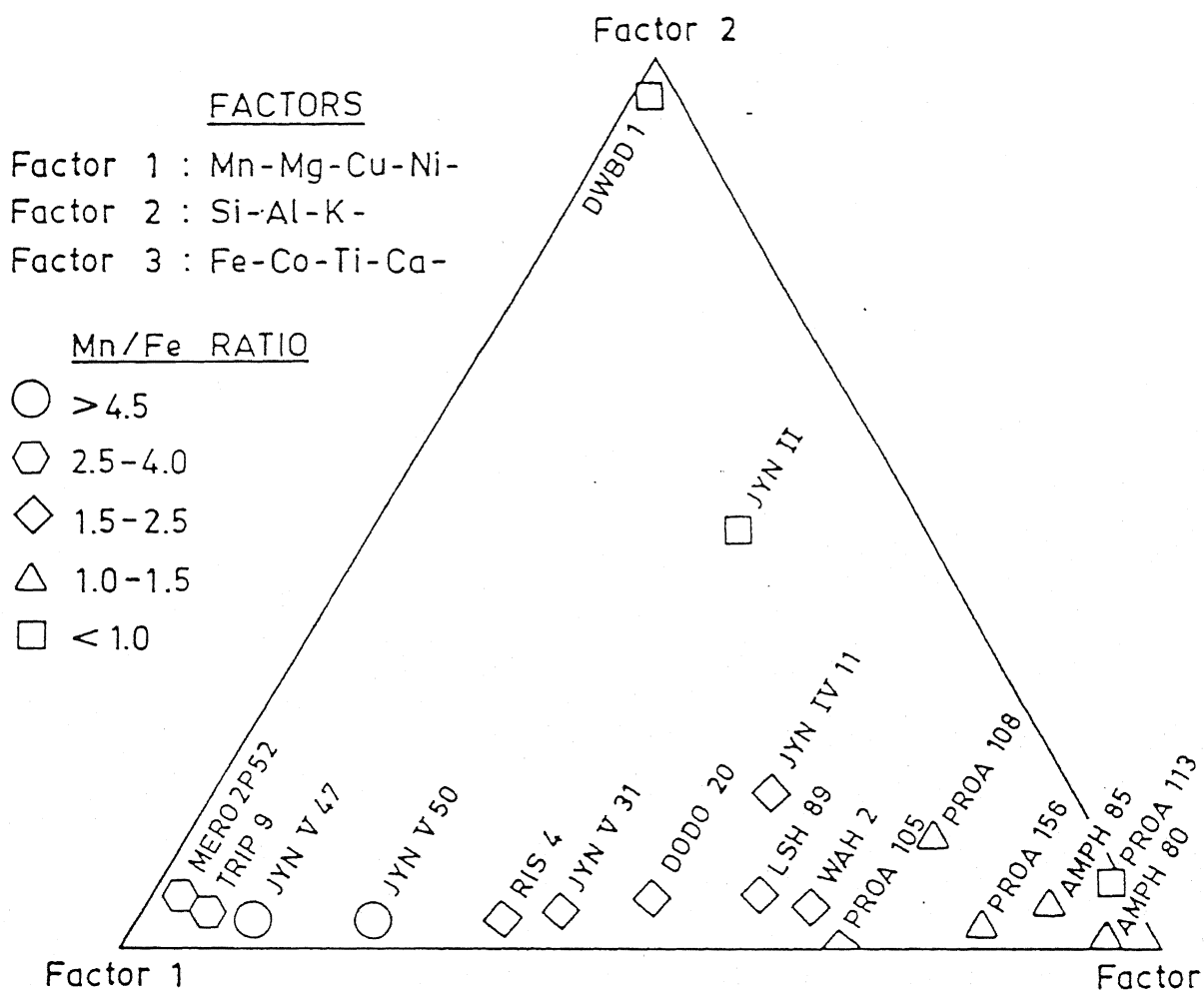


Fig. VI.10. Three co-ordinate diagram of normalized varimax factor loadings of nodules from different locations in Pacific ocean, the corresponding Mn/Fe ratio are superimposed. Bulk composition of nodules used in factor analysis (after Calvert and Price (1960)).

6.2 SEM/BSE-Mode/EDAX Studies

6.2.1 BSE vs. SE Mode:

BSE/Z-contrast images (Figure VI.11(a), and VI.11(c)) from typical internal features in nodules are compared with corresponding SE images (Figure VI.11(b) and VI.11(d)). The micrographs in Figure VI.11 illustrate the superiority of contrast in BSE mode over SE mode. The contrast is inferior in SE mode because in SE mode the atomic number of elements present does not contribute in the image formation. The contrast in BSE mode is due, among other factors, to the difference in atomic number of elements present (vide Appendix-G). Because of superiority of contrast in BSE mode, detailed microstructural studies were carried out in this mode.

6.2.2 Microfeatures and Chemical Characteristics:

The BSE micrographs in Figure VI.12 illustrate the general view of nodule internal features. The heterogeneous nature of the nodule internal structure need to be noted. The nature and level of heterogeneity are further elucidated in the BSE/Z-contrast images (Figure VI.13) of distinct morphologies observed in the micrographs of Figure VI.12. Typical segregation patterns which were identified include columnar and radial pattern (Figure VI.13(a)), dendritic segregation (Figure VI.13(b)), compact type of morphology (Figure VI.13(c)) and fragment of detrital material embedded in nodule matrix (Figure VI.13(d)). The distinct regions in the different morphologies are marked (Figure VI.13) and their chemical compositions (based on X-ray microanalysis) are presented in Table VI.8.

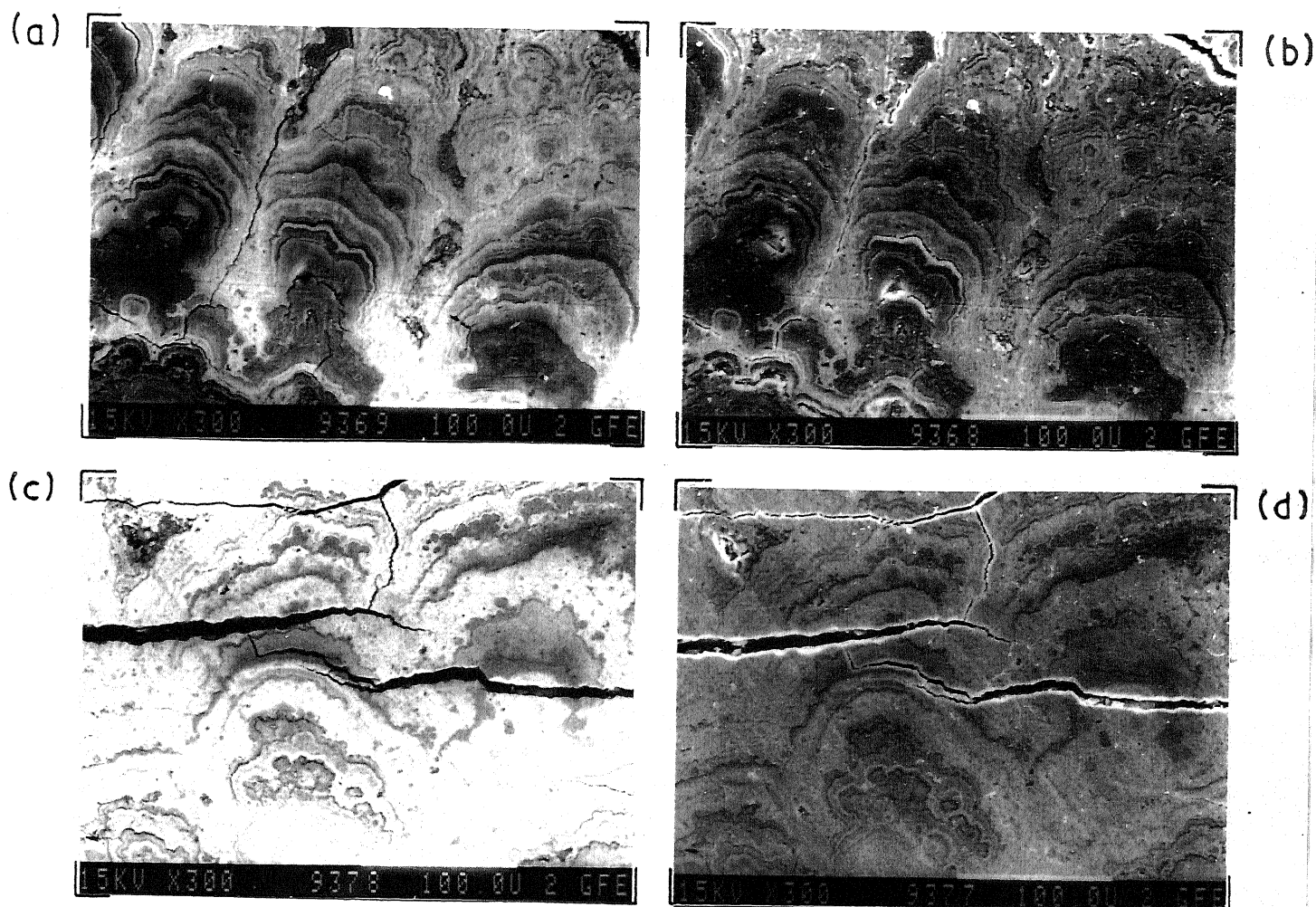
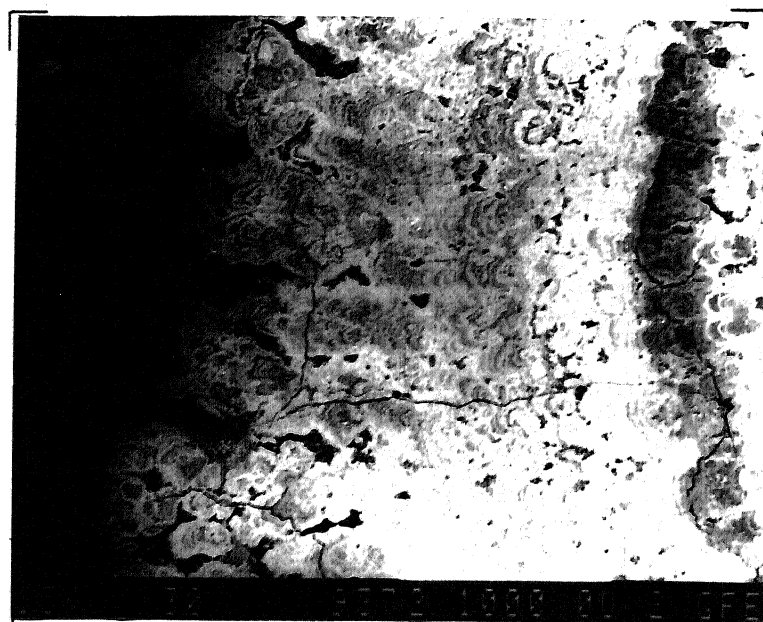
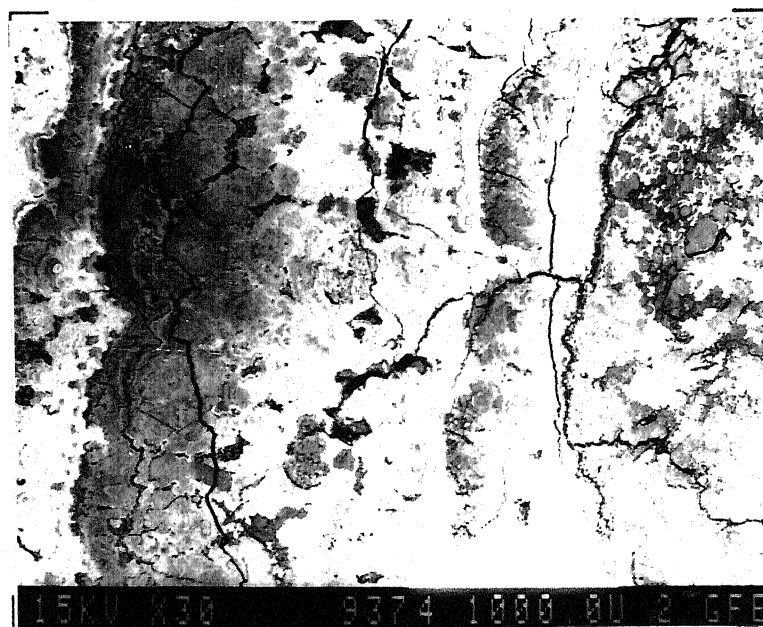


Fig. VI.11. SEM micrographs illustrating the superiority of Z-contrast BSE images ((a),(c)) over corresponding SE images ((b),(d)).



(a)



(b)

Fig. VI.12. BSE micrographs illustrating the overall view of internal features in nodule internal structure.

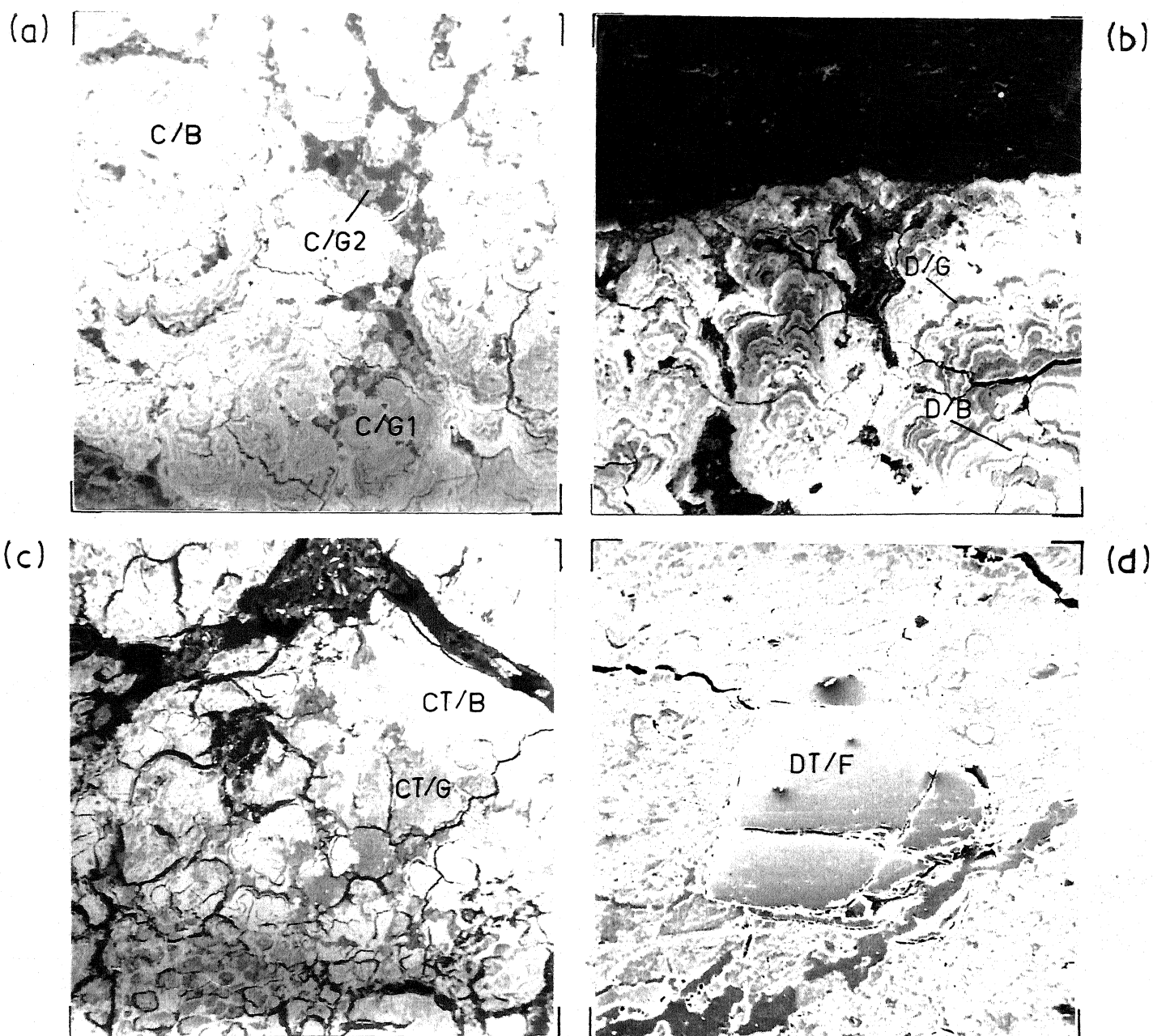
200 μm 

Fig. VI.13. BSE micrographs of typical morphological features (a) columnar and radial pattern, (b) dendritic segregation, (c) compact type of morphology and (d) detrital fragment embedded in nodule matrix. The distinct regions in different morphologies are marked.

Table VI.8: X-ray microanalysis of selected regions in different textural patterns (Figure VI.13). ZAF corrections were not applied, so the results are only semiquantitative

Textural characteristics and region description	Composition, wt %										
	Mn	Fe	Ni	Cu	Ti	Si	Al	Ca	K		
	Max-Min	Max-Min	Max-Min	Max-Min	Max-Min	Max-Min	Max-Min	Max-Min	Max-Min	Max-Min	Max-Min
Columnar/Bright (C/B)	19 - 15	8.0-5.0	1.2-0.4	0.6-0.2	NIL	3.0-0.4	1.5-0.5	0.6-0.3	0.4-0.2		
Dendritic/Bright (D/B)	32 - 28	2.0-0.0	2.1-1.8	1.4-1.1	NIL	0.6-0.0	1.0-0.0	0.7-0.6	0.5-0.3		
Compact type/Bright (CT/B)	32 - 11	7.0-1.0	0.8-0.5	0.6-0.3	NIL	3.0-1.0	1.5-1.0	0.6-0.3	0.6-0.2		
Columnar/Grey (C/G1)	16 - 10	20 - 9.0	NIL	NIL	0.8-0.4	4.0-2.0	2.0-1.0	1.4-0.5	0.1-0.0		
Columnar/Dark Grey (C/G2)	1.0- 0	15 - 10	NIL	NIL	0.2-0.1	14 - 10	3.0-1.0	0.2-0.1	1.0-0.8		
Dendritic/Grey (D/G)	12 - 10	18 - 10	0.4-0.2	0.3-0.2	0.8-0.4	4.0-1.0	2.0-1.0	1.1-0.8	0.4-0.0		
Compact type/Grey (CT/G)	1.0-0.0	15 - 4.0	NIL	NIL	0.5-0.0	20 - 8.0	6.0-2.5	0.2-0.0	1.5-0.5		
Detrital Fragment (DT/F)	0.2- 0	0.2- 0	NIL	NIL	0.04-0.0	29 - 28	9-8	6-4	3.0-2.5*		

* (Na + K).

Columnar and radial patterns (Figure VI.13(a)) are typical of laminated zones in nodules' internal structure (25). The chemical compositions of the bright (C/B, Figure VI.13(a)) and grey regions (CG1 and CG2) are highly variable (Table VI.8) indicating that these consist of more than one phase. X-ray maps (Figure VI.14) corresponding to a small region in columnar and radial kind of morphology (Figure VI.13) indicate the following: (i) Mn is segregated more in the bright regions, (ii) Fe, which is distributed in both grey and bright regions, is intimately associated with Mn and (iii) Minor elements (Ni, Co and Cu) are also segregated with Mn and Fe.

The concentration profiles of Ni and Cu across a typical region (Figure VI.15) show close resemblance with Mn. Co seems to be associated with Fe. Typical EDAX spectra of bright (C/B) and grey (CG1) regions are given in Figure VI.16(a) and VI.16(b). These regions are characterized by positive correlation of Ni and Cu with Mn/Fe ratio. Ti correlates negatively with Mn/Fe ratio. The correlation of Co is not clear because of the overlapping of the weak CoK_α line with the strong FeK_β line.

EDAX spectra from the bright region (D/B) in dendritic segregation (Figure VI.13(b)) are presented in Figure VI.17. The bright regions (D/B) contain the highest concentration of manganese and these are the ones having the maximum concentration of Ni and Cu (Table VI.8). These regions are more or less uniform in composition i.e. they appear to consist of single phase material. The composition of grey regions (D/G) separating bright regions (D/B) is similar to that of grey regions (C/G1) observed in columnar and radial patterns (Figure VI.16(b), Table VI.8).

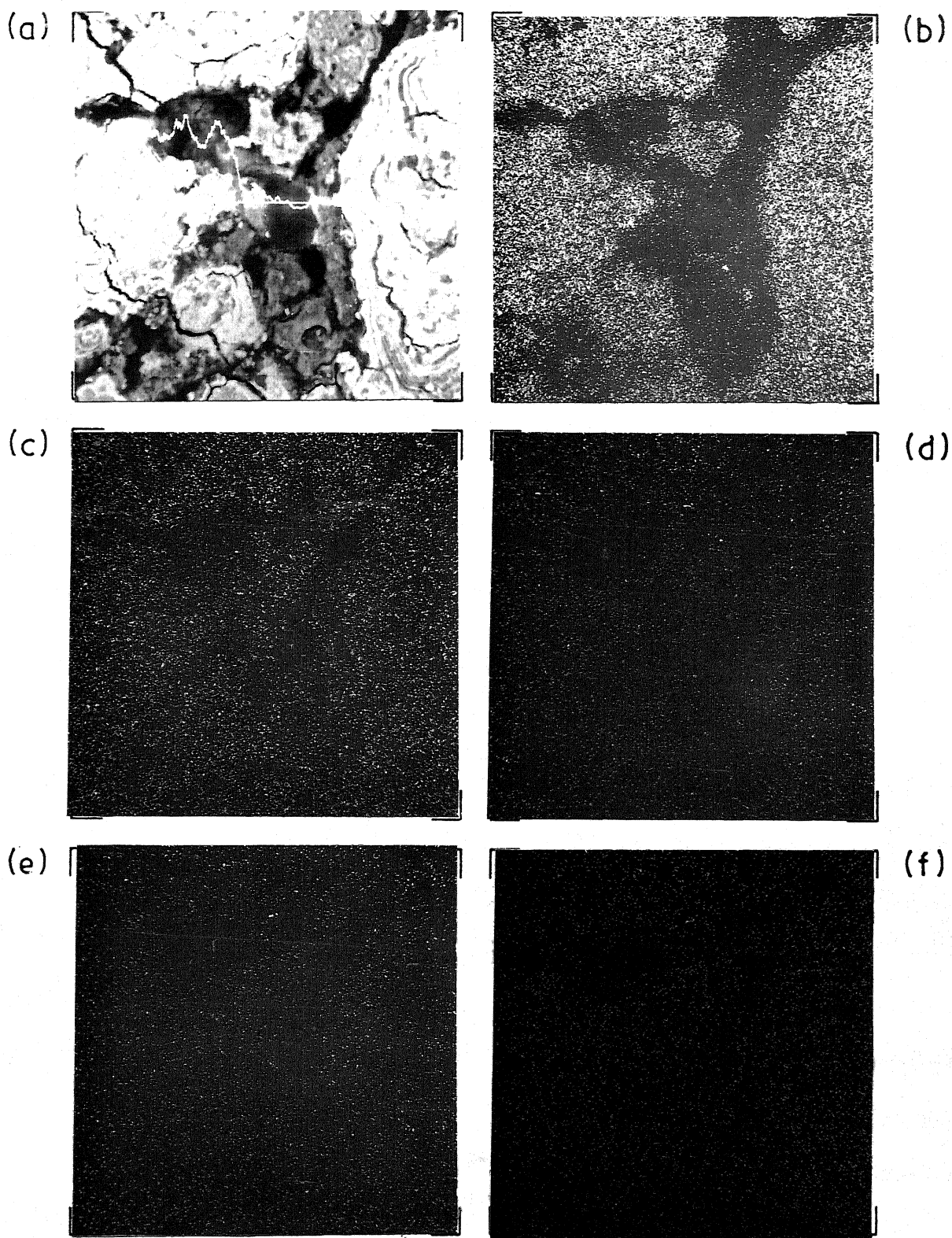


Fig. VI.14. X-ray maps for BSE micrograph in (a), (b) Mn, (c) Fe, (d) Ni, (e) Co and (f) Cu.

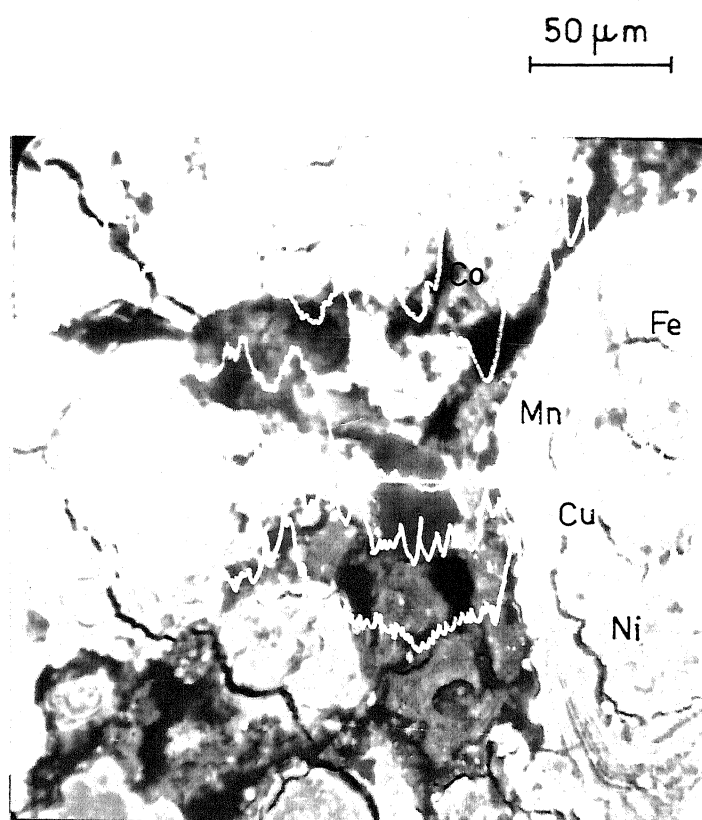


Fig. VI.15. Concentration profiles of major (Mn, Fe) and minor (Ni, Co and Cu) elements superimposed on a typical region in columnar and radial pattern to illustrate the elemental association.

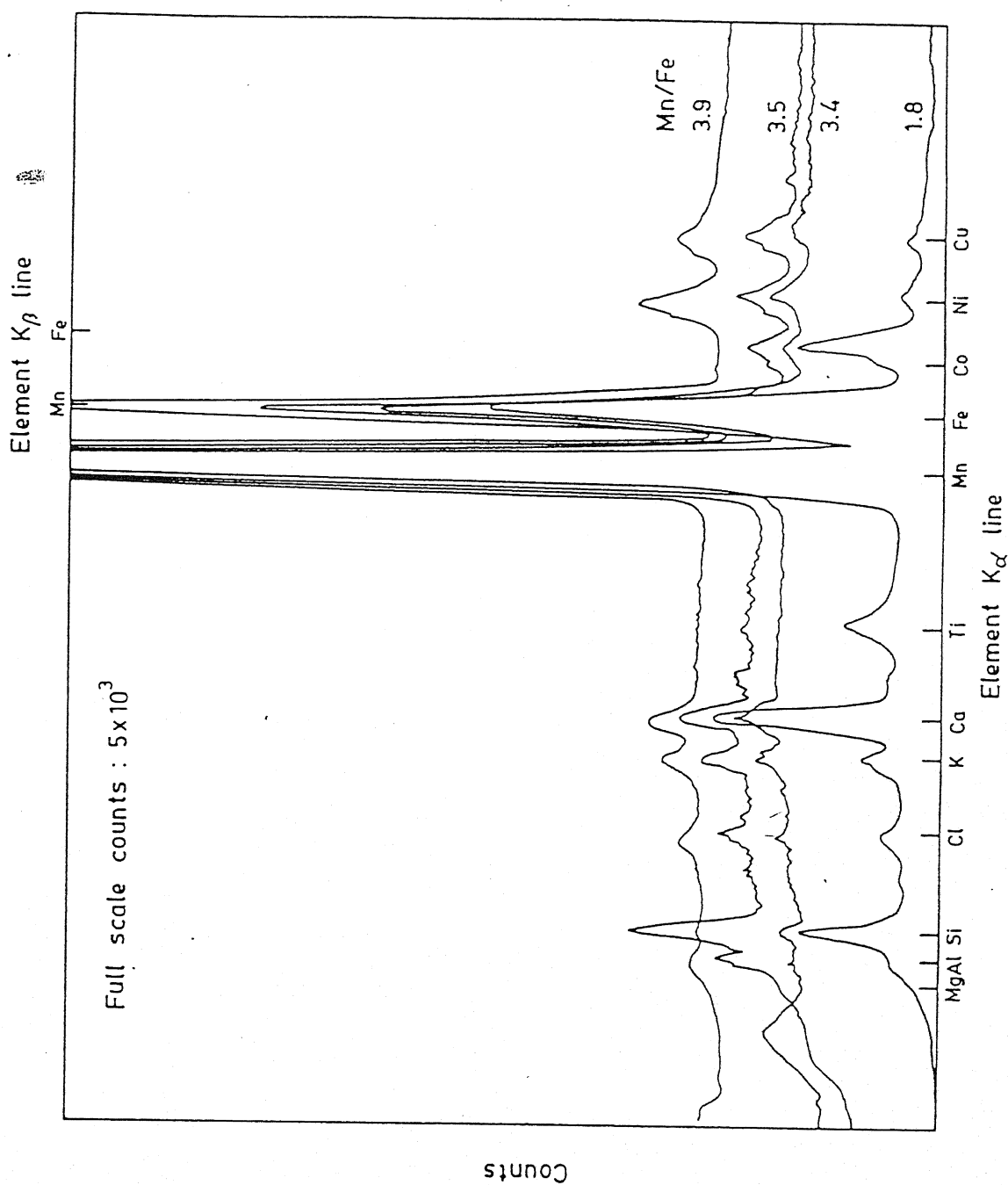


Fig. VI.16(a). X-ray spectra from bright regions (C/B) in columnar and radial pattern. The diagram illustrate the relationship between Mn/Fe ratio and minor elements concentration.

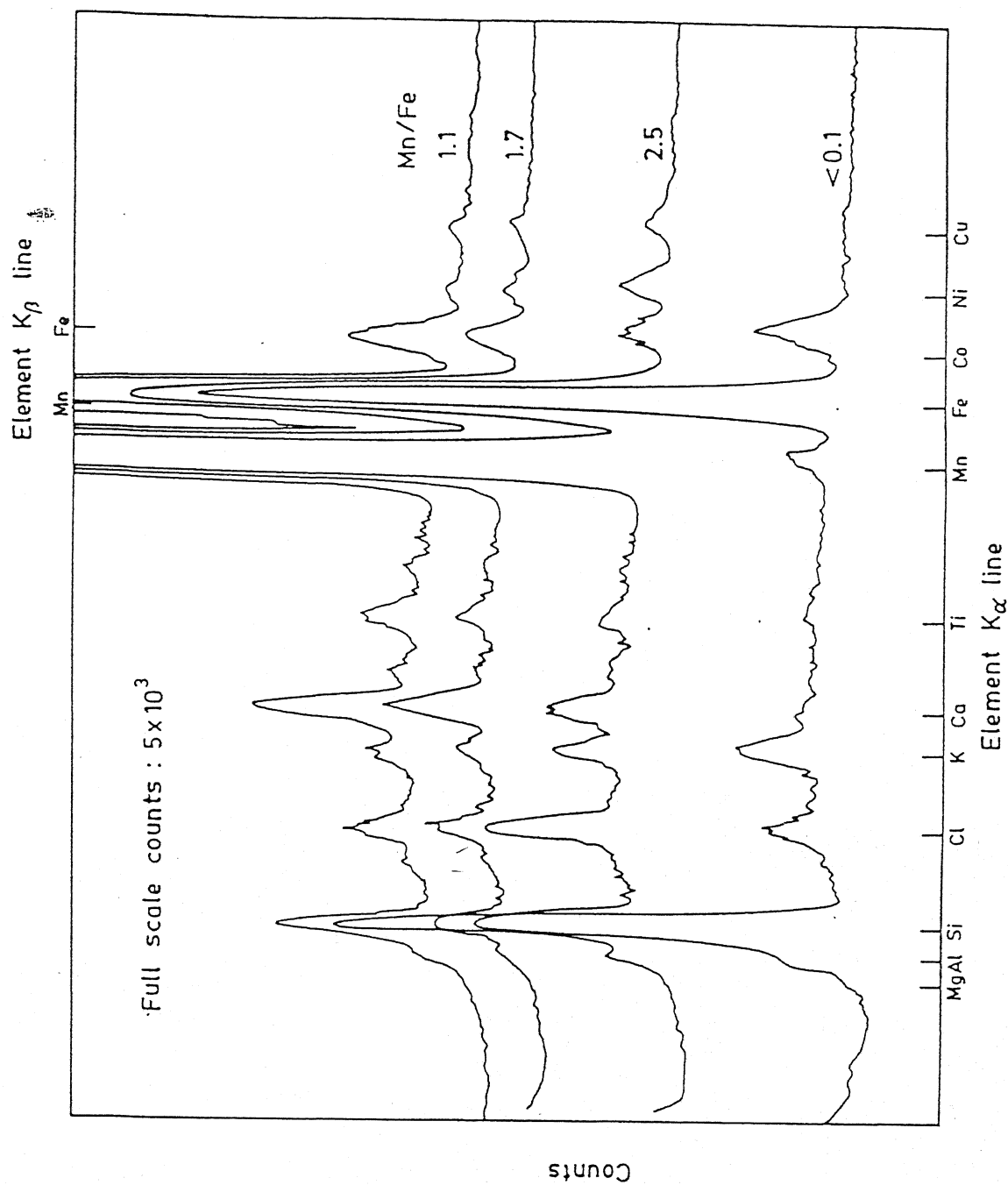


Fig. VI.16(b). X-ray spectra from grey regions (C/G1) and (D/G) in columnar and radial pattern and dendritic segregation.

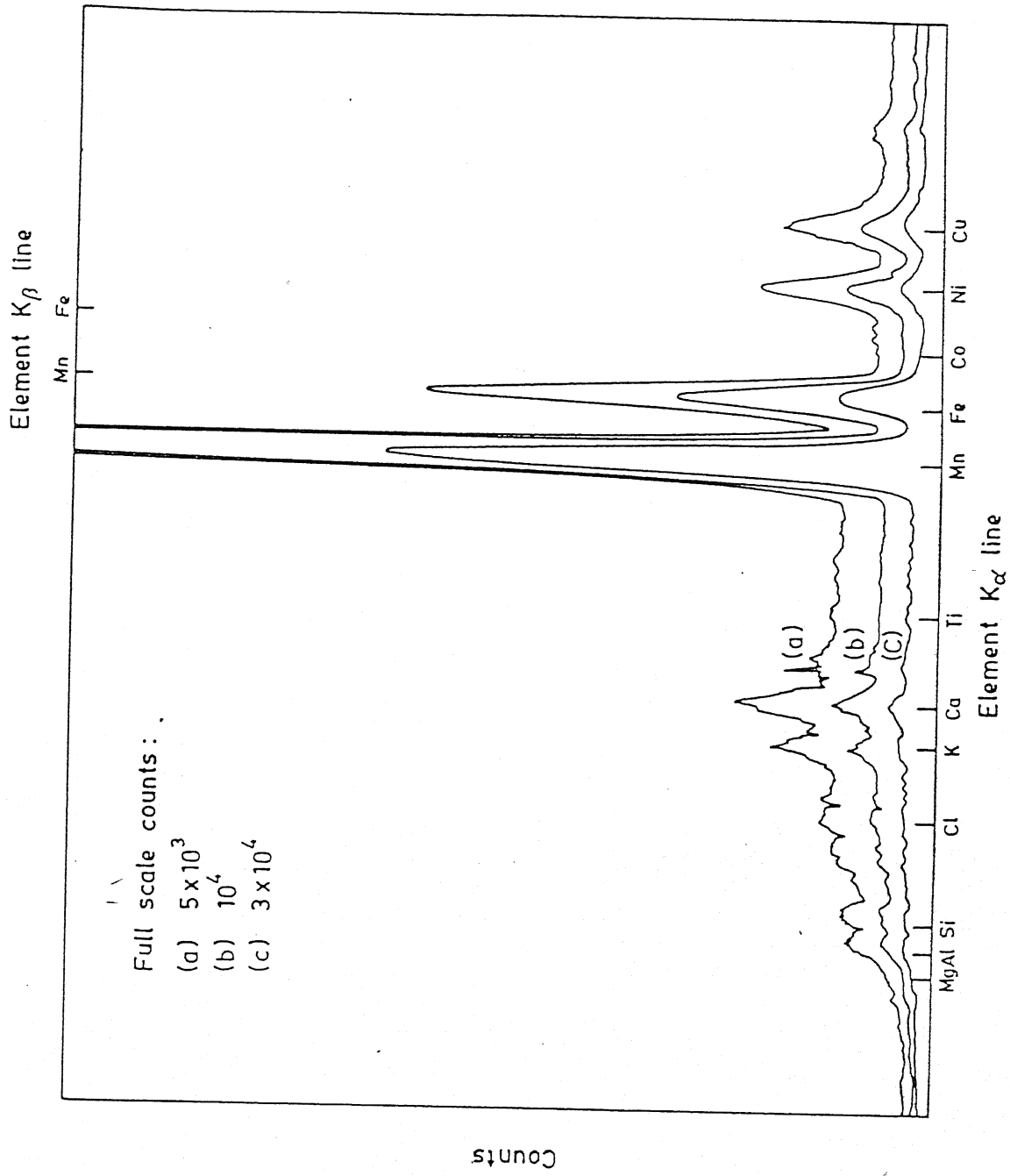


Fig. VI.17. X-ray spectra from bright regions (D/B) in dendritic segregation.

The material just surrounding the nodule core consists mainly of compact type of morphology (Figure VI.13(c)). Large scale variations in the composition of bright (CT/B) and grey (CT/G) regions here indicate the heterogeneous nature of these regions. The bright material embedded in nodule matrix (Figure VI.18) also shows composition similar to the bright region (CT/B). X-ray mapping for Mn, Fe, Ni and Cu (Figure VI.19) in a typical region of compact type of morphology depicted similar distribution patterns as observed for radial and columnar type of morphology (Figure VI.14). Concentration profiles of Ni, Co and Cu show close resemblance with the profile of Mn (Figure VI.20). The different behaviour of Co in columnar and radial patterns (Figure VI.15) on the one hand and compact type of morphology (Figure VI.20) on the other needs to be specially noted because it explains the positive correlation of Co with either Fe or Mn in terms of microstructural features. It is striking to note that Ni and Cu show negative correlation with Mn/Fe ratio for CT/B regions (Figure VI.21). This behaviour of Ni and Cu in CT/B is distinct from their behaviour in C/G and C/B (Figure VI.16). The grey material (CT/G) is enriched with Si, Fe, Al, K and Ti (Figure VI.22, Table VI.8). Here it may be added that the grey region (C/G2) has composition very similar to CT/G. The variation of Si, Al, K and Ti correlates positively with Fe variation (Figure VI.22).

Very dark regions in all the morphologies (Figure VI.13) correspond to cracks filled with different amounts of resin and nodule material. Some typical EDAX spectra from such regions are presented in Figure VI.23.

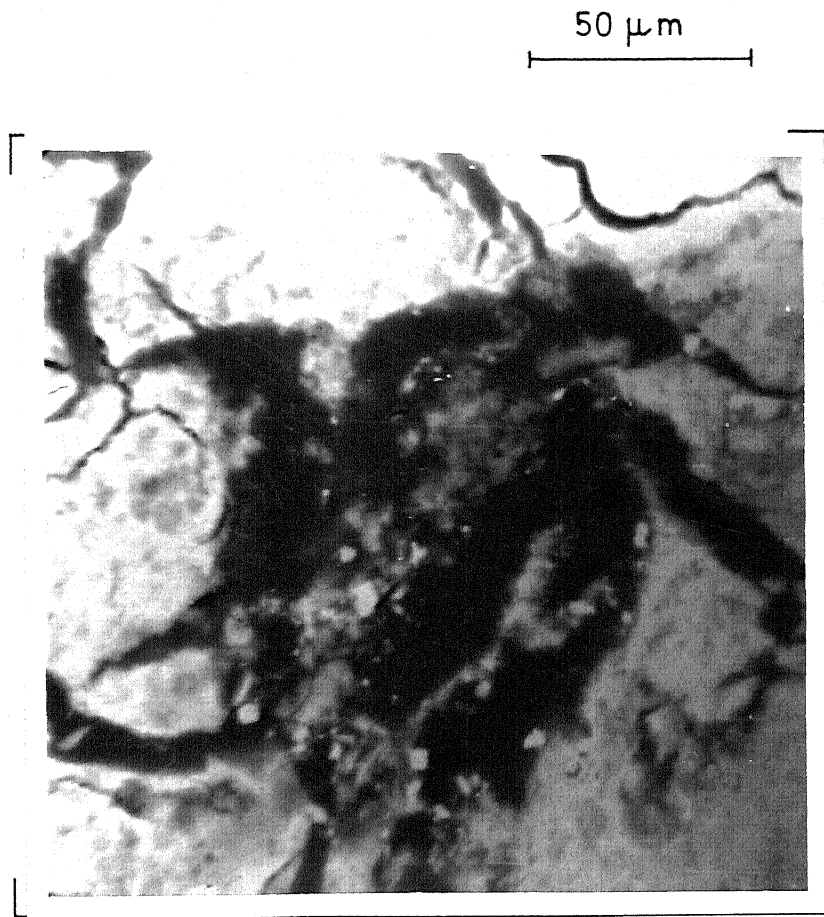


Fig. VI.18. BSE micrograph of (CT/B) material present in cracks.

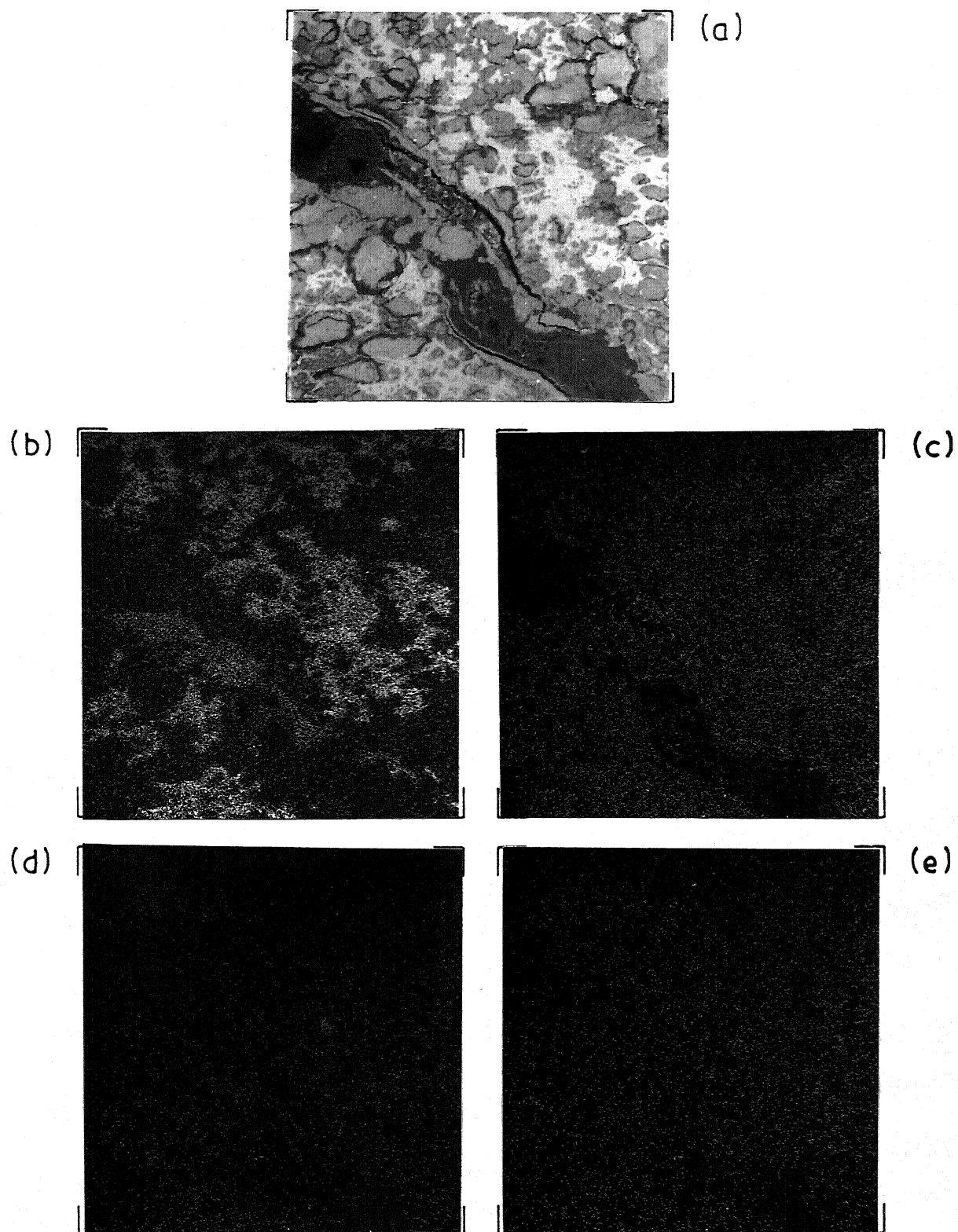
200 μm 

Fig. VI.19. X-ray maps for BSE micrograph in (a), (b) Mn, (c) Fe, (d) Ni and (e) Cu.

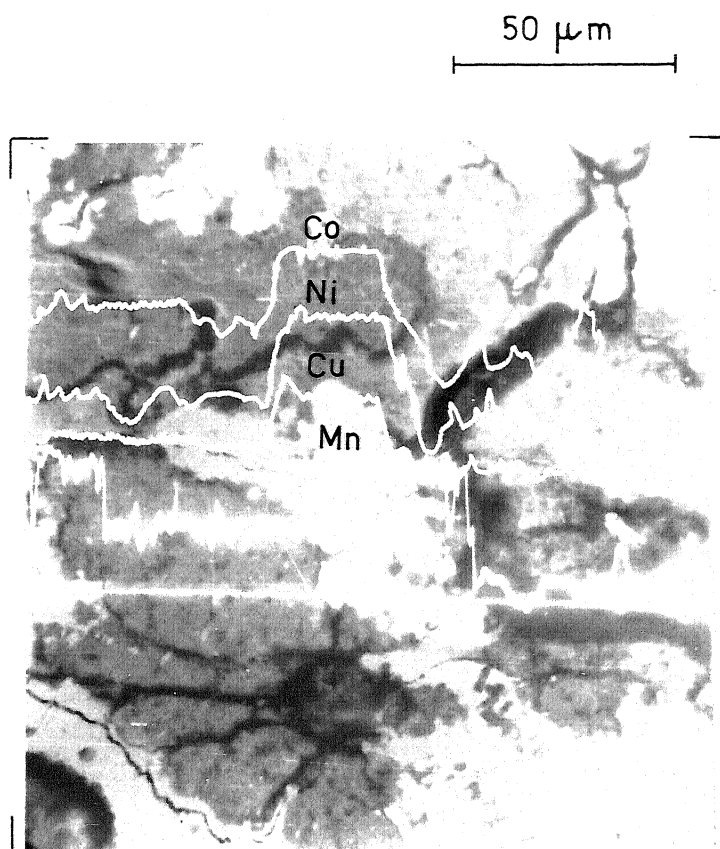


Fig. VI.20. Concentration profiles of Mn and minor elements (Ni, Co, Cu) superimposed on a typical region in compact type of morphology to illustrate the elemental association.

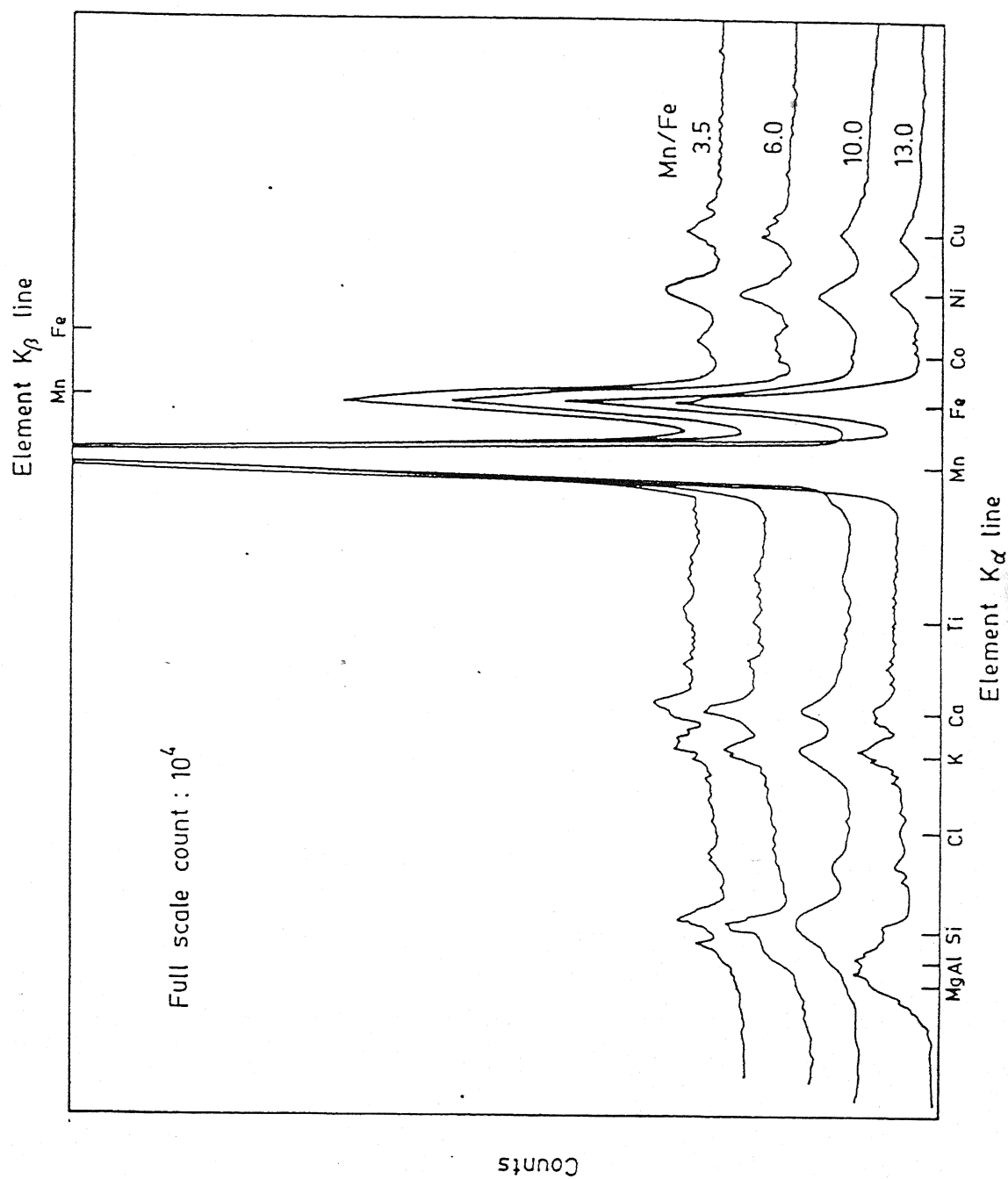


Fig. VI.21. X-ray spectra of bright regions (CT/B) in compact type of morphology illustrating negative correlation of Ni and Cu with Mn/Fe ratio.

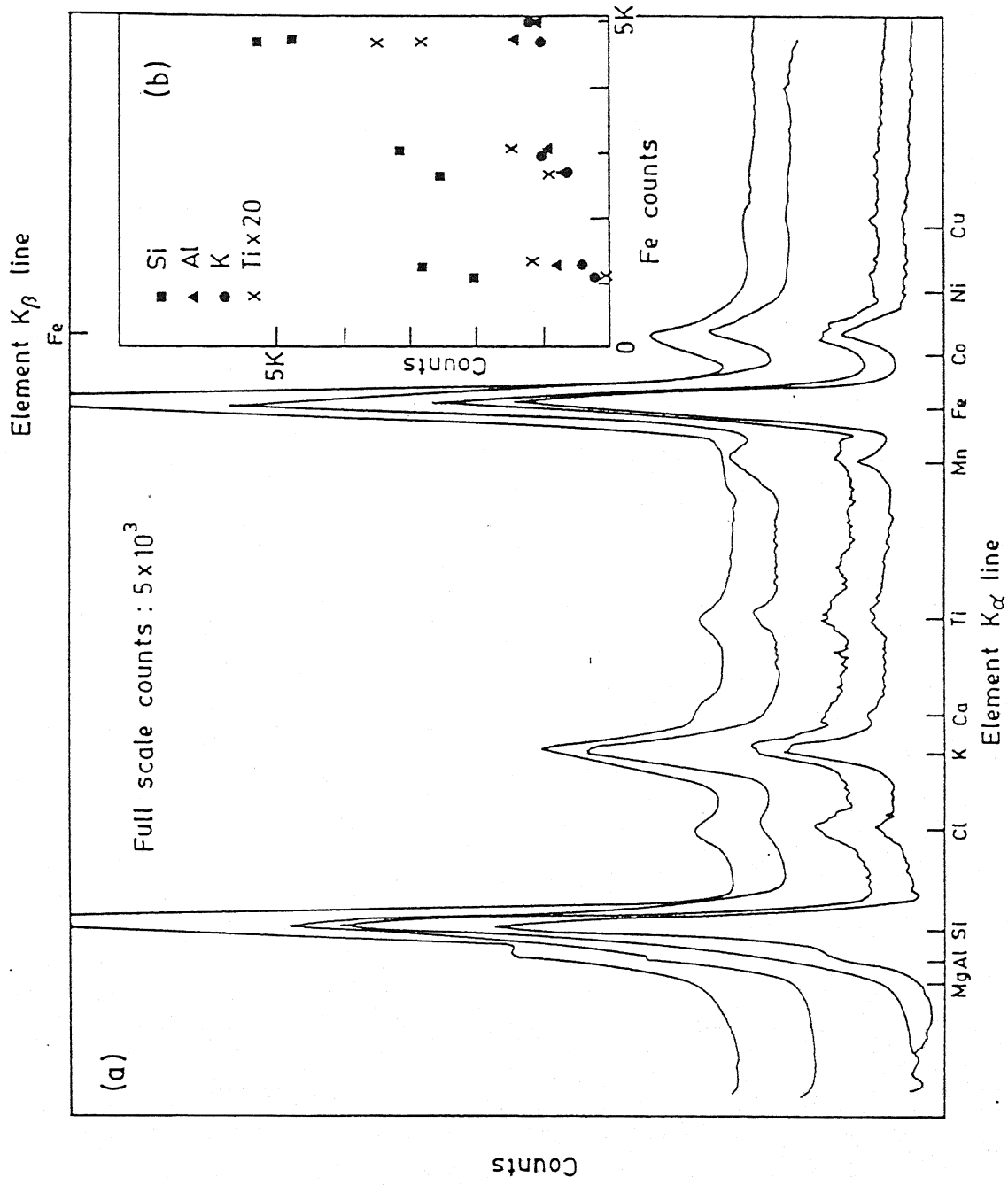


Fig. VI.22. (a) X-ray spectra of grey regions (CT/G) in compact type of morphology, (b) the diagram illustrating positive correlation between Fe concentration and concentration of other elements (Si, Al, K, Ti) in CT/G regions.

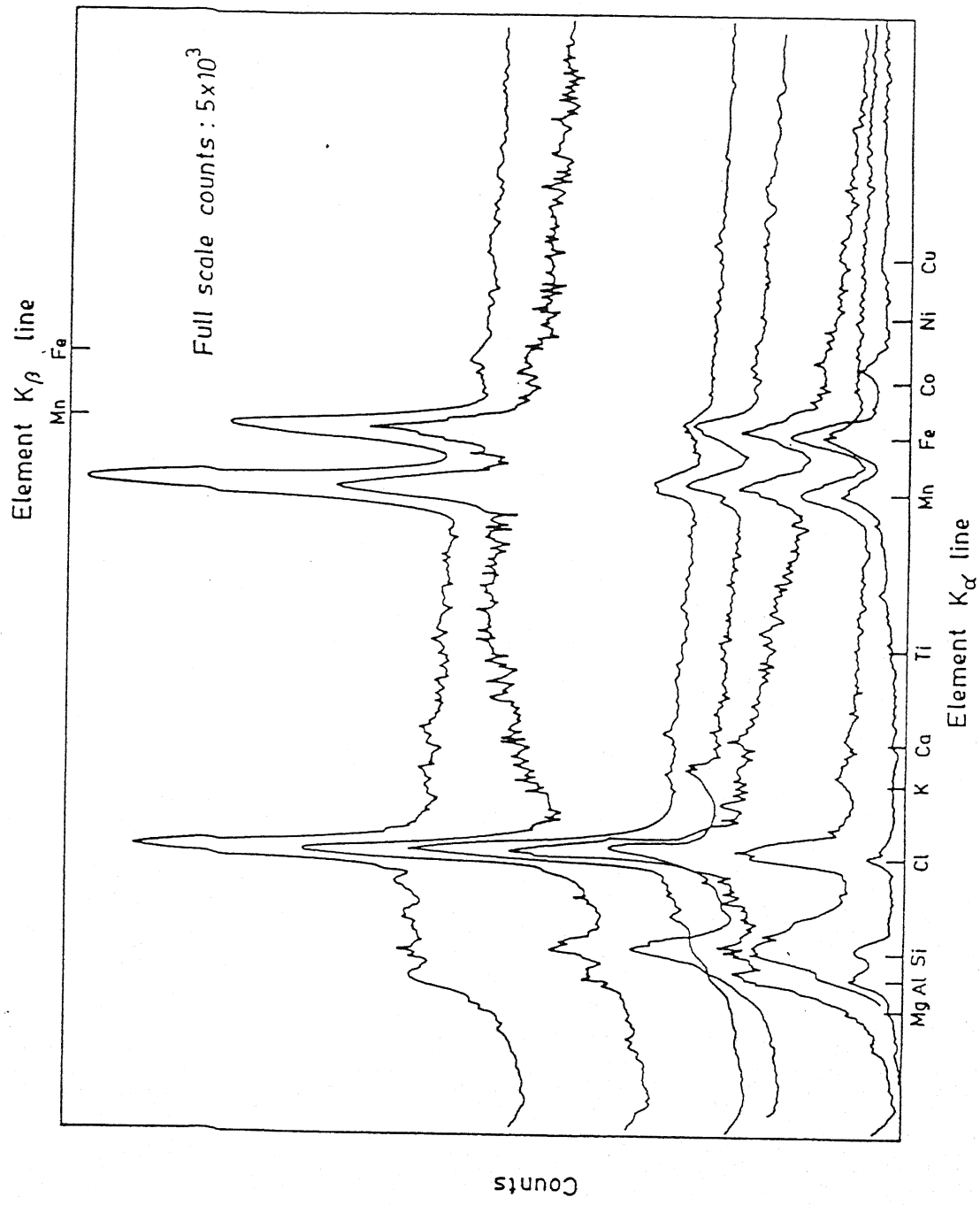


Fig. VI.23. X-ray spectra of dark and very dark regions in different morphologies.

6.2.3 . Factor Analysis:

The chemical compositions (in terms of X-ray counts) of 28 distinct regions from different morphologies (growth features only, Figure VI.13) are given in Table VI.9. Data in Table VI.9 were transformed as a fraction of the maximum value of the variable and used for Q-mode factor analysis. The objective of factor analysis was two fold: (i) to correlate the distinct regions with the different phase constituent/s; using elemental associations in the factors, phase detected by XRD and TEM and available informations in the literature (25, 100) and (ii) to discriminate among the different regions in terms of factor loadings, Mn/Fe ratio and genesis. The factor loadings for the different regions and factor scores of elements are given in Tables VI.10(a) and VI.10(b) respectively. The four factors together explain 97% of the variance in the scaled data set. Communality (i.e. $\sum f_r^2$; $r = 1$ to 4) at each observation point is high (~ 1). Factors 1, 2 and 3 (Table VI.1(a) and VI.1(b)) are based on elemental associations similar to Factor 1, 2A and 3, as described before for SEM/SE/EDAX data (Tables VI.5(b) and VI.7(b)). Elements like Co, Mg etc. which are not included in calculation of factor model (Table VI.10(b)) can be assigned to respective factors by comparison with elemental associations observed for factors in the analysis of SEM/SE/EDAX data (Table VI.5(b)). Minor factor-4, which is based on positive factor score of Mn and negative scores for Ni, Cu etc. is retained because it shows significant loadings for CT/B regions and is essential to explain the Mn-enrichment and negative correlation of Ni and Cu with Mn/Fe ratio in these regions.

Table VI.9: X-ray microanalysis data for distinct regions in different morphologies

S. No.	Morphology* /Region	X-ray counts for elements (K _α line)										Mn/Fe ratio
		Mn	Fe	Ni	Cu	Ti	Si	Al	Ca	K		
1	CT/B	7500	2131	303	210	-	368	236	276	197	3.5	
2	CT/B	12000	1220	237	131	-	368	210	263	211	10	
3	BS	20526	-	263	263	-	789	263	400	395	>10	
4	CT/B	18421	-	263	263	-	263	263	263	263	>10	
5	C/B	10789	1976	473	263	-	105	105	315	263	5.4	
6	C/B	9211	2616	316	290	-	737	289	421	263	3.5	
7	C/(B/G1)	9105	5068	53	53	368	684	263	1052	263	1.8	
8	C/(B/G1)	6052	1763	184	105	-	132	79	263	157	3.4	
9	CT/B	6842	526	211	132	-	53	53	53	132	13.0	
10	CT/B	7816	1316	302	97	-	342	237	263	224	5.9	
11	D/G	6184	5842	132	105	263	237	237	632	197	1.1	
12	D/B	18473	-	789	631	-	-	-	474	-	>10	
13	D/B	16421	-	736	526	-	150	150	420	211	>10	
14	D/B	15900	-	711	578	-	53	-	447	263	>10	
15	D/B	15800	-	684	578	-	53	53	526	342	>10	
16	D/B	16000	-	710	578	-	27	27	-	-	-	
17	CT/G	211	4737	-	53	210	5263	1368	-	1052	<1	
18	CT/G	79	4842	-	53	158	4737	1000	-	1079	<1	
19	CT/G	264	3078	-	-	106	3158	894	-	1000	<1	
20	CT/G	26	1263	-	-	92	2842	1000	-	447	<1	
21	C/G2	290	3947	-	53	79	3000	631	158	737	<1	
22	C/G1	7105	2894	-	158	171	974	394	395	381	2.5	
23	C/G2	237	3684	-	-	66	2986	394	105	434	<1	
24	CT/G	-	1236	-	-	-	2000	842	132	237	<1	
25	CT/G	211	2684	-	-	132	2500	606	105	579	<1	
26	D/G	6763	6026	79	105	342	1052	316	842	236	1.0	
27	C/G1	6157	3553	132	132	237	460	263	711	184	1.7	
28	CT/G	132	2132	-	-	92	3421	1236	447	315	<1	

CT - Compact type
D - Dendritic
C - Columnar and radial
BS - Bright spots in cracks
B - Bright/Light
G - Grey
B/G1 - Distinction not clear
(vide Figure VI.13 for more details)
- Values taken as zero in the factor model calculation

Table VI.9: X-ray microanalysis data for distinct regions in different morphologies

S. No.	Morphology* /Region	X-ray counts for elements (K _α line)										Mn/Fe ratio
		Mn	Fe	Ni	Cu	Ti	Si	Al	Ca	K		
1	CT/B	7500	2131	303	210	-	368	236	276	197	3.5	
2	CT/B	12000	1220	237	131	-	368	210	263	211	10	
3	BS	20526	-	263	263	-	789	263	400	395	>10	
4	CT/B	18421	-	263	263	-	263	263	263	263	>10	
5	C/B	10789	1976	473	263	-	105	105	315	263	5.4	
6	C/B	9211	2616	316	290	-	737	289	421	263	3.5	
7	C/(B/G1)	9105	5068	53	53	368	684	263	1052	263	1.8	
8	C/(B/G1)	6052	1763	184	105	-	132	79	263	157	3.4	
9	CT/B	6842	526	211	132	-	53	53	263	132	13.0	
10	CT/B	7816	1316	302	97	-	342	237	263	224	5.9	
11	D/G	6184	5842	132	105	263	237	237	632	197	1.1	
12	D/B	18473	-	789	631	-	-	-	474	-	>10	
13	D/B	16421	-	736	526	-	150	150	420	211	>10	
14	D/B	15900	-	711	578	-	53	-	447	263	>10	
15	D/B	15800	-	684	578	-	53	53	526	342	>10	
16	D/B	16000	-	710	578	-	27	27	-	-	>10	
17	CT/G	211	4737	-	53	210	5263	1368	-	1052	<1	
18	CT/G	79	4842	-	53	158	4737	1000	-	1079	<1	
19	CT/G	264	3078	-	-	106	3158	894	-	1000	<1	
20	CT/G	26	1263	-	-	92	2842	1000	-	447	<1	
21	C/G2	290	3947	-	53	79	3000	631	158	737	<1	
22	C/G1	7105	2894	-	158	171	974	394	395	381	2.5	
23	C/G2	237	3684	-	-	66	2986	394	105	434	<1	
24	CT/G	-	1236	-	-	-	2000	842	132	237	<1	
25	CT/G	211	2684	-	-	132	2500	606	105	579	<1	
26	D/G	6763	6026	79	105	342	1052	316	842	236	1.0	
27	C/G1	6157	3553	132	132	237	460	263	711	184	1.7	
28	CT/G	132	2132	-	-	92	3421	1236	447	315	<1	

CT - Compact type
D - Dendritic
C - Columnar and radial
BS - Bright spots in cracks

B - Bright/Light
G - Grey
B/G1 - Distinction not clear
(vide Figure VI.13 for more details)

- Values taken as zero in the factor model calculation

Table VI.10(a): Factor loadings and communality for distinct regions in different morphologies (Figure VI.13(a-c), Table VI.9)

S. No.*	Factor loadings, f_r				Communality $\sum_{r=1}^4 f_r^2$
	1	2	3	4	
1	0.8631	0.3076	0.3578	-0.0752	0.9731
2	0.8690	0.2384	0.3006	0.2582	0.9691
3	0.8652	0.1863	0.1726	0.4049	0.9769
4	0.8979	0.1258	0.1363	0.3860	0.9896
5	0.9426	0.1449	0.2691	-0.0628	0.9858
6	0.8292	0.3360	0.3998	-0.0596	0.9638
7	0.2378	0.2978	0.9202	0.0624	0.9960
8	0.7996	0.2366	0.4883	-0.0124	0.9339
9	0.9609	0.1282	0.1330	0.0653	0.9618
10	0.9078	0.2926	0.2781	0.0094	0.9871
11	0.2982	0.3229	0.8876	-0.0728	0.9864
12	0.9714	-0.1031	0.1186	-0.0239	0.9688
13	0.9829	0.0322	0.1434	-0.0351	0.9890
14	0.9742	0.0088	0.1698	-0.1003	0.9880
15	0.9695	0.0149	0.1365	-0.0340	0.9600
16	0.9567	-0.0699	-0.0342	-0.1054	0.9325
17	0.0938	0.9600	0.2404	-0.0141	0.9884
18	0.1081	0.9472	0.2505	-0.0716	0.9767
19	0.1060	0.9533	0.1842	-0.0003	0.9539
20	0.0656	0.9648	0.0848	0.1290	0.9590
21	0.1551	0.9084	0.3356	-0.0965	0.9711
22	0.4047	0.5498	0.6930	0.1423	0.9666
23	0.0913	0.8736	0.3791	-0.1458	0.9366
24	0.1140	0.9139	0.0656	0.1449	0.8735
25	0.0835	0.9174	0.3668	-0.0144	0.9833
26	0.2464	0.3632	0.8934	-0.0059	0.9907
27	0.3763	0.2954	0.8633	0.0327	0.9752
28	0.0671	0.9618	0.1052	0.1043	0.9515
Variance	60.6	26.7	7.7	1.8	
Cumulative variance	60.6	87.3	95.0	96.8	

* The characteristics of corresponding regions are listed in Table VI.9 in the same order.

Table VI.10(b): Varimax factor scores for the factors listed in Table VI.10(a)

Element	Varimax factor scores (l_{jr}), Columns = Factors			
	1	2	3	4
Mn	0.6449	-0.1290	0.1606	0.5852
Fe	-0.0601	0.3267	0.8183	-0.4896
Cu	0.7086	-0.0637	-0.1558	-0.6949
Ni	0.6645	-0.0427	-0.0932	-0.5425
Ti	-0.2079	0.1049	0.8426	0.0546
Si	-0.0093	0.7016	-0.1412	-0.1594
Al	0.0273	0.7175	-0.1145	0.2281
Ca	0.1567	-0.1715	0.7972	0.1705
K	0.1350	0.6526	-0.0429	-0.1288

High communality value at each observation point allows the presentation of factor loadings data (Table VI.10(a)) as f_r^2 on a triangular diagram (Figure VI.24). The diagram in Figure VI.24 has been plotted assuming ($\sum f_r^2 = 1$) at each observation point in different morphologies. The sum ($f_3^2 + f_4^2$) has been treated as single variable for following reasons: (i) simplification purpose, so that data can be represented on a triangular diagram and (ii) factor 4 shows significant loadings only for CT/B regions. The similarity in distribution of points in Figure VI.24 and Figure VI.9 needs to be noted. The scatter of points observed in Figures VI.6 and VI.8 disappears in Figure VI.24 because data are recorded from distinct regions and possibility of measurement on phase boundaries was eliminated. To achieve the final goal of correlating internal structure with chemical composition and genesis, the locations of different regions in Figure VI.24 are superimposed with corresponding morphology type, nature of region (bright, grey etc.) and Mn/Fe ratio.

Bright regions (D/B) (Figure VI.13) are characterized with Mn/Fe ratio >10 and these are loaded heavily with diagenetic factor-1 (vide p. 149 for the genetic significance of factors). Grey regions (D/G) and (C/G1) are significantly loaded with hydro-genetic factor-3, and characteristic Mn/Fe ratio varies in the range 1-2. Factors 1 and 3 show intermediate loadings for C/B regions. Higher Mn/Fe ratio for C/B or C/G regions means increasing effect of factor-1. Bright regions in compact type of morphology are most complex. These regions (CT/B) show high loadings for diagenetic factor along with variable loadings for factor 2, 3 and 4. The Mn/Fe ratio is greater than 5 for CT/B regions. Grey regions (CT/G) and

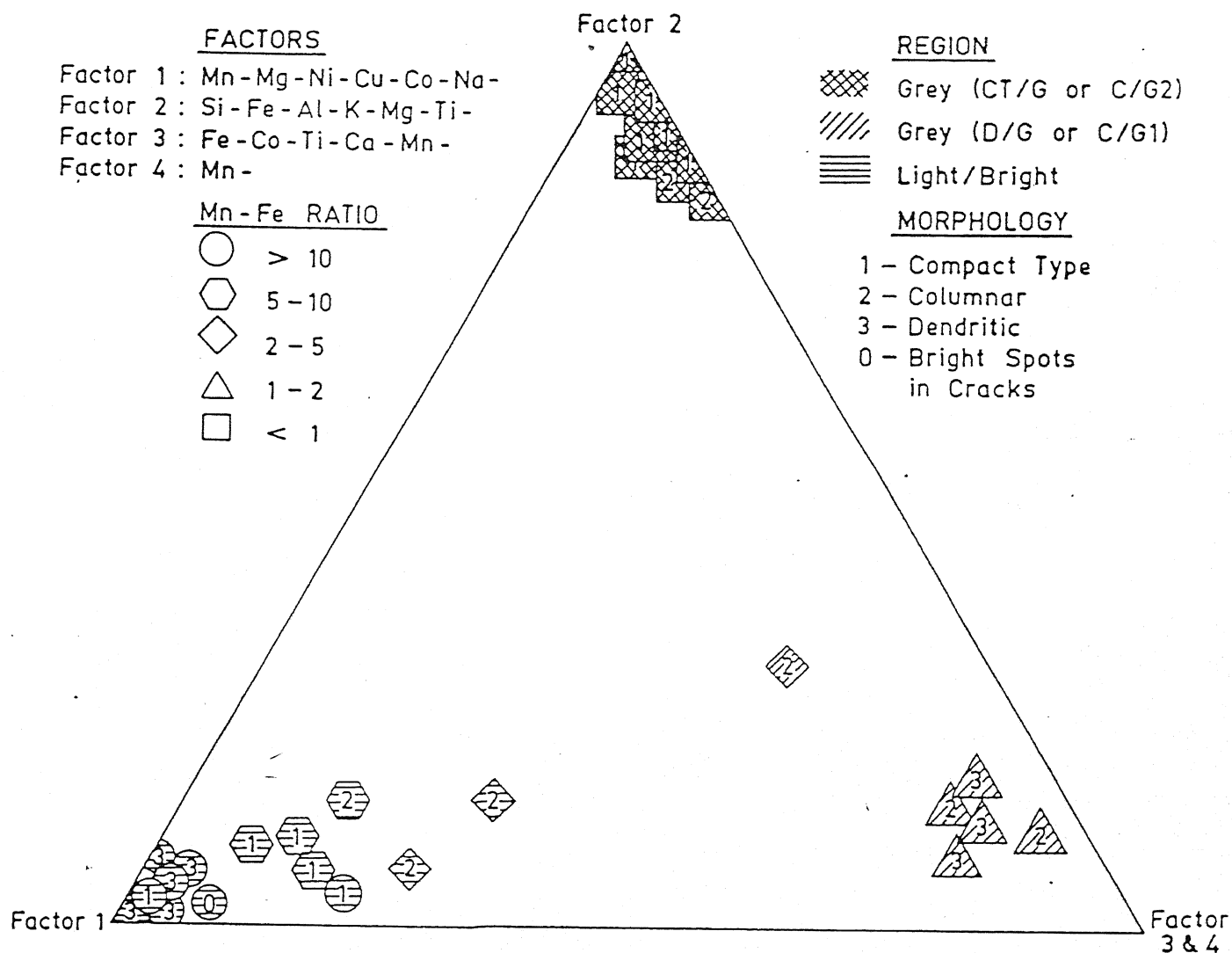


Fig. VI.24. Classification of distinct regions in different morphologies in terms of factor loadings and Mn/Fe ratio.

(C/G2) are characterized by Mn/Fe ratio less than one and very high loadings for Fe rich aluminosilicate factor-3.

6.2.4 Internal Structure, Chemical Composition and Genesis:

The chemical composition of columnar and radial segregation patterns (Table VI.8) present in the laminated growth zones of nodule internal structure is very similar to the one reported in literature (25, 35, 100, 138, 139, 190). These consist of intimate mixture of δ -MnO₂, X-ray amorphous FeOOH.XH₂O (or ferroxhyte) and aluminosilicates (25, 138, 139). The occurrence of ferroxhyte and δ -MnO₂ is consistent with TEM results (Figure V.11). The substance in columnar and radial segregation patterns represent the dominant oxide material in nodules growing on the slope of abyssal hill (i.e. hydrogenetic nodules) (138). So the laminated part of the nodules are built through the precipitation from the sea water (138). Marchig and Halbach (138) suggest that laminated zones must have grown during period of nodule growth history when remobilization from sediment was disturbed e.g. during erosional conditions. Positive correlation of Ni and Cu with Mn/Fe ratio indicate that most of these elements are concentrated in δ -MnO₂ phase. Decreasing Mn/Fe ratio and Ni and Cu content represent increasing influence of hydrogenetic factor (Figures VI.9 and VI.24) as illustrated in BSE micrographs shown in Figure VI.25. Li (214) has explained that enrichment of transition elements in δ -MnO₂ compared to oxyhydroxide of iron and aluminosilicate can be explained on the basis of physico-chemical factors (e.g. surface area, pH_{zpc} or pH_{IEP} , dielectric constant of oxide material and ionic radii of elements) affecting free energy of adsorption ΔG_{ads} . Association of cobalt

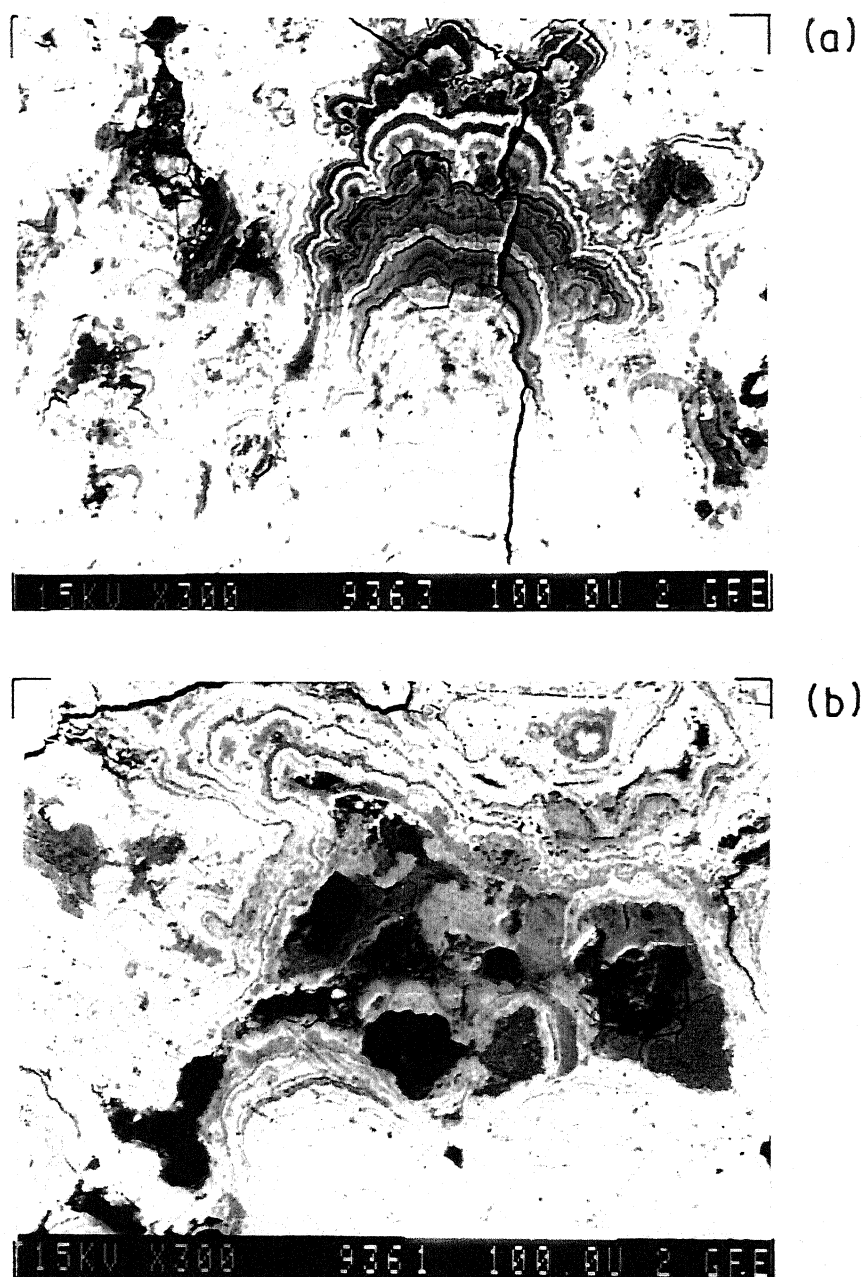


Fig. VI.25. BSE micrographs illustrating increasing influence of hydrogenetic factor .

with Fe (Figure VI.15) indicates that low spin Co^{3+} ($r = 0.53 \text{ \AA}^0$) may substitute for Fe^{3+} ($r = 0.53 \text{ \AA}^0$) in the host phase (27, 101). Halbach et al. (169) have proposed that enrichment of Co in hydrogenetic substance is attributed to specific surface adsorption and subsequent oxidation of Co^{2+} to Co^{3+} in the strong electric field of Si^{4+} . Robust complexes of Co(III) and $\equiv \text{FeH}_2\text{SiO}_4^-$ prevent most of the cobalt from being available for manganese oxide phase. However, no conclusive experimental evidence is available regarding substitution of Co^{3+} for Fe^{3+} .

Bright diagenetic substance (D/B) is richest in Mn, Ni, Cu and Mg. The XRD pattern in Figure V.1(b), which was recorded from material contained in the periphery of a nodule corresponds to the material rich in diagenetic substance. The most likely phase present in diagenetic substance is todorokite (vide Section 5.1 and ref. 25, 26, 33, 100, 138). Elements like Ni, Cu and Mg are essential for the stability of this phase (20, 101, 114). Possible mode of occurrence of Ni, Cu, Mg etc. in the structure of todorokite have been discussed by Burns et al. (p. 42, (20, 85)). Essential conditions for the formation of todorokite are critical Eh and pH of sediment column (25). Under the conditions in which Mn^{2+} , Ni^{2+} and Cu^{2+} are mobilized in sediment column, the solubility of iron is scarce (25). Homogeneity of diagenetic substance suggests that its growth rate has been faster compared to hydrogenetic substance (100).

From the genetic point of view, compact type of morphology is very complex as indicated by the factor loadings. High loadings of factor 2, 3 and 4 for CT/B regions indicate multimineralic nature of these regions. Grey regions are highly loaded with factor-2

(iron rich silicate material). The diffuse boundary between light (CT/B) and grey (CT/G) regions in the BSE micrograph of Figure VI.26 indicates the following: (i) authigenic origin of CT/G and CT/B regions and (ii) role of silica in the fractionation of Mn and Fe in CT/B and CT/G regions respectively.

The micrographs in Figures VI.13(c) and VI.26 provide direct microstructural support to the contention of Lyle et al. (26, 171) that biological silica plays a role in the separation of manganese and iron in manganese nodules. Giovanoli et al. (297) point out that amorphous silica and co-precipitating ferric oxide hinder the nucleation of buserite which results in the fractionation of mixture of Z-disordered buserite, ferric hydroxide and silica from well ordered buserite. Burns and Burns (18) have suggested that when both iron and manganese are available for incorporation into forming ferromanganese oxides, epitaxial intergrowth of $\delta\text{-MnO}_2$ with $\text{FeOOH} \cdot \text{XH}_2\text{O}$ may occur which inhibit the formation of other manganese minerals; by contrast when iron is removed from the system by reaction with something else, silica for example, epitaxial intergrowth would not occur and other manganese minerals such as todorokite and birnessite would be able to form (18). The overlying water in Central Indian basin lies in the region of high biological productivity and siliceous ooze are accumulating below CCD (calcium compensation depth) (37). According to Wyrteki (298), dissolved oxygen level in the bottom water of Central Indian basin is lower than in the other major basins of this ocean. Dissolved oxygen level, while not being the sole influence on redox potential, may be leading to a potential in bottom waters, low enough to cause abundant todorokite formation.

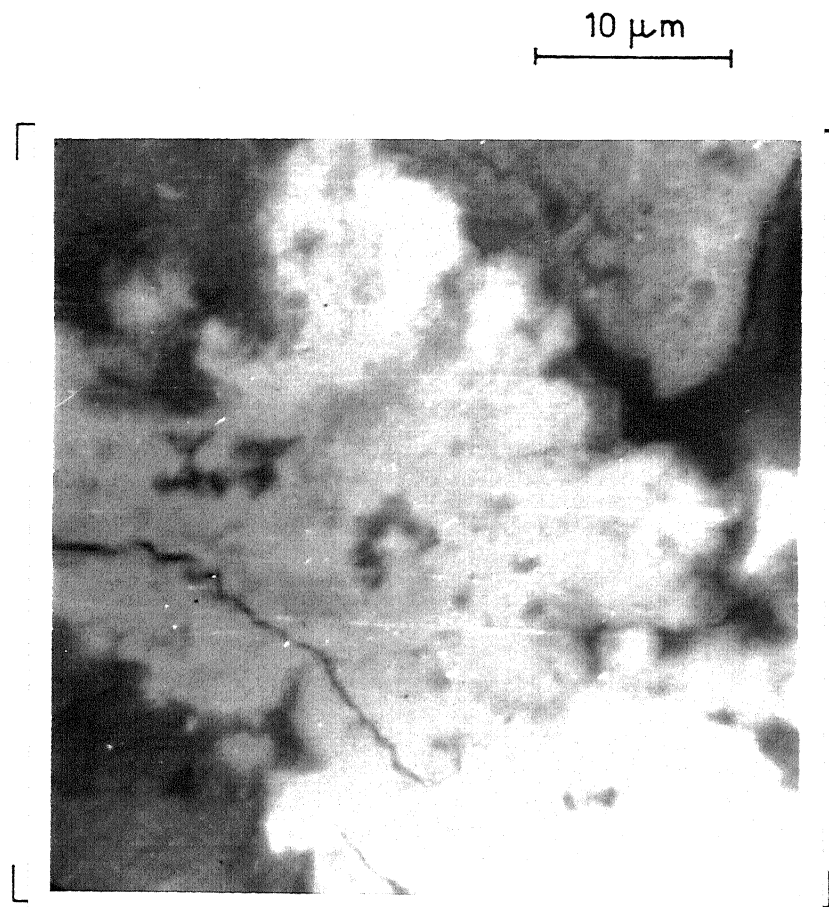


Fig. VI.26. BSE micrograph illustrating diffuse boundary between bright region (CT/B) and grey region (CT/G) in compact type of morphology.

The formation of substance in compact type of morphology perhaps corresponds to the period of very high biological productivity. This will result in dual effects (i) excessive population of sinking siliceous ooze and (ii) high organic carbon content in sediment, which will lead to highly reducing environment. Excessive concentration of siliceous ooze will favour the removal of iron as iron silicate on one hand. On the other hand highly reducing atmosphere in the sediment will result in excessive mobilization of manganese. This will create a situation favourable to the formation of buserite/birnessite (25, 26). Excessive mobilization of manganese causes unfavourable situation for the incorporation of Ni and Cu. This result in factor-4 which is based upon positive factor score of Mn and negative scores for Ni, Cu etc. The XRD pattern reported in Figure V.1(C), corresponds to the nodule core material predominantly consisting of compact type of morphology. The chemical and genetic characteristics of nodule core material further suggests (refer to earlier discussion, p. 96) that it might be disordered buserite or buserite-todorokite assemblage.

The light region (CT/B) may contain birnessite/buserite of varying degree of crystallinity depending on the extent of iron removal and mobilization of manganese (25). Negative correlation of Ni and Cu with Mn/Fe ratio in CT/B regions suggest that increasing Mn/Fe ratio will mean an increase in the amount of birnessite. Ni and Cu are expected to be present deep inside the structure of birnessite rather than randomly adsorbed on the surface (80). The association of Co with Mn in compact kind of morphology (Figure VI.20) is against Halbach et al. (169) contention that Co^{3+} forms robust complexes with $\equiv \text{FeH}_2\text{SiO}_4^-$. It is more likely that removal

of iron by silica creates a situation in which cobalt enrichment in manganese oxide fraction may be favoured. Co^{3+} ($r = 0.53 \text{ \AA}^0$) may substitute for Mn^{4+} ($r = 0.54 \text{ \AA}^0$) in the structure (27, 80).

Summing Up:

The SEM/EDAX elemental correlations e.g. positive correlation of Ni, Cu and Mg with Mn, Ti with Fe, Co with Fe or Mn, Si with Al, which have been determined for the nodule studied (Central Indian basin), are very similar to the normally observed correlations. The correlations derived from X-ray microanalysis data compare well with the correlations observed from bulk analysis i.e. the coherent chemical variation on regional scale seems to persist down to microlevel in a single nodule. The elemental correlations are generally corroborated by metal partitioning results in sequential extraction.

Three distinct kinds of textural growth patterns viz. dendritic segregation, columnar and radial pattern and compact type of morphology have been identified and characterized completely in terms of elemental associations, phase constituents and genesis. The material in dendritic segregation consists of diagenetic substance (D/B) which is distinctly separated from (D/G) intimate association of ($\text{FeOOH} \cdot \text{XH}_2\text{O} + \delta\text{-MnO}_2$) and aluminosilicates (Figure VI.13(b)). The diagenetic substance most enriched in Mn-Ni-Cu-Mg is single phase (10 \AA^0 -phase/todorokite) material. Columnar and radial patterns which are built up of hydrogenetic substance ($\delta\text{-MnO}_2 + \text{FeOOH} \cdot \text{XH}_2\text{O}$, aluminosilicates) are characterized by elemental association Fe-Ti-Ca-K-Co-Mn-. Diagenetic factor shows variable influence on hydrogenetic factor. This is reflected by

increase in Mn/Fe ratio and positive correlation of Ni and Cu with Mn. Co is associated with Fe in hydrogenetic substance. The material in compact kind of morphology (Fe rich material embedded in Mn rich 10 A⁰-phase matrix) which constitute mainly the core material might have formed under highly reducing environment. The 10 A⁰-phase in this morphology which show variable composition, Mn-enrichment, negative correlation with Mn/Fe ratio may be todorokite-buserite assemblage. Co is associated with Mn in compact kind of morphology.

Compact kind of morphology provides direct microstructural evidence regarding role of biological silica in the fractionation of manganese and iron in manganese nodules.

CHAPTER - VII

PHYSICO-CHEMICAL NATURE AND LEACHING BEHAVIOUR OF PURE AND Ni, Co AND Cu BEARING MANGANESE(IV) OXYHYDROXIDES

The characterization and leaching studies on pure and doped oxyhydroxide phases form an extension of manganese nodule characterization work. The idea has been to study the dissolution of the host and doped elements from the synthetic samples vis-a-vis their physical characteristics, including the method of doping. The scope of this chapter encompasses structure and leachability aspects of pure and doped manganese oxyhydroxide minerals namely birnessite and $\delta\text{-MnO}_2$. The structural relationship between birnessite ($T(2,\infty)$ structure) and other manganese minerals, viz. buserite ($T(3,\infty)$ and todorokite ($T(3,n)$, $n = 1, 2, \dots$) was noted earlier (Table II.4). $\delta\text{-MnO}_2$ is a randomly stacked variety of birnessite. Since birnessite and $\delta\text{-MnO}_2$ represent the same basic phase, it makes the clubbing together and comparison between these two phases possible.

The contents of this chapter are sub-divided in two sections; the results of samples characterization are presented and discussed in section one and leaching studies are covered in section two. A sub-section which contain general considerations and brief review related to leaching of pure and doped oxides is included as a prelude in the second section.

The samples were characterized in terms of chemical composition, specific surface area, phase constituents, structure, crystallinity and morphology of particles. The details of synthesis methods and characterization techniques, namely analytical methods, surface area estimation, X-ray diffraction (original and samples

intercalated with dodecylammonium chloride) and transmission electron microscopy have been covered in Chapter-IV. The leaching media employed were sulfuric acid and sulfurous acid (vide Section 4.3 for details of leaching conditions employed).

The mineral birnessite was doped with Ni, Co and Cu in ion exchange and coprecipitation mode. $\delta\text{-MnO}_2$ was doped in sorption mode. Mode of doping refers to method of doping and not occurrence of doped element. Ion exchange* and sorption* refer to interaction of solid phase with the solution of respective metal nitrate at pH 3.5-5.2 and pH 8.2 respectively. Coprecipitation is incorporation of doped element during synthesis of parent buserite used for the preparation of respective birnessite (vide Section 4.1.2).

7.1 Characterization of Samples

7.1.1 Chemical Composition and Surface Area:

The chemical composition and specific surface area data in Table VII.1 are presented on weight basis of samples dried at 120°C and equilibrated over CaCl_2 in vacuum to get the constant weight. The chemical composition of B-O and V-O show reasonable match with the compositions reported in literature (Table VII.1) (93, 107, 122). The differences in compositions are mainly attributed to different washing and drying procedures adopted (299) (e.g. samples were dried over P_2O_5 in vacuum by Giovanoli et al. (107)). Chemical composition data for the similar doped samples are not available in literature for comparison.

* Vide Appendix-L for a brief critical review on the interaction of hydrous manganese oxides with Ni, Co and Cu in solution.

Table VII.1: Chemical composition and specific surface area (SA) of samples

S. No.	Sample description	Chemical composition, wt %					x or (Mn/O)	Mole ratio**		SA (m ² /g)	
		Mn _T	Mn(II)	R	Na	K		Y	z	-210+149 μm	-63+53 μm
1	B-O	53.1* (52.5)	9.0	-	5.7 (6.4)	-	10.9 (10.0)	5.88	0.257	25.8	32.4
2	B-Ni(C)	51.0	6.6	2.71	8.3	-	6.5	5.62	0.384	35.0	35.1
3	B-Co(C)	52.0	6.1	2.74	8.2	-	5.0	6.00	0.378	25.8	38.6
4	B-Cu(C)	49.8	6.0	2.90	8.0	-	8.5	5.85	0.380	24.8	48.5
5	B-Ni(I)	50.5	9.0	10.6	0.24	-	8.9	2.69	0.011	45.1	59.0
6	B-Co(I)	42.6	-0.6 ≥2.56 [⊕]	16.7	0.29	-	11.1	≤2.73	0.016	30.8	47.8
7	B-Cu(I)	44.7	2.8	15.4	0.28	-	10.4	2.77	0.015	30.6	55.2
8	V-O	48.5* (47.7)	<1.0	-	-	9.0 (9.0)	11.0	-	0.262	-	149
9	V-Ni(S)	48.5	<1.0	1.27	-	7.5	11.2	-	0.218	-	138
10	V-Co(S)	48.5	<1.0	1.27	-	7.8	10.7	-	0.226	-	138
11	V-Cu(S)	48.5	<1.0	1.32	-	7.5	11.1	-	0.218	-	138

* Values reported in literature (93, 107, 122) ** $y = \frac{[Mn_T]}{([Mn(II)] + [R])}$, $z = \frac{[K]}{[Na]}$ or $\frac{[K]}{[Mn_T]}$
[⊕] Calculated refer text. [] - Means moles.

The samples in different subcategories namely coprecipitation, ion exchange and sorption show similar and distinct compositional features viz. similar mole ratio 'y' and 'z' (vide Table VII.1). Wide variation in water content of different samples needs to be noted. B-R(I) samples contain more water compared to B-R(C).

The sample B-Co(I) exhibits a (O/Mn) ratio ≈ 2 , indicating presence of total manganese in +(IV) oxidation state. Leaching results for this sample (discussed later) have shown that at least 2.56% manganese is present in +(II) oxidation state. Taking this fact into account, the (O/Mn) ratio in this sample turns out to be 1.94 or less. The discrepancy between the observed and calculated oxidation state arises probably due to partial oxidation of Co(II) to Co(III) during synthesis. Co(III) present in the sample consumes excess amount of oxalate and in turn results in apparent increase in (O/Mn) ratio (60). Our contention regarding occurrence of Co(III) is supported by XPS data of Crowther et al. (300) for cobalt doped in Na-birnessite in ion exchange mode. Computed weight percent of oxidized cobalt in B-Co(I) sample turns out to be 4.4% or more.

Comparison of doped birnessite compositions with pure birnessite (B-O) (Table VII.1) reveals that incorporation of doped element in birnessite involves exchange with structural Mn(II), Na^+ and Mn(IV) or perhaps Mn(III) in the original birnessite structure [the estimation of (O/Mn) ratio by oxalate method (Section 4.2.1) does not distinguish between Mn(III) and mixture of Mn(IV) and Mn(II)]. The exchange with H^+ was additionally noted during synthesis of metal birnessites in ion exchange mode (vide Section 4.1.2).

The structure of birnessite (or buserite) consists of layers of manganese(IV) ions octahedrally coordinated to oxygen and or hydroxyl ions. The layers have a permanent negative charge caused by vacancies and/or diadochic substitution of Mn(II) or Mn(III) for Mn(IV). Successive interlayers are separated by an interlayer region containing Na^+ , water molecules and Mn(II) ions (107). The doped divalent transition element may occupy the vacant lattice sites in (MnO_6) octahedra, substitute for Mn(II) in (MnO_6) octahedra and/or Mn(II) and Na^+ in the interlayer (27, 80, 282).

Chemical compositions of birnessite samples are presented in percent chemical equivalent (CE_i) (Table VII.2), to elucidate the nature of doped element substitution in birnessite structure. The chemical equivalent fraction of an ion i with valency Z_i is calculated using the following formula

$$(\text{CE}_i) = \left[Z_i \cdot \left(\frac{\text{wt \% } i}{M_i} \right) / \sum (Z_i \cdot \frac{\text{wt \% } i}{M_i}) \right] \times 100$$

In calculating (CE_i) , it is assumed that (i) Mn(III) present in the birnessite structure is equivalent to mixture of Mn(II) and Mn(IV), (ii) exchange with H^+ is not significant and (iii) only Mn(IV), Mn(II), R(II), R(III) and Na^+ are involved in substitution.

The total number of chemical equivalent (i.e. denominator in CE_i calculation) in B-O and doped samples reveal that the correspondence between B-O and doped sample is not 1:1. The total number of equivalent shows upto 6% deviation compared with B-O. Assuming idealized situation in which (i) there is 1:1 correspondence between doped samples and pure birnessite and (ii) vacancies are not involved in exchange, the composition of doped samples are compared with B-O in Table VII.2.

Table VII.2: Chemical equivalent balance in birnessites

Sample description	Σ	Z _i wt % i		CE _i , %					$\Delta_i = (CE_i)_{\text{doped}} - (CE_i)_{\text{B-O}}$				
		M _i		Mn(IV)	Mn(II)	R(II)	R(III)	Na ⁺	Mn(IV)	Mn(II)	R(II)	R(III)	Na ⁺
B-O	3.78			84.8	8.6	0	-	6.5	0	0	0	0	0
B-Ni(C)	3.92			82.3	6.1	2.34	-	9.2	-2.5	-2.5	2.34	-	2.7
B-Co(C)	4.01			83.3	5.5	2.10	-	8.9	-1.5	-3.1	2.10	-	2.4
B-Cu(C)	3.85			82.9	5.7	2.37	-	9.0	-1.9	-2.9	2.37	-	2.5
B-Ni(I)	3.72			81.7	8.6	9.71	-	0.03	-3.1	0.0	9.71	-	-6.47
B-Co(I)	3.66			79.5	2.5	11.4	6.1	0.04	-5.3	-6.1	11.4	6.1	-6.46
B-Cu(I)	3.65			83.5	2.8	13.3	-	0.03	-1.3	-5.8	13.3	-	-6.47

It appears (vide Table VII.2) that Mn(IV) in original birnessite phase may be substituted by divalent Ni, Co and Cu. Ionic radii and crystal field stabilization energy (CFSE) criteria are often invoked to explain the substitution by transition metal ions (63, 69, 301).

The crystal field stabilization is a quantum mechanical effect in which the degenerate d^n metal ion (first transition series elements) orbitals split to different energy levels due to asymmetric nature of d orbitals, in the electric field produced by ligands, and attain higher stability by preferential filling of low energy levels (vide Appendix-M) (63, 69, 302). Depending upon electronic configuration, the splitting of levels influences ionic radius due to variations in the shielding of core electrons. This in turn influences the bond strength (or interaction energy between metal ion and surrounding ligands) and stability of minerals. Crystal field stabilization energies and ionic radii of selected metal ions are listed in Table III.3.

Substitution of Mn(IV) by divalent ions is unlikely because of large difference in ionic radii of Mn(IV) and Ni(II), Co(II) and Cu(II) and loss in CFSE. It is more likely that anomaly, regarding Mn(IV) substitution by divalent metal ions, results due to violation of assumption made e.g. 1:1 correspondence between doped and pure birnessite, role of vacancies etc. Variation in surface area and water content among birnessites (Table VII.1) indicates that incorporation of doped element is indeed accompanied by structural break-up and/or rearrangement. The substitution of Mn(IV) ($r = 0.53 \text{ \AA}^0$, $\text{CFSE} = 393.3 \text{ kJ mol}^{-1}$) by low spin Co(III) ($r = 0.545 \text{ \AA}^0$,

Table VII.3: Crystal field stabilization energies (CFSE) and ionic radii of selected ions in an octahedral field (69, 70, 301)

Ions	Number of 3d electrons	Electronic configuration	Octahedral CFSE (kJ mol ⁻¹)	Ionic radius Å ^o
Mn ⁴⁺	3	t _{2g} ³	393.3	0.53
Mn ³⁺	4	t _{2g} ³ e _g ¹	150.6	0.645
Mn ²⁺	5	t _{2g} ³ e _g ²	0	0.83
Co ³⁺	6	t _{2g} ⁶	533.5	0.545*
Co ²⁺	7	t _{2g} ⁵ e _g ²	92.9	0.745
Ni ²⁺	8	t _{2g} ⁶ e _g ²	122.2	0.69
Cu ²⁺	9	t _{1g} ⁶ e _g ³	90.4	0.73

* Low spin configuration.

CFSE = 533.5 kJ mol⁻¹) is suggested by gain in CFSE and similar ionic radii. This also explains the very large difference in CE_{Mn(IV)} value between B-O and B-Co(I) (Table VII.2).

Other things being equal, there will be gain in CFSE due to substitution of Mn(II) by Ni(II), Co(II) and Cu(II). Chemical composition data in Tables VII.1 and VII.2 strongly suggest the substitution of Mn(II) by divalent doped elements in B-R(C). It is striking to note that doping in B-R(C) samples is associated with higher uptake of Na⁺. It is proposed that incorporation of doped element in coprecipitation mode is associated with filling up of more sites in (MnO₆) octahedra, resulting in a more negative charge on (MnO₆) octahedra sheets and in turn higher uptake of Na⁺.

Substitution of cobalt in B-Co(I) can be almost completely explained in terms of exchange with Na^+ , Mn(II) and Mn(IV). Also there is a good match between equivalent of Cu(II) incorporated in B-Cu(I) and Mn(II) and Na^+ replaced (Table VII.2). Nickel in B-Ni(I) substitutes for Na^+ . It is striking to note that against the background of CFSE, Mn(II) is not substituted by Ni(II) in B-Ni(I). It appears that in B-Ni(I) sample, where the (MnO_6) sheet structure is already built before ion exchange, the effect of gain in CFSE is offset by large discrepancy between ionic radii of Mn(II) (0.83 \AA) and Ni(II) (0.69 \AA). This is in contrast with B-Ni(C), where Ni(II) can occupy all those sites which are amenable to Mn(II) substitution in the growing busserite phase.

The sorption of Ni, Co and Cu on V-O can be explained in terms of exchange with K^+ . Sorption of Ni, Co and Cu on $\delta\text{-MnO}_2$ results in almost complete removal of metal ions from solution phase. The change in surface area of $\delta\text{-MnO}_2$ after sorption (which is an indication of structural rearrangement during sorption) need to be noted (Table VII.1).

7.1.2 Phase Constituents, Structure and Crystallinity:

X-ray Diffraction: XRD patterns of busserite (Bu) and respective birnessite samples (before and after intercalation) are presented in Figure VII.1-4. XRD patterns of busserites are included because structure of birnessites are expected to be governed by the parent busserites used for synthesis.

Bu-R(I) samples show marked decrease in the 10 \AA basal spacing, observed in Bu-O (Figure VII.1(a)), to a lower value of 9.6 \AA (Figure VII.1(e), (f) and (g)). These samples are also

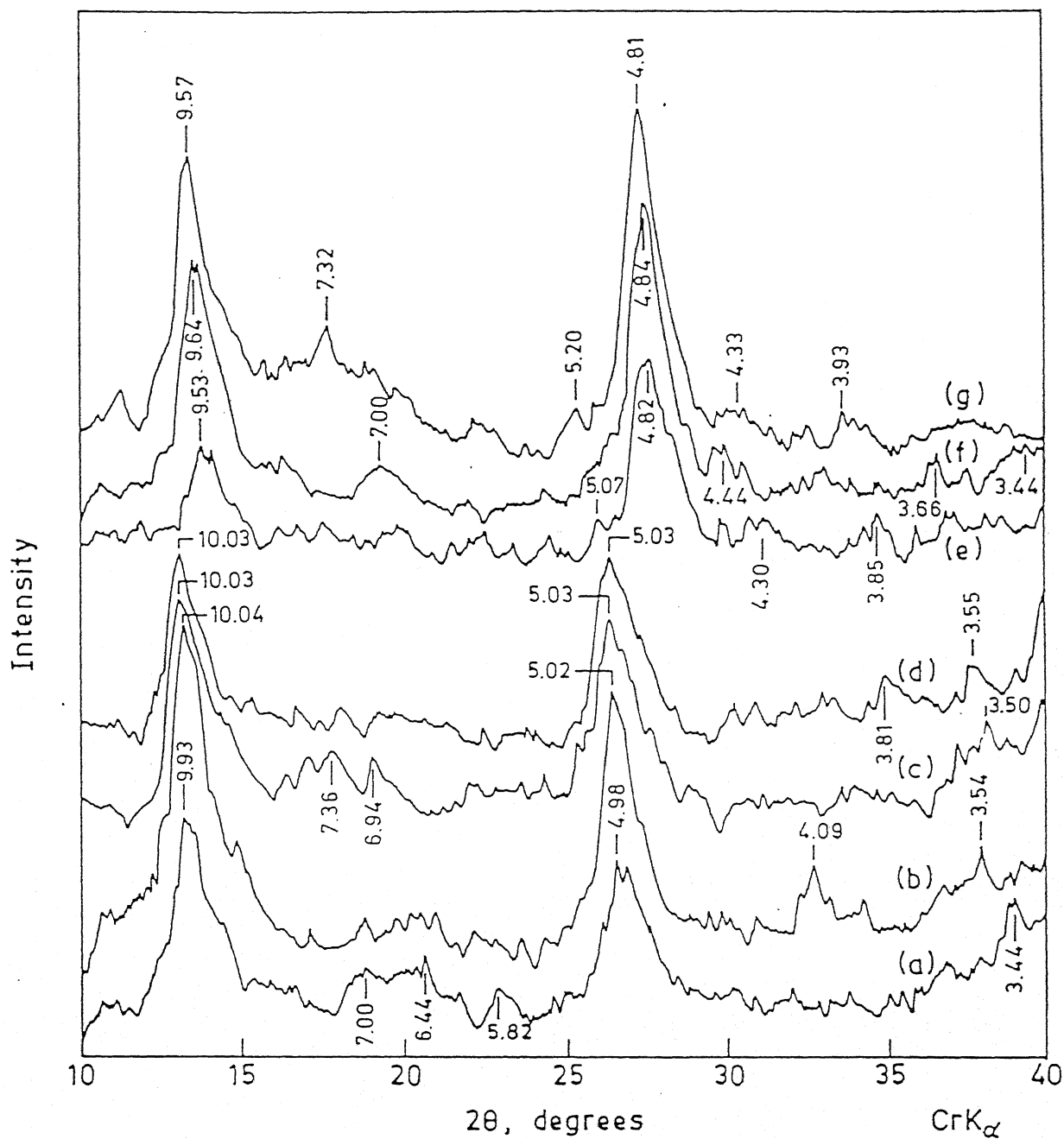


Fig. VII.1. XRD patterns of buserites (a) Bu-O, (b) Bu-Ni(C), (c) Bu-Co(C), (d) Bu-Cu(C), (e) Bu-Ni(I), (f) Bu-Co(I) and (g) Bu-Cu(I).

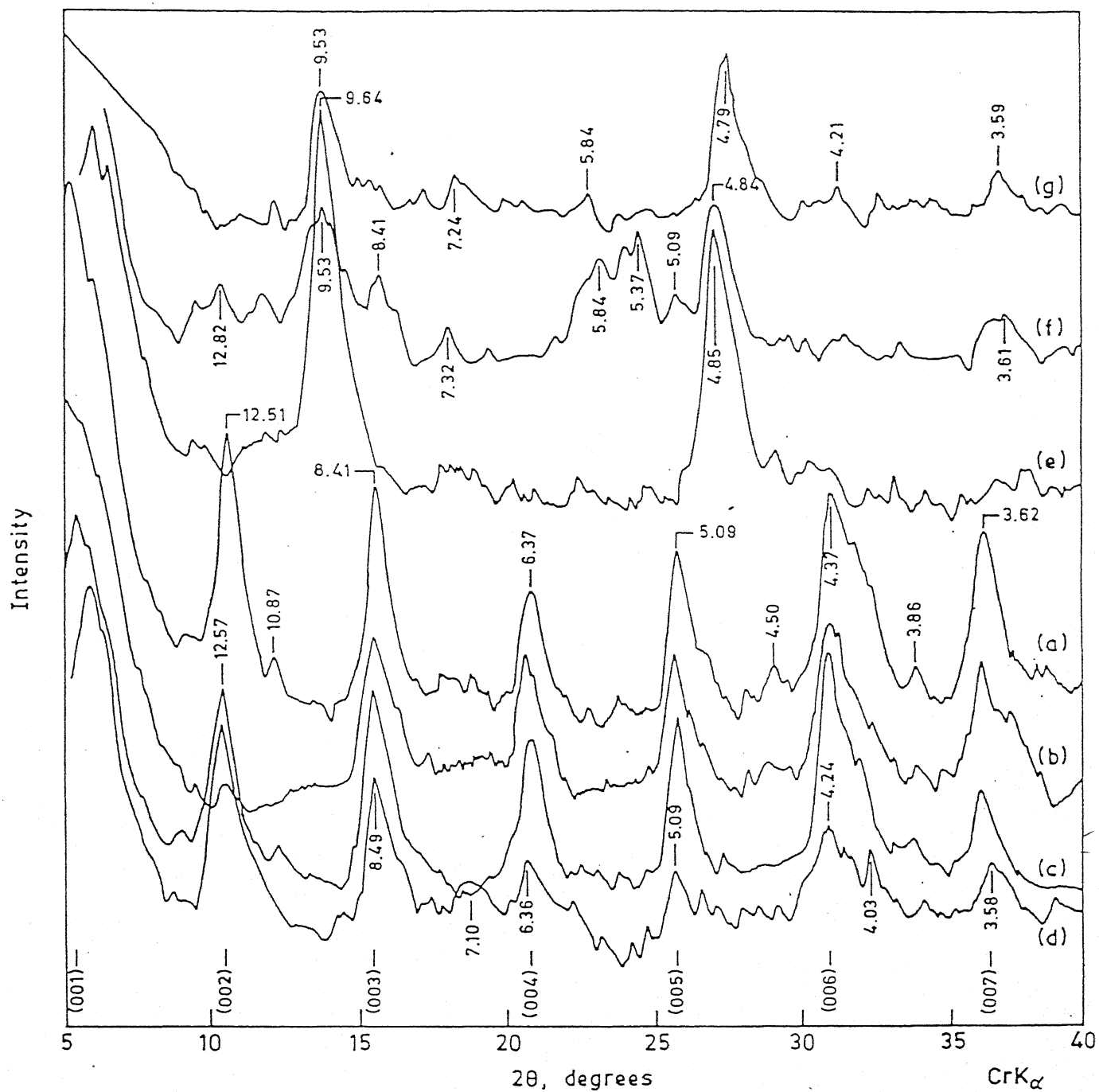


Fig. VII.2. XRD patterns of buserites (Bu) intercalated with dodecylammonium chloride (a) Bu-O, (b) Bu-Ni(C), (c) Bu-Co(C), (d) Bu-Cu(C), (e) Bu-Ni(I), (f) Bu-Co(I) and (g) Bu-Cu(I).

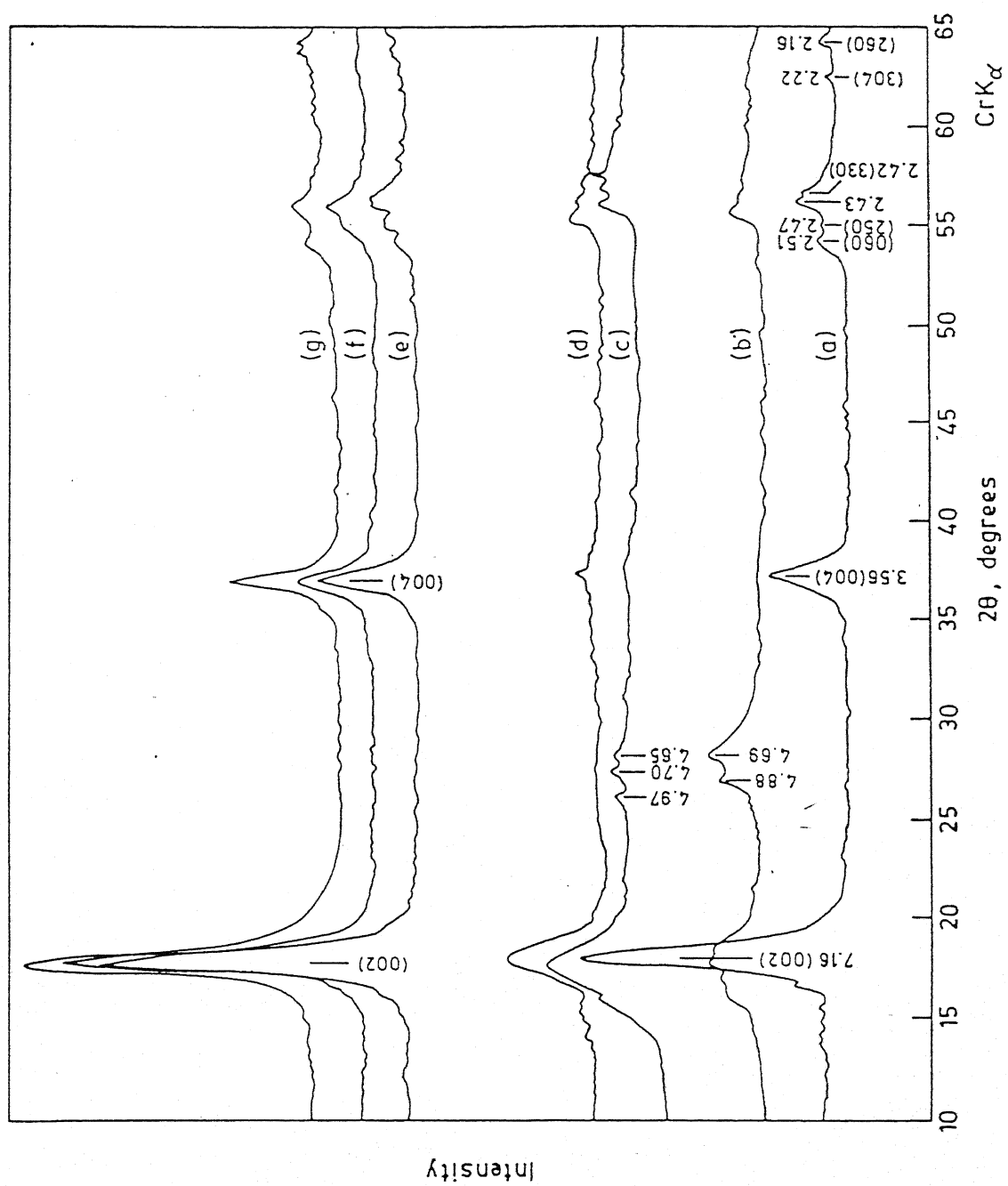


Fig. VII.3. XRD patterns of birnessite samples (a) B-O, (b) B-Ni(I), (c) B-Co(I), (d) B-Cu(I), (e) B-Ni(C), (f) B-Co(C) and (g) B-Cu(C).

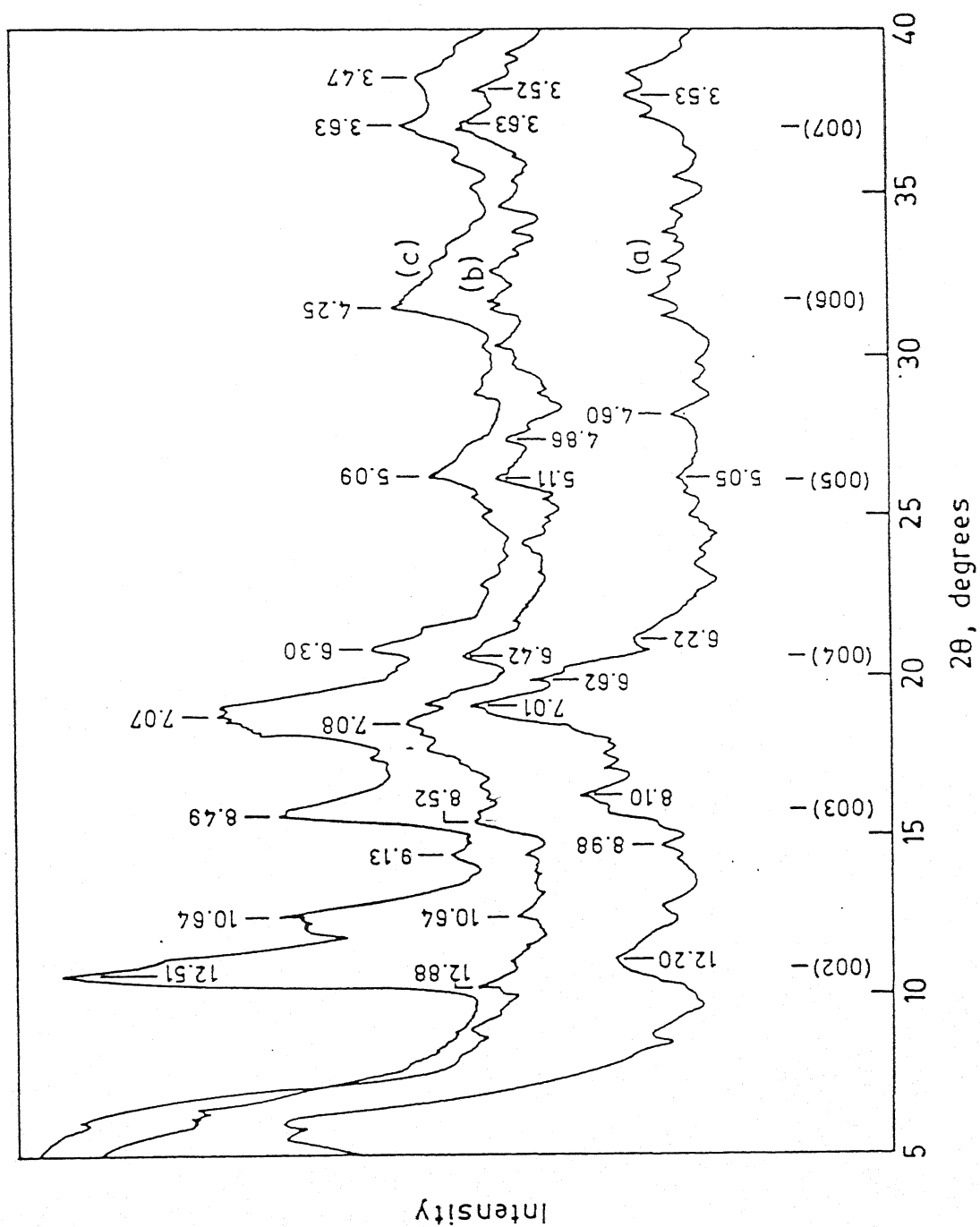


Fig. VII.4. XRD patterns of birnessites (B-R(C)) intercalated with dodecylammonium chloride (a) B-Ni(C), (b) B-Co(C) and (c) B-Cu(C).

characterized by negative (for Bu-Ni(I) and Bu-Cu(I), Figure VII.2(e), (g)) and poor (for Bu-Co(I), Figure VII.2(f)) response to intercalation by dodecylammonium chloride. The position of the 10 \AA^0 line remains the same for the samples belonging to Bu-R(C) category (Figure VII.1(b), (c), (d)) which respond positively to intercalation treatment (Figure VII.2(b), (c), (d)). Thus, XRD results indicate that incorporation of Ni, Co and Cu in ion exchange mode causes more severe structural changes as compared with coprecipitation mode. As compared to Bu-R(C) samples (simple layered structure), Bu-R(I) samples might have more complex structure (e.g. highly disordered layer, hybrid layer or tunnel structure), as indicated by intercalation-XRD results (Figure VII.2).

XRD pattern of B-O in Figure VII.3(a) corresponds to Na-birnessite ($\text{Na}_2\text{Mn}_{13}\text{O}_{27} \cdot 9\text{H}_2\text{O}$) (ASTM 23-1046). The doped samples contain the 7 \AA^0 line which is characteristic of birnessite (Figure VII.3). Additional lines appear between $4.5\text{--}5.0 \text{ \AA}^0$ for B-Ni(I) and B-Co(I) samples. These lines may be attributed to incomplete conversion during buserite to birnessite transformation [line at 4.8 (or $(\frac{9.6}{2}) \text{ \AA}^0$ may result due to (002) reflection of disordered buserite (Figure VII.1(e), (f))] and/or formation of new phases. The line at 4.8 \AA^0 also corresponds to the (002) reflection in todorokite (ASTM 13-164). X-ray data are inadequate to elucidate this point any further.

Positive response of B-R(C) samples to intercalation treatment (Figure VII.4) highlights the relationship between birnessites and parent buserite (Bu-R(C)) structures (Figures VII.1 and VII.2). B-R(I) samples also have complex structures similar to Bu-R(I) (282). Negative and poor response of Bu-Ni(I) and Bu-Co(I) samples

respectively to intercalation, coupled with appearance of extra line, between $4.5\text{-}5.0\text{ \AA}^{\circ}$ (Figure VII.3), indicate the possibility of the formation of new phases during ion exchange. Paterson et al. (282) have attributed the varying intercalation response of phyllo-manganates (Bu-R(I), B-R(I)) to the element doped. The intercalation-XRD results on Bu-R(C) and Bu-R(I) indicate that it may not be the element doped but the structure, which determines the response to intercalation. Typically it may be noted that B-Ni(C) responds to intercalation and B-Ni(I) does not.

Fewer number of lines observed in doped samples as compared to B-O (Figure VII.3) means that there is a decrease in the crystallinity of samples after doping. B-R(C) and B-R(I) samples show distinct behaviour with respect to line broadening for the 7 \AA° line (002 reflection). There is no line broadening for B-R(C) samples as compared with B-O ($\Delta 2\theta \simeq 1^{\circ}$) (Figure VII.3). This implies that there is no structural disorder and/or break-up of crystals in c-direction and line broadening results due to structural disorder and/or break-up in a-, b-directions. Line broadening in B-R(I) samples is quite large and varies in the following order B-Ni(I) (3.5°) > B-Co(I) (2.5°) > B-Cu(I) (1.5°). Surface area is inversely proportional to thickness for the sheet structure minerals. Break-up of crystals in 001 direction results in much higher specific surface area for B-R(I) samples compared to B-R(C). According to Scherrer equation (281), thickness of crystals (MCD_{002} or t_{002}) is inversely proportional to line broadening ($\Delta 2\theta_{002}$) i.e. we should have a linear relationship between line broadening and specific surface area ($SA = \text{const. } t_{002}$). There is no direct relationship between the ratio of line broadening and surface area for B-R(I)

and B-O (Table VII.1). This indicates the discrepancy between the coherently scattering domain size and particle size or structural disorder present in B-R(I) samples.

XRD pattern of pure $\delta\text{-MnO}_2$ sample (V-O) showed three lines at 3.6, 2.4 and 1.4 \AA . The sample synthesized in this investigation is more crystalline in nature (three XRD lines, SA $\sim 150 \text{ m}^2/\text{g}$) as compared to the highly disordered variety (two lines, 2.4 and 1.42 \AA , SA $\sim 300 \text{ m}^2/\text{g}$) reported by Buser and coworkers (92, 122). No new phase formation was detected in doped V-R(S) samples.

Transmission Electron Microscopy: To complement XRD data, TEM studies were carried out to determine the finer structural details and morphology of particles. A substantial number of electron diffraction patterns were recorded from the different samples. Some typical electron micrographs and corresponding SAED patterns are shown in Figure VII.5. Indexing details for the spot and ring patterns are presented in Tables VII.4A and VII.4B. The interplanar angles ϕ_1 and ϕ_2 in Table VII.4 refer to the angle between reciprocal lattice vectors \vec{R}_1 and \vec{R}_2 (corresponding to d_1 and d_2) and \vec{R}_1 and \vec{R}_3 respectively. \vec{R}_3 is diagonal of the parallelogram formed by \vec{R}_1 and \vec{R}_2 (vide p. 83).

The electron micrograph and SAED pattern in Figure VII.5(a)-(d) are typical of large number of particles examined in B-O and B-R(C) samples. The particles showed flake kind of morphology and preferred orientation perpendicular to c-direction (Figure VII.5(a), (c) and Table VII.4A). Streaking in the SAED pattern was a common feature observed for all the samples (Figure VII.5(b), (d)). The structural similarities between the hexagonal birnessite cell

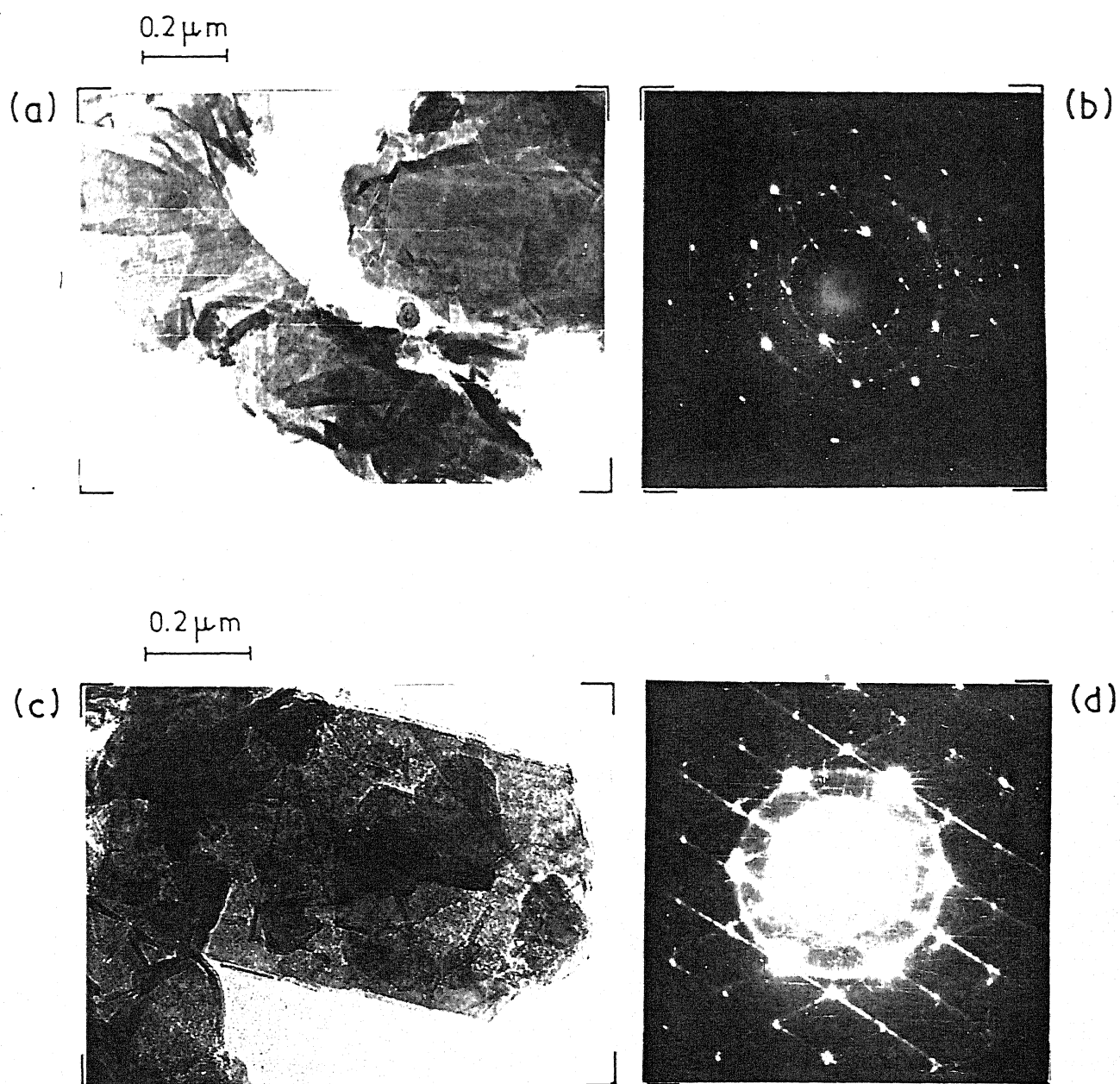


Fig. VII.5. Some typical electron micrographs and SAED patterns from birnessite samples (a), (b) B-O, (c), (d) B-Co(C) (similar features observed for B-Ni(C) and B-Cu(C)).

Contd. ...

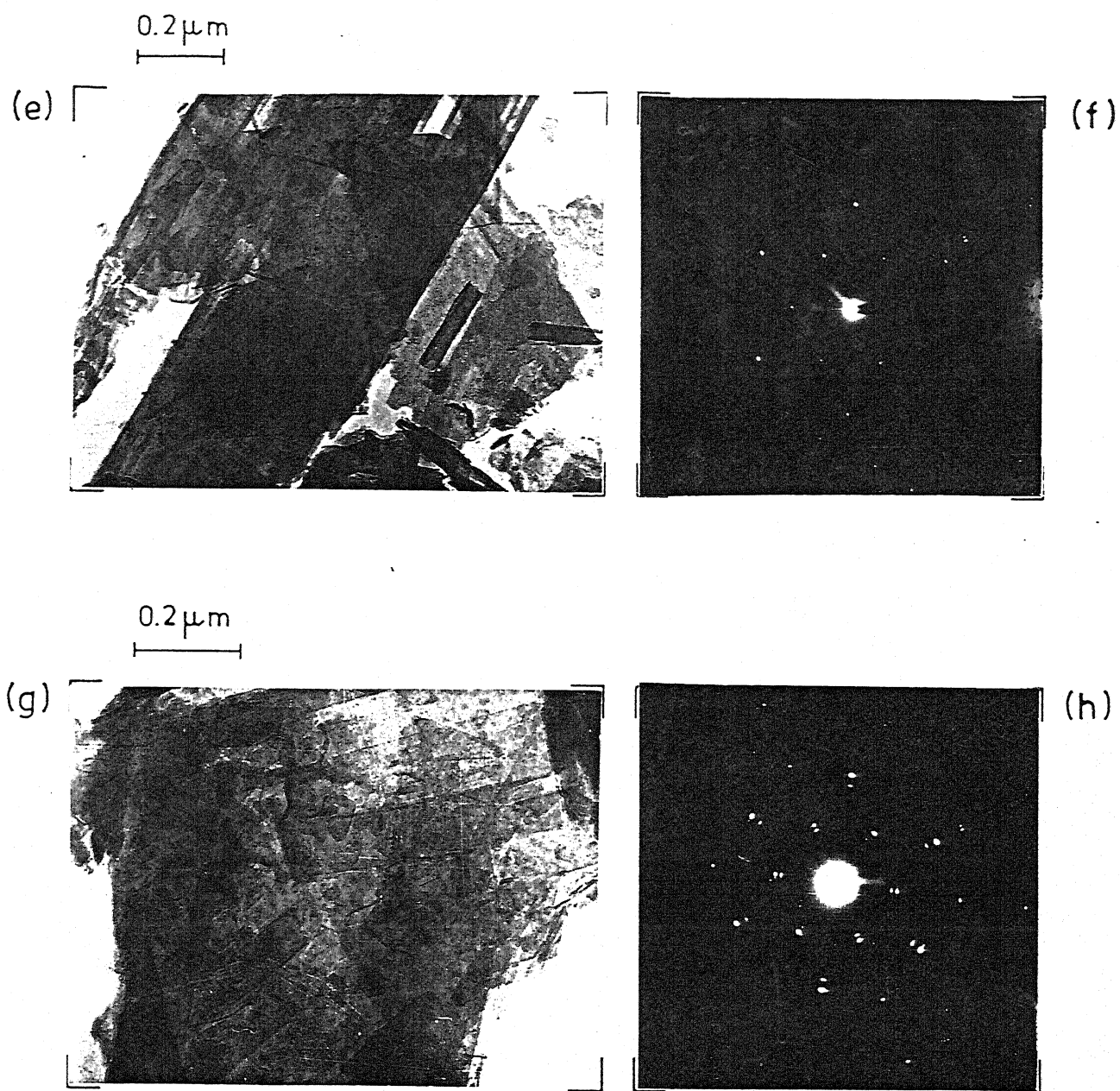


Fig. VII.5. Electron micrographs and SAED patterns (e), (f) B-Ni(I) and (g), (h) B-Co(I).

Table VII.4: Indexing of selected area electron diffraction (SAED) patterns

A. SPOT PATTERNS

Sample description	Experimental						(hkl) _i			Theoretical						Beam direction [HKL]	Possible mineral*	Remark Fig. VII
	d ₁ o _A	d ₂ o _A	d ₃ o _A	φ ₁ deg- rees	φ ₂ deg- rees	φ ₂ deg- rees	i=1	i=2	i=3	d ₁ o _A	d ₂ o _A	d ₃ o _A	φ ₁ deg- rees	φ ₂ deg- rees	φ ₂ deg- rees			
B-O, B-R(C)	2.53	2.57	1.47	61.5	31.0	330	060	390	060	2.49	2.57	1.47	61.0	30.0	001	BO	5(a)-(d)	
B-O, B-R(C)	2.42	2.42	1.45	60.0	30.0	100	010	110	010	2.46	2.46	1.42	60.0	30.0	001	BH	-	
B-O, B-R(C)	2.46	2.51	1.44	58.0	29.0	330	330	600	330	2.49	2.49	1.42	58.1	29.0	001	BO	-	
B-O, B-Ni(C)	4.17	4.11	2.40	60.0	30.0	200	131	331	4.27	4.20	2.45	60.5	30.5	026	BO	-		
B-Co(C)	2.16	2.19	1.27	60.5	30.5	400	260	660	2.14	2.20	1.25	59.0	29.0	001	BO	-		
B-Cu(C)	4.53	4.53	2.57	61.0	30.0	130	130	060	4.40	4.40	2.57	62.0	31.0	001	BO	-		
						200	110	310	4.49	4.55	2.60	59.6	29.6	001	MM	-		
B-Ni(I)	2.44	2.44	1.41	60.0	30.0	210	210	020	2.46	2.46	1.43	60.6	30.3	001	TO	5(e), (f)		
						210	400	610	2.46	2.44	1.41	59.7	30.0	001	TO	-		
						100	010	110	2.46	2.46	1.42	60.0	30.0	001	BH	-		
B-Co(I)	2.42	2.42	1.40	60.0	30.0	100	010	110	2.46	2.46	1.42	60.0	30.0	001	AH	5(g), (h)		
	2.62	2.62	1.52	60.0	30.0	100	010	110	2.63	2.63	1.52	60.0	30.0	001		-		
B-Cu(I)	4.45	4.45	2.59	61.0	30.0	130	130	060	4.40	4.40	2.57	61.9	31.0	001	BO	-		
	2.10	2.10	1.21	59.5	30.0	420	350	730	2.06	2.09	1.19	58.3	28.9	001	BO	-		

B. RING PATTERNS

Sample description	Observed 'd' spacings, Å ^o		Possible mineral
B-O	3.54, <u>2.56</u> ⁺	2.26, 2.46, <u>1.51</u> , <u>1.46</u> , 1.42, 1.26	BO
B-O, B-R(C)	<u>2.56</u> , 2.26, <u>1.52</u>		BO
B-Co(C)	<u>4.90</u> , <u>2.91</u> , <u>2.52</u> , 1.88, <u>1.66</u> , 1.43, 1.07		- **
B-Ni(I)	<u>2.46</u> , <u>1.41</u>		BH, TO
B-Co(I)	<u>2.64</u> , <u>2.46</u> , 2.13, 1.52, <u>1.40</u> , 1.21, 0.892, 0.781		AH
B-Cu(I)	2.44, 2.25, 1.52, 1.41		BO, BH

* BO - Na-birnessite (ASTM 23-1046), BH - Na-free birnessite (ASTM 23-1239, TO - Todorokite (ASTM 13-164))
 AH - Asbolane (77, 84), MM - Manganite (ASTM 18-805)

** Unidentified, observed only once. + Underline means strong reflection.

($a_H = 2.84 \text{ \AA}$, $c_H = 7.27 \text{ \AA}$) and orthorhombic Na-birnessite cell ($a_O = 8.52 \text{ \AA}$, $b_O = 15.39 \text{ \AA}$, $c_O = 14.26 \text{ \AA}$) have been illustrated by Giovanoli et al. (107). The streaking in the SAED patterns result due to topotactic intergrowth of the hexagonal cell with the orthorhombic cell ($a_O = 3 a_H$, $b_O \sim \sqrt{3.3} a_H$, $c_O \sim 2 c_H$) (107). The growth takes place across a crystallographic shear plane. The disorder in the shear plane may cause streaking of diffraction spots while ordering may lead to superstructure reflections in SAED pattern (303). Occurrence of superstructure reflections for Na-birnessite is reported in literature (107). No separate phase of Ni, Co and Cu was detected in any of the doped samples. Unconfirmed rare occurrence of the mineral manganite was detected in sample B-Cu(C). The pattern indexed for manganite can also be indexed for Na-birnessite type structure with slightly large error (3.3%).

The electron micrograph and SAED pattern (Figure VII.5(e), (f)) correspond to a typical particle observed in B-Ni(I). The SAED pattern (Figure VII.5(f)) shows no streaking and can be indexed for both hexagonal cell of layered structure birnessite (or buserite) and orthorhombic cell of tunnel structure todorokite (variable 'a' parameter, multiple of 4.88 \AA (83)). In both the cases the beam-direction is $\langle 001 \rangle$ (Table VII.4). It may be recalled that XRD pattern of B-Ni(I) shows a diffuse line at 7 \AA and additional strong line at 4.8 \AA . Also, the sample is characterized by negative response to intercalation, indicating the absence of simple layer structure. Hence it is proposed that todorokite kind of tunnel structure phases with varying tunnel width may be present in B-Ni(I), if not as a separate phase at least as an artefact in the sheet structure phase.

Giovanoli (22) have used the term 'nucleation' while describing the conversion of birnessite ($T(2,\infty)^*$) to nsutite ($\gamma\text{-MnO}_2$; $T(1,1)$ and $T(1,2)$ structure) on acidification. Mn(IV) has negligible solubility in dilute acid (e.g. HNO_3) and the kinetics of birnessite to nsutite transformation is very fast in acidic solution. Therefore, a nucleation and growth kind of mechanism for the birnessite \rightarrow nsutite transformation does not seem to be likely. Buser (304) has noted that substances which show structurally conditioned defects such as lattice regions with different degree of order, have a pronounced reactivity even at room temperature. The reactivity is related to ionic migration in the interstitial lattice (304). Keeping in view the structural transformations in several systems which involve edge and corner sharing of (MO_6) octahedra (303), it is suggested that the transformation such as the one reported by Giovanoli et al. (22) involves the movement of complete blocks of (MnO_6) octahedra and is greatly facilitated by diffusion of exchangeable divalent cations and structural disorder e.g. stacking fault and vacancies. By analogy with the structural transformation $T(2,\infty) \rightarrow T(1,1)$, $T(1,2)$, the reaction $T(3,\infty) \rightarrow T(3,n)$ ($n = 1, 2, \dots$) seems to be quite likely and may be favoured by the presence of Na^+ , Mn^{2+} , Ni^{2+} and H_2O . Larger tunnels might be stabilized in the presence of water and divalent transition ions like Ni^{2+} .

There are two sets of reflections which occur in the SAED pattern (Figure VII.5(h)) of a typical particle (Figure VII.5(g)) observed in B-Co(I). One set of reflections shows 'd' spacings and interplanar angles similar to B-Ni(I) (Table VII.4A). The other

* Vide Table II.4.

set of reflections ($d_1 = 2.62 \text{ \AA}$, $d_2 = 2.62 \text{ \AA}$, $d_3 = 1.52 \text{ \AA}$ and interplanar angles $\varphi_1 = 60^\circ$, $\varphi_2 = 30^\circ$ (Table VII.4)) could not be indexed for Mn(IV) oxide minerals listed in Table II.4. Chukhrov et al. (77) have reported the occurrence of mixed hybrid layer asbolane minerals with two hexagonal sub-lattices (sub-lattice-I $a = 2.834 \text{ \AA}$, $c = 9.34 \text{ \AA}$; sub-lattice-II $a = 3.04 \text{ \AA}$, $c = 9.34 \text{ \AA}$) consisting of alternate arrangement of (MnO_6) and (CoO_6) octahedral sheets. It is interesting to note that the second set of reflections obtained for B-Co(I) can be indexed for sub-lattice-II, for the same beam direction $\langle 001 \rangle$ as for sub-lattice-I. Presence of sub-lattice-II may explain the presence of the line at $4.67 \text{ (} 9.34/2 \text{)} \text{ \AA}$ in the XRD pattern of B-Co(I). Presence of reflections at $d = 2.64 \text{ \AA}$ and $d = 1.52 \text{ \AA}$ in the ring SAED pattern of particles (Table VII.4B) can only be explained in terms of the second sub-lattice. Thus, SAED features coupled with poor response of B-Co(I) to intercalation treatment suggest that B-Co(I) is likely to have a mixed hybrid layer structure.

All the SAED patterns recorded from B-Cu(I) sample, can be indexed for a Na-birnessite kind of orthorhombic lattice (Table VII.4). The particles show preferred orientation perpendicular to $\langle 001 \rangle$ direction. The B-Cu(I) sample is characterized by broadening of the (002) reflection, absence of lines between $4.5\text{--}5.0 \text{ \AA}$ and negative response to intercalation. The negative intercalation response of this sample may be assumed to be due mainly to stacking disorder in $\langle 001 \rangle$ direction, and not due to formation of a new phase as observed in B-Ni(I) and B-Co(I).

The foregoing discussion on doped birnessite samples shows that doping of Ni, Co and Cu may result in a variety of structural

arrangement and/or disorder in the host phase. Thus, the deviations observed in the chemical equivalent balance (Table VII.2) are quite understandable.

V-O samples yielded two kind of morphologies and SAED patterns (Figure VII.6). The morphology shown in Figure VII.6(a) is typical of $\delta\text{-MnO}_2$ phase (83). The diffraction rings in SAED pattern of Figure VII.6(b) and Figure VII.6(d) correspond to $d \sim 2.4$, 1.4 \AA and $d \sim 3.6$, 2.4 , 1.4 \AA i.e. the $\delta\text{-MnO}_2$ sample may consist of birnessites having varying amount of random stacking of (MnO_6) octahedra sheets (22, 122). No separate phase of Ni, Co and Cu was detected in the doped samples.

7.1.3 Summary of Characterization Studies:

The incorporation of Ni(II), Co(II) and Cu(II) in the host manganese oxide phases may take place via simple exchange reactions involving Mn^{2+} , K^+ , Na^+ and H^+ or exchange reaction with electron transfer step (as observed in this work and by others for Co (300, 301, 305)). The exchange reactions can be partly understood in terms of CFSE and ionic radii of difference ions.

The exchange reactions take place deep inside the bulk phases and are accompanied by structural breakdown, disorder or rearrangement, leading to formation of new phases. Thus, the mineral name birnessite and $\delta\text{-MnO}_2$ can be used only in a broad sense for the doped samples.

Since birnessite and $\delta\text{-MnO}_2$ represent the same basic phase, the doped samples can be mutually compared to elicit the effect of the nature of doping. As revealed by surface area, XRD and TEM data, the doped samples can be arranged in terms of structural

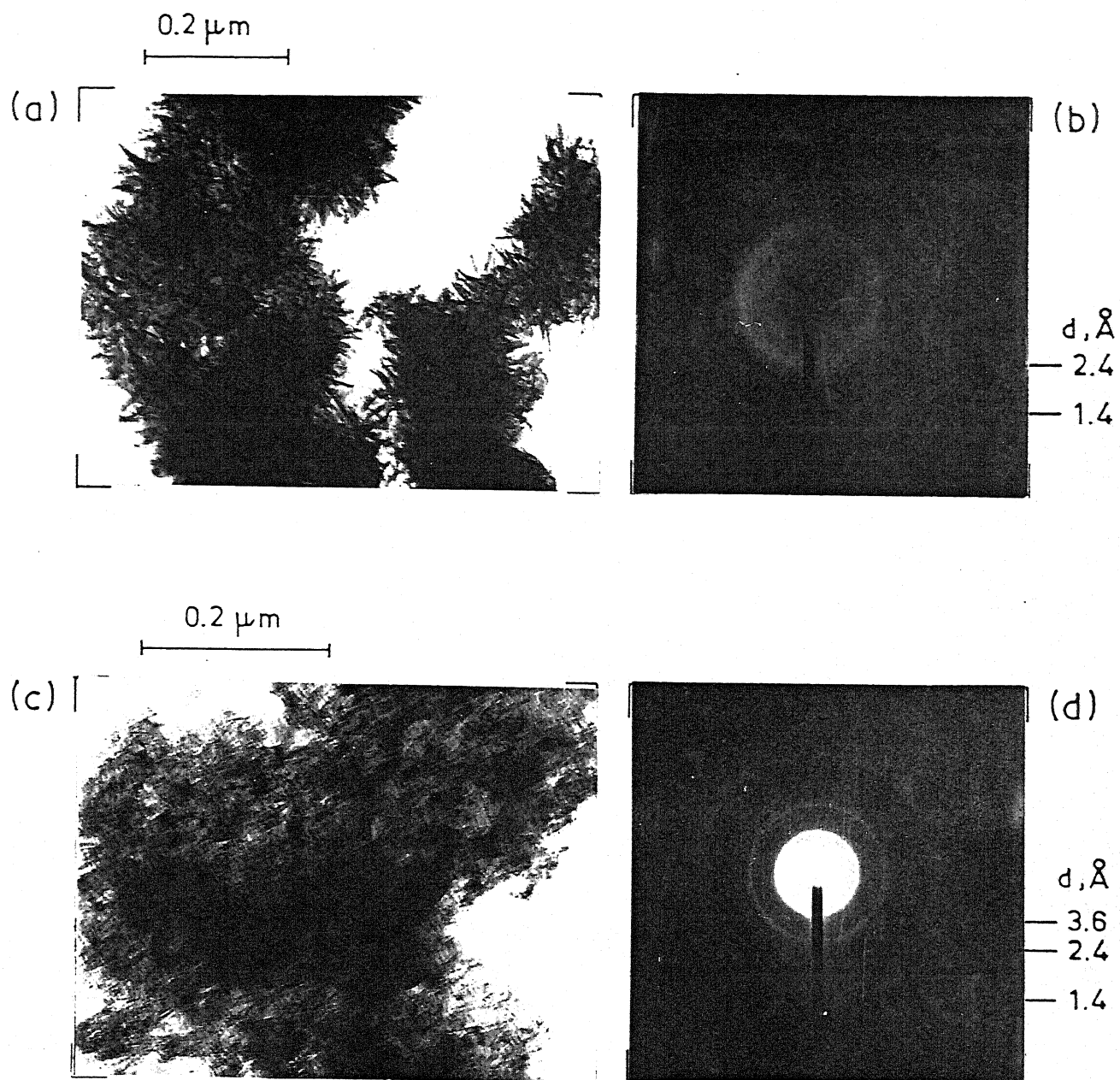


Fig. VII.6. Electron micrographs (a), (c) and corresponding SAED patterns (b), (d) from V-O.

complexities* as follows: sorption > ion exchange > coprecipitation mode.

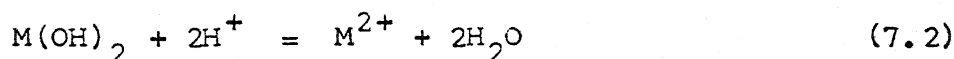
Although synthesis conditions employed in preparing the different samples are far from the conditions that may be actually encountered in natural systems, there are marked structural similarities between the synthetic and natural minerals observed in manganese nodules. The poor crystallinity, large surface area and morphological feature of synthetic V-O and V-R(S) samples are very similar to the δ -MnO₂ phase observed in natural manganese nodules. Synthetic B-O and B-R(C) samples represent those manganese oxyhydroxide phases in manganese nodules which have simple layered structure. Although simple layered structure phase was not observed in the manganese nodule characterized in this investigation, the existence of such a phase has been reported by other workers (112). B-R(I) samples, which responds negatively or poorly to intercalation treatments by dodecylammonium chloride, are analogous to those phases in nodules which have complex structure (e.g. hybrid layer, large stacking and structural disorder etc.) in nodules. The 10 Å⁰ phases observed in the nodules investigated fall in this category (vide Figure V.2). As in the case of natural manganese nodules, no separate phase of Ni, Co and Cu is observed in any of the synthetic phases. Thus the term 'synthetic structural analog of natural phases' is justified to describe the synthetic samples.

* Structural complexities are defined in terms of crystallinity, surface area, intercalation response and complexities observed in electron micrographs and corresponding SAED patterns.

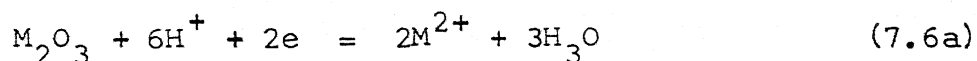
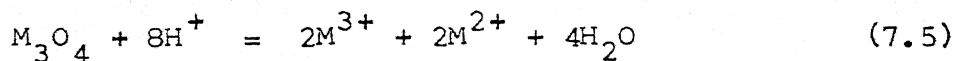
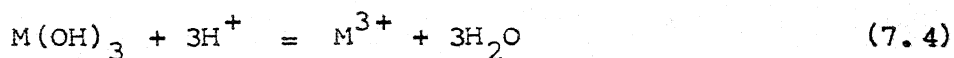
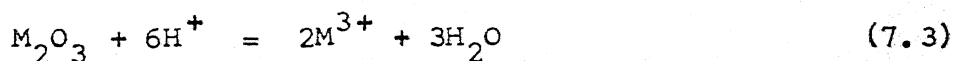
7.2 Leaching Studies

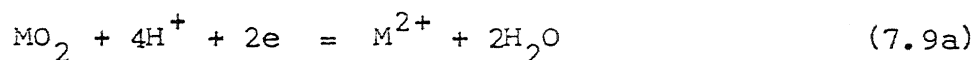
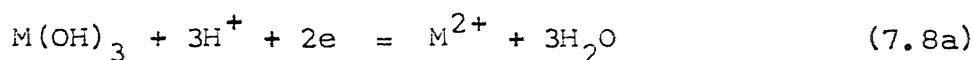
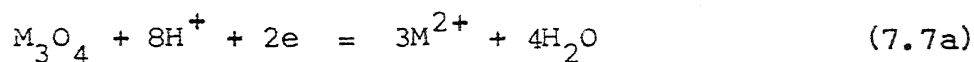
7.2.1 General Considerations and Review:

There have been several attempts to study the dissolution behaviour of pure oxide/hydroxide of Ni, Co, Cu and Mn in acids including sulfurous acid (237, 306-317). However, literature regarding leaching of elements from doped oxyhydroxide of manganese is somewhat scanty. Prosser (260) has studied the effect of mineralogical factors on dissolution of minerals in general. Terry (318) and Hiskey and Wadsworth (319) have reviewed the mechanisms of oxides dissolution in acids. Ions on the surfaces of a crystal, such as cleavage faces, show more susceptibility to removal in solution because of large number of broken bonds. The chemical reaction of oxides/hydroxides with sulfuric acid involves dissociation reactions for sulfuric acid and dissolution reaction. The general dissolution reactions for divalent oxides/hydroxides in acid (e.g. H_2SO_4 , HNO_3) can be written as follows:

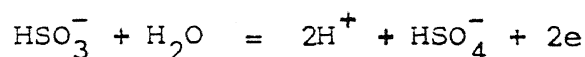


and for higher valency oxides,



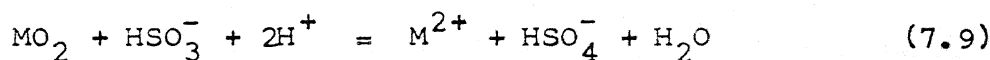
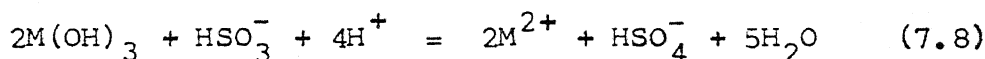
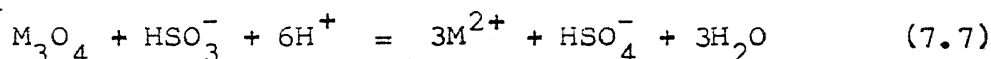
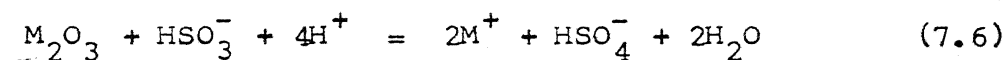


Reactions (7.6a)-(7.9a) are cathodic half cell reactions for dissolution of higher valency oxides/hydroxides and will not be feasible in sulfuric acid which is an oxidizing agent. However, these reactions can be completed in sulfurous acid (reducing) through anodic half cell reaction such as:



(HSO_3^- and $\text{SO}_2(\text{aq})$ are dominant species in acidic solution (317)).

The overall dissolution reaction in sulfurous acid may be written as:



Free energy change ($\Delta G_{r,298}^\circ$) for reactions (7.1)-(7.9) are tabulated in Table VII.5. Reactions such as (7.3)-(7.5) are of little significance because higher valency ions like Co^{3+} and Mn^{4+} have negligible solubilities in dilute acid (e.g. H_2SO_4 , HNO_3) (314, 320). The reactions of higher valency oxides of manganese and cobalt with sulfurous acid are thermodynamically feasible (Table VII.5).

Table VII.5: Standard free energy change ($\Delta G_{f, 298}^{\circ}$)⁺ for the dissolution reactions listed in the text

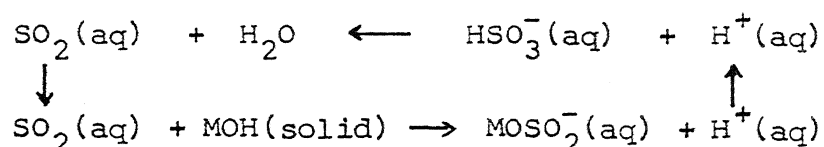
Element (M)	Reaction, $\Delta G_{f, 298}^{\circ}$ kJ mole ⁻¹								
	1 (II)*	2 (II)	3 (III)	4 (III)	5 (II, III)	6 (III)	7 (II, III)	8 (III)	9 (IV)
Ni	-70.2	-72.7	-	-	-	-316.5	-359.7	-424.5	-
Co	-77.4	-70.6	-	5.98	12.7	-	-325.6	-332.5	-
Cu	-43.6	-49.6	-	-	-	-	-	-	-
Mn	-102.3	-87.4	6.4	-	-	-274.3	-337.3	-358.3	-241.4

⁺ $\Delta G_{f, 298}^{\circ}$ values which are taken from reference (215, 314, 320-322) have been tabulated in Appendix-N,

* Oxidation state of M,

- Incomplete data available.

Apart from dissolution reactions involving H^+ ions, dissolution of divalent oxides of nickel, cobalt and copper in sulfurous acid may involve complexation reaction (237)



Khalafalla and Pahlman (237) have studied the dissolution behaviours of mixed and pure oxides of Ni and Co in sulfurous acid. Leaching tests (237) have indicated that (i) solubilization of cobalt(II) and nickel(II) from their respective hydroxide in sulfurous acid was rapid, (ii) cobalt(II) hydroxide was leached completely before the leaching of cobalt(III) hydroxide begun from a mixed valence cobalt hydroxide precipitate and (iii) from a blended Ni-Co hydroxide, nickel is not as easily leached out as cobalt(II).

The tetravalent manganese oxides are normally easily soluble in sulfurous acid (315-317). Rates of dissolution of manganese minerals in sulfurous acid may differ depending upon the mineralogy (315, 316). Sometimes an oxidizing roast (e.g. for mineral manganite (γ - $MnOOH$) and hausmanite (Mn_3O_4)) may enhance the rate of dissolution (315). Dithionate and sulfate both may form during reaction of manganese dioxides with dissolved sulfur dioxide (323). The amount of dithionate decreases with decreasing pH (323). Studies, by Miller and Wan (317), have revealed that kinetics of MnO_2 dissolution in aqueous sulfur dioxide solution is controlled by an electrochemical surface reaction.

The free energy values (Table VII.5) and other existing informations on dissolution of pure oxides/hydroxides provide some

tentative idea about the feasibility and nature of dissolution reaction in sulfuric and sulfurous acid. The calculation of $\Delta G_{r,298}^{\circ}$ assumes the different oxide/hydroxide in its standard state. However, the situation is expected to be more complex in mixed oxides which are the subject matter of this investigation.

Giovanoli (22) studied the interaction of doped busserites (Bu-R(I) type) with H^{+} ions in dilute HNO_3 . Although collapse of busserite structure and formation of nsutite was noted during acidification reaction, its significance with regard to leaching of doped elements was however not highlighted. The chemical composition data for the leach liquors were also not reported.

Removal of ions within a crystal structure will depend on whether reacting ions (e.g. H^{+}) can penetrate into the environment about the ion. The dissolution of host phase can influence the dissolution of doped element present in the structure.

7.2.2 Sulfuric Acid Leaching:

The behaviour of pure and doped manganese oxyhydroxides with regard to the dissolution of manganese(II), and Ni, Co and Cu is illustrated in Figures VII.7 and VII.8* respectively. Fraction of metals reacted at some selected time intervals are given in Table VII.6. The dissolution curves (Figures VII.7 and VII.8) are characterized by an initial fast release of metals, in the first few minutes, followed by a very slow dissolution. The transition from initial fast release to slow dissolution is quite sharp for B-O and B-R(C) samples.

* Tabulated leaching data for all the figures in this chapter are given in Appendix-0.

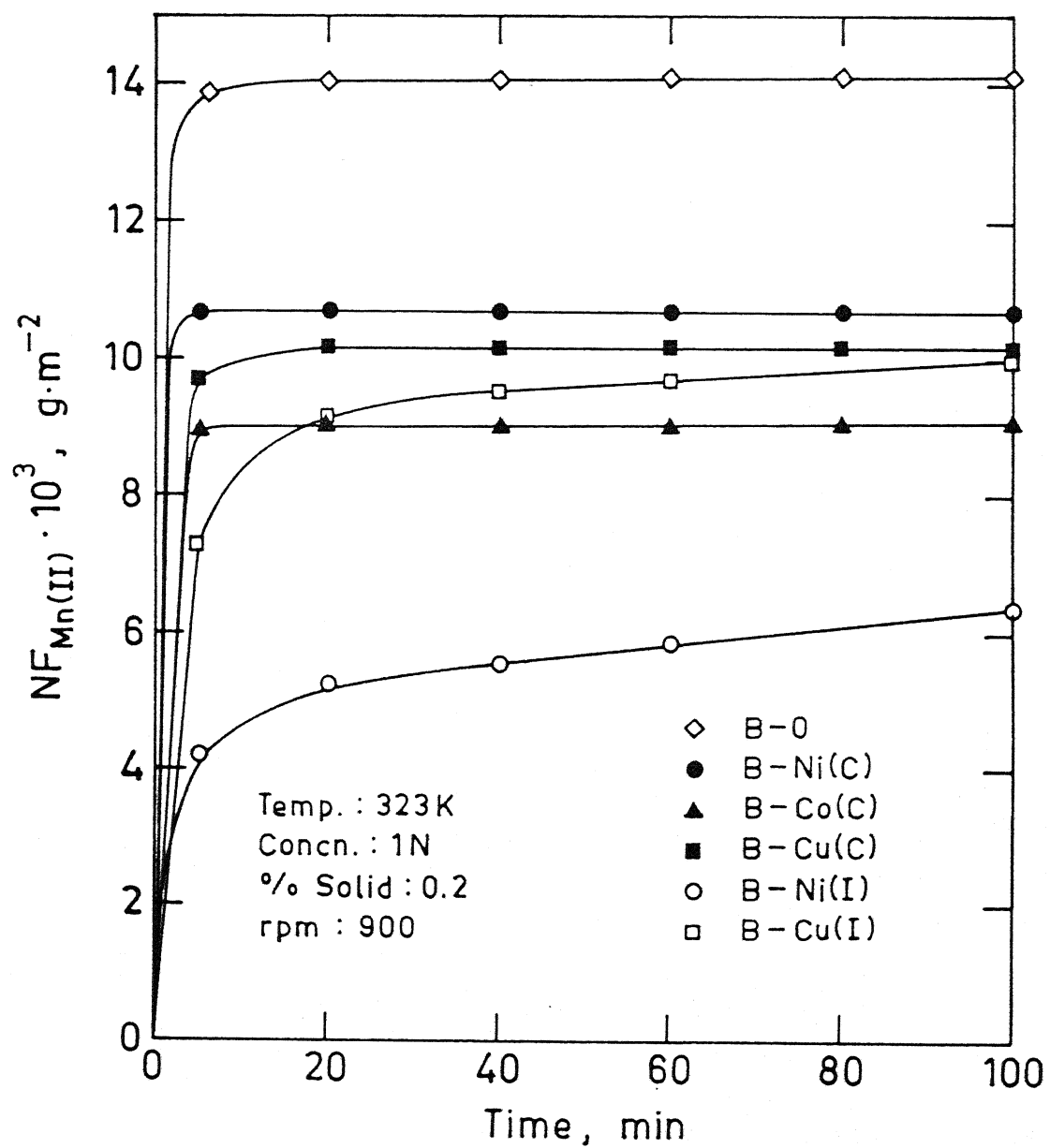


Fig. VII.7. Dissolution of manganese (II) from different birnessite samples in sulphuric acid.

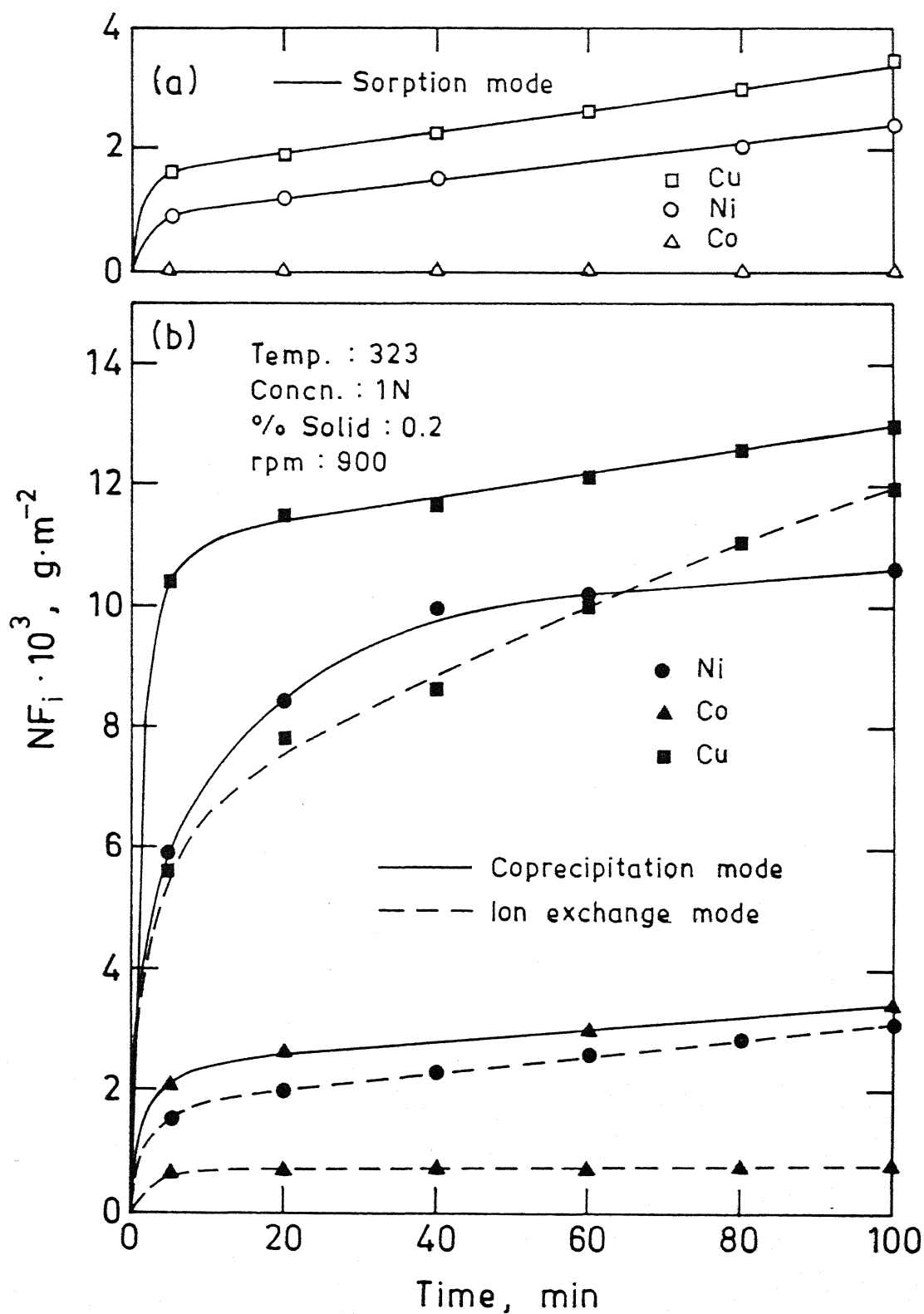


Fig. VII.8. Dissolution of doped Ni, Co and Cu in sulphuric acid (a) sorption mode (V-R(S) samples) and (b) coprecipitation and ion exchange mode (B-R(C) and B-R(I) samples).

Table VII.6:

Fraction of manganese and minor elements reacted in sulfuric and sulfurous acid leaching at different time intervals*

sample description	Sulfuric acid						Sulfurous acid					
	T = 5 min			T = 100 min			T = 0.5 min			T = 5 min		
	F _{Mn}	F _{Mn(II)}	F _R	F _{Mn}	F _{Mn(II)}	F _R	F _{Mn}	F _R	F _{Mn}	F _R	F _{Mn}	F _R
B-O	0.079	0.451	-	0.081	0.458	-	0.543	-	0.998	-	0.998	-
B-Ni(C)	0.051	0.377	0.208	0.051	0.377	0.373	0.258	0.308	0.879	0.909	0.879	0.909
B-Co(C)	0.046	0.349	0.080	0.046	0.349	0.137	0.465	0.529	0.954	0.966	0.954	0.966
B-Cu(C)	0.059	0.472	0.506	0.063	0.501	0.633	0.293	0.265	0.927	0.930	0.927	0.930
B-Ni(I)	0.046	0.251	0.089	0.069	0.377	0.183	0.406	0.379	0.860	0.966	0.860	0.966
B-Co(I)	0.057	-	0.029	0.060	-	0.035	0.352	0.378	0.899	0.945	0.899	0.945
B-Cu(I)	0.026	0.404	0.308	0.037	0.557	0.650	0.456	0.516	0.966	0.962	0.966	0.962
V-O	0.002	-	-	0.002	-	-	0.803	-	1.000	-	1.000	-
V-Ni(S)	0.001	-	0.129	0.001	-	0.325	0.803	0.789	1.000	1.000	1.000	1.000
V-Co(S)	0.001	-	0.000	0.001	-	0.000	0.803	0.693	0.995	1.000	0.995	1.000
V-Cu(S)	0.001	-	0.218	0.001	-	0.468	0.802	0.614	0.995	0.998	0.995	0.998

* - vide Appendix-0 for detailed tabulated data.

The XRD patterns of leach residues (Figure VII.9) obtained by us reveal that the leaching is accompanied by collapse of original structure (vide Figure VII.3) (disappearance or reduction in intensity of 7 \AA° and 4.8 \AA° lines) and formation of new phases like nsutite (ASTM 17-510) and cryptomelane (ASTM 20-908). X-ray diffraction evidence for the formation of cryptomelane is particularly strong in the residue obtained after leaching of B-Cu(C) sample. The formation of cryptomelane has not been reported in earlier study by Giovanoli (22) on interaction of doped layered structure oxyhydroxides with H^+ ions in HNO_3 . The mineral nsutite (T(1,1) structure, Table II.4) shows intergrowth features with cryptomelane (T(1,2) structure) in natural ores (76). Such features are likely to be present in the leach residue also.

Nsutite and cryptomelane (T(1,1), T(1,2) structure) have a compact structure compared with more open original structure viz. birnessite (T(2, ∞)). The leachability of elements, after the initial fast release, will be governed by the structure of the new phases formed. Phases with more compact structures are expected to have poor leachability. Thus it is likely that the poor leachability of phases at latter time intervals results due to structural collapse and formation of new and more compact poorly leachable phases.

The nature of leaching curves (Figures VII.7 and VII.8) can also be interpreted in terms of different structural sites in the birnessite structure. Based on radiochemical studies, Buser (324) could distinguish three kinds of exchange rates, in layered structure manganates(IV), of which half times were of the order of (i) minutes, (ii) half an hour and (iii) 40 hours, respectively. Buser (324) attributed the fastest reaction to the exchange in the

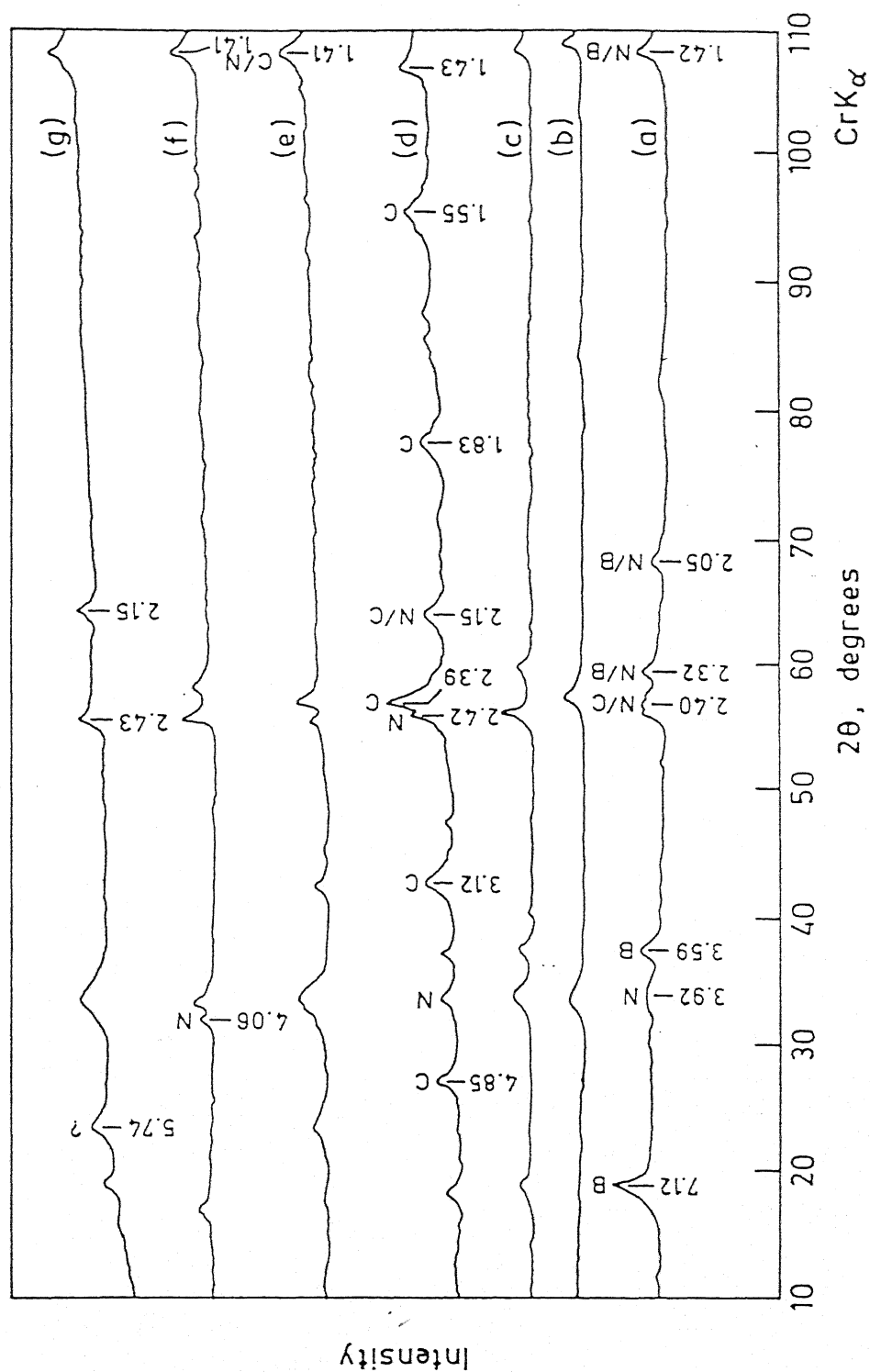


Fig. VII.9. XRD patterns of leach residues obtained after sulfuric acid leaching of birnessites (a) B-O (b) B-Ni(C) (c) B-Co(C) (d) B-Cu(C) (e) B-Ni(I) (f) B-Co(I) (g) B-Cu(I). B-Birnessite, C: Cryptomelane N: Nsutite.

intermediate layer and slowest to the exchange in the main layer edifice. The initial fast leaching of elements (Figures VII.7 and VII.8) is likely to be the result of leaching of ions from intermediate layers. The leaching of metal ions from intermediate layer result in the structural collapse and formation of new phases. The possibility of interlayer diffusion is significantly reduced after the structural change from birnessite to nsutite and cryptomelane. This means that both structural change and leaching of metal ions from main layer edifice can result in the slow nature of leaching after initial fast release of metal ions.

Six percent of total manganese is extracted from B-Co(I) sample after 100 minutes leaching (Table VII.6). Mn(IV) is practically insoluble in dilute sulfuric acid (314). It turns out that at least 2.56% manganese in B-Co(I) is present in +(II) oxidation state. Since the total amount of Mn(II) is not known precisely in B-Co(I), the $NF_{Mn(II)}$ values could not be calculated for this sample, and it is not included in Figure VII.7. The variation of leachability parameter $NF_{Mn(II)}$ with time (Figure VII.7) indicates that the variations in dissolution behaviour of Mn(II) from different samples cannot be explained on the basis of total initial Mn(II) content and surface area alone, and evidently the structure of phases has a role to play in the dissolution process. B-R(I) samples (complex structure) show more time-dependence for Mn(II) dissolution compared with B-R(C) or B-O (simple layered structure) (Figure VII.7). The amount of Mn dissolved from δ -MnO₂ samples was less than 1% of the total manganese content (Table VII.6).

Two significant observations were made for the dissolution of Ni, Co and Cu from the doped samples (Figure VII.8): (i) for the same doped element in different mode of doping, the degree of

leachability is observed to vary in the following sequence: sorption < ion exchange < coprecipitation mode and (ii) for the same mode of doping, leachability of doped elements varies in the following order $\text{Cu} > \text{Ni} > \text{Co}$. As summarized before in the previous section on characterization, the complexities of structure increase among the different categories of samples as sorption > ion exchange > coprecipitation mode. It is striking to note that there is a direct relationship between the increasing structural complexities (as defined in the footnote of p. 210) and poor leachability. Leaching sequence observed for the doped element in any particular mode of doping (i.e. leachability of $\text{Cu} > \text{Ni} > \text{Co}$) indicate that the interaction of doped element with the host Mn(IV) phases is specific in nature. Significantly it may be noted that the leaching sequence observed for divalent Ni, Cu and Mn exhibit direct correlation with their CFSE* (Tables VII.3 and VII.6, Figure VII.8). The dissolution behaviour of cobalt is expected to be more complicated due to its oxidation in the structure of the host phase. Co(III) has a very large crystal field stabilization energy (Table VII.3).

It is amazing to note that in spite of very large surface area of $\delta\text{-MnO}_2$, the doped samples (V-R(S)) show poorest leachability for Ni, Co and Cu (Figure VII.8). Buser (324) has proposed that the mineral $\delta\text{-MnO}_2$ may be considered to consist of 'two dimensional crystals' (missing or very weak basal reflection in XRD). It appears quite likely that the exchange of doped element with K^+ (during synthesis) is followed by subsequent incorporation

* Vide Appendix-M for details.

in the $\delta\text{-MnO}_2$ structure. The leaching results for V-R(S) samples (Figure VII.8) corroborate Burns's (95) contention that the elements are incorporated in the vacant lattice sites during sorption of Ni, Co and Cu on $\delta\text{-MnO}_2$. The leaching data for Co in V-Co(S) indicate that Co(II) sorbed on $\delta\text{-MnO}_2$ is completely oxidized (Figure VII.8). It may be recalled that from thermodynamic point of view the dissolution of tetravalent cobalt in sulfuric acid is not feasible. Our leaching data are in conformity with XPS data of Murray and Dilard (221), for Co sorbed on $\delta\text{-MnO}_2$, which indicated the oxidation of Co(II) to Co(III).

Possible Leaching Mechanisms in Sulfuric Acid:

Apart from the mass transfer steps in solution phase, the other kinetic steps which will be involved in the dissolution of metal ions from doped manganese oxyhydroxide phase are as follows:

1. Diffusion of hydronium ion (H_3O^+) from solid-solution interface to the doped metal ions (surrounded by O^{2-} or OH^- or H_2O ligands, octahedral coordination) in the crystal structure of host manganese oxyhydroxide.
2. Chemical reaction of hydronium ions with metal ion in the solid structure, leading to the formation of hydrated metal ion $\text{M}(\text{H}_2\text{O})^{2+}$.
3. Diffusion of hydrated metal ion from inside the solid to the solid solution interface.

Among the kinetic steps 1-3, steps 1 and 3 are mass transfer steps and step 2 is a chemical reaction step.

Diffusion in the solid phase may be facilitated by structural vacancies, interlayers etc. Since the size of hydrated

metal ion $M(H_2O)^{Z+}$ is bigger than the hydronium ion (H_3O^+), mass transfer step 3 is expected to affect the reaction kinetics and leachability of metal ions much more as compared with step 1. As we have noted from the leaching data that for a particular doped element the degree of leachability varies in the following order: sorption < ion exchange < coprecipitation; it is likely that the resistance for the diffusion of $M(H_2O)_6^{Z+}$ will follow the reverse order.

The predominant mechanism of hydrated metal ion migration in V-R(S) (highly disordered structures) and B-R(C) (simple layered structure) samples are likely to be vacancy diffusion and interlayer diffusion (at least before collapse of B-R(C) structure) respectively. Vacancy diffusion is expected to be slower as compared with interlayer diffusion. Thus poor leachability of doped element from V-R(S) samples as compared to B-R(C) samples is understandable. B-R(I) samples which are characterized by complex structure, for example, hybrid layer, layered structure with large stacking and structural disorder, will offer intermediate resistance (between coprecipitation and sorption mode) and in turn their leaching behaviour will fall between B-R(C) and V-R(S) samples.

The structural collapse for a simple layered structure phase will be easier as compared to a phase with more complex structure. Easier structural collapse means more sharp transition from the initial fast leaching to the slow leaching. This explains why the initial faster release of elements like Mn(II), Cu and Ni from simple layered structure phases is followed up by a more slower leaching as compared to complex structure phases (Figures VII.7 and VII.8).

The chemical reaction of metal ion, in solid oxyhydroxide structure, with hydronium ion can be represented by reaction mechanism shown in Figure VII.10(a). The mechanism involves the formation of a seven coordinate transition state. The reaction mechanism (Figure VII.10(a)) has been formulated by analogy with bimolecular substitution reaction in solution phase which bear resemblance with the leaching reaction (63, 302).

The chemical reaction mechanism (Figure VII.10(a)) involves the following steps:

- (a) a hydronium ion (H_3O^+) approaches the octahedrally coordinated central transition metal ion (M).
- (b) an activated complex possessing a pentagonal bipyramidal symmetry is formed. The H_3O^+ ion forms the seventh group, and is bound through the lone pair electrons of oxygen atom.
- (c) the activated complex disproportionates to give a water molecule and hydrated metal ion surrounded by five OH^- group. The process is repeated to yield a hexahydrated metal ion.

The reaction scheme proposed in Figure VII.10(a) can be looked at in two different ways: (i) in terms of breaking of metal-oxygen or metal-hydroxide bond, the metal ion which form stronger chemical bond may be expected to show poor leachability and (ii) in terms of activation energy E_a for the formation of activated-transition-complex. Higher activation energy means poor leachability ($k = A \exp(-E_a/RT)$).

Since the ionic radii of O^{2-} or OH^- ligands are fixed, the radii of doped metal ions will be one of the most important factors to govern the bond strength between metal ion (M) and

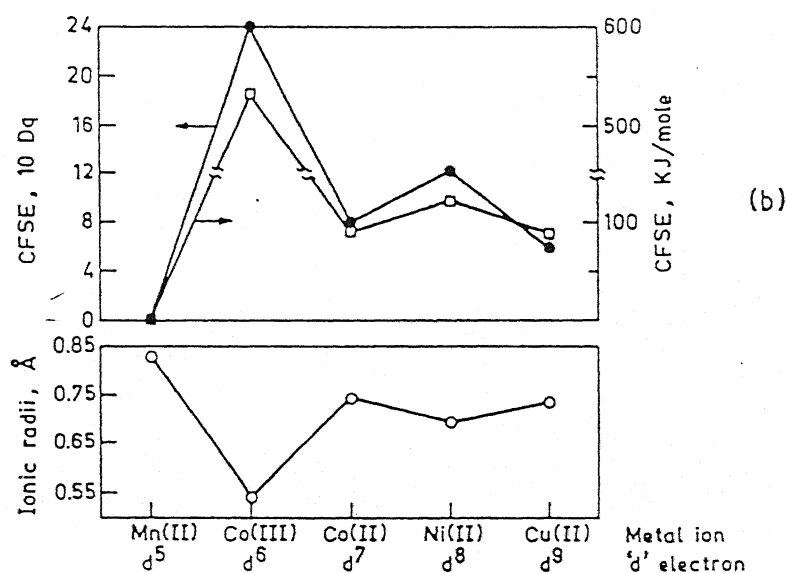
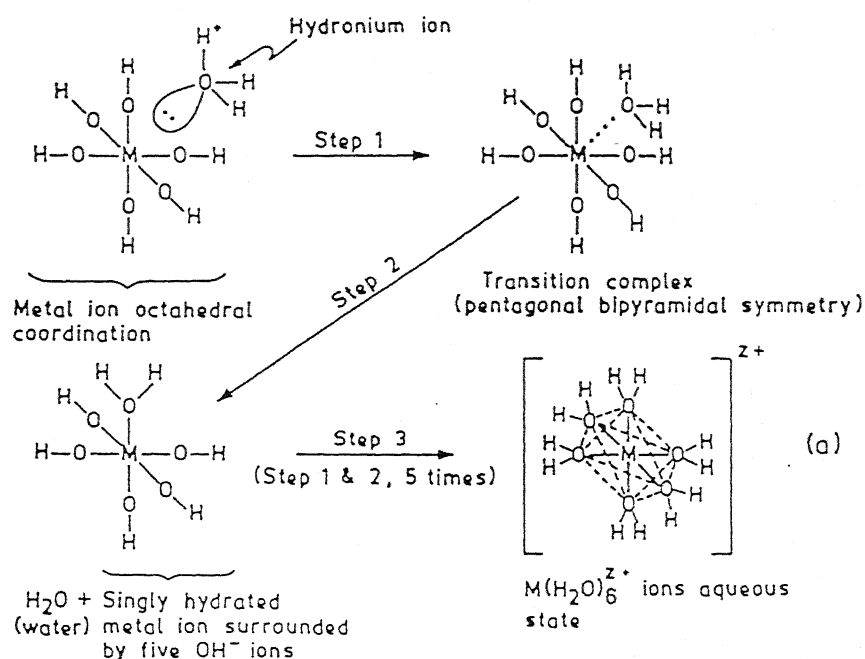


Fig. VII.10. (a) Reaction mechanism for octahedrally coordinated metal ion in solid oxyhydroxide structure (adopted from references (63, 302)), (b) relationship between electronic configuration, crystal field stabilization energy (CFSE) and ionic radii of some selected metal ions (63, 69).

ligands (302). Element with lower ionic radius will have higher bond strength (bond energy $\propto \frac{1}{r}$, bond between metal ion and O^{2-} or OH^- is predominantly ionic in nature). The radii of d^n metals ion are governed by variations in the shielding of core electrons which results from crystal field effect. Figure VII.10(b) illustrate the relationship between electronic configuration, crystal field stabilization energy (CFSE) and ionic radius of elements of interest. It follows from Figure VII.10(b) that elements can be arranged as follows in terms of bond strength: $Co(III) > Ni(II) > Cu(II) > Co(II) > Mn(II)$. Interestingly this sequence is consistent with the leachability order observed for the doped elements in a particular mode of doping.

The difference between the CFSE of metal ion in six coordinate initial state and seven coordinate transition state (i.e. crystal field activation energy (CFAE), ΔE_a) may be regarded as a contribution to the total activation energy (E_a). A large positive value of ΔE_a will slow down the reaction. The CFAE for different ions are listed below (302)

Ion	Mn(II)	Co(II)	Ni(II)	Cu(II)	Co(III)*
Electronic configuration	d^5	d^7	d^8	d^9	d^6
CFAE (ΔE_a) (in 10 Dq)	0	~ 0	4.26	1.07	8.52

* Low spin.

The above value of ΔE_a indicate that metal ions in the structure will be resistant to leaching in the following order: $Co(III) > Ni(II) > Cu(II) \simeq Co(II) > Mn(II)$.

Thus both bond energy and activation energy concepts lead to the same end conclusion (supported by experimental results)

regarding the leachability of metal ions in the structure of manganese oxyhydroxide. The similar conclusions are also expected to emerge for dissolution of pure oxides and hydroxide of doped elements. So the occurrence of doped element in the host manganese(IV) oxyhydroxides can be described as "occluded as part of structure in substitution mode". Occlusion follows from close correspondence between CFSE and leachability of doped element; and occurrence as part of structure in substitution mode follows from chemical equivalence balance calculations, role of structure in leaching and structural collapse accompanied by leaching of doped elements.

7.2.3 Sulfurous Acid Leaching:

Leaching data (in terms of NF_i or F_i) for dissolution of different samples in sulfurous acid are presented in Figures VII.11 to VII.13 and Table VII.6.

Leaching experiments on the pure (B-O and V-O) and doped samples (B-R(C), B-R(I) and V-R(S)) indicated that the solubilization of manganese and doped elements was very rapid in sulfurous acid (Table VII.6). All the manganese and doped elements were extracted almost completely from the different samples (0.25 g) within 10 minutes with 250 ml of leach solution containing 0.0078 mole (0.2 wt % SO_2) of SO_2 . Leaching results for doped elements are quite expected because the host oxide matrix containing Mn(IV) is solubilized in dissolved SO_2 .

All the doped birnessite samples (B-R(I or C)) show more resistance to leaching compared with pure birnessite (Figures VII.11 and VII.12). This indicates that the incorporation of doped

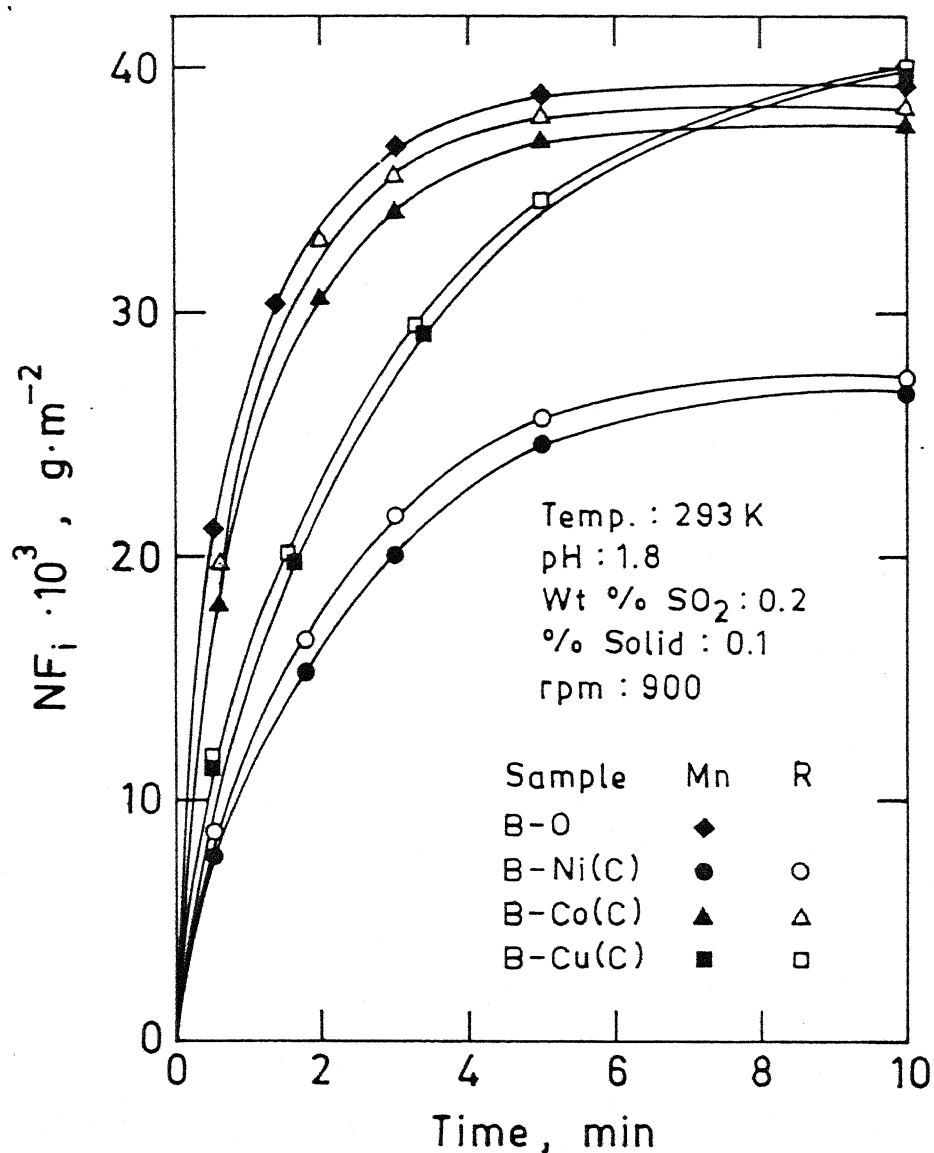


Fig. VII.11. Dissolution behaviour of birnessites doped with Ni, Co or Cu in coprecipitation mode compared with pure birnessite (leaching medium—sulfurous acid).

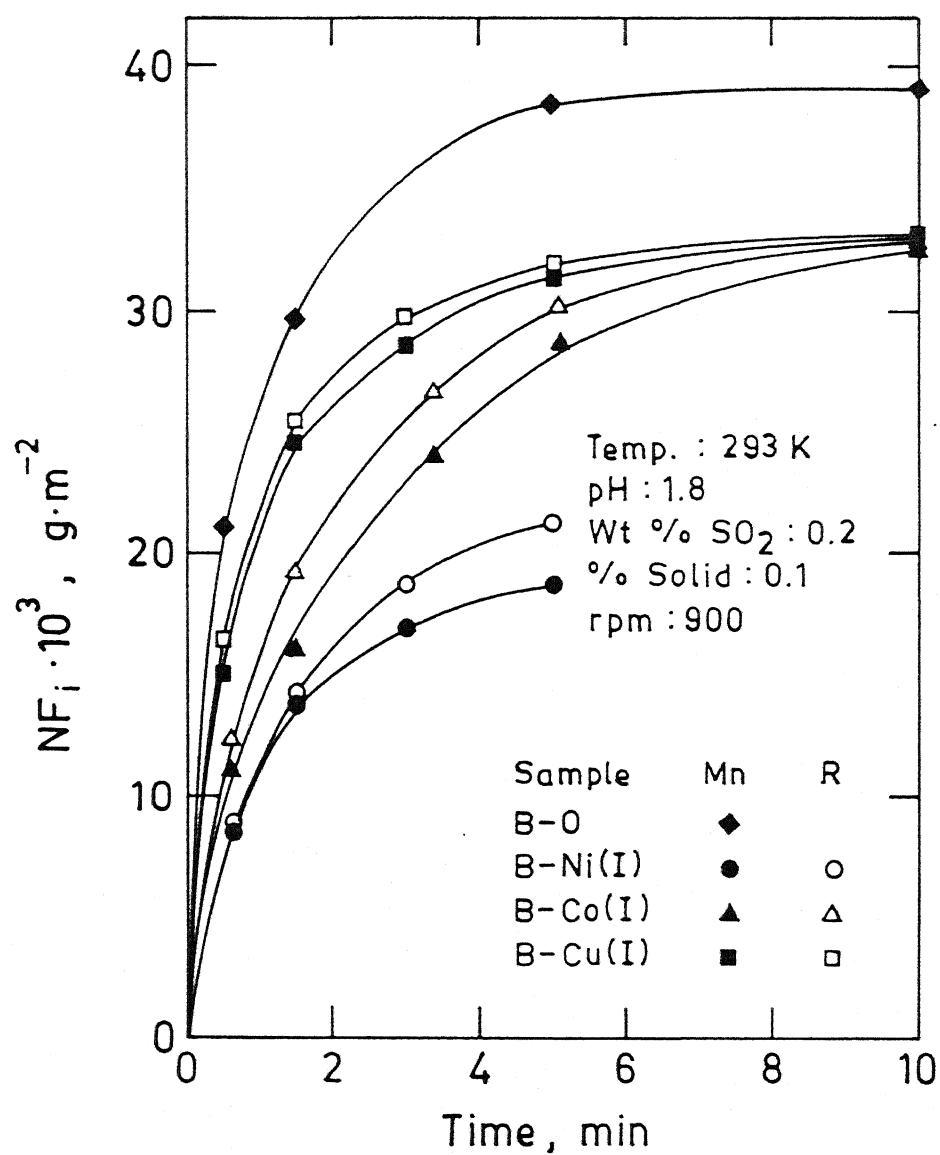


Fig. VII.12. Dissolution behaviour of birnessites doped with Ni, Co or Cu in ion exchange mode compared with pure birnessite (leaching medium—sulfurous acid).

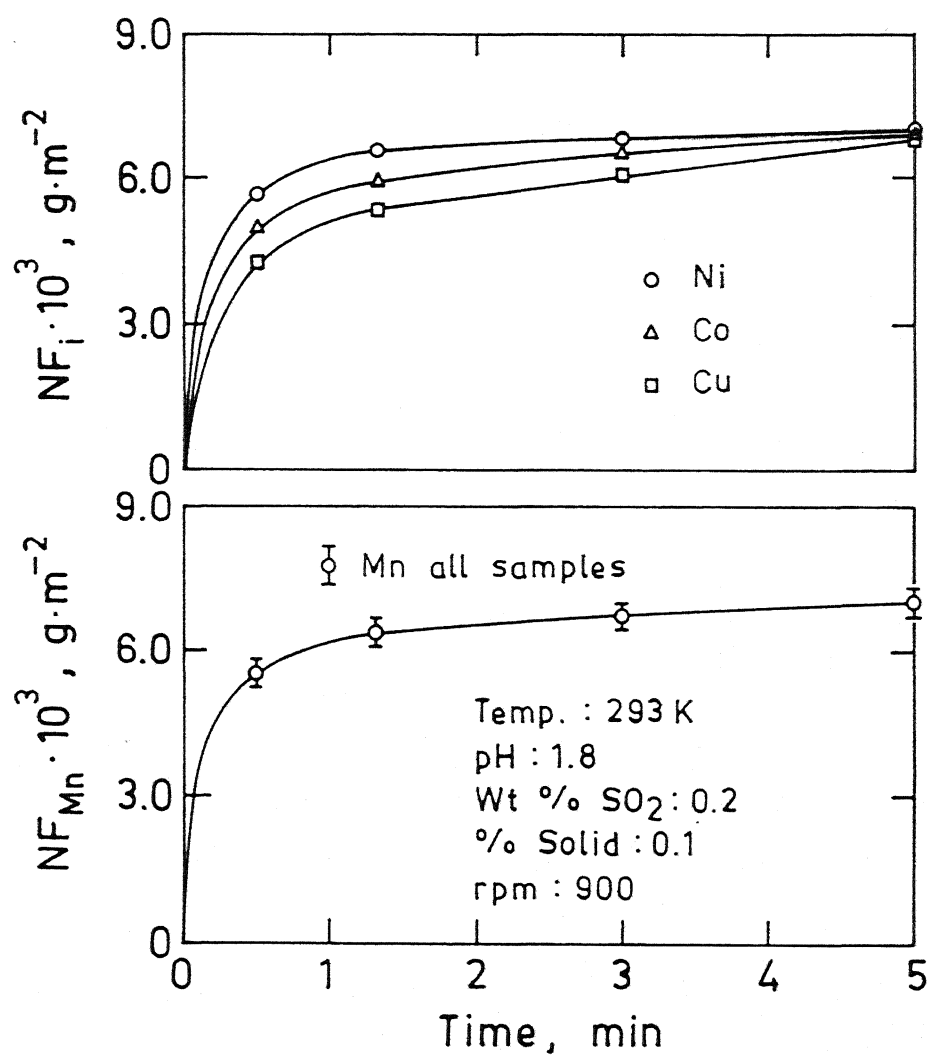


Fig. VII.13. Dissolution behaviour of V-O and V-R(s) samples in sulfurous acid.

elements in the birnessite structure leads to stabilization of doped phases with respect to pure birnessite. The doping of Ni leads to maximum stabilization.

The dissolution of doped elements correlates well with the dissolution of host manganese oxide phases (Figures VII.11 to VII.13). This further corroborates our earlier contention (p. 228) that the doped elements occur as part of the host birnessite or $\delta\text{-MnO}_2$ structure. Each synthetic sample shows its characteristic leaching curve. This means that each synthetic sample represent a distinct phase and that mineralogy of the host phase can influence the leaching behaviour of the doped element.

Non-preferential dissolution of manganese and doped element should result in 1:1 correspondence between NF_{Mn} and NF_{R} . The leaching curves in (Figures VII.11 to VII.13) illustrate that the correspondence between NF_{Mn} and NF_{R} is not exactly 1:1. Small deviations from 1:1 correspondence, which are observed for B-R(C), B-Cu(I) and V-Ni(S), fall well within the analytical error limits ($\pm 2-4\%$). However deviations are particularly significant for B-Ni(I), B-Co(I), V-Co(S) and V-Cu(S). This may be attributed to structural inhomogeneity and/or preferential dissolution of doped or host element.

It may be noted that the concentration* of SO_2 in the leach liquor decreases from 0.2 wt % ($t = 0$) to approximately zero at the end of leaching. Since the dissolution of manganese involves the reduction from +(IV) to +(II) oxidation state, it is likely that the dissolution of manganese will be more sensitive to decreasing

* The total amount of dissolved SO_2 was more than the stoichiometric requirement.

concentration of SO_2 . All the leaching curves for doped birnessites (Figures VII.11 and VII.12) reveal that dissolution of doped elements show some preference over manganese. Interestingly, this trend is reversed for V-R(S) sample i.e. manganese dissolves preferentially as compared to the doped elements. It is possible that manganese dissolves preferentially from V-R(S) samples because these samples have significantly large surface area ($\sim 140 \text{ m}^2/\text{g}$) as compared with B-R(I/C) samples ($20\text{--}50 \text{ m}^2/\text{g}$). Large surface area of V-R(S) samples is associated with poor crystallinity and large structural disorder. Since crystal imperfections represent high energy regions, they can accelerate manganese (major) dissolution and lead to its preferential dissolution over the doped elements (minor). Thus dissolution of manganese may be affected by the nature of the doped element and crystallinity and structural disorder in the host phase. Unlike sulfuric acid leaching, no specific leachability order is observed for dissolution of doped element in sulfurous acid leaching. This indicates that dissolution mechanism/s operating in sulfurous acid are much more complex.

Nickel dissolution from B-Ni(I or C) samples show inferior leachability as compared with cobalt and copper dissolution from B-R(I or C) samples (Figures VII.11 and VII.12). Leachability trends for Co and Cu dissolution differ in ion exchanged and coprecipitated birnessite samples. The possible different factors which could influence leachability sequence are (i) mineralogy of host phase i.e. structure, crystallinity etc., (ii) presence of oxidized cobalt in the structure, (iii) reduction of Cu^{2+} to Cu^+ , etc. The influence of mineralogy on dissolution has been discussed

before in this sub-section. Preferential dissolution of Co(II) over Co(III) during mixed valence cobalt oxide dissolution in sulfurous acid has been noted by Khallafalla and Pahlman (237). Cu^+ ions which form due to reduction of Cu^{2+} in sulfurous acid are insoluble, and can catalyse the dissolution of tetravalent manganese by a reduction step (41, 234).

CHAPTER - VIII

PHYSICO-CHEMICAL NATURE OF PURE AND Ni, Co AND Cu BEARING GOETHITES

Goethite is the most frequently observed iron-bearing mineral present in the deep-sea nodules.* In this chapter, the results of investigation on characterization and dissolution behaviour of pure and doped synthetic goethite samples are reported and discussed. The samples were doped in coprecipitation and sorption mode. In the case of coprecipitation, the presence of Ni, Co and Cu modifies the crystallization conditions and thus crystal growth rate and in turn crystal size, morphology and degree of structural order. All these factors are expected to influence dissolution behaviour of samples. In order to correlate the Fe dissolution behaviour in different samples, samples were characterized in terms of surface area, crystallinity, structural disorder, particle morphology etc. The effect of method of doping on the mode of incorporation of minor elements in the host phase and on the dissolution of minor elements as well as Fe has also been investigated.

8.1 Characterization of Samples

8.1.1 Chemical Composition and Surface Area:

Chemical composition and surface area of different samples are listed in Table VIII.1. Higher potassium content (potassium ions come from KOH added during synthesis) of G-R(C) samples

* Unlike the oxyhydroxide of manganese (Chapter VII) goethite is not a mixed valence mineral. Iron in goethite is present in trivalent oxidation state.

Table VIII.1: Chemical composition and surface area of different goethite (α -FeOOH) samples

Sample description	Chemical composition			Surface area (m ² /g)
	wt. % Fe	wt. % R	wt. % K	
G-O	60.6	-	0.17	41.5
G-Ni(S)	59.6	0.80	0.17	41.5
G-Co(S)	59.6	0.72	0.18	41.5
G-Cu(S)	59.6	1.31	0.15	41.5
G-Ni(C)	57.7	2.44	0.57	71
G-Co(C)	58.6	2.42	0.30	74
G-Cu(C)	58.6	2.37	0.74	77

compared to other samples is attributed to higher surface area of these samples or substitution of Fe(III) by R(II) in the goethite structure. Excess potassium may be required for charge balance.

In spite of the fact that sorption experiments for Ni, Co and Cu were carried out under identical conditions of pH, temperature etc., Cu has been found to behave differently than the other two i.e. the amount of Cu sorbed is much higher compared with Ni and Co (Table VIII.1).

Based on 'Surface Complexation Model' (325) Balistrieri et al. (326) have shown a positive linear correlation between equilibrium constant for the adsorption reaction ($\text{SOH} + \text{R}^{z+} \longrightarrow \text{SOR}^{(z-1)+} + \text{H}^+$, SOH represents a surface-OH group on α -FeOOH) and hydrolysis constant of adsorbing element e.g. Ni, Co, Cu etc. Thus, the behaviour of Cu may be linked with its higher hydrolysis constant (K_1^*). Cu has got a higher hydrolysis constant ($\log K_1^* < 8.19$) compared to Ni ($\log K_1^* = -10.2$) and Co ($\log K_1^* = 9.94$).

8.1.2 XRD Studies:

Phase Constituents: XRD traces of the different samples are presented in Figure VIII.1. Goethite is the only iron bearing phase present in the different samples except G-Cu(C). The presence of small amount of hematite is indicated by XRD pattern of G-Cu(C) (Figure VIII.1(d)).

Goethite samples are known to show preferred orientation in the b-c plane (278). The relative intensity (I_{110}/I_{111}) is very sensitive to this effect and can provide valuable qualitative information on the proportion of well crystallized goethite to poorly crystalline goethite and untransformed $\text{Fe}(\text{OH})_3$ in the total sample volume. As the proportion of poorly crystalline and untransformed material increases, the particles become less prone to preferred orientation and the ratio (I_{110}/I_{111}) decreases correspondingly (278-280).

It can be inferred from the (I_{110}/I_{111}) values (Table VIII.2) that the amount of poorly crystalline goethite (which may include untransformed $\text{Fe}(\text{OH})_3$ gel) increases in the following order: G-Cu(C) > G-Ni(C) \approx G-Co(C) > G-O = G-R(S).

No separate phase of Ni, Co and Cu is observed in any of the doped samples. There are at least three possible minor element-goethite associations possible in G-R(C) samples, namely adsorption, intimate intergrowth and lattice substitution. The changes in lattice parameters (Table VIII.2) of G-R(C) samples compared to G-O suggest that at least a fraction of the minor element content is present in the goethite lattice. Intrinsic aspects of processes involved in the sorption of transition metal ions onto the surface

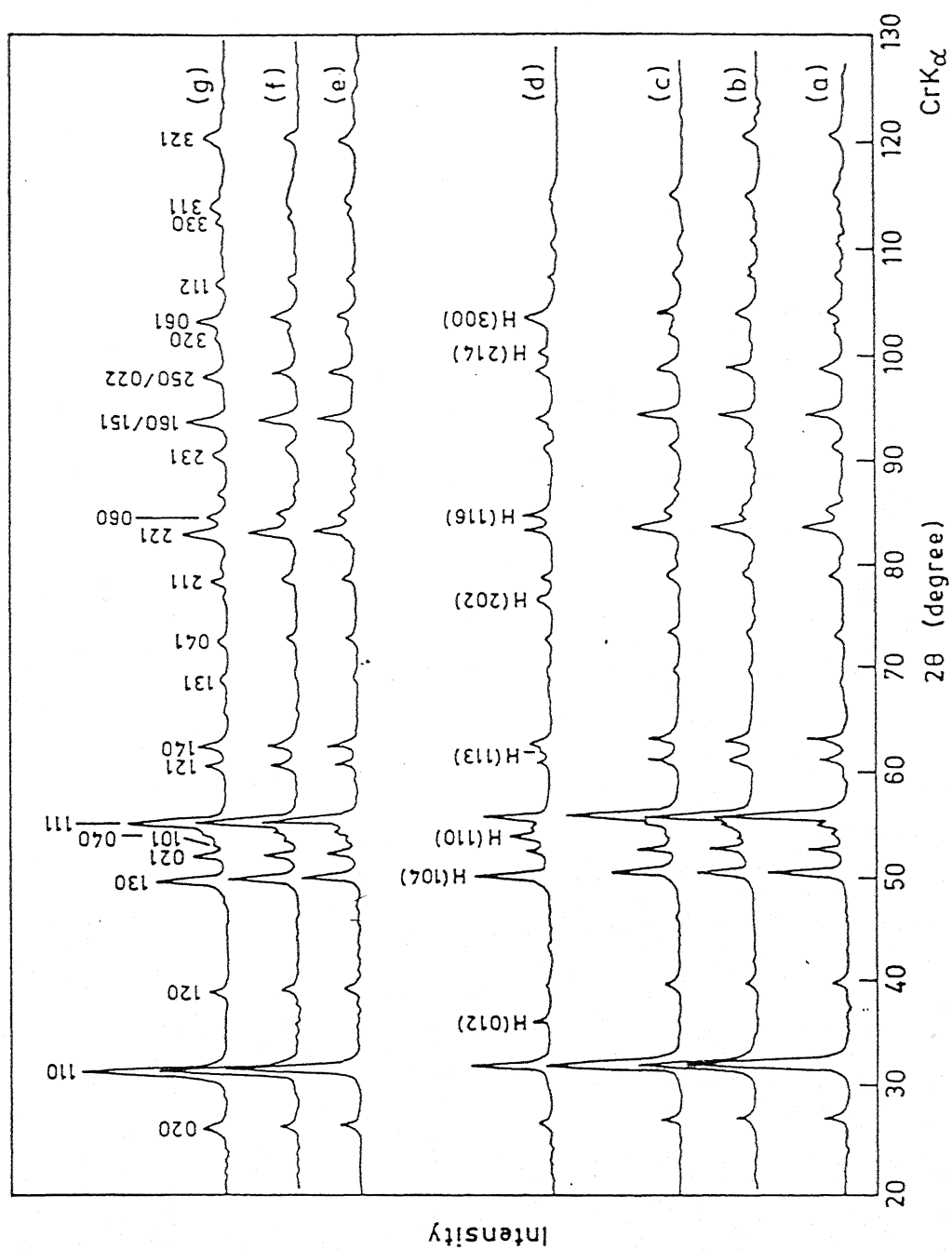


Fig. VIII.1. XRD patterns of goethite samples (a) G-0, (b) G-Ni(C), (c) G-Co(C), (d) G-Cu(C), (e) G-Ni(S), (f) G-Co(S) and (g) G-Cu(S). Peaks corresponding to hematite in G-Cu(C) are marked with H.

Table VIII.2: I_{110}/I_{111} and lattice parameter values

Sample description	I_{110}/I_{111}	Lattice parameters, Å		
		a	b	c
G-O	1.48	4.6095	9.9428	3.0162
G-Ni(S)	1.49	-	-	-
G-Co(S)	1.51	-	-	-
G-Cu(S)	1.51	4.6099	9.9425	3.0170
G-Ni(C)	1.42	4.6167	9.9445	3.0135
G-Co(C)	1.38	4.6015	9.9314	3.0129
G-Cu(C)	1.13	4.6095	9.9822	3.0210

of hydrous oxide of Fe and Mn have been reviewed by Varentsov et al. (327). The multistages in the sorption process may involve ion exchange, surface complex formation etc. X-ray photoelectron spectroscopy (XPS) analysis of cobalt adsorbed on the surface of goethite at $\text{pH} \geq 8.0$ has revealed that cobalt is present on the surface as a mixture of CoO and CoOOH (266).

Crystallite Size and Structural Disorder: Microcrystalline dimensions MCD_{hkl} along with MCD_a , MCD_b and MCD_c (calculated for 9 diffraction lines) for G-O and G-Cu(C) are tabulated in Table VIII.3. MCD_a and MCD_b values from Table VIII.3 are plotted in the a-b plane (Figure VIII.2(a), (b)). The good agreement in MCD_a value calculated from different diffraction lines of G-O indicates

Table VIII.3: Microcrystalline dimensions (in nm) for G-O and G-Cu(C)*

hkl	G-O			G-Cu(C)				
	MCD _{hkl}	MCD _a	MCD _b	MCD _c	MCD _{hkl}	MCD _a	MCD _b	MCD _c
020	63.9	-	63.9	-	55.8	-	55.8	-
110	39.9	36.2	16.8	-	90.0	82.1	37.9	-
120	42.9	31.5	29.1	-	115.1	84.6	48.4	-
130	55.2	32.3	44.7	-	76.1	44.5	61.7	-
021	103.0	-	53.4	88.0	102.9	-	53.3	87.3
101 ^{**}	29.1	16.0	-	24.3	48.1	26.4	-	40.1
040 ^{**}	42.3	-	42.3	-	34.3	-	34.3	-
111	56.5	30.2	13.9	45.9	104.3	55.7	25.7	84.7
140	69.7	33.2	61.4	-	69.9	33.3	61.6	-

* Vide Appendix-E for details of other samples

** Values not included in calculation because of superposition of these lines with strong neighbouring lines.

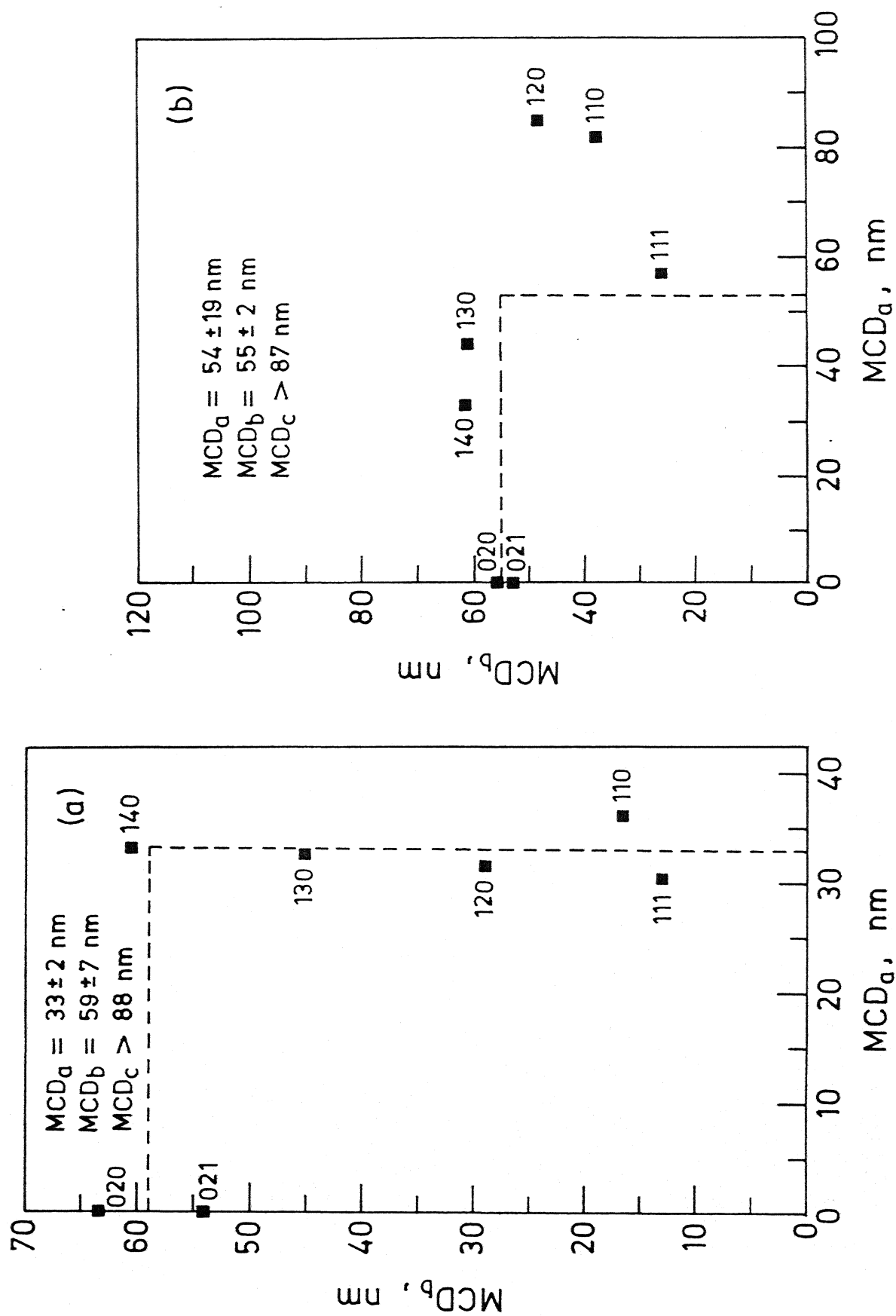


Fig. VIII.2. MCD_a vs MCD_b values for selected goethite lines (a) for G-O and (b) for G-Cu(C).

that line broadening is mainly due to domain size alone rather than structural defects. The results for G-0 are well in contrast with G-Cu(C) where the sample shows larger MCD_a value (54 nm) and larger value of standard deviation (S.D.) in mean MCD_a (+19) indicating presence of large amount of structural disorder (Figure VIII.2(b)). As discussed later, these results are corroborated by TEM observations. Mean microcrystalline dimension MCD_a and MCD_b and minimum value of MCD_c are listed in Table VIII.4. Other important crystallite dimension (328) MCD_{110} and MCD_{111} are also included in Table VIII.4. There is no direct correlation between microcrystalline dimension (Table VIII.4) and surface area (Table VIII.1) because (i) the particle size and coherently scattering domain size need not be the same, and (ii) microcrystalline dimension does not take into account untransformed goethite.

Table VIII.4: Mean crystalline dimension (MCD) along the a, b and c axes and MCD_{110} and MCD_{111} as calculated from the XRD data*

Sample description	Mean crystalline dimension, nm			MCD_{110} , nm	MCD_{111} , nm
	MCD_a	MCD_b	MCD_c		
G-0	33 \pm 2	59 \pm 7	>88	39.9	56.5
G-Ni(S)	33 \pm 2	59 \pm 7	>88	41.9	59.2
G-Co(S)	34 \pm 2	59 \pm 7	>88	41.9	63.8
G-Cu(S)	34 \pm 2	59 \pm 7	>88	41.9	63.8
G-Ni(C)	28 \pm 2	41 \pm 4	>62	33.8	56.5
G-Co(C)	32 \pm 4	71 \pm 18	>88	37.0	56.1
G-Cu(C)	54 \pm 19	55 \pm 2	>87	90.3	104.3

* Vide Appendix-E for details.

8.1.3. Transmission Electron Microscopy:

TEM gives independent data on particle size, shape, structural disorder and mineral assemblages, which complement the XRD data.

Some selected electron micrographs and respective SAED patterns recorded from the different samples are given in Figure VIII.3(a)-(h). Goethite present in G-0 and G-R(S) (Figure VIII.3(a), (b)) is acicular in nature (265). Lath shape particles shows preferred orientation in b-c (110) plane. In addition to acicular goethite (e.g. Figure VIII.3(a)-(d)) gel kind of material (Figure VIII.3(e), (f)) which gave only three or four diffraction rings at 3.39, 2.15, 1.76 and 1.21 Å⁰ was observed in varying proportion in G-R(C) samples. This material is expected to be goethite in the intermediate stage of transformation i.e. Fe(OH)₃ to α-FeOOH. Attempts to record single crystal electron diffraction patterns from this material failed because of geometrical limitation of the microscope. The particle size was smaller than the smallest selected area available. The amount of the gel kind of material observed in the case of G-Ni(C) and G-Co(C) was very small and the diffraction rings were quite sharp. However, the amount of this material was quite large in G-Cu(C) and rings observed were faint indicating the presence of significant amount of untransformed Fe(OH)₃. It is to be noted that the presence of the gel kind of material observed under TEM is closely related with value of (I_{110}/I_{111}) recorded by XRD (Table VIII.2).

The formation of twinned goethite crystals (Figure VIII.3(g), (h)), which was additionally noted in G-Cu(C) sample, is related

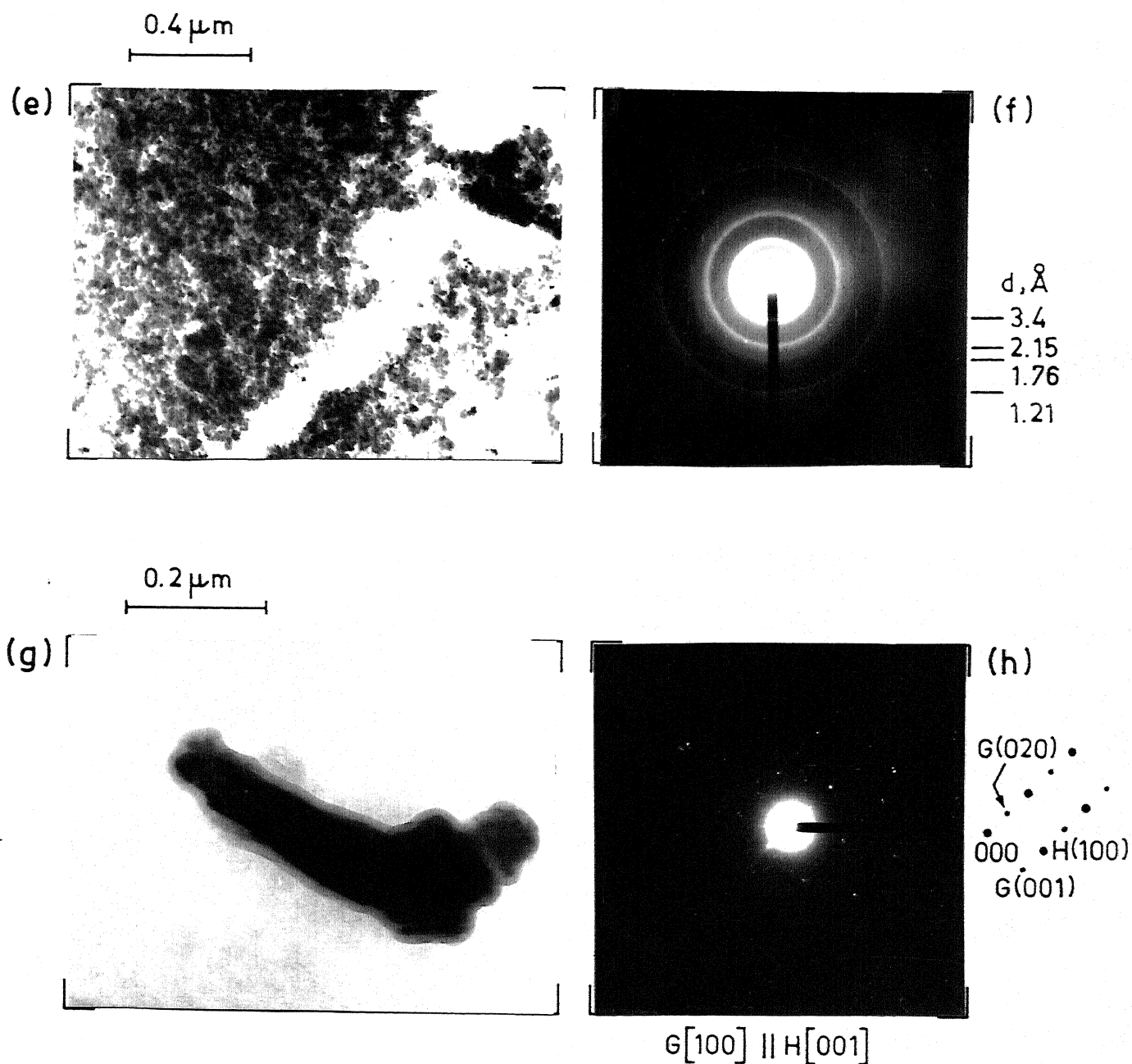


Fig. VIII.3. Electron micrographs and SAED patterns (e), (f) poorly crystalline goethite in G-Ni(C) and (g), (h) goethite outgrowth on hematite in G-Cu(C).

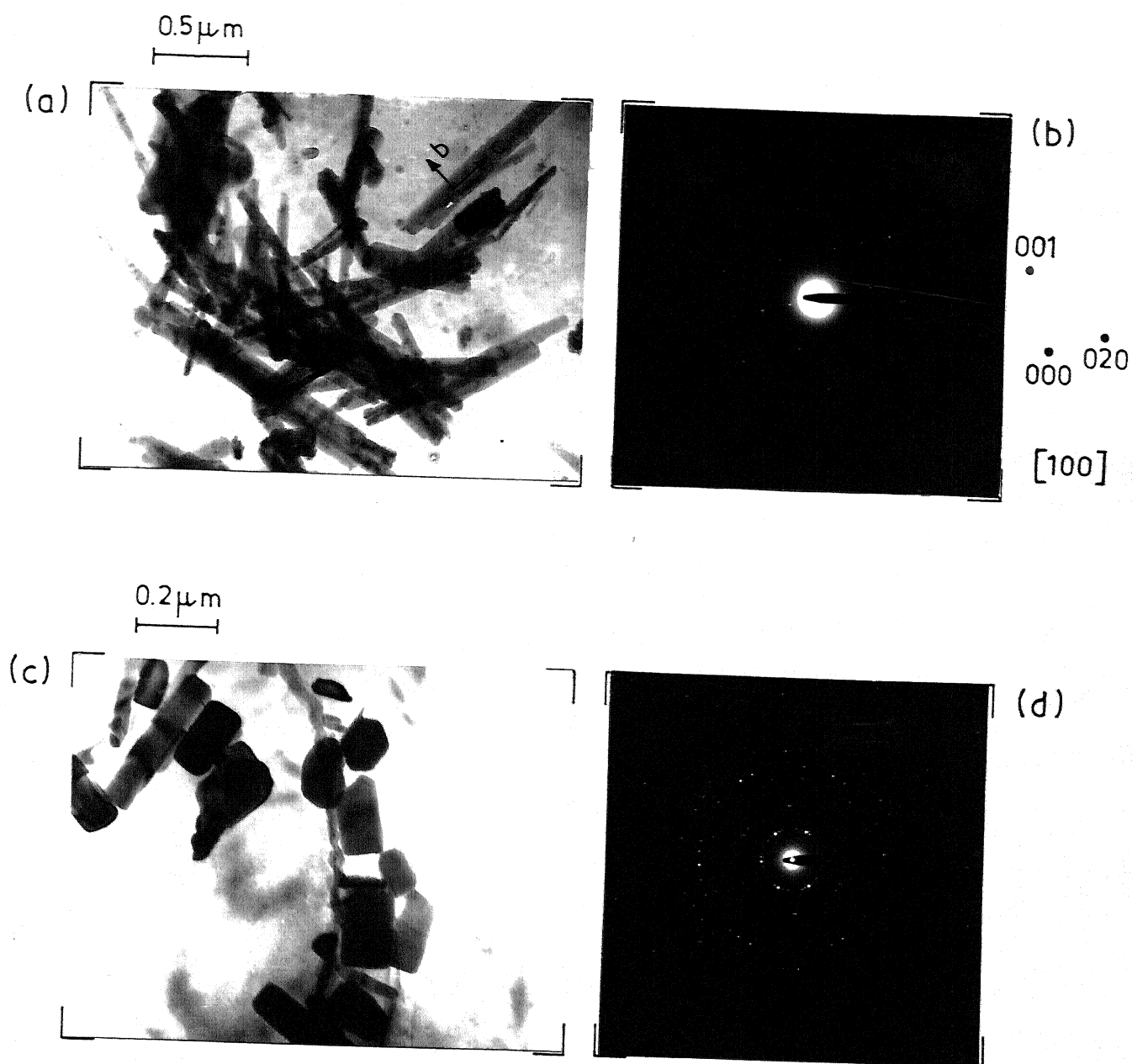


Fig. VIII.3. Typical electron micrographs and SAED patterns (a), (b) G-O, (c), (d) G-Ni(C) (lath shaped particles were observed for all other samples also).

Contd. ...

to the epitaxy outgrowth of goethite on hematite (265). The epitaxial relationship between goethite and hematite is as follows (265, 329) (vide Figure II.3)

Cell direction	Cell parameter
$G[100] \parallel H[001]$	$3a_G = c_H$
$G[010] \parallel H[010]$	$b_G = 2a_H$
$G[001] \parallel H[210]$	$2c_G = \sqrt{3}a_H$

The mechanisms of formation of acicular and twinned goethite are discussed by Atkinson et al. (265). Acicular and twinned goethite grow respectively from goethite and hematite nuclei formed during early stage of precipitation in ferric nitrate solution. Twinned crystals therefore result from nucleation under conditions which were more favourable to hematite nuclei formation. It appears that the presence of Cu inhibits the formation of goethite nuclei by adsorption on initially formed ferric oxide gel and favours the formation of hematite by distortion of lattice parameters which occur on their inclusion in crystal nuclei. The growth of goethite on hematite was variable ranging from goethite crystal apparently free from hematite to hematite crystal with goethite overgrowth. Hematite crystal free from goethite were not observed.

The results of TEM observations on the nature of goethite present in different samples and particle size measured from electron micrographs are summarized in Table VIII.5. Crystal size observed under TEM are also compared with coherently scattering domain size measured by XRD. The particle size measured on electron micrographs does not always match with the coherently scattering domain size indicating that the two need not be the same.

Table VIII.5: Summary of TEM observations and comparison of average length and width of particles as measured from XRD and TEM

S. No.	Sample description observed	Nature of goethite observed	Size of crystal [*] as observed under TEM, nm		Width XRD (MCD _b)		Length XRD (MCD _c)	
			b-direction	c-direction	Width TEM	Length TEM		
1	G-O	Acicular	74 ± 25	206 ± 63	0.80		>0.43	
2	G-R(S)	Same	Same	Same	Same		Same	
3	G-N1(C)	(i) Acicular (ii) Very small amount of goethite of very small crystallite size	72 ± 30	270 ± 134	0.60		>0.23	
4	G-Co(C)	Same	72 ± 22	184 ± 28	0.99		>0.48	
5	G-Cu(C)	(i) Acicular (ii) Twinned goethite (iii) Goethite of very small crystallite size with significant amount of untransformed Fe(OH) ₃ gel	24 ± 6 154 ± 45	391 ± - 206 ± -	2.25 0.35		>0.23 >0.42	

* based on 10-12 measurements

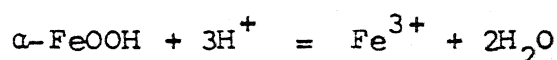
- means only 2-3 measurements were used.

Extinction contours in an acicular crystal are shown in Figure VIII.4(a). Also shown in the same Figure VIII.4(b) is a star shaped twin observed in G-Cu(C). TEM and HRTEM studies by Schwertmann (328) and Cornell et al. (330) on partially dissolved goethite samples have revealed that extinction contours and centre of twin (shown in Figure VIII.4(b)), which represent high energy regions, are preferentially attacked in acid leaching.

8.2 Leaching Studies

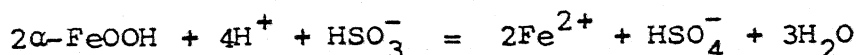
8.2.1 General Considerations:

At low pH, the reaction of goethite with sulfuric acid can proceed as follows



The standard free energy of formation ($\Delta G_{f,298}^\circ$) value for goethite depends on the crystallinity (71). Consequently, $\Delta G_{r,298}^\circ$ value for the above reaction may vary from -4.3 to -8.8 kJ/mole (vide Appendix-N). Dependence of $\Delta G_{f,298}^\circ$ or $\Delta G_{r,298}^\circ$ on crystallinity can lead to preferential dissolution of poorly crystalline goethite.

The dissolution reaction in sulfurous acid involves the reduction of ferric iron to ferrous iron. Typical overall dissolution reaction may be expressed as follows



$$\Delta G_{f,298}^\circ = -120 \text{ to } -129 \text{ kJ/mole}$$

The mechanism of goethite dissolution in sulfurous acid is open to question. Warren and Hay (331) and Byerley et al. (332) proposed

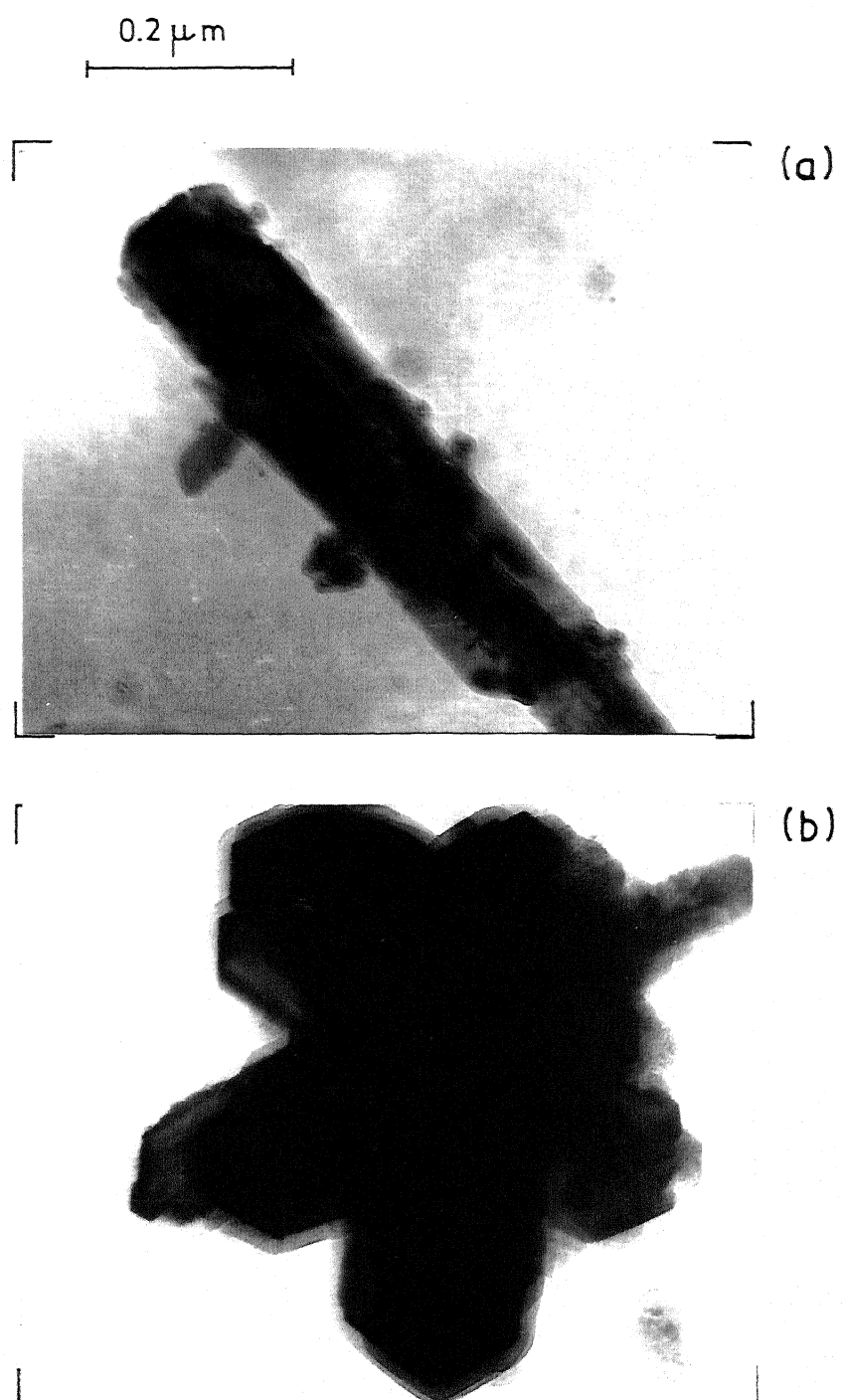


Fig. VIII.4. Electron micrographs (a) extinction contours in G-Ni(C) and (b) star shaped twins in G-Cu(C).

a 'surface adsorption' model in which iron dissolves as a ferric ion complex of SO_2 and subsequently reduced to ferrous iron in the solution phase. According to Nicol (333) the dissolution proceeds via an electrochemical reaction on the surface.

8.2.2 Dissolution Behaviour of Iron:

Figures VIII.5 and VIII.6 show the variation of mole of iron leached per cm^2 with time for different samples in sulfuric and sulfurous acid leaching. Fraction of iron reacted at selected time intervals is given in Table VIII.6. Fraction of Fe reacted (F_{Fe}) varies from sample to sample. Maximum amount of Fe dissolved does not exceed 31% and 13% (at the end of leaching test) in sulfuric acid and sulfurous acid leaching respectively. The distinction between dissolution of Fe from goethites and Mn from manganese oxyhydroxide samples, in sulfurous acid (complete Mn dissolution), needs to be noted.

It is revealed from the data presented (Figures VIII.5 and VIII.6) that surface area alone is not adequate to explain the differences in the dissolution behaviour of different samples i.e. the reaction kinetics is heterogeneous in nature. In order to have deeper insight into the nature of iron dissolution, linear and multilinear correlations were sought between the fraction of Fe dissolved (F_{Fe} at $t = 5$ min, vide Table VIII.6) and physical characteristics of the samples. The correlation coefficients and parameters of regression equations are listed in Table VIII.7.

In the sulfuric acid leaching, F_{Fe} (at $t = 5$ min) shows a strong correlation with surface area but larger discrepancies were observed for the G-R(C) samples in the following increasing order:

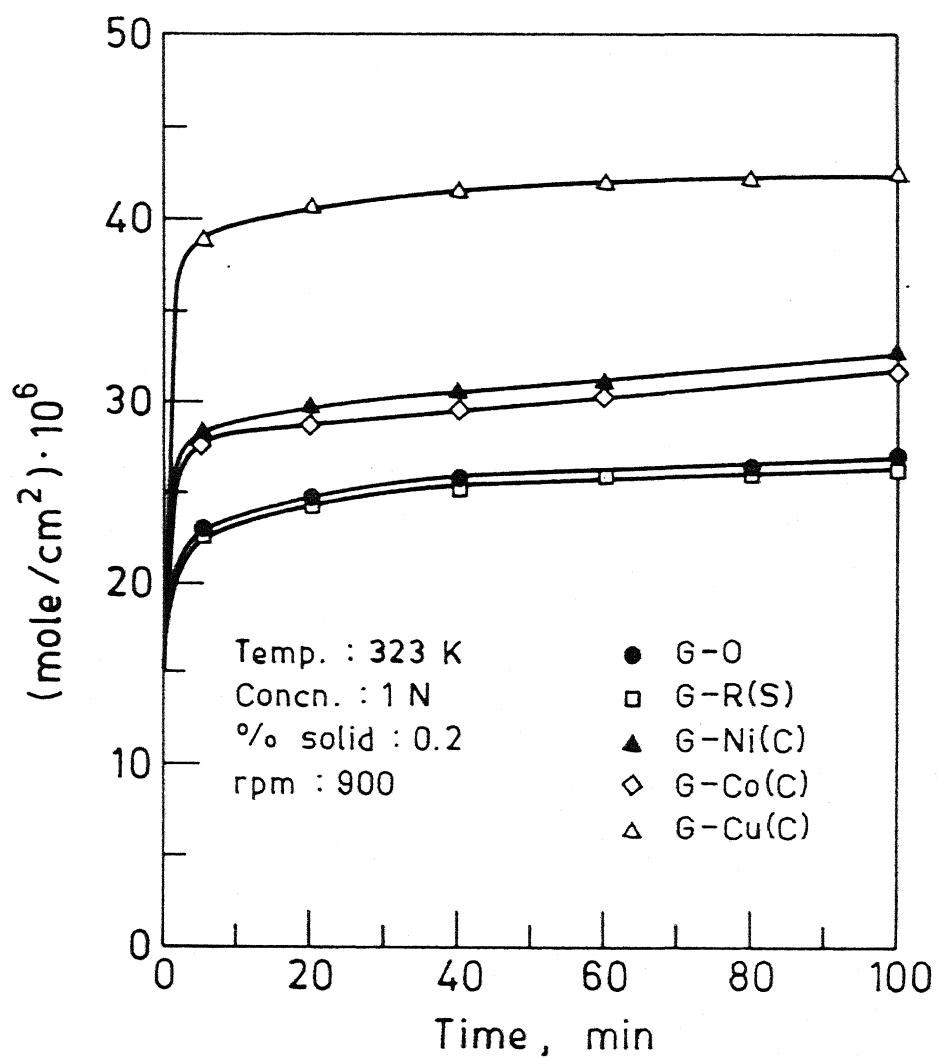


Fig. VIII.5. Dissolution of iron from different goethite samples in sulfuric acid.

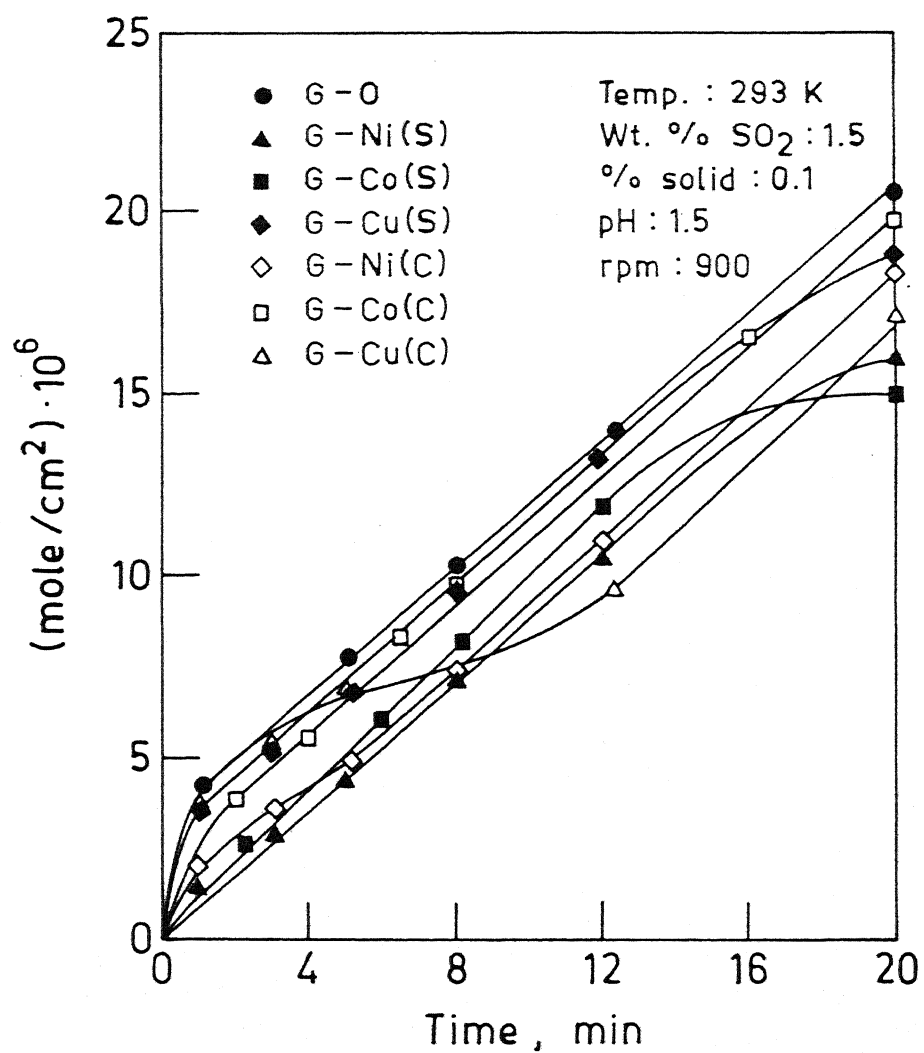


Fig. VIII.6. Dissolution of iron from different goethite samples in sulfurous acid.

Table VIII.6: Fraction of iron and minor elements reacted in sulfuric and sulfurous acid leaching at different times

Sample description	Sulfuric acid						Sulfurous acid					
	T = 5 (min)			T = 100 (min)			T = 5 (min)			T = 20 (min)		
	F _{Fe} ¹	F _R ¹	MCR ²	F _{Fe}	F _R	MCR	F _{Fe}	F _R	MCR	F _{Fe}	F _R	MCR
G-O	8.7	-	-	10.3	-	-	4.0	-	-	7.8	-	-
G-Ni(S)/75 ³	8.8	68.7	10	10.2	80.0	10	1.7	39	3.5	6.2	75.0	6.4
G-Co(S)/87	8.8	77.0	10	10.3	92.0	10	1.8	68	2.5	5.7	79.0	6.3
G-Cu(S)/52	8.7	77.0	6	10.3	85.9	6	2.5	63	2.1	7.2	67.0	5.5
G-Ni(C)/25	20.6	53.3	9.0	23.8	60.7	9.0	3.3	13	4.1	12.5	44.0	7.10
G-Co(C)/25	20.8	24.7	20.7	23.8	27.5	20.8	4.7	10	14.7	14.0	19.0	19.5
G-Cu(C)/28	28.9	14.6	55.7	31.0	16.4	53.0	5.2	2.6	39.2	13.0	7.0	50.7

1 - Fraction of Fe or R reacted x 10²; 2 - Molar concentration ratio (C_{Fe}/C_R) in leach liquor;
3 - (Mole of Fe/Mole of R) ratio in solid sample.

Table VIII.7: Linear and multilinear correlation between fraction of iron reacted (at $t = 5$) and physical characteristics of the samples

Property		I					II			Significance level (F-test) (%)
1	2	b _O	b ₁	b ₂	r	b _O	b ₁	b ₂	r	
Surface area	-	-10.5	0.46	-	0.968	-0.63	0.069	-	0.885	>99
MCD _a	-	-5.24	0.57	-	0.582	-0.01	0.089	-	0.560	Not significant
MCD ₁₁₀	-	2.54	0.26	-	0.628	1.33	0.040	-	0.569	-do-
MCD ₁₁₁	-	-5.08	0.31	-	0.638	0.34	0.043	-	0.550	-do-
Surface area	I ₁₁₀ /I ₁₁₁	32.4	0.31	-24.38	0.998	6.79	0.043	-4.22	0.921	>99
MCD _a	S.D	74.5	-2.19	3.82	0.993	11.1	-0.030	0.534	0.889	>99
MCD _a	I ₁₁₀ /I ₁₁₁	163.9	-0.629	-89.4	0.989	25.89	-0.096	-13.63	0.916	>99
MCD ₁₁₀	I ₁₁₀ /I ₁₁₁	165.6	-0.316	-95.8	0.984	27.49	-0.054	-15.37	0.939	>99
MCD ₁₁₁	I ₁₁₀ /I ₁₁₁	158.0	-0.286	-87.6	0.965	28.24	-0.058	-14.99	0.938	>99

I - Sulfuric acid and II - Sulfurous acid leaching
 b_0 - Constant term, b_1 and b_2 partial regression coefficient
 r - Correlation coefficient.

$G\text{-Cu(C)} > G\text{-Co(C)} > G\text{-Ni(C)}$. The linear correlations between microcrystalline dimensions and F_{Fe} are not significant. The multilinear correlations using surface area or microcrystalline dimension (e.g. MCD_a , MCD_{110} etc.) and I_{110}/I_{111} or standard deviation (S.D.) in mean microcrystalline dimension result in a very high correlation coefficient and most of the variance in the data set can be explained. These results are quite understandable because presence of amorphous material and structural disorder which are reflected by parameter (I_{110}/I_{111}) or standard deviation in microcrystalline dimension (e.g. MCD_a) are not accounted for in surface area or microcrystalline dimension. One of the important conclusions which can be drawn from these observed correlations is that the dissolution behaviour of iron for the different samples in sulfuric acid leaching can be explained in terms of microcrystalline dimensions, structural disorder and surface area irrespective of the factors which cause changes in these physical parameters.

It is striking to note from the Table VIII.7 that the correlation coefficients observed in sulfurous acid leaching are inferior compared to sulfuric acid leaching. This implies that the leaching behaviour of iron in sulfurous acid (reducing medium) is more complex and suffers from the interference by minor elements. Minor elements may interfere in the following ways: (i) reduction in the effective surface area available for Fe dissolution, (ii) preferential dissolution of Ni, Co and perhaps Cu in the initial stage of leaching in sulfurous acid. This is reflected by the much lower molar concentration (C_{Fe}/C_R) in leach liquor obtained in sulfurous acid. The preferential dissolution of Ni

and Co in sulfurous acid has been observed by Khalafalla and Pahlman (237) and (iii) electrochemical effects e.g. catalytic effect of Cu^{2+} on iron dissolution from goethite in sulfurous acid (331, 332).

8.2.3 Dissolution Behaviour of Minor Elements:

NF_1 vs. time plots in Figures VIII.7 and VIII.8 illustrate the dissolution behaviour of minor elements in sulfuric and sulfurous acid leaching. The minor elements in sorption mode are much more easily leachable compared to coprecipitation mode (Figures VIII.7 and VIII.8, Table VIII.6). The behaviour observed for the different elements is specific to their interaction with goethite substrate (sorption mode) or goethite precipitation (coprecipitation mode) and leaching medium.

Schwertmann (328) has noted 1:1 correspondence between Fe and Al dissolution in HCl leaching of goethite samples coprecipitated with aluminium. The Fe/R mole ratio in the G-R(C) samples before leaching was approximately 25. In the course of sulfuric acid leaching this value changes over to some specific values which remain constant over the entire leaching period (Table VIII.6). This means that the minor elements in different samples have different multiple associations (both in terms of iron bearing constituents and mode of occurrence e.g. sorption, lattice substitution etc.). The ease with which minor elements will be leached out are expected to follow the sequence: sorption > occlusion or intergrowth > structural substitution. Thus $(C_{\text{Fe}}/C_{\text{R}})$ ratio in the leach liquor can provide information on the predominant mode of occurrence.

In the case of G-Cu(C), the $C_{\text{Fe}}/C_{\text{Cu}}$ ratio in the leach liquor jumps up to a very high value (Table VIII.6) i.e. iron is

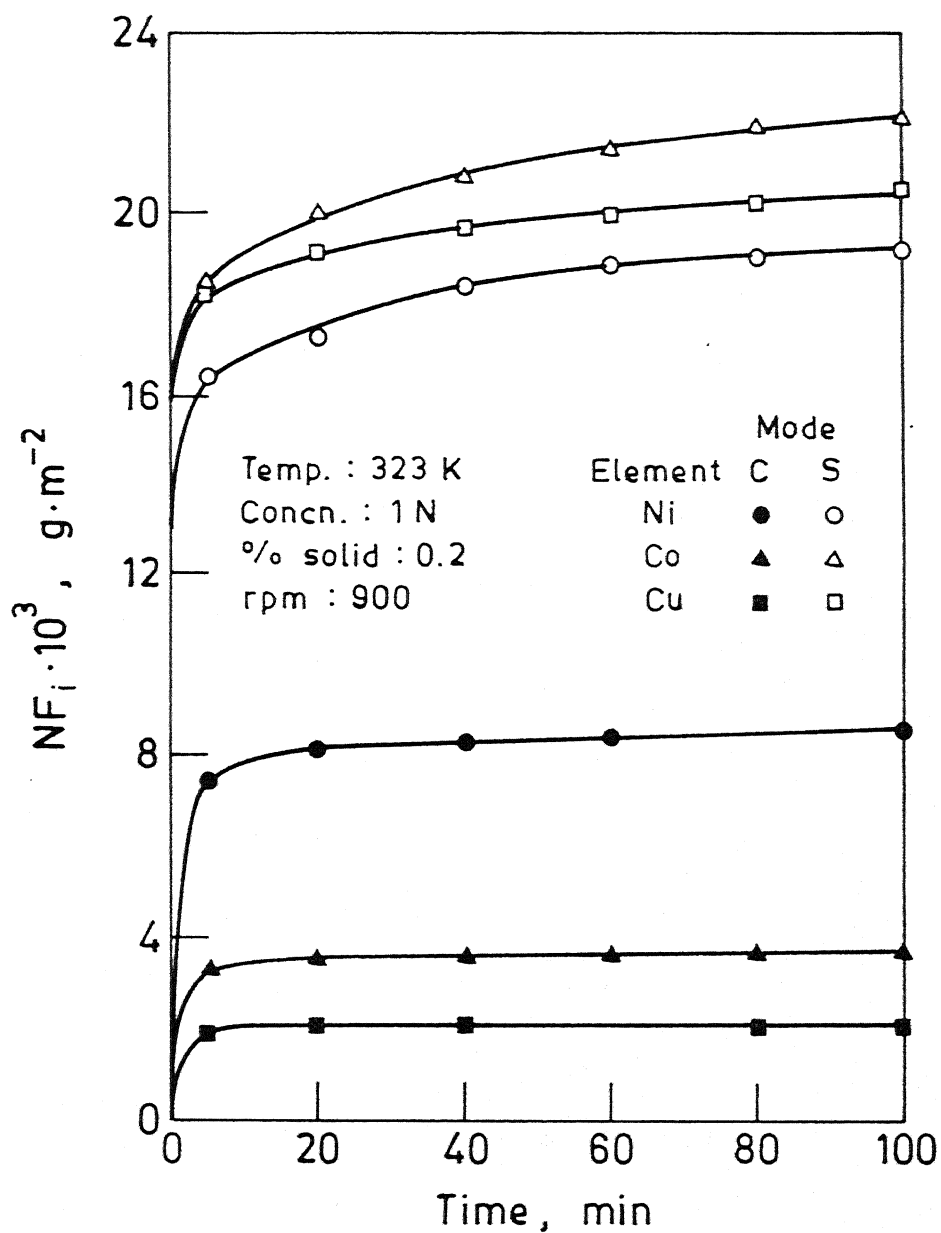


Fig. V.III.7. Effect of mode of doping on the dissolution of Ni, Co and Cu from doped goethite samples in sulfuric acid.
C-coprecipitation, S-sorption

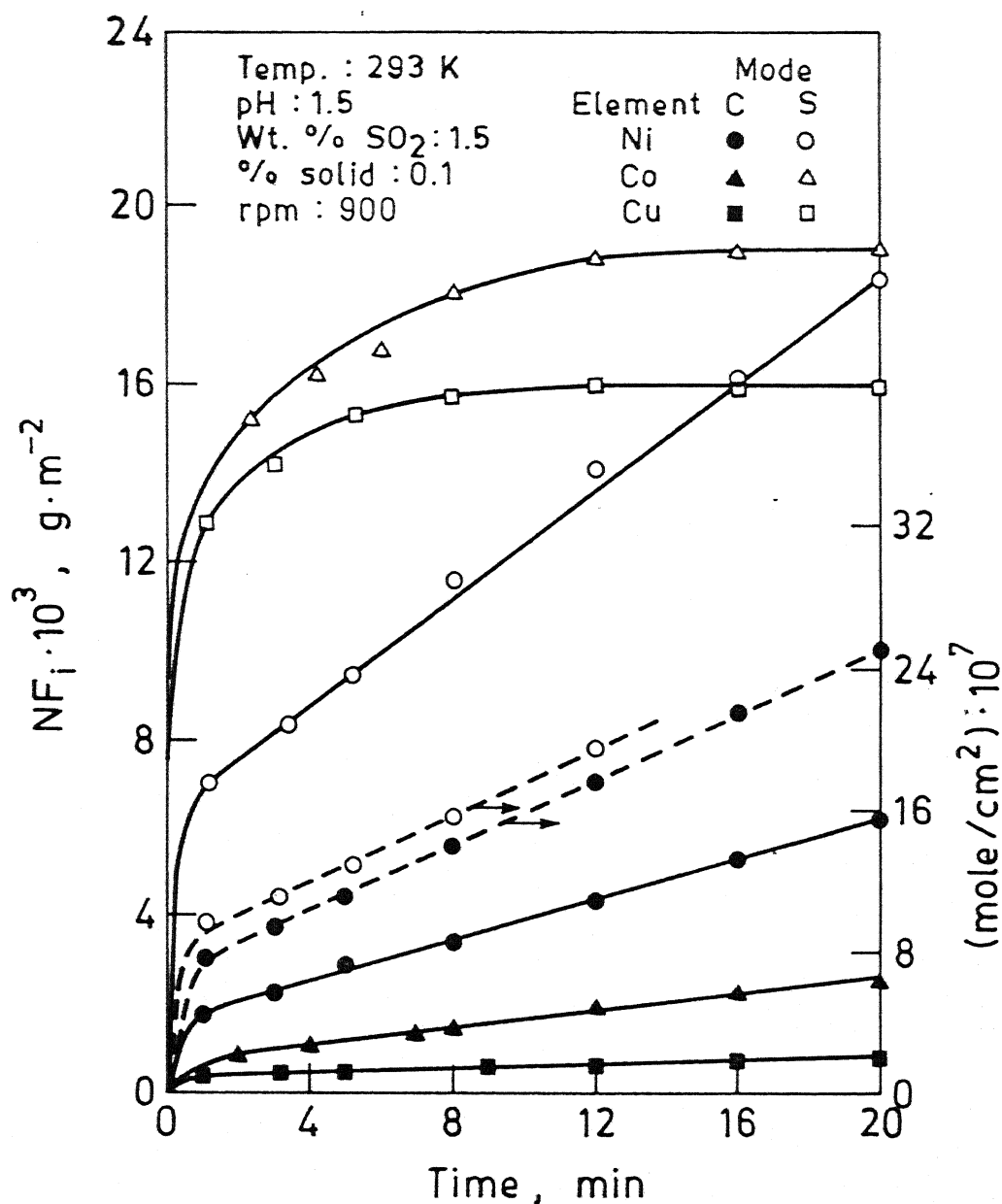


Fig. VIII.8. Effect of mode of doping on the dissolution of Ni, Co and Cu from doped goethite samples in sulfurous acid. The similarity in the dissolution behaviour of Ni in sorption and coprecipitation mode is illustrated. C—coprecipitation, S—sorption

much more preferentially dissolved compared with copper. This implies that the coprecipitation of iron with copper results in the formation of Cu-deficient poorly crystalline goethite and $\text{Fe}(\text{OH})_3$ and Cu-rich well crystalline hematite-goethite epitaxial intergrowth. X-ray studies on the leach residue from this samples have revealed that I_{110}/I_{111} ratio for the residue is much higher (~ 2.10) compared to the original samples (1.13) i.e. the Cu deficient poorly crystalline material dissolves at a faster rate leaving the Cu rich well crystalline material behind.

Inouye et al. (268) have proposed a theory to explain the effect of Cu(II) on the crystallization of $\alpha\text{-FeOOH}$. According to these workers JAHN-TELLER effect* (which operates in one direction of octahedral complex) in the coordination complex embracing Cu could be related to the distortion of total crystal structure which leads to the ease of structural transformation in some cases and to amorphous state. It appears that formation of poorly crystalline and well crystalline fractions and enrichment of Cu(II) in well crystalline fraction, with respect to poorly crystalline fraction, are inter-related.

In the case of G-Ni(C), two points need to be noted (i) similarity between dissolution curve of Ni in G-Ni(C) and G-Ni(S) (Figures VIII.7 and VIII.8) and (ii) lower value of fraction of Ni reacted in G-Ni(C) compared to G-Ni(S) (Table VIII.6). These results imply that the nickel in the solid is mainly present

* Jahn Teller effect results due to asymmetric filling of doubly degenerate e_g level in Cu(II) (d^9) (vide Appendix-M). The effect causes tetragonal distortion of octahedral co-ordination which leads to greater stabilization.

in adsorbed/occluded state. This results in a significantly lower value of (C_{Fe}/C_{Ni}) in the leach liquor.

Lussiez and Osseo-Asare (267) have proposed that the differences in the leachability of Cu^{2+} and Ni^{2+} from the goethite samples coprecipitated with these elements may be a result of differences in the concentration of their respective hydroxo complexes, as well as differences in the affinities of various complexes for adsorption site on goethite nuclei under conditions of synthesis. Through their abilities to form hydrogen bonds, hydroxyl group in an aqueous complex play a significant role in the uptake of metal by oxide colloids in alkaline medium (267). Higher the OH group concentration in an aqueous complex is, more interfacially active it will be (267). If hydroxyl group concentration were the only criterion, Co(II) (which contain $\sim 70\%$ $Co(OH)_3^-$, 20% $Co(OH)_2^0$, 10% $Co(OH)_4^{2-}$; OH/Co ratio ~ 2.9 at pH 13 in 0.1 M Co(II) solution (334)) should have leached out more easily compared to Ni(II) (which contain 50% $Ni(OH)_3^-$ and 50% $Ni(OH)_4^{2-}$, under identical conditions (334)). However this is not the case (Table VIII.6, Figures VIII.7 and VIII.8). Incidentally, it may be noted that Cu(II) at pH 13 contains only $Cu(OH)_4^{2-}$ species (334) and the behaviour of Cu and Ni can be explained only on the basis of interaction of hydroxo complexes with the colloidal oxide species of iron (267).

Recently Crerar et al. (335) have discussed the factors involved in the chemical stability of minerals. Factors like crystal field stabilization energy (CFSE) and Z_i/r_i (where Z_i and r_i are valency and ionic radius of the ion of interest) play important role in the mineral stability. During coprecipitation, the element with higher CFSE is expected to form compound of its own

rather than substituting the major element. The CFSE* of Co(II) (electronic configuration of d orbital electrons, $t_{2g}^5 e_g^2$) in octahedral field is $(-8 Dq_{oct})$ as compared to Ni(II) ($t_{2g}^6 e_g^2$, $-12 Dq_{oct}$) and Cu(II) ($t_{2g}^6 e_g^3$, $-6 Dq_{oct}$) (334). Since Ni(II) has a larger CFSE, it will form stronger bond with OH^- ligands as compared with Co(II) and Cu(II). Thus it is likely that Ni(II) will prefer surface induced precipitation over structural incorporation. On the other hand, Co(II) has smaller CFSE compared with Ni(II) i.e. the incorporation of Co(II) in goethite lattice will be favoured more compared to Ni(II). This possibly explains the intermediate behaviour of Co between Ni and Cu (Figures VIII.7 and VIII.8) in G-R(C) samples. There is only very small difference in the Fe/Co mole ratio in solid (~ 25) and solution (~ 21) in sulfuric acid leaching. These results indicate that cobalt may be predominantly present in G-Co(C) as a part of the goethite structure.

In sulfuric acid leaching, the elements doped in G-R(S) samples are easily leached out compared with V-R(S) samples (Table VIII.6, Figure VIII.7, Table VII.6, Figure VII.8). This indicates that minor elements sorbed on the surface of goethite are not incorporated in the goethite structure. Cobalt, which is not leached from V-Co(S) sample in sulfuric acid (Table VII.6) is almost completely ($F_{Co} = 0.92$, after 100 minutes) leached out from G-Co(S) sample. Since Co^{3+} is insoluble in sulfuric acid (vide Section 7.2.1), it appears that Co sorbed on α -FeOOH surface is not significantly oxidized to Co^{3+} and presence of CoOOH as detected in XPS measurement of Schenck et al. (266), is expected

* Vide Appendix-M, Table VII.3, Figure VII.10(b).

to be very small. It is interesting to note that the leachability of Co, Cu and Ni in sulfuric acid (Figure VIII.7) shows close correspondence with the CFSE (vide Table VII.3) of Co(II) (92.9 kJ/mole), Cu(II) (90.4 kJ/mole) and Ni(II) (122.2 kJ/mole) suggesting that chemical nature of these elements acts as a major controlling factor on the dissolution behaviour. Cobalt shows higher leachability compared to copper and nickel in sulfurous acid leaching also (Figure VIII.8). The dissolution behaviour of Cu in sulfurous acid seems to be complicated (Figure VIII.8) due to formation of cuprous ion (331, 332, 336). The solubility of cuprous ions at acidic pH is poor (296) and cuprous ions can also catalyze the dissolution of iron from the goethite substrate (331, 332).

CHAPTER - IX

CHARACTERIZATION AND LEACHING RESULTS ON SYNTHETIC PHASES - CRITICAL DISCUSSION

Having discussed the characterization and leaching results on synthetic oxyhydroxide of manganese and iron in the previous two chapters, the objective of this chapter is as follows: (i) to summarize the main findings on synthetic phases, (ii) to compare the results on oxyhydroxide of manganese and iron and (iii) to highlight the implications of results in the processing and genesis of manganese nodules.

9.1 Effect of Method of Doping on Mode of Occurrence

Synthetic manganese and iron oxyhydroxides showed different response to the method of doping, i.e. sorption, ion exchange and coprecipitation, of minor elements.

It has been observed that irrespective of the method of doping, elements (Ni, Co and Cu) get incorporated in the structure of birnessite and δ -MnO₂. The theory that the doped elements have been structurally incorporated is supported by (i) equivalence balance calculations (Table VII.2), (ii) failure to detect any separate phase formation for Ni, Co and Cu by XRD and TEM, (iii) structural changes detected by XRD and TEM for doped samples, (iv) structural collapse accompanied with leaching of doped elements (Figure VII.9), (v) sulfuric acid leaching data (poor leachability of doped elements from V-R(S) samples could not be explained otherwise) and (vi) sulfurous acid leaching data (close correspondence between dissolution of doped element and host phase).

The incorporation of elements in birnessite and $\delta\text{-MnO}_2$ is accompanied with structural breakdown and disorder and/or rearrangements leading to the formation of new phases. Although Giovanoli (22) hinted that incorporation of doped element in the birnessite and buserite structure in ion exchange mode might involve structural rearrangement, the nature of structural rearrangements was not highlighted. In this investigation, the structural changes that occur during doping of elements were studied in more detail, using XRD (original and intercalated samples), TEM (SAED and imaging mode) and surface area measurements, for a larger variety of samples doped in different ways. Incorporation of element in B-R(I) samples result in significant increase in surface area due to intense nature of ion exchange reaction which lead to break-up of host phase structure. The structural rearrangement in B-R(I) probably involves formation of disordered layered structure phase (e.g. B-Cu(I)) and hybrid layered or more complex tunnel structure phases (e.g. B-Co(I) and B-Ni(I)). The structural rearrangement in poorly crystalline $\delta\text{-MnO}_2$ (after doping) is evident from change in surface area (Table VII.1). Doping in coprecipitation mode is mainly characterized by break-up of crystal in a-b plane and smaller change in surface area.

In the case of sorption on goethite (G-R(S)) samples the occurrence of doped element can be described in terms of 'surface complexation model' of James et al. (325). When the doped elements are added in coprecipitation mode (G-R(C) samples) incorporation in the host phase takes place in different ways. Copper gets incorporated in the structure of goethite accompanied with structural rearrangement ($\alpha\text{-FeOOH}$ to Fe_2O_3) and formation of well

crystallized Cu-rich twinned goethite and poorly crystallized Cu-deficient phase. Ni in G-Ni(C) occurs predominantly in occluded and sorbed state. Co in G-Co(C) appeared to occur as part of the goethite structure.

The doped element causes different changes in the physical characteristics of host birnessite and goethite. Typically for the same amount of doped element (Ni/Co/Cu) in coprecipitation mode, the surface area of birnessite (B-R(C)) changes only marginally compared to pure birnessite; on the other hand, the surface area of doped goethite (G-R(C)) changes up to two times compared with that of pure goethite. Doping of elements in birnessite through the ion exchange route causes strikingly large change in surface area as discussed before.

9.2 Leaching Behaviour of the Synthetic Phases

Together with the leaching medium and conditions employed, the other factors which are relevant to the leaching of the doped elements are structure and leachability of the host phase, mode of occurrence and chemical effects (CFSE).

9.2.1 Sulfuric Acid Leaching:

Iron from α -FeOOH can dissolve in dilute sulfuric acid as Fe^{3+} ions. However the solubility of Mn^{4+} is negligible in dilute sulfuric acid (say upto 3-4N (314)). This difference in solubility of Mn^{4+} and Fe^{3+} imparts different significance to the crystallinity of manganese(IV) oxide samples and goethite. For α -FeOOH, poor crystallinity and large structural disorder means higher solubility of the host phase and diminishing effect of the mode of

occurrence. On the other hand for manganese(IV) oxides (birnessite, δ -MnO₂ etc.), higher surface area and structural disorder means greater probability of incorporation of minor elements in Mn(IV) sublattice (p. 222, also ref. (304, 324)). Since the solubility of Mn(IV) is negligible in sulfuric acid, higher surface area and structural disorder will cause poor leachability of doped element in sulfuric acid.

The dissolution behaviour of Ni(II), Cu(II) and Mn(II) from the hydrous manganese oxide samples (birnessite, δ -MnO₂) can be adequately explained in terms of the structural complexities and crystal field stabilization energy (CFSE). This is because the mode of occurrence gets eliminated as a factor i.e. irrespective of mode of doping, the elements get incorporated in the structure. The behaviour of cobalt is complicated by its presence in +(II) and +(III) state. Co(III) has a much higher CFSE compared with Ni(II), Cu(II), Co(II) and Mn(II) and negligible solubility in sulfuric acid.

The leaching of birnessites (T(2, ∞) type structure) in sulfuric acid is accompanied with collapse of birnessite structure and formation of new phases like nsutite and cryptomelane (T(1,1), T(1,2) type structures). Since the newly formed phases have more compact structure compared with the original birnessite structure, the initial fast leaching of doped elements is followed with a significantly slow leaching (Figure VII.8). Slow leaching can also be attributed to different structural sites (in MnO₆ framework structure, interlayers etc.) occupied by the doped element.

In the case of G-R(S) samples, both mode of occurrence and structural complexities can be eliminated as factors. There appears

to be reasonable correspondence between the CFSE for Ni(II), Co(II) and Cu(II) (vide Table VII.3) and their dissolution behaviour. The doped element in G-R(S) samples were easily leachable compared with V-R(S) (Tables VIII.6 and VII.6). The dissolution behaviour of the doped elements from G-R(C) samples is complicated by all the factors mentioned in the beginning of this section i.e. structure and leachability of host goethite phase, mode of occurrence and CFSE. The mode of occurrence, viz. structural incorporation, sorption, occlusion etc., seems to have maximum influence on dissolution. The elements doped in coprecipitation mode (G-R(C) samples) show inferior leachability as compared with the elements doped in sorption mode (G-R(S) samples).

The dissolution behaviour of Fe from G-O, G-R(S) and G-R(C) samples correlates well with surface area and structural disorder or microcrystalline dimension and structural disorder.

9.2.2 Sulfurous Acid Leaching:

Birnessite and δ -MnO₂ samples were almost completely and rapidly soluble in sulfurous acid concentration as small as 0.2 wt. % SO₂ (per 100 ml H₂O). On the other hand, it was found that goethite samples showed only 20-30% dissolution even in larger concentration (3-4 wt. %) of sulfurous acid. Dissolution of host manganese oxide matrix facilitates complete dissolution of the doped element. However dissolution of doped elements from G-R(C) samples is hampered due to poor leachability of goethite.

The mechanisms of dissolution of synthetic phases in sulfurous acid (reducing) may be more complex as compared with sulfuric acid viz. electrochemical dissolution of higher valency

oxides, preferential dissolution, complexation reactions involving aqueous SO_2 , reduction reaction like Cu^{2+} to Cu^+ etc.

9.3 Implications in Manganese Nodules Genesis and Processing

The synthetic phases were prepared under conditions which are far from the conditions encountered in the natural marine environment. However the synthetic phases had marked structural and chemical similarities with phases in manganese nodules. This makes the data on dissolution behaviour of synthetic phases directly relevant in nodules processing.

From the manganese nodules point of view, characterization and leaching results for B-R(I/C), V-R(S) and G-Co(C/S) are of particular significance because Ni and Cu correlate positively with Mn, and Co correlates positively with either Mn or Fe. This significance may be elaborated in the following section.

9.3.1 Mode of Occurrence and Leaching Behaviour of Nodules:

The characterization and leaching studies have suggested that irrespective of the mode of doping, the doped element (Ni, Co, Cu) get incorporated in the structure of synthetic birnessite and $\delta\text{-MnO}_2$. It means that the structure of manganese(IV) oxide phases in nodules has an important role in the uptake of Ni, Co and Cu in manganese nodules.

Fuerstenau and Han's (223) contention that for lattice substitution to be the mechanism of incorporation of minor element in manganese nodules, the minor element should show close correspondence with dissolution behaviour of major element, is not necessarily justified for oxyhydroxide phases of manganese in nodules;

there are structural peculiarities associated with them. These structural features which were noted by Buser and coworkers (305, 322) are highlighted below: (i) manganese oxide minerals in nodules are mixed valence e.g. Na-birnessite is sodium manganese(II,III), manganate(IV) and (ii) manganese oxide minerals, which are relevant to nodules, show structurally conditioned defects (such as lattice regions with different degree of order); this imparts to them pronounced reactivity even at room temperature. Higher reactivity will result in preferential dissolution of divalent Ni, Co and Cu in sulfuric acid without appreciably attacking the Mn(IV)O_6 framework structure.

Figure IX.1 illustrates some typical leaching curves of nodules in sulfuric acid under similar experimental conditions as employed by us for synthetic samples. Comparison of Figure IX.1 with Figure VII.8 (for synthetic samples) reveals some striking similarities: (i) leachability order ($\text{Cu} > \text{Ni} > \text{Co}$) for nodules is same as observed for synthetic manganese oxide sample (same mode of doping), (ii) for the same mode of doping the dissolution of Ni showed more time dependence compared with Cu, and (iii) leaching curves are characterized by an initial fast release of elements.

The leaching sequence is consistent with the CFSE of Cu(II) , Ni(II) and Co(III) (Table VII.3). In some investigations on sulfuric acid leaching of nodules (39, 223) cobalt has shown higher leachability compared with Cu and Ni. Also fraction of Co reacted did not show any increase with time. Elemental correlations in manganese nodules have shown that quite often cobalt

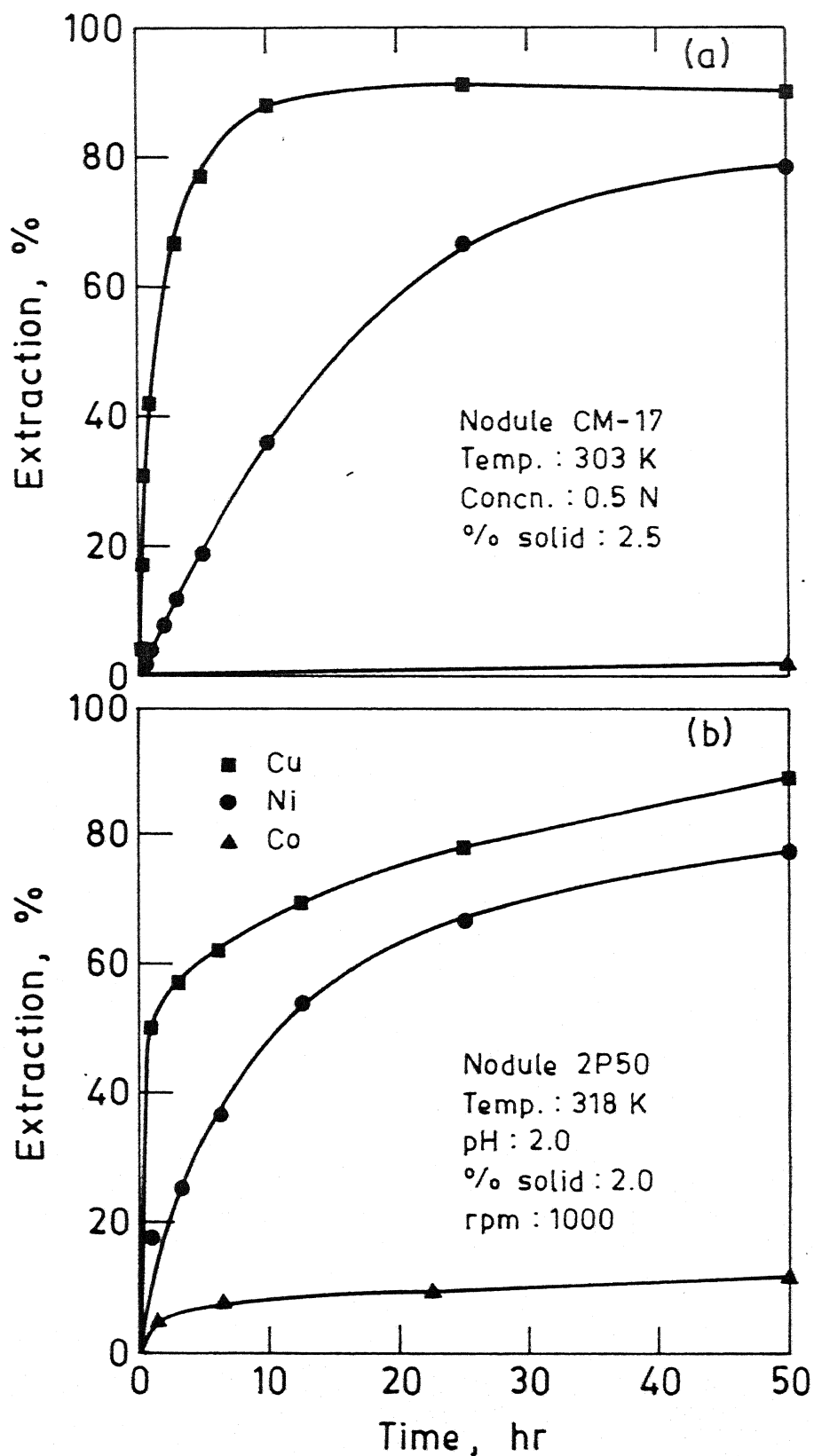


Fig. IX.1. Dissolution behaviour of Ni, Co and Cu from manganese nodule in sulfuric acid. Adopted from (a) Itoh et al. (225) and (b) Fuerstenau et al. (15).

correlates positively with iron (p. 39). Our leaching results on G-Co(S) suggest that cobalt adsorbed on α -FeOOH remain predominantly in +II oxidation state. The higher leachability of cobalt may be attributed to positive association with iron and/or lower oxidation state. The CFSE of Co(II) is very similar to Cu(II) (Table VII.3).

Keeping in view the similarities in mineralogy and dissolution behaviour of synthetic phases with manganese nodules it is proposed that (i) elements like Ni, Co and Cu are incorporated in manganese oxide phases of nodules in lattice substitution mode, (ii) multiple substitution sites are available in structure of host manganese oxide phases (p. 190) and (iii) the interaction of nickel, cobalt and copper with host manganese(IV) oxide phases in nodules is specific in nature i.e. chemical effects like CFSE are involved in the interaction.

The precise mechanisms of substitution of Ni, Co and Cu in the structure of manganese(IV) oxide phases (e.g. phyllomanganate) are not well understood and these are expected to be complicated by the presence of Mn(III) in the structure.

The synthetic cobalt-bearing goethite samples (doped in sorption and coprecipitation mode) do not provide much insight regarding mode of occurrence (sorption/coprecipitation) of Co in iron-bearing minerals present in nodules. The crystallinity of iron bearing minerals in nodules, e.g. goethite (Figure V.7), is very poor compared with the synthetic samples (Figure VIII.3, Table VIII.5). Poor crystallinity means large number of broken bonds. Thus effect of mode of occurrence (sorption/coprecipitation) will not be very pronounced for natural manganese nodules.

Unlike the cobalt-bearing manganese oxyhydroxide samples (e.g. V-Co(S)), there is no evidence to suggest oxidation of doped Co(II) in G-Co(S/C) to higher oxidation state. Halbach et al. (169) have suggested that cobalt can form robust complex with $\equiv \text{FeH}_2\text{SiO}_4^-$ in natural manganese nodule, and can be oxidized to higher oxidation state in strong electric field of Si^{4+} . There is no definite experimental evidence available to support this contention except the positive association of Co with Fe in radial and columnar type of morphology. The role of Mn^{4+} , in oxidation of cobalt from +(II) to +(III) state, was suggested by Crowther et al. (300). Halbach et al. (169) has drawn analogy between the role of Mn^{4+} and Si^{4+} in oxidation of Co(II) to higher oxidation state. It may be pointed out that oxidation of Co(II) can be facilitated in strong electric field of Mn^{4+} because it can undergo reduction to lower valency state i.e. +II. This possibility is ruled out for Si^{4+} . The substitution of low spin Fe^{3+} ($r = 0.55 \text{ \AA}$) by low spin Co^{3+} ($r = 0.53 \text{ \AA}$), as suggested by some workers (80, 101), is also open to question because low spin configuration for Fe^{3+} is unstable. This suggests that more definite evidence is required to support the occurrence of Co(III) in iron bearing phases. The present work suggests that oxidation of Co(II) in iron bearing minerals is not likely.

The collapse of birnessite structure and formation of new phases like nsutite and cryptomelane have very important significance for the sulfuric acid leaching of nodules. Since nsutite and cryptomelane (T(1,1), T(1,2) type of structure) have more compact structure compared with birnessite (T(2, ∞) structure), the

structural changes during leaching of synthetic phases and similar phases in nodules can result in a drastic decrease in the dissolution rate.

The future attempts to minimize the degree of structural collapse, during leaching of elements, may have far-reaching implications for recovery of metals in sulfuric acid leaching. Hypothetically the problem lies in finding out element/s or their organic complexes which can enter into the structure of layered tunnel structure phases and remain in structure during leaching without adversely affecting the dissolution of valuable minor elements present in the structure.

In contrast with sulfuric acid leaching, no specific leachability order, for doped elements, is observed in sulfurous acid leaching of nodules (39, 224, 237). Similar observations made in this investigation for sulfurous acid leaching of synthetic manganese oxide samples were attributed to complex dissolution mechanisms. The complex dissolution mechanisms in sulfurous acid may involve electrochemical dissolution of higher valency oxides, preferential dissolution governed by crystallinity and structural disorders and nature of doped element/s, preferential dissolution of Co(II) over Co(III), complexation reactions involving aqueous SO_2 , reduction reaction like Cu^{2+} to Cu^+ (unstable). Thus, in addition to the physico-chemical characteristics of phases, the dissolution will be influenced by other complex chemical effects resulting from the interaction of SO_2 .

The complex nature of sulfurous acid leaching has led to many apparent conclusions, not always justifiable, regarding the mode of occurrence of elements in manganese nodules. Han and

Fuerstenau (224) studied the leaching behaviour of nodules with respect to Cu and other major and minor elements dissolution in reducing media namely sulfurous and sulfuric acid. These workers contended that since there was no direct correspondence between Cu and major element dissolution, Cu occur in nodules in sorption mode. The factors which have not been considered in arriving at this conclusion are mineralogical and chemical heterogeneity of nodules sample used, the behaviour of Cu in reducing environment etc. Our leaching results on synthetic samples have shown that mineralogy of host phase can significantly influence the dissolution of doped element. Nodule sample may contain $\delta\text{-MnO}_2$ and 10 A° phase. SEM/EDAX results (Chapter VI) have shown that 10 A° phase is relatively more enriched with Cu as compared to $\delta\text{-MnO}_2$ phase. Preferential dissolution of any of the two phases can lead to apparent discrepancy between Cu and Mn dissolution. Cu^+ ions (unstable, poor solubility) which form due to leaching of Cu in reducing environment may take part in several side reactions e.g. Cu^+ can catalyse the dissolution of ferric iron from goethite (vide Section 8.2). All these complexities in sulfurous acid leaching make it unsuitable for prediction of mode of occurrence of elements in natural nodules.

9.3.2 Significance of Internal Structure in Leachability of Nodules:

The internal structure of manganese nodules and minerals present therein constitute important mineralogical factors in nodules processing. The internal structure of nodules is governed by growth environment (vide Chapter VI). Typically, nodules which form in highly oxidizing environment or the one which grow in

seamount regions have predominantly columnar and radial kind of morphology (Figure VI.13). Nodules with columnar and radial pattern kind of morphology ($\delta\text{-MnO}_2 + \text{FeOOH} \cdot \text{XH}_2\text{O}$ assemblage) are expected to have inferior leachability in sulfuric acid leaching (under identical conditions) compared with nodules having compact type of morphology (forms in highly reducing environment, manganese mineral disordered buserite-todorokite assemblage) or dendritic segregation (forms in reducing environment, tunnel structure 10 \AA^0 phase) (25, 26). In brief, we want to emphasize that in addition to total (Ni + Co + Cu) content and abundance, predominant mineralogy is an equally important parameter in deciding the ore grade of nodules.

Published literature on extraction of metals from manganese nodules lacks detailed description of nodules used in terms of internal structure, mineralogy and elemental associations. We expect our data on synthetic phases to prove more useful if used in conjunction with leaching data on nodules having predominantly one kind of internal structure (Figure VI.13).

9.3.3 Other Considerations:

Detailed kinetic studies on the synthetic samples are expected to provide more insight relevant to processing of nodules in sulfuric and sulfurous acid. The time dependant structural changes during leaching of birnessites in sulfuric acid need to be paid due attention in kinetic studies and incorporated in the mathematical models on kinetics.

The leaching studies on the synthetic phases represent idealized situation. However in actual nodules, manganese bearing minerals are found associated with iron bearing minerals and silicates. The effect of iron bearing minerals and silicates on the dissolution behaviour of elements from manganese minerals needs special studies. Some silicates dissolve in acid with extensive release of silica (262). The leached out silica can interact with metal ions in solution and result in apparent decrease in metal extraction (262).

CHAPTER - X

CONCLUSIONS AND RECOMMENDATIONS

This investigation was undertaken to study (i) the microfeatures, viz. the constituent minerals, internal structure, elemental and mineral assemblages in the Indian Ocean manganese nodules and (ii) the role of physico-chemical characteristics of synthetic oxyhydroxides of manganese and iron on the dissolution behaviour of major (Mn and Fe) and minor elements (doped Ni, Co and Cu) in sulfuric and sulfurous acid leaching. The characterization work which has been carried out on nodules from the Central Indian Basin is expected to enhance our understanding of the structural features of nodules from different growth environments in general. The systematic characterization and leaching work on the synthetic phases, which is perhaps the first of its kind, is expected to serve as the starting point for any future studies attempting to correlate the structure of nodules and their leaching behaviour.

The major conclusions of this work are as follows:

1. XRD and TEM (SAED, EDAX and imaging mode) studies on leach residues (obtained after sequential extractions) and synthetic oxyhydroxides of manganese and iron can significantly facilitate the identification of minerals in nodules. The multimineralic nature of nodules makes the use of computer programme for indexing of SAED spot patterns indispensable.
2. The following minerals have been identified in nodules from the Central Indian Ocean Basin.

Manganese Minerals: 10 Å⁰ phase (Buserite/Todorokite),
Birnessite, δ-MnO₂ (vernadite);

Iron Minerals: Ferroxhyte, Goethite, Ferrihydrite;

Silicates: α-quartz, Labradorite, Kaolinite, Montmorillonite;

Biogenics: Calcite.

3. (a) The structure of the 10 Å⁰ phase in the nodules investigated is not a simple layered structure like synthetic Na-buserite/birnessite.
- (b) The crystallite size of iron bearing minerals is of the order of ~ 200 Å⁰ or smaller.
- (c) The mineral δ-MnO₂ is found intimately associated with the iron bearing mineral ferroxhyte.
4. The elemental correlations derived from X-ray microanalysis data (SEM/SE/EDAX) are very similar to the correlations derived from bulk chemical analysis data from nodules in different regions of the Central Indian Ocean Basin. The correlations of minor elements (e.g. Ni, Mg, Co, Ti etc.) with the major elements are corroborated by the results of sequential extraction. A significant proportion of iron in the nodules is associated with the silicate fraction.
5. BSE/Z-contrast imaging with simultaneous X-ray microanalysis provide valuable insight on the internal structure vis-a-vis chemical composition of manganese nodules. Statistical analysis of X-ray microanalysis data for Z-contrast/BSE/SEM images by Q-mode factor analysis results in factors which are typical of phases observed in XRD and TEM investigation. These factors are also related to the genesis of the different

structural features in the nodules. Factor loadings for different regions in different growth morphologies enable one to find correlations among the textural patterns, chemical composition, minerals present and genesis.

6. Three distinct kinds of growth features namely compact type morphology, dendritic segregation and columnar and radial pattern indicate that the growth of nodules in Central Indian Ocean Basin has possibly taken place in three kinds of environments. For example, compact kind morphology reflects highly reducing diagenesis and excessive mobilization of elements in the sediment; dendritic segregation signifies moderate mobilization of Mn^{2+} , Ni^{2+} and Cu^{2+} ions; columnar and radial patterns form by hydrogenetic growth during the period of erosional conditions. Microstructural evidence regarding role of silica in the fractionation of manganese and iron in compact kind of morphology has been presented.
7. The elemental correlations based on SEM/SE/EDAX data provide only a broad picture. Positive association does not always mean positive correlation e.g. both in compact kind of morphology and columnar and radial patterns, Ni and Cu are associated with manganese phase but they show negative correlation in one case (i.e. compact type) and positive correlation in the other case (i.e. columnar and radial pattern). Cobalt is associated with iron bearing fraction in radial and columnar pattern and with manganese fraction in compact type of morphology.
8. (a) The synthetic phases show marked structural similarities with the phases in manganese nodules.

- (b)
 - (i) Irrespective of the method of doping, the doped elements get incorporated in the structure of host birnessite and $\delta\text{-MnO}_2$ phases.
 - (ii) Doping in oxyhydroxides of manganese is accompanied by structural breakdown, disorder or rearrangements leading to the formation of new phases.
 - (iii) In terms of structural complexities the doped samples can be arranged as follows: sorption > ion exchange > coprecipitation.
 - (c) The doping of goethite in sorption mode does not lead to structural incorporation of the doped element. Elements doped in coprecipitation mode may be present in the structure of the host goethite phase or remain in occluded/sorbed state.
9. Both structure of host phases and method of doping can influence leaching behaviour of major and minor elements in sulfuric acid leaching, viz., (a) leachability of minor elements can be adequately explained in terms of CFSE (for elements doped on goethite surface) or CFSE and structural complexities (all synthetic manganese oxyhydroxide samples), (b) the elements doped in goethite in coprecipitation mode show complex leaching behaviour due to multiple modes of occurrence (e.g. structural incorporation of Cu in goethite and fractionation in poorly crystalline (Cu-deficient) and well crystalline (Cu-rich) goethite constituents, occurrence of Ni in occluded and sorbed state etc.) and (c) the dissolution behaviour of iron from goethites correlates well with

surface area and structural disorder or microcrystalline dimension and structural disorder.

10. Crystal structures of manganese hydroxide phases play a very important role in the uptake of minor elements in manganese nodules. The mode of occurrence of Ni, Co and Cu in oxyhydroxide phases of manganese in nodules is predominantly structural substitution.
11. The leaching behaviour of minor elements from manganese nodules in sulfuric acid show marked similarities (in terms of leachability and nature of leaching curves) with the leaching behaviour of doped elements from synthetic manganese oxyhydroxide phases. The leaching kinetics may be explained in terms of multiple structural sites (e.g. in intermediate layer or main layer edifice) and/or structural collapse during leaching which leads to poorly leachable phases like nsutite and cryptomelane.
12.
 - (a) Manganese oxyhydroxide samples are rapidly and completely leached in sulfurous acid.
 - (b) Slow dissolution of goethites influences the dissolution behaviour of elements doped in coprecipitation mode.
 - (c) The elements are preferentially attacked in sulfurous acid depending upon crystallinity and structural disorder of samples, and chemistry of elements in reducing environment.
13. Complex mechanistic factors, which affects the dissolution of elements in sulfurous acid leaching, makes the leaching data unsuitable for diagnostic certification of mode of occurrence of minor elements in manganese nodules.

Scope for Further Research

The areas identified for further research are:

1. HRTEM studies on 10 \AA^0 phase from distinct internal morphologies to establish the identity of phase (as todorokite or buserite) vis-a-vis internal features.
2. Phase identification with TEM/EDAX vis-a-vis internal structure (i.e. use of ion-beam thinning and replica techniques in sample preparation for TEM).
3. Detailed studies on the kinetics of leaching of synthetic phases in different media under varied leaching conditions.
4. Studies on the mechanisms of lattice substitution reactions in birnessite and other manganese(IV) oxide phases for different methods of doping.
5. Detailed spectroscopic (e.g. ESCA) and HRTEM studies on the synthetic phases (before and after leaching).
6. Leaching studies on nodules having predominantly one kind of mineralogy and internal structure in sulfuric acid and other leaching media.
7. Further detailed studies on the structural transformations during sulfuric acid leaching.
8. Sulfuric acid leaching under controlled reduction potential i.e. addition of small amounts of sulfites at different stages of leaching by sulfuric acid.
9. Evolving the ideal flowsheet for metal recovery from manganese nodules.

REFERENCES

1. Mero, J.L., The Mineral Resources of the Sea (Elsevier, Amsterdam, 1965) 312 pp.
2. Mero, J.L., Potential economic value of ocean floor manganese nodule deposits. In: D.R. Horn (ed.) Ferro-manganese Deposits of Ocean Floor (National Science Foundation, Washington, D.C., 1972) pp. 91-203.
3. Siddiquie, H.N., Dasgupta, D.R., Sengupta, N.R., Shrivastava, P.C. and Mallik, T.K., Manganese-iron nodules from the Indian ocean, Indian J. Mar. Sci., Vol. 7 (1978) pp. 239-253.
4. Marchig, V., Marine manganese nodules. In: Topics in Current Chemistry, Vol. 99 (Springer-Verlag, Berlin, 1981) pp. 100-126.
5. Manjula, R.S., Metals from the Sea Bed - Prospects for Mining Polymetallic Nodules by India (Oxford and IBH Publishing Co., N. Delhi, 1982) 165 pp.
6. Moncrieff, A.G., Presidential address, Institute of Mining and Metallurgy, London, May 21, 1987.
7. Lee, J.J.H., Zeitlin, H. and Fernando, Q., Selective separation of molybdenum as volatile halides from deep-sea ferro-manganese nodules. Sep. Sci. Technol., Vol. 15, No. 10 (1980) p. 1709.
8. Malenbaum, W., World Demand for Raw Materials in 1985 and 2000 (McGraw Hill, New York, 1978).
9. Jena, P.K., Director's address, National Seminar on Processing of Manganese Nodules, Regional Research Laboratory, Bhubwaneswar, 28th February-1st March, 1985.
10. Murthy, T.K.S. and Nagle, R.A., Nodules from the Sea, Science Today, November 1985, pp. 52-55.
11. Archer, A.A., Manganese nodules as a source of nickel, copper, cobalt and manganese. Trans. Inst. Min. Metall., Vol. 90 (1981) pp. 1-6.
12. Mero, J.L., Economic aspects of nodule mining. In: G.P. Glasby (ed.) Marine Manganese Deposits (Elsevier, Amsterdam, 1977) pp. 325-355.
13. RakeshKumar, Ray, R.K. and Biswas, A.K., Manganese and iron oxide phase in manganese nodules and occurrence of nickel, cobalt and copper - a review, Paper presented in 'National Seminar on Processing of Manganese Nodules' at Regional Research Laboratory, Bhubwaneswar (India), February 28th-March 1st, 1985.

14. Buser, W. and Grutter, A., *Über die natur der manganknollen.* Schweiz. Miner. Petrogr. Mitt., Vol. 36 (1956) pp. 49-62.
15. Fuerstenau, D.W., Herring, A.P. and Hoover, M., *Characterization and extraction of metals from sea floor nodules,* Trans. AIME, Vol. 254 (1973) pp. 205-211.
16. Sorem, R.K., *Mineral recognition and nomenclature in marine manganese nodules.* Acta Miner. Petrogr. Szeyed, Vol. 20 (1972) pp. 383-84 (Abstract).
17. Sorem, R.K. and Foster, A.R., *Internal structure of manganese nodules and implications in beneficiation.* In: D.R. Horn (ed.) *Ferromanganese Deposits on the Ocean Floor* (National Science Foundation, Washington, D.C., 1972) pp. 167-181.
18. Burns, R.G. and Burns, V.M., *Mineralogy.* In: G.P. Glasby (ed.) *Marine Manganese Deposits* (Elsevier, Amsterdam, 1977) pp. 185-248.
19. Heimendahl, M. Von, Hubred, G.L., Fuerstenau, D.W. and Tomas, G., *A transmission electron microscopy study of deep sea manganese nodules.* Deep Sea Research, Vol. 23 (1976) pp. 69-79.
20. Burns, R.G., Burns, V.M. and Stockman, H.W., *A review of todorokite-buserite problem: implications to the mineralogy of marine manganese nodules,* Amer. Miner., Vol. 68 (1983) pp. 972-980.
21. Giovanoli, R., *A review of the todorokite-buserite problem: implications to the mineralogy of marine manganese nodules: discussion.* Amer. Miner., Vol. 70 (1985) pp. 202-204.
22. Giovanoli, R., *On natural and synthetic manganese nodules.* In: I.M. Varentsov and G. Grasselly (eds.) *Geology and Geochemistry of Manganese,* Vol. 1 (Akademiai Kiado, Budapest, 1980) pp. 159-202.
23. Giovanoli, R., *Vernadite is random-stacked birnessite.* Mineral. Deposita (Berl.) Vol. 15 (1980) pp. 251-253.
24. Glasby, G.P. and Read, A.J., *Deep sea manganese nodules.* In: K.H. Wolf (ed.) *Handbook of Stratabound and Stratiform Ore Deposits* (Elsevier, Amsterdam, 1976), pp. 295-340.
25. Halbach, P., Scherhang, C., Hebisch, V. and Marchig, V., *Geochemical and mineralogical control of different genetic type of deep-sea manganese nodules from the Pacific ocean.* Mineral. Deposita (Berl.) Vol. 16 (1981) pp. 59-84.
26. Lyle, M., *The formation and growth of ferromanganese oxides on the Nazea Plate.* In: L.D. Kulm, J. Dymond, E.J. Dasch and D.M. Hussong (eds.) *Geol. Soc. Amer. Memoir,* Vol. 54 (1981) pp. 269-295.

27. Haynes, B.W., Law, S.L., Barron, D.C. and David, C.B., Mineralogical and Elemental Description of Pacific Manganese Nodules. Information Circular 8906 (US Department of Interior Bureau of Mines, 1983).
28. Dilard, J.G., Crowther, D.L. and Murray, J.W., The oxidation state of cobalt and selected metals in Pacific ferromanganese nodules, *Geochem. Cosmochem. Acta*, Vol. 46 (1982) pp. 755-59.
29. Horn, D.R. (ed.) *Ferromanganese Deposits on the Ocean Floor* (National Science Foundation, Washington, D.C., 1972) 293 pp.
30. Morgenstein, M. (ed.) *Papers on the Origin and Distribution of Manganese Nodules in the Pacific and Prospects for Exploration* (Hawaii Institute of Geophysics, 1973) 175 pp.
31. Glasby, G.P. and Hubred, G.L., *Comprehensive Bibliography of Marine Manganese Nodules*. New Zealand Oceanographic Institute Memoir, 71, 1976.
32. Glasby, G.P. (ed.) *Marine Manganese Deposits* (Elsevier, Amsterdam, 1977) 523 pp.
33. Calvert, S.E., *Geochemistry of oceanic ferromanganese deposits*. *Phil. Trans. R. Soc. London*, Vol. A290 (1978) pp. 43-73.
34. Bischoff, J.L. and Piper, D.Z. (eds.) *Marine Geology and Oceanography of the Pacific Manganese Nodule Province* (Plenum Publishing Corp., N.Y., 1979).
35. Sorem, R.K. and Fewkes, R.H., *Manganese Nodules Research Data and Method of Investigation*, (Plenum Publishing Corp., N.Y., 1980).
36. Burns, R.G. (ed.) *Marine Minerals, Review of Mineralogy*, Vol. 6 (Mineralogical Society of America, Washington, D.C., (1979).
37. Cronan, D.S., *Underwater Minerals* (Academic Press, London, 1980) 362 pp.
38. Varentsov, I.M. and Grasselly, G. (eds.) *Geology and Geochemistry of Manganese* (Akademiai Kiado, Budapest, 1980).
39. Fuerstenau, D.W. and Han, K.N., *Metallurgy and Processing of Marine Manganese Nodules. Mineral Processing and Technology Review*, Vol. I (1983) pp. 1-83.
40. Hubred, G.L., *Manganese Nodule Extractive Metallurgy Review 1973-1978*, *Mar. Min.*, Vol. 2 (1980) pp. 191-212.
41. Haynes, B.W., Law, S.L. and Maeda, R., *Updated Process Flowsheets for Manganese Nodule Processing*. Information Circular 8924 (Bureau of Mines, US Department of the Interior, Washington, D.C., 1983).

42. Hillman, C.T., Manganese Nodules Resources of Three Areas in Northeast Pacific Ocean: With Proposed Mining-Beneficiation System and Cost. Inf. Circ. 8933 (Bureau of Mines, US Department of the Interior, Washington, D.C., 1983) 60 pp.
43. Ritcey, G.M., Lucas, B.H. and MacKennon, D.J., DCOM Deep Ocean Mining Study - A Review and Comparisons of Routes for Processing Manganese Nodules. Mineral Sciences Laboratory Report MRP/MSL 77-194 (Canada Department of Energy, Mines and Resources, Ottawa, Ontario, February 1977) 32 pp.
44. Agarwal, J.C., Beecher, N., Davies, D.S., Hubred, G.L., Kakaria, V.K. and Moslen, H.J., Comparative economics of recovery of metals from ocean nodules. Mar. Min., Vol. 2, No. 1-2 (1979) pp. 119-149.
45. Boin, U., Limits and possibilities of deep sea mining for the extraction of mineral raw materials - the case of manganese nodules. Min. Mag., January (1980) pp. 43-47.
46. Lalou, C. (ed.) La Genese de Nodules de Manganese (Editions du Centre National de La Recherche Scientifique, Paris, 1979).
47. Halbach, P. and Winter, P. (eds.) Marine Mineral Deposits: New Research Results and Economic Prospects (Gluckauf. Essen., West Germany, 1983).
48. Siddiquie, H.N., Gujar, A.R., Hasmi, N.H. and Valsangkar, A.B., Surficial mineral resources of the Indian ocean. Deep Sea Res., Vol. 31 (1984) pp. 763-812.
49. Roonwal, G.S., The Indian Ocean Explorable Mineral and Petroleum Resources (Springer-Verlag, Berlin, Heidelberg, 1986) 198 pp.
50. Cronan, D.S., Deep-sea nodules: distribution and geochemistry. In: G.P. Glasby (ed.) Marine Manganese Deposits (Elsevier, Amsterdam, 1977) pp. 11-44.
51. Qasim, S.Z., Bonanza from the sea. Science Today, June (1981) p. 19.
52. Skornyakova, N.S., Zonal regularities in occurrence, morphology and chemistry of manganese nodules of the Pacific Ocean. In: J.L. Bischoff and D.Z. Piper (eds.) Marine Geology and Oceanography of the Pacific Manganese Nodule Province (Plenum Publishing Corp., 1979).
53. Johnson, C.E. and Glasby, G.P., Mössbauer determination of particle size in microcrystalline iron-manganese nodules. Nature, Vol. 222 (1968) pp. 376-377.

54. Burns, R.G. and Burns, V.M., Manganese oxide. In: R.G. Burn (ed.) Review of Mineralogy (Mineralogical Society of America, Washington, D.C., 1979) pp. 1-46.
55. Turner, S. and Buseck, P.R., Manganese oxide tunnel structure and their intergrowths. *Science*, Vol. 203 (1979) pp. 456-458.
56. Wakeham, S. and Carpenter, R., Electron spin resonance spectra of manganese nodules. *Trans. Amer. Geophys. Union*, Vol. 54, No. 4 (1973) p. 339.
57. Wakeham, S. and Carpenter, R., Electron spin resonance spectra of marine and freshwater manganese nodules. *Chem. Geol.*, Vol. 13 (1974) pp. 39-47.
58. Anderman, G., An evaluation of analytical techniques to obtain spectroscopic characterization of molecular properties of manganese nodules. In: Inter-University Program of Research on Ferromanganese Deposits on the Ocean Floor - Phase I Report (National Science Foundation, IDOE, Washington, D.C., 1973) pp. 39-43.
59. Lee, J.J.H., Gilje, J.W., Zeitlin, H. and Fernando, Q., Selective separation of metals from deep-sea ferromanganese nodules by sulfur dioxide reduction. *Sep. Sci. Technol.*, Vol. 15, No. 10 (1980) pp. 1721-1732.
60. Murray, J.W., Balistrieri, L.S. and Paul, B., The oxidation state of manganese in marine sediments and ferromanganese nodules. *Geochim. Cosmochim. Acta*, Vol. 48 (1984) pp. 1237-1247.
61. Piper, D.Z., Basler, J.R. and Bischoff, J.L., Oxidation state of marine manganese nodules. *Geochim. Cosmochim. Acta*, Vol. 48 (1984) pp. 2347-2355.
62. Murray, J.W. and Dillard, J.G., The oxidation of Co(II) adsorbed on manganese dioxide. *Geochim. Cosmochim. Acta*, Vol. 43 (1979) pp. 781-787.
63. Burns, R.G., Mineralogical application of crystal field theory (Cambridge University Press, Cambridge, 1970), 168 pp.
64. Gager, H.M., Mössbauer-spectra of deep sea iron-manganese nodules. *Nature*, Vol. 220 (1968) pp. 1021-1023.
65. Herzenberg, C.L. and Riley, D.L., Interpretation of Mössbauer spectra of marine iron-manganese nodules. *Nature*, Vol. 224 (1969) pp. 259-260.
66. Carpenter, R. and Wakeham, S., Mössbauer studies of marine and freshwater manganese nodules. *Chem. Geol.*, Vol. 11 (1973) pp. 109-116.
67. Hryniewicz, A.Z., Sawicka, B.D. and Sawicki, J. A., The Mössbauer effect in the Pacific ocean Fe-Mn nodules.

- Phys. Stat. Sol., Vol. 3 (1970) pp. 1039-1045.
68. Hryniewicz, A.Z., Pustowka, A.J., Sawicka, B.D. and Sawicki, J.A., Mössbauer effect analysis of Fe-Mn nodules from various Pacific ocean locations. Phys. Stat. Sol., Vol. 10 (1972) pp. 281-287.
 69. Henderson, P., Inorganic Geochemistry (Pergamon Press, 1982) pp. 353 pp.
 70. Shannon, R.D., Revised effective ionic radii and systematic study of interatomic distances in halides and chalcogenides. Acta Cryst., Vol. A32 (1976) pp. 751-767.
 71. Murray, J.W., Iron oxides. In: R.G. Burns (ed.) Marine Minerals (Mineralogical Society of America, Washington, D.C., 1979) pp. 47-98.
 72. Giovanoli, R. and Arrhenius, G., Structural chemistry of marine manganese and iron minerals and synthetic model compounds. In: P. Halbach (ed.) Marine Mineral Deposits: New Research Results and Economic Prospects (Gluckauf, Essen., W. Germany, 1983).
 73. Giovanoli, R., Manganese oxide minerals. Transactions of XIIIth Congress of International Society of Soil Science (Hamburgh, 13th to 20th August 1986); Symposia Papers, Hamburgh, 1987, pp. 335-345.
 74. Bernal, J.D., Dasgupta, D.R. and Mackay, A.L., The oxides and hydroxides of iron and their structural inter-relationships. Clay Minerals Bull., Vol. 4, No. 21 (1959) pp. 15-30.
 75. Fasiska, E.J., Structural aspects of the oxides and oxyhydrates of iron. Corrosion Sci., Vol. 7 (1967) pp. 833-839.
 76. Turner, S. and Buseck, P.R., Todorokites: A family of naturally occurring manganese oxides. Science, Vol. 212, No. 4498 (1981) pp. 1024-1027.
 77. Chukhrov, F.V., Gorshkov, A.I., Vitovskaya, I.V., Drits, V.A. and Sivtsov, A.V., On the nature of Co-Ni asbolane; a component of some supergene ores. In: G.C. Amstutz et al. (eds.) Ore Genesis - The State of the Art (Springer Verlag, Berlin, 1982) pp. 230-239.
 78. Francombe, M.H. and Rooksby, H.P., Structure transformations effected by the dehydration of diaspor, goethite and delta ferric oxide. Clay Minerals Bull., Vol. 4, No. 21 (1959) pp. 1-14.
 79. Kauffman, K. and Hazel, F., Infrared and Mössbauer spectroscopy, electron microscopy and chemical reactivity of ferric chloride hydrolysis products. J. Inorg. Nucl. Chem., Vol. 37 (1975) pp. 1139-1148.

80. Haynes, B.W., Law, S.L. and Barron, D.C., The mineralogy and geochemistry of Pacific manganese nodules. Paper presented in 27th International Geological Congress, August 4-14, 1984, Moscow, USSR.
81. Haynes, B.W., Law, S.L., Barron, D.C., Kramer, G.W., Maeder, R. and Magyar, M.J., Pacific Manganese Nodules: Characterization and Processing, Bulletin 679 (Bureau of Mines, US Department of Interior, Washington, D.C., 1985).
82. Haynes, B.W., Law, S.L., Barron, D.C., An Elemental Description of Pacific Manganese Nodules. *Mar. Min.*, Vol. 5, No. 3 (1986) pp. 239-276.
83. Chukhrov, F.V., Gorshkov, A.I., Beresovskaya, V.V. and Sivtsov, A.V., Contribution to the mineralogy of authigenic manganese phases from marine manganese deposits. *Mineral. Deposita (Berl.)*, Vol. 14 (1979) pp. 249-261.
84. Chukhrov, F.V., Gorshkov, A.I., Drits, L.E., Sheterenberg, A.V. and Sakharov, B.A., Mixed layer asbolan-buserite minerals and asbolans in oceanic iron-manganese concretions. *Internat. Geol. Rev.*, Vol. 25 (1983) pp. 838-847.
85. Burns, R.G., Burns, V.M. and Stockman, H.W., The todorokite-buserite problem: further considerations. *Amer. Mineral.*, Vol. 70 (1985) pp. 205-208.
86. Ostwald, J., Some observations on chemical composition of todorokite. *Mineral. Mag.*, Vol. 50 (1986) pp. 336-340.
87. Chukhrov, F.V., Gorshkov, A.I., Sivtsov, A.V. and Beresovskaya, V.V., New data on natural todorokites. *Nature*, Vol. 278 (1979) pp. 631-632.
88. Turner, S., Malcolm, D. and Buseck, P.R., Structure features of todorokite intergrowth in manganese nodules. *Nature*, Vol. 296 (1982) pp. 841-842.
89. Giovanoli, R., Layer structures and tunnel structures in manganates. *Chem. Erde*, Vol. 44 (1985) pp. 227-244.
90. Giovanoli, R., Burki, P., Giuffredi, M. and Stumm, W., Layer structured manganese oxide hydroxides. IV: the buserite group; structure stabilization by transition elements. *Chimia*, Vol. 29, No. 12 (1975) pp. 517-520.
91. Paterson, E., Intercalation of synthetic buserite by dodecylammonium chloride. *Amer. Mineral.*, Vol. 66 (1981) pp. 424-427.
92. Buser, W. and Graf, P., Differenzierung von mangan(II) manganit und δ -MnO₂ durch oberflächenmessung nach Brunauer-Emmett-Teller. *Helv. Chim. Acta*, Vol. 38 (1955) pp. 830-834.

93. Mckenzie, R.M., The synthesis of birnessite, cryptomelane and some other oxide hydroxides of manganese. *Mineral. Mag.*, Vol. 38 (1971) pp. 493-502.
94. Burns, R.G. and Burns, V.M., The mineralogy and crystal chemistry of deep-sea manganese nodules, a polymetallic resource of twenty-first century. *Phil. Trans. R. Soc. London*, Vol. A286 (1977) pp. 283-301.
95. Burns, R.G., Uptake of cobalt into ferromanganese nodules, soils and synthetic manganese(IV) oxides. *Geochim. Cosmochim. Acta*, Vol. 40, No. 1 (1976) pp. 95-102.
96. Johnston, J.H. and Glasby, G.P., The secondary iron oxide hydroxide mineralogy of some deep-sea and fossil manganese nodules: A Mössbauer and X-ray study. *Geochem. J.*, Vol. 12 (1978) pp. 153-164.
97. Thijs, A., Roy, G.D., Vansant, E.F., Glasby, G.P. and Thijssen, T., Mössbauer effect studies of iron in manganese nodules and associated marine sediments in five areas in equatorial and S.W. Pacific. *Geochem. J.*, Vol. 15 (1981) pp. 25-37.
98. Buser, W., The nature of the iron and manganese compounds in manganese nodules. In: M. Sears (ed.) *Prep. Int. Oceanogr. Congress*, Vol. 1 (1959) pp. 962-963.
99. Barnes, S.S., Minor element composition of ferromanganese nodules. *Science*, Vol. 157 (1967) pp. 63-65.
100. Usui, A., Minerals, metal contents and mechanism of formation of manganese nodules from the Central Pacific basin (GH 76-1 and GH 77-1 areas). In: J.L. Bischoff and D.Z. Piper (eds.) *Marine Geology and Oceanography of the Pacific Manganese Nodule Province* (Plenum Publishing Corp., N.Y., 1979) pp. 651-679.
101. Glasby, G.P. and Thijssen, T., Control of the mineralogy and composition of marine manganese nodules by the supply of divalent transition metal ions. *N. Jb. Miner. Abh.*, Vol. 145, No. 3 (1982) pp. 291-307.
102. Giovanoli, R. and Burki, P., Comparison of X-ray evidence of marine manganese nodules and non-marine manganese ore deposits. *Separatum of Chimia*, Vol. 29, No. 6 (1975) pp. 266-269.
103. Perseil, E.A. and Giovanoli, R., Mineralogie. *C. R. Acad. Sc. Paris*, Vol. 294, Series-II (1982) pp. 199-202.
104. Perseil, E.A. and Giovanoli, R., Contribution à La connaissance des constituants des nodules polymétalliques. à partir des données fournies par l'étude des produits de synthèse, ainsi que des oxydes dans les gisements terrestres. *Bull. Mus. natn. His. nat.*, Paris, Vol. 4, No. 5, Section C(2) (1983) pp. 163-190.

105. Crerar, D.A. and Barnes, H.L., Deposition of deep sea manganese nodules. *Geochim. Cosmochim. Acta*, Vol. 38 (1974) pp. 279-300.
106. Tooms, J.S., Summerhayes, C.P. and Cronan, D.S., Geochemistry of marine phosphate and manganese deposits. *Oceanogr. Mar. Biol. Ann. Rev.*, Vol. 7 (1969) pp. 49-100.
107. Giovanoli, R., Stahli, E. and Feitknecht, W., Über oxidhydroxide des vierwertigen mangans mit schichtengitter natrium(II,III) manganat(IV). *Helv. Chim. Acta*, Vol. 53, No. 2 (1970) pp. 209-220.
108. Scott, R.B., Rona, P.A., Butler, L.W., Nalwalk, A.J. and Scott, M.R., Manganese crusts of Atlantic fracture zone. *Nature Phys. Sci.*, Vol. 239 (1972) pp. 77-79.
109. Cronan, D.S. and Tooms, J.S., The geochemistry of manganese nodules and associated pelagic deposits from the Pacific and Indian oceans. *Deep Sea Res.*, Vol. 16 (1969) pp. 335-359.
110. Burns, R.G. and Fuerstenau, D.W., Electron-probe determination of interelement relationship in manganese nodules. *Amer. Mineral.*, Vol. 51 (1966) pp. 895-902.
111. Giovanoli, R., Feitknecht, W. and Fischer, F., Über oxidhydroxide des vierwertigen mangans mit schichtengitter: Reduktion von mangan(III)-manganat(IV) mit zimtalkohol. *Helv. Chim. Acta*, Vol. 54 (1971) pp. 1112-1124.
112. Ostwald, J. and Dubrawski, J.V., An X-ray diffraction investigation of a marine 10 Å⁰ manganate. *Mineral. Mag.*, Vol. 51 (1987) pp. 463-466.
113. Siegel, M.D. and Turner, S., Crystalline todorokite associated with biogenic debris in manganese nodules. *Science*, Vol. 219 (1983) pp. 172-174.
114. Usui, A., Nickel and copper accumulation as essential elements in 10 Å⁰ manganite of deep-sea manganese nodules. *Nature*, Vol. 279, No. 5712 (1979) pp. 411-413.
115. Halbach, P., Ozkara, M. and Hense, J., The influence of metal content on the physical and mineralogical properties of pelagic manganese nodules. *Mineral. Deposita (Berl.)*, Vol. 10 (1975) pp. 397-411.
116. Arrhenius, G.O. and Tsai, A.G., Structure, phase transformation and prebiotic catalysis in marine manganate minerals. *Reference Series*, 81-28, Scripps Institution of Oceanography, 1981, pp. 1-19.
117. Jones, L.H.P. and Milne, A.A., Birnessite, a new manganese oxide mineral from aberdeenshire, Scotland, *Mineral. Mag.*, Vol. 31 (1956) pp. 283-288.

118. Glover, E.D., Characterization of marine birnessite. *Amer. Mineral.*, Vol. 62 (1977) pp. 278-285.
119. Chukhrov, F.V., Gorshkov, A.I., Rudnitskaya, E.S. and Sivtsov, A.V., Characteristics of birnessite. *Izvest. Akad. Nauk SSSR Ser. Geol.*, Vol. 9 (1978) pp. 67-76.
120. Giovanoli, R. and Brutsch, R., Über oxidhydroxide des drei- und vierwertigen mangans. *Chimia*, Vol. 24 (1970) pp. 49-61.
121. Brown, B.A., Geochemical investigation of interelement relations in deep-sea manganese nodules. Ph.D. Thesis, Univ. of Oxford (1971) 293 pp.
122. Buser, W. and Graf, P. and Feitknecht, W., Beitrag zur kenntnis der mangan(II)-manganite und des δ -MnO₂. *Helv. Chim. Acta*, Vol. 37 (1954) pp. 2322-2333.
123. Chukhrov, F.V., Gorshkov, A.I., Rudnitskaya, E.S., Berezovskaya, V.V. and Sivtsov, A.V., Vernadite. *Izvest. Akad. Nauk. SSSR Ser. Geol.*, Vol. 6 (1978) pp. 5-19.
124. Chukhrov, F.V. and Gorshkov, A.I., Iron and manganese oxide minerals in soils. *Trans. R. Soc., Edinburgh: Earth Science*, Vol. 72 (1981) pp. 195-200.
125. Brown, B.A., A low temperature crushing technique applied to manganese nodules. *Amer. Mineral.*, Vol. 57 (1972) pp. 284-287.
126. Faulring, G.M., A study of Cuban todorokite. In: M. Muller (ed.) *Advances in X-ray Analysis*, Vol. 5 (Plenum, New York, 1962) pp. 117-126.
127. Fleischmann, W. and Heimendahl, von M., Electron microscopic investigation on Pacific manganese concretions. *Mineral Deposita (Berl.)* Vol. 12 (1977) pp. 155-162.
128. Gradel, G. and Heimendahl, von M., Extraction replica and ion beam thinning techniques - new tools in manganese nodule research. *Mineral. Deposita (Berl.)* Vol. 14 (1979) pp. 219-226.
129. Potter, R.M. and Rossman, G.R., The tetravalent manganese oxides: Identification, hydration and structural relationship by infrared spectroscopy. *Amer. Mineral.*, Vol. 64 (1979) pp. 1199-1218.
130. Dyar, M.D., Precision and interlaboratory reproducibility of measurements of the Mössbauer effect in minerals. *Amer. Mineral.*, Vol. 69 (1984) pp. 1127-1144.
131. Bowen, L.H., Mössbauer spectroscopy of ferric oxides and hydroxides. *Mössbauer Effect Reference and Data Journal*, Vol. 2, No. 3 (1979) pp. 76-94.

132. Johnston, J.H. and Logan, N.E., A precise iron-57 Mössbauer spectroscopic study of iron(III) in the octahedral and channel sites of akaganeite (β -iron hydroxide oxide). J. Chem. Soc., Dalton Trans. (1979) pp. 13-16.
133. Murad, E. and Schwertmann, U., The influence of crystallinity on the Mössbauer spectrum of lepidocrocite. Mineral. Mag., Vol. 48 (1984) pp. 507-511.
134. Bischoff, J.L., Piper, D.Z. and Leong, K., The aluminosilicate fraction of north Pacific manganese nodules. Geochim. Cosmochim. Acta., Vol. 45 (1981) pp. 2047-2063.
135. Glasby, G.P. and Thijssen, T., The nature and composition of the acid insoluble residue and hydrolysate fraction of manganese nodules from selected areas in the equatorial and S.W. Pacific. TSPM Tschermaks Min. Petr. Mitt., Vol. 30 (1982) pp. 205-225.
136. Mohapatra, B.K. and Sahoo, R.K., Merlinoite in manganese nodules from Indian ocean. Mineral. Mag., Vol. 51, No. 5 (1987) pp. 749-750.
137. Nadiradze, V.R., On a source of metals of iron-manganese concretions in the earth's recent basin. In: I.M. Varentsov and G. Grasselly (eds.) Geology and Geochemistry of Manganese, Vol. 3 (Akademiai Kiado, Budapest, 1980) pp. 23-30.
138. Marchig, V. and Halbach, P., Internal structure of manganese nodules related to conditions of sedimentation. TSPM Tschermaks Min. Petr. Mitt., Vol. 30 (1982) pp. 81-110.
139. Usui, A., Takenouchi, S. and Shoji, T., Mineralogy of deep-sea manganese nodules and synthesis of manganese oxides: Implications to genesis and geochemistry. Min. Geol., Vol. 28 (1978) pp. 405-420.
140. Greenslate, J.L., Frazer, J.Z. and Arrhenius, G., Origin and deposition of selected transition elements in the sea-bed. In: M. Morgenstein (ed.) Papers on the Origin and Distribution of Manganese Nodules in the Pacific and Prospects for Exploration (Hawaii Institute of Geophysics, 1973) pp. 45-70.
141. Marchig, V. and Gundlach, H., Material balance and manganese nodule formation (North Central Pacific). Geochim. Cosmochim. Acta, Vol. 46 (1982) pp. 693-695.
142. Hubred, G., Deep-sea manganese nodules: A review of literature. Min. Sci. Eng., Vol. 7 (1975) pp. 71-85.
143. Ottow, J.C.G., Mechanisms of ferromanganese nodule formation in the sediment-water interface of the deep-sea. In: W.E. Krumbein (ed.) Environmental Biogeochemistry and Geomicrobiology, Vol. 3 (Ann Arbor Science Publs. Inc., Michigan, USA, 1978) pp. 879-885.

144. Crerar, D.A., Cormick, R.K. and Barnes, H.L., Geochemistry of manganese: An overview. In: I.M. Varentsov, G. Grasselly (eds.) *Geology and Geochemistry of Manganese*, Vol. 1 (Akademiai Kiado, Budapest, 1980) pp. 293-334.
145. Schweisfurth, R., Manganknollen in meer. *Naturwiss*, Vol. 58 (1971) pp. 344-347.
146. Ehrlich, H.L., The role of microbes in manganese nodule genesis and degradation. In: D.R. Horn (ed.) *Ferromanganese Deposits on the Ocean Floor* (National Science Foundation, Washington, D.C., 1972) pp. 63-70.
147. Ehrlich, H.L., The formation of ores in the sedimentary environment of the deep sea with microbiol precipitation: The case of ferromanganese concretions. *Soil. Sci.*, Vol. 119 (1975) pp. 36-41.
148. Heye, D., Wachstumsverhältnisse von Manganknollen. *Geol. Jb.*, Vol. E5 (1975) pp. 3-122.
149. Schutt, C. and Ottow, J.C.G., Distribution and identification of manganese-precipitating bacteria from non-contaminated ferromanganese nodules. In: W.E. Krumbein (ed.) *Environmental Biogeochemistry and Geomicrobiology*, Vol. 3 (Ann Arbor Science Publ. Inc., Michigan, USA, 1978) pp. 869-878.
150. Raab, W., Physical and chemical features of Pacific deep-sea manganese nodules and implications to the genesis of nodules. In: D.R. Horn (ed.) *Ferromanganese Deposits on the Ocean Floor* (Nat. Sci. Found., Washington, D.C., 1972) pp. 31-49.
151. Ku, T.L. and Broecker, W.S., Radiochemical studies on manganese nodules of deep-sea origin. *Deep Sea Res.*, Vol. 16 (1969) pp. 625-637.
152. Lalou, C. and Brichet, E., Signification des mesures radiochimiques dans L'évaluation de La Vitesse de croissance des nodules de manganese. *Aquat. Sci. Fish.*, Vol. 3, No. 1 (1973) p. 10 (Abstract).
153. Glasby, G.P. and Singleton, R.J., Underwater photographs of manganese nodules from the South Western Pacific. *N.Z.J. Geol. Geophys.*, Vol. 18 (1975) pp. 597-604.
154. Menard, H.W., Time, chance and origin of manganese nodules. *Amer. Sci.*, Vol. 64 (1976) pp. 519-529.
155. Glasby, G.P., Stoffers, P., Sioulas, A., Thijssen, T. and Friedrich, G., Manganese nodule formation in the Pacific ocean: A general theory. *Geo-Marine Lett.*, Vol. 2 (1982) pp. 47-53.

156. Halbach, P. and Ozkara, M., Morphological and geochemical classification of deep sea ferromanganese nodules and its genetical interpretation. In: C. Lalou (ed.) *La Genese des Nodules de Manganese* (Coll. Int. du C.N.R.S., No. 289, Paris, 1979) pp. 77-78.
157. Halbach, P., Hebisch, U. and Scherhag, C., Geochemical variations of ferromanganese nodules and crusts from different provinces of the Pacific ocean and their genetic control. *Chem. Geol.*, Vol. 34 (1981) pp. 3-17.
158. Halbach, P., Manheim, F.T. and Otten, P., Co-rich ferromanganese deposits in the marginal seamount regions of the Central Pacific basin - results of Midpac '81. *Erzmetall.*, Vol. 35, No. 9 (1982) pp. 447-453.
159. Calvert, S.E., Price, N.B., Heath, G.R. and Moore, T.C., Relationship between ferromanganese nodule compositions and sedimentation in a small survey area of the equatorial Pacific. *J. Mar. Res.*, Vol. 36, No. 1 (1978) pp. 161-183.
160. Calvert, S.E. and Price, N.B., Geochemical variation in the ferromanganese nodules and associated sediments from the Pacific ocean. *Mar. Chem.*, Vol. 5 (1977) pp. 43-74.
161. Marchig, V. and Gundlach, H., Changes in chemical composition of some Pacific manganese nodules during their growth. In: J.L. Bischoff and D.Z. Piper (eds.) *Marine Geology and Oceanography of the Pacific Manganese Nodule Province* (Plenum, New York, 1979) pp. 729-746.
162. Schnier, C., Marchig, V. and Gundlach, H., The chemical composition of sea water and pore water in manganese nodule area of Central Pacific. *Geol. Rundschau*, Vol. 70, No. 3 (1981) pp. 1152-1163.
163. Schnier, C., Gundlach, H. and Marchig, V., Trace elements in the pore water and sea water in the radiolarian ooze area of the Central Pacific as related to the genesis of manganese nodules. In: W.E. Krumbein (ed.) *Environmental Biogeochemistry and Geomicrobiology*, Vol. 3 (Ann Arbor Science Publs. Inc., Michigan, 1978) pp. 859-867.
164. Bonatti, E., Kraemer, T. and Rydell, H., Classification and genesis of submarine iron-manganese deposits. In: D.R. Horn (ed.) *Ferromanganese Deposits on the Ocean Floor* (Nat. Sci. Found., Washington, D.C., 1972) pp. 149-166.
165. Krauskopf, K.B., Separation of manganese from iron in sedimentary processes. *Geochim. Cosmochim. Acta*, Vol. 12 (1957) pp. 61-84.
166. Hein, J.R., Yeh, H.W. and Alexander, E.R., Origin of iron-rich montmorillonite from the manganese nodule belt of north equatorial Pacific. *Clays and Clay Minerals*, Vol. 27 (1980) pp. 185-193.

167. Marchig, V. and Gundlach, H., Diagenetic changes in the radiolarian oozes of the Central Pacific and their influence on the growth of manganese nodules. In: C. Lalou (ed.) *La Genese des Nodule de Manganese* (Colloques Internationaux du C.N.R.S., Paris, 1979) pp. 55-60.
168. Marchig, V. and Gundlach, H., Separation of iron from manganese and growth of manganese nodules as a consequence of diagenetic aging of radiolarians. *Marine Geology*, Vol. 40 (1981) pp. M35-M43.
169. Halbach, P., Giovanoli, R. and Borstel, D., Geochemical processes controlling the relationship between Co, Mn and Fe in early diagenetic deep-sea nodules. *Earth and Planet. Sci. Lett.*, Vol. 60 (1982) pp. 226-236.
170. Hein, J.R., Ross, C.R., Alexander, E. and Yeh, H.W., Mineralogy and diagenesis of surface sediments from DOME areas A, B and C. In: J.L. Bischoff and D.Z. Piper (eds.) *Marine Geology and Oceanography of the Pacific Manganese Nodule Province* (Plenum, New York, 1979) pp. 365-396.
171. Lyle, M., Dymond, J. and Heath, G.R., Copper-nickel-enriched ferromanganese nodules and associated crusts from the bauer basin, northwest Nazca plate. *Earth Planet. Sci. Lett.*, Vol. 35 (1977) pp. 55-64.
172. Bischoff, J.L., Piper, D.Z. and Quinterno, P., Nature and origin of metalliferous sediment in DOMEs site c, Pacific manganese nodule province. In: C. Lalou (ed.) *International Colloquium on the Genesis of Manganese Nodules* (Colloques Internationaux du C.N.R.S., Paris, 1979).
173. Piper, D.Z. and Williamson, M.E., Composition of Pacific ocean ferromanganese nodules. *Mar. Geol.*, Vol. 23 (1977) pp. 285-303.
174. Hartmann, M. and Muller, P.J., Trace metals in interstitial waters from Central Pacific ocean sediments. In: F. Manheim and K. Fanning (eds.) *Dynamic Environment of the Ocean Floor* (D.C. Heath and Co., Lexington, Massachusetts, 1981).
175. Heye, D. and Marchig, V., Relationship between the growth rate of manganese nodules from the Central Pacific and their chemical constitution. *Mar. Geol.*, Vol. 23 (1977) pp. M19-M25.
176. Lyle, M., Estimating growth rates of ferromanganese nodules from chemical compositions: implications for nodule formation process. *Geochim. Cosmochim. Acta*, Vol. 46 (1982) pp. 2301-2306.
177. Halbach, P., Segl, M., Puteanus, D. and Mangini, A., Co-fluxes and growth rates in ferromanganese deposits from Central Pacific seamount areas. *Nature*, Vol. 304, No. 5928 (1983) pp. 716-719.

178. Murray, J. and Renard, A.F., Deep sea deposits. Rep. Sci. Results Explor. Voyage Challenger (1891) 525 pp.
179. Cameron, E.N., Ore Microscopy (Wiley, New York, 1961) 249 pp.
180. Arrhenius, G., Pelagic Sediments. In: M.N. Hill (ed.) The Sea, Vol. 3 (Interscience, New York, 1963) pp. 655-727.
181. Friedrich, G., Resner, B. and Domirsoy, S., Erzmikroskopische und mikroanalytische uniersuchungen an manganerzkonkretionen aus dem Peizifischen Ozean. Mineral. Deposita (Berl.) Vol. 4 (1969) pp. 289-307.
182. Friedrich, G.H., Kunzendorf, H. and Pluger, W.L., Geochemical investigation of deep sea manganese nodules from the Pacific on board R/V Valdivia - an application of EDX technique. In: M.Morgenstein (ed.) The Origin and Distribution of Manganese Nodules in Pacific and Prospects for Exploration (Howaii Inst. Geophys. Honolulu, 1973) pp. 31-43.
183. Andruschenko, P.F. and Skornyakova, N.S., The texture and mineral composition of the iron-manganese concretions from the southern part of the Pacific ocean. Oceanology, Vol. 9 (1969) pp. 229-242.
184. Woo, C.C., Scanning electron micrograph of marine manganese micronodules, marine pebble-sized nodules and fresh water nodules. In: M. Morgenstein (ed.) The Origin and Distribution of Manganese Nodules in the Pacific and Prospects for Exploration (Howaii Inst. Geophys. Honolulu, 1973) pp. 171-174.
185. Fewkes, R.H., External and internal features of marine manganese nodules as seen with scanning electron microscopy and their implications in nodule origin. In: M. Morgenstein (ed.) The Origin and Distribution of Manganese Nodules in the Pacific and Prospects for Exploration (Howaii Inst. Geophys., Honolulu, 1973) pp. 21-29.
186. Dunham, A.C. and Glasby, G.P., Petrographic and electron microprobe investigation of some deep sea and shallow water manganese nodules. N.Z. J. Geol. Geophys., Vol. 17 (1974) pp. 929-953.
187. Margolis, S.V. and Glasby, G.P., Microlaminations in marine manganese nodules as revealed by scanning electron microscopy. Bull. Geol. Soc. America, Vol. 84 (1973) pp. 3601-3610.
188. Sorem, R.K. and Fewkes, R.H., Internal characteristics. In: G.P. Glasby (ed.) Marine Manganese Deposits (Elsevier, N.Y., 1977) pp. 147-184.

189. Ostwald, J. and Frazer, F.W., Chemical and mineralogical investigations on deep sea manganese nodules from southern ocean. *Mineral. Deposita* (Berl.), Vol. 8 (1978) pp. 303-311.
190. Mortek, K.A. and Vassiliou, A.H., Textural characteristics and mineralogy of ferromanganese nodules from Pacific ocean. In: R.D. Hagni (ed.) *Process Mineralogy II* (The Metallurgical Society of AIME, 1982) pp. 469-493.
191. Thijssen, T., Glasby, G.P., Wiechowski, A.S., Friedrich, G., Kunzendorf, H., Muller, D. and Richter, H., Reconnaissance survey of manganese nodules from the northern sector of Peru basin. *Mar. Min.*, Vol. 2, No. 4 (1981) pp. 385-428.
192. Moore, W.S., Ku, T.H., Macdougall, J.D., Burns, V.M., Burns, R.G., Dymond, J., Lyle, M. and Piper, D.W., Fluxes of metals to a manganese nodule: radiochemical, chemical, structural and mineralogical studies. *Earth Planet. Sci. Lett.*, Vol. 52 (1981) pp. 151-171.
193. Raab, W. and Meylan, M.A., Morphology. In: G.P. Glasby (ed.) *Marine Manganese Deposits* (Elsevier, New York, 1977) pp. 109-146.
194. Goldberg, E.D., Chemical scavengers of sea-marine geochemistry. *J. Geol.*, Vol. 62 (1954) pp. 249-265.
195. Mero, J.L., Ocean floor manganese nodules. *Econ. Geol.*, Vol. 57 (1967) pp. 747-767.
196. Glasby, G.P., Tooms, J.S. and Howarth, R.J., Geochemistry of manganese concretions from the Northwest Indian ocean. *N.Z. J. Sci.*, Vol. 17 (1974) pp. 387-407.
197. Frakes, L.A. and Brien, G.O., Nickel-rich nodules in the southeastern Indian ocean. In: I.M. Varentsov and G. Grasselly (eds.) *Geology and Geochemistry of Manganese*, Vol. III (Akademiai Kiado, Budapest, 1980) pp. 185-193.
198. Glasby, G.P., Friedrich, G., Thijssen, T., Pluger, W.L., Kunzendorf, H., Ghosh, A.K. and Roonwal, G.S., Distribution, morphology and geochemistry of manganese nodules from the Valdivia 13/2 area, Equatorial North Pacific, *Pacific Science*, Vol. 36, No. 2 (1982) pp. 241-263.
199. Frakes, L.A., Metal chemistry of manganese nodules from the Cape Leeuwin Field, Southeast Indian ocean. *Mar. Geol.*, Vol. 47 (1982) pp. M1-M10.
200. Cronan, D.S. and Tooms, J.S., A microscopic and electron probe investigation of manganese nodules from north-west Indian ocean. *Deep Sea Res.*, Vol. 15 (1968) pp. 215-223.

201. Stiff, A.C., Fernando, Q. and Zeitlin, H., Electron microprobe analysis of Pacific ocean ferromanganese nodules. *Mar. Min.*, Vol. 3, No. 3-4 (1982) pp. 271-284.
202. Bancroft, G.M., Brown, J.R. and Fyfe, W.S., Advances in, and applications of X-ray photoelectron spectroscopy (ESCA) in mineralogy and geochemistry. *Chem. Geol.*, Vol. 25 (1979) pp. 227-243.
203. Siegbahn, K. and others, *Electron Spectroscopy for Chemical Analysis: Atomic, Molecular and Solid State Structures Studies by Means of Electron Spectroscopy* (Almquist and Wiksells, 1967).
204. Dillard, J.G., Koppelman, M.H., Crowther, D.L., Schenck, C.V. Murray, J.W. and Balistrieri, L., XPS studies of the chemical nature of metal ions adsorbed on clay and minerals. In: P. Tiwari (ed.) *Adsorption from Aqueous Solutions* (Plenum Press, 1981) pp. 273-339.
205. Kanungo, S.B. and Sahoo, R.K., ESR and XPS studies of some ferromanganese nodules of the Indian ocean. Paper presented in National Seminar on Processing of Manganese Nodules, February 28-March 1, 1985, RRL, Bhubaneswar (India) (Abstract).
206. Varentsov, I.M., Dikov, Y.P. and Bakova, N.V., On the study of Fe-Mn ore formation in recent basins' experiments on the synthesis of Mn, Fe, Ni, Co hydroxide phases on iron hydroxides (γ -FeOOH). In: I.M. Varentsov and G. Grasselly (eds.) *Geology and Geochemistry of Manganese*, Vol. III (Akademiai Kiado, Budapest, 1980) pp. 91-104.
207. Chukhrov, F.V., Gorshkov, A.I., Sivtsov, A.V. and Baresovskaya, V.V., On the manganese mineralogy in lateritic weathering crusts of ultrabasic rocks. In: A.J. Melfi and A. Carvalho (eds.) *Laterisation Processes* (Instituto Astronomico e Geofisico, University of Sao Paulo, Brazil, 1983) pp. 155-156.
208. Chukhrov, F.V., Gorshkov, A.I., Vitovskaya, I.V., Dritz, V.A. Sivtsov, A.V. and Dikov, U.P., On the crystochemical nature of Ni-asbolite. *Proc. USSR Acad. Sci.*, No. 9 (1980) pp. 108-120.
209. Chukhrov, F.V., Gorshkov, A.I., Dritz, V.A., Sivtsov, A.V. and Dikov, U.P., The new structural variety of asbolite. *Proc. USSR Acad. Sci.*, No. 6 (1982) pp. 55-66.
210. Murray, J.W. and Brewer, P.G., Mechanisms of removal of manganese, iron and other trace metals from sea water. In: G.P. Glasby (ed.) *Marine Manganese Deposits* (Elsevier, Amsterdam, 1977) pp. 291-

211. Glasby, G.P., Mechanisms of incorporation of manganese and associated trace elements in marine manganese nodules. *Oceanogr. Mar. Biol. A Rev.*, Vol. 12 (1974) pp. 11-40.
212. Sevast'yanov, V.F. and Volkov, I.I., The chemical composition of ferromanganese concretions of black sea. *Dokl. Akad. Nauk. SSSR*, Vol. 166 (1966) pp. 701-704.
213. Goldberg, E.D. and Arrhenius, G., Chemistry of Pacific pelagic sediment. *Geochim. Cosmochim. Acta*, Vol. 13 (1958) pp. 153-212.
214. Li, Y.H., Ultimate removal mechanisms of elements from the ocean. *Geochim. Cosmochim. Acta*, Vol. 13 (1958) pp. 153-212.
215. Hem, J.D., Redox processes at surfaces of manganese oxide and their effect on aqueous metal ions. *Chem. Geol.*, Vol. 21 (1978) pp. 199-218.
216. Marshall, K.C., Biogeochemistry of manganese minerals. In: P.A. Turdinger and D.J. Swaine (eds.) *Biogeochemical Cycling of Mineral Forming Elements* (Elsevier, Amsterdam, 1979) 253 pp.
217. Arrhenius, G. and Bonatti, E., Neptunism and vulcanism in the ocean. In: M. Sear (ed.) *Progress in Oceanography*, Vol. 3 (Pergamon, 1965) p. 7.
218. Burns, R.G., Formation of Co(III) in amorphous $\text{FeOOH} \cdot \text{XH}_2\text{O}$ phase of manganese nodules. *Nature*, Vol. 205 (1965) p. 999.
219. Han, K.N., Geochemistry and extraction of metals from ocean floor manganese nodules. Ph.D. Thesis, University of California, Berkeley, July, 1971.
220. Varentsov, I.M. and Pronina, N.V., On the study of mechanism of iron-manganese ore formation in recent basins: The experimental data on nickel and cobalt. *Mineral Deposita (Berl.)*, Vol. 8 (1973) pp. 161-178.
221. Murray, J.W. and Dilard, J.G., The oxidation of cobalt(II) adsorbed on manganese dioxide. *Geochim. Cosmochim. Acta*, Vol. 43 (1979) pp. 781-787.
222. Ehrlich, H.L., Yang, S.H. and Mainwaring, J.D. Jr., Bacteriology of manganese nodules, fate of copper, nickel, cobalt and iron during bacterial and chemical reduction of manganese(IV). *Z. Allg. Mikrobiol.*, Vol. 13 (1973) pp. 39-48.
223. Fuerstenau, D.W. and Han, K.N., Extractive metallurgy. In: G.P. Glasby (ed.) *Marine Manganese Deposits* (Elsevier, Amsterdam, 1977) pp. 357-390.
224. Han, K.N. and Fuerstenau, D.W., Extraction behaviour of metal elements from deep-sea manganese nodules in reducing media. *Mar. Min.*, Vol. 2, No. 3 (1980) pp. 155-169.

225. Itoh, H., Okuwaki, A. and Okabe, T., Processing of Pacific ocean manganese nodules. Paper presented in 12th Offshore Technology Conference, Houston, Texas, May 5-8, 1980, pp. 359-364.
226. Khalafalla, S.E. and Pahlman, J.E., Selective extraction of metals from Pacific sea nodules with dissolved sulfur dioxide. *J. Metals*, Vol. 33, No. 8 (1981) pp. 37-42.
227. Brooke, J.N. and Prosser, A.P., Manganese nodules as a source of copper and nickel - mineralogical assessment and extraction. *Trans. Inst. Min. Metall.*, Vol. 78, Section-C (1969) pp. 64-73.
228. Hoover, M.P., On the mechanism and kinetics of chlorination of copper, nickel and cobalt from ocean manganese nodules. Ph.D. Thesis, Univ. California, Berkeley, 1972 (Unpublished).
229. Kane, W.S., McCutchen, H.L. and Cardwell, P.H., U.S. Patent 3,940,470 (1976).
230. Schobert, H.H., Field, R.C. and Cardsell, P.H., U.S. Patent 3,950,182 (1976).
231. Hoover, M.P., Han, K.N., Fuerstenau, D.W., Segregation roasting of nickel, copper and cobalt from deep sea manganese nodules. *Int. J. Miner. Process.*, Vol. 2 (1975) pp. 173-185.
232. Nagaya, Y., Fukawa, M. and Kosuke, M., Japanese Patent 75,56,513 (1974).
233. Wilder, T.C., Andreola, J.J. and Galin, W.E., Reduction processes for manganese nodules using fuel oil. *J. Metals*, Vol. 33 (1981) pp. 64-69.
234. Agarwal, J.C., Barner, H.E., Beecher, N., Davies, D.S. and Kust, R.N., The Development of the Cuprion Process for Ocean Nodules (Kennecott Copper Corp., Information Center, Lexington, Mass., 1978) 21 pp.
235. Agarwal, J.C., Barner, H.E., Beecher, N., Davies, D.S. and Kust, R.N., Kennecott process for recovery of copper, nickel, cobalt and molybdenum from ocean nodules. *Min. Eng.*, Vol. 31 (1979) pp. 1704-1707.
236. King, D.E.C. and Pasho, D.W., A generalized estimating model for the Kennecott joint venture, manganese nodule processing facility (Canada Department of Energy, Mines and Resources, Ottawa, Ontario, December, 1979) 38 pp.
237. Khalafalla, S.E. and Pahlman, J.E., Selective extraction of metals from Pacific sea nodules with dissolved sulfur dioxide. Bureau of Mines, Report of Investigation No. 8518 (US Department of Interior, Washington, D.C., 1981).

238. Han, K.N. and Fuerstenau, D.W., Preferential acid leaching of nickel, copper and cobalt from ocean-floor manganese nodules. Trans. Inst. Min. Met. (London), Vol. 84 (1975) pp. C105-110.
239. Hiroshi, M., Awakura, Y., Sasaki, Y. and Teranishi, T., Reductive dissolution of manganese dioxide in the presence of ferrous ions. J. Chem. Soc. Japan, Vol. 4(2) (1980) pp. 59-63 (Japanese).
240. Das, S.C., Anand, S., Das, R.P. and Jena, P.K., Leaching of Indian ocean manganese nodules with dilute sulfuric acid in presence of carbon, RRL, Bhubaneswar, 1985 (unpublished).
241. Simon, P.K., Metal extraction from manganese nodules, M.Tech. Thesis, I.I.T. Kanpur (India) February 1986 (unpublished).
242. Okuwaki, A. and Chida, T., The reactions and rates of leaching of manganese nodules with ammonium sulfite solution. J. Chem. Soc. Japan (Chem. and Ind. Chem.) Vol. 8 (1980) pp. 1230-1242.
243. Watanabe, A., Miwa, S. and Sakakibara, S., Sulfuric acid leaching process of manganese nodules at elevated temperatures. Rept. Govt. Ind. Res. Inst., Nagoya, Vol. 31, No. 6.7 (1982) pp. 190-194 (Japanese).
244. Han, K.N. and Fuerstenau, D.W., Acid leaching of ocean manganese nodules at elevated temperatures. Int. J. Miner. Process., Vol. 1 (1975) pp. 215-230.
245. Das, S.C., Anand, S., Sarma, P.V.R.B., Nathsarma, K.C., Gopalkrishna, P., Das, R.P. and Jena, P.K., Process for recovering copper, nickel, cobalt and manganese from Indian ocean nodules using dilute sulfuric acid leaching at elevated temperature and pressure, RRL, Bhubaneswar, 1985 (Unpublished). Also S. Anand, S.C. Das, R.P. Das and P.K. Jena, Hydromet., Vol. 20, No. 2 (1988) pp. 155-168 (on high pressure sulfuric acid leaching).
246. Lester, J.S., Recovery of metal values from manganese deep sea nodules using ammonical cuprous leach solution, U.S. Patent 3,983,017, 1976.
247. Skarbo, R.R., Extraction of copper and nickel from manganese nodules, U.S. Patent 3,723,095, 1973.
248. Acharya, S. and Das, R.P., Kinetics and mechanism of the reductive ammonia leaching of ocean nodules by manganous ions. Hydromet., Vol. 19 (1987) pp. 169-186. Also R.P. Das, S. Anand, S.C. Das and P.K. Jena, Hydromet., Vol. 16 (1986) pp. 335-344 (on glucose reductant) and S.B. Kanungo and R.P. Das, Hydromet., Vol. 20 (1988) pp. 135-146 (on sulfuric acid leaching).

249. Nilsen, D.N., Siemens, R.E. and Rhoads, S.C., Solvent extraction of nickel and copper from laterite-ammonical leach liquors. Bu.Mines Report of Investigation 8605 (US Dept. Interior, Washington, D.C., 1982) 29 pp.
250. Okuwaki, A., Kudo, M., Itoh, H. and Okabe, T., Solvent extraction of nickel from an ammonical solution by LIX 64N. J. Chem. Soc. Japan (Chem. Ind. Chem.) Vol. 1 (1979) pp. 65-70.
251. Itoh, H., Tatsuruham, K., Takagi, S., Okuwaki, A. and Okabe, T., Sulfuric acid leaching heavy metals from coarsely crushed manganese nodules and kinetics of copper and nickel leaching. J. Chem. Soc. Japan (Chem. Ind. Chem.) Vol. 8 (1977) pp. 1113-1118.
252. Ritcey, G.M., Some aspects of the extraction of metal from acidic solution by Kelex 100. Can. Min. Met. Bull., February (1974) p. 87.
253. Brooks, P.T., Dean, K.C. and Rosenbaum, J.B., Experiments in processing manganese nodules. IX Int. Mineral. Proc. Congr., Czechoslovakia, 1970, pp. 329-333.
254. Okuwaki, A., Kawamura, H., Tatsuruham, K., Itoh, H. and Okabe, T., Solvent extraction of copper from a leaching solution of manganese nodules. J. Chem. Soc. Japan (Chem. Ind. Chem.) Vol. 8 (1977) p. 1119 (in Japanese).
255. Itoh, H., Okayasu, H., Okuwaki, A. and Okabe, T., Interference of aluminium ion in cementation of nickel and removal of aluminium ion from nickel sulfate solutions. J. Chem. Soc. Japan (Chem. Ind. Chem.) Vol. 1 (1982) pp. 44-48.
256. Murakami, K., Advances of solvent extraction in nonferrous metallurgy. Shinkinzoku Kougiyo, Vol. 20 (1975) p. 315 (Japanese).
257. Glasby, G.P., The three-million-tons-per-year manganese nodule 'mine site': An optimistic assumption. Mar. Min., Vol. 4, No. 1 (1983) pp. 73-77.
258. Haynes, B.W., Barron, D.C., Kramer, G.W., Maeda, R. and Maggar, M.J., Laboratory Processing and Characterization of Waste Materials from Manganese Nodules. BuMines RI 8938 (US Department of Interior, Washington, D.C., 1985) 16 pp.
259. Schutt, C. and Ottow, J.C.G., Reductive microbial dissolution of manganese nodules as a possible hazard of deep-sea mining. Helgolander Meeresunters, Vol. 33 (1980) pp. 443-451.
260. Prosser, A.P., Influence of mineralogical factors on the rates of chemical reaction of minerals. Mineral Processing and Extractive Metallurgy (Institute of Mining and Metallurgy, London, 1970) pp. 59-79.

261. Han, K.N. and Fuerstenau, D.W., Kinetics of the extraction of metals from deep-sea manganese nodules: Part I, The pore diffusion controlling case: Part II, Pore diffusion with chemical reaction. *Trans. Inst. Min. Met.*, Vol. 7B (1976) pp. 679-692.
262. Terry, B., The acid decomposition of silicate minerals, Part I and II. *Hydromet.*, Vol. 10 (1983) pp. 135-171.
263. Buser, W. and Graf, P., Radiochemische untersuchungen festkorperverbindungen III. ionen-isotopenaust-ausreaktionen an mangandioxyden and manganiten. *Helv. Chim. Acta*, Vol. 38, No. 3 (1955) pp. 810-829.
264. Raab, W. and Meylan, M.A., Morphology. In: G.P. Glasby (ed.) *Marine Manganese Deposits* (Elsevier, Amsterdam, 1977) pp. 109-146.
265. Atkinson, R.J., Posner, A.M. and Quirk, J.P., Crystal nucleation in Fe(III) solutions and hydroxide gels. *J. Inorg. Nucl. Chem.*, Vol. 30 (1968) pp. 2371-2381.
266. Schenck, C.V., Dilard, J.G. and Murray, J.W., Surface analysis and adsorption of Co(II) on goethite. *J. Coll. Interf. Sci.*, Vol. 95, No. 2 (1983) pp. 398-409.
267. Lussiez, P. and Osseo-Asare, K., Synthesis, characterization and dissolution behaviour of cuperiferous and nickeliforous goethites. In: D.M. Hausen and W.C. Park (eds.) *Process Mineralogy* (The Metallurgical Society of AIME, Warrendale, 1981) pp. 291-304.
268. Inouye, K., Ishii, S., Kaneko, K. and Ishikawa, T., The effect of copper(II) on the crystallization of α -FeOOH. *Z. Anorg. Allg. Chem.*, Vol. 391 (1972) pp. 86-96.
269. Cornell, R.M. and Giovanoli, R., The influence of copper on the transformation of ferrihydrite ($5\text{Fe}_2\text{O}_3 \cdot 9\text{H}_2\text{O}$) into crystalline products in alkaline media. *Polyhedron*, Vol. 7, No. 5 (1988) pp. 385-391.
270. McKenzie, R.M., The adsorption of lead and other heavy metals on oxides of manganese and iron. *Aust. J. Soil Res.*, Vol. 18 (1980) pp. 61-73.
271. Kodama, K., *Methods of Quantitative Inorganic Analysis, An Encyclopedia of Gravimetric, Titrimetric and Colorimetric Methods* (Interscience, N.Y., 1963).
272. Fortune, W.B. and Mellon, M.G., Determination of iron with o-phenanthroline - A spectroscopic study. *Ind. Eng. Chem., Anal. Ed.*, Vol. 10, No. 2 (1938). Also Ryan, J.A. and Botham, G.H., *Anal. Chem.*, Vol. 21, No. 12 (1949) p. 1521.

273. Chilton, J.M., Simultaneous colorimetric determination of copper, cobalt and nickel as diethyldithiocarbamate. *Anal. Chem.*, Vol. 25, No. 4 (1953) p. 1274.
274. Classen, A. and Bastings, L., The photometric determination of copper by extraction as the diethyldithiocarbamate. *Z. Anal. Chem.*, Vol. 153 (1956) p. 30. Also Cheng, K.L. and Bray, R.H., *Anal. Chem.*, Vol. 25, No. 4 (1953) p. 655.
275. Williams, W.J., *Handbook of Anion Determination* (Butterworths, London, 1979) pp. 589-590.
276. Bower, C.A. and Goertzen, J.O., Surface area of soils and clays by an equilibrium ethylene glycol method. *Soil Sci.*, Vol. 87 (1959) pp. 288-292.
277. Carter, D.L., Heilman, M.D. and Gonzalez, C.L., Ethylene glycol monoethyl ether (EGME) for determining surface area of silicate minerals. *Soil Sci.*, Vol. 100, No. 5 (1965) pp. 356-360.
278. Schulze, D.G., and Schwertmann, U., The influence of aluminium on iron oxides: X. Properties of Al-substituted goethites. *Clay Minerals*, Vol. 19 (1984) pp. 521-539.
279. Cambier, P., Infrared study of goethites of varying crystallinity and particle size: II Crystallographic and morphological changes in series of synthetic goethites. *Clay Minerals*, Vol. 21 (1986) pp. 201-210.
280. Brown, G., Associated minerals. In: G.W. Brindley and G. Brown (eds.) *Crystal Structure of Clay Minerals and Their X-ray Identification* (Mineralogical Society, London, 1980) pp. 361-410.
281. Klug, H.P. and Alexander, L.E., *X-ray Diffraction Procedures for Polycrystalline and Amorphous Materials*. 2nd Ed. (John Wiley and Sons, New York, 1974) pp. 491-538.
282. Paterson, E., Bunch, J.L. and Clark, D.R., Cation exchange in synthetic manganates: 1. Alkylammonium exchange in a synthetic phyllomanganate. *Clay Minerals*, Vol. 21 (1986) pp. 949-955.
283. Jones, A.A. and Saleh, A.M., Electron diffraction and study of ferrihydrite coatings on kaolinite. *Clay Minerals*, Vol. 21 (1986) pp. 85-92.
284. Wetlaufer, P.H., Foley, N.K. and Hayba, D.O., Applications of doubly polished sections to the study of ore deposits. In: R.D. Hagni (ed.) *Process Mineralogy II* (Metallurgical Society of AIME, Warrendale, PA, 1982) p. 48.
285. Lloyd, G.E., Atomic number and crystallographic contrast images with SEM: A review of back-scattered electron technique. *Min. Mag.*, Vol. 51 (1987) pp. 3-19.

286. Mack, C., Essentials of Statistics for Scientists and Technologist (Heinemann Educational Book Ltd., London, 1966).
287. Davis, J.C. and Sampson, R.J., Statistics and Data Analysis in Geology (John Wiley and Sons, 1973) pp. 412-536.
288. Robinson, G.D., Sequential chemical extractions and metal partitioning in hydrous Mn-Fe oxide coatings: reagents choice and substrate composition affect results. Chem. Geol., Vol. 47 (1984-1985) pp. 97-112.
289. Van de Giessen, A.A., The structure of iron(III) oxide-hydrate gels. J. Inorg. Nucl. Chem., Vol. 28 (1966) pp. 2155-2159.
290. Towe, K.M. and Bradley, W.F., Mineralogical constitution of colloidal "hydrous ferric oxides". J. Coll. Interf. Sci., Vol. 24 (1967) pp. 384-392.
291. Zvyagin, B.B., Electron-Diffraction Analysis of Clay Mineral Structures (Plenum Press, New York, 1967).
292. Deer, W.A., Howie, R.A. and Zussman, J., Rock-Forming Minerals, Vol. 3, Sheet Silicates (Longmans, Green and Co. Ltd., 1967) 270 pp.
293. Audrieth, L.F. and Mohr, P.H., Auto-oxidation of hydrazine-effect of dissolved metals and deactivators. Ind. Eng. Chem., Vol. 43, No. 8 (1951) p. 1774.
294. Moews, P.C. and Audrieth, L.F., The auto-oxidation of hydroxylamine. J. Inorg. Nucl. Chem., Vol. 11 (1959) p. 242.
295. Sizilard, I., Stability constants of metal ions hydroxylamine complexes in aqueous solution. Acta Chem. Scand., Vol. 17, No. 10 (1963) p. 2674.
296. Cotton, F.A. and Wilkinson, G., Advanced Inorganic Chemistry (John Wiley and Sons, 1980) pp. 800-821.
297. Giovanoli, R., Layer structured manganese oxide hydroxides. VI. recrystallization of synthetic buserite and the influence of amorphous silica and ferric hydroxide on its nucleation. Chimia, Vol. 34, No. 7 (1980) pp. 308-310.
298. Wyrteki, K., Oceanographic Atlas of the International Indian Ocean Expedition (U.S. National Science Foundation, Washington, D.C., 1971).
299. Jeffries, D.S. and Stumm, W., The metal-adsorption chemistry of buserite. Canadian Mineralogist, Vol. 14 (1976) pp. 16-22.

300. Crowther, D.L., Dilard, J.G. and Murray, J.W., The mechanism of Co(II) oxidation on synthetic birnessite. *Geochim. Cosmochim. Acta*, Vol. 47 (1983) pp. 1399-1403.
301. Loganathan, P. and Bureau, R.G., Sorption of heavy metal ions by hydrous manganese oxide. *Geochim. Cosmochim. Acta*, Vol. 37 (1973) pp. 1277-1293.
302. Basolo, F. and Pearson, R.G., Mechanisms of Inorganic Reactions, A Study of Metal Complexes in Solution (John Wiley and Sons, Inc., New York, 1967) 701 pp.
303. Eyring, L. and Tai, L.T., The structural chemistry of some complex oxides: Ordered and disordered extended defects. In: N.B. Hannay (ed.) *Treatise on Solid State Chemistry*, Vol. 3, Crystalline and Non-Crystalline Solids, 1976, pp. 167-252.
304. Buser, W., Radiochemische untersuchungen und festkorperverbindungen I. Isotopenaustauschversuche in system festkorper-losung, Vol. 37, No. 7 (1954) pp. 2334-2344.
305. McKenzie, R.M., The sorption of some metals by the lower oxides of manganese. *Geoderma*, Vol. 8 (1972) pp. 29-35.
306. Valverde, N., Investigations on the rate of dissolution of metal oxides in acidic solutions with addition of redox couples and complexing agents. *Ber. Bunsenges Phys. Chem.*, Vol. 80 (1976) pp. 333-340.
307. Burkin, A.R., The Chemistry of Hydrometallurgical Processes (E and FN Spon, London, 1966) 157 pp.
308. Nii, K., On the dissolution behaviour of NiO. *Corros. Sci.*, Vol. 10 (1970) pp. 571-583.
309. Jones, C.F., Segall, R.L., Smart, R.C. and Turner, P.S., Semiconducting oxides: the effect of electronic and surface structure on the dissolution kinetics of nickel oxide. *J. Chem. Soc. Faraday Trans.*, Vol. 74, No. 1 (1978) pp. 1615-1623.
310. Arinson, B.J., Segall, R.L., Smart, R.C. and Turner, P.S., Semiconducting oxides: the effects of solids and solution properties on the dissolution kinetics of cobaltous oxide. *J. Chem. Soc. Farad. Trans.*, Vol. 77, No. 1 (1981) pp. 535-545.
311. Bhuntumkomol, K., Han, K.N. and Lawson, F., The leaching behaviour of nickel oxides in acid and in ammonical solutions. *Hydromet.*, Vol. 8 (1982) pp. 147-160.
312. Lussiez, P., Osseo-Asare, K. and Simkovich, G., Effect of solid state impurities on the dissolution of nickel oxide. *Metall. Trans., Section-B*, Vol. 12 (1981) pp. 651-657.

313. Majima, H., Awakwa, T., Yazaki, T. and Chikamori, Y., Acid dissolution of cupric oxide. *Metall. Trans., Section-B*, Vol. 11 (1980) pp. 209-214.
314. Ruetschi, P. and Giovanoli, R., The behaviour of MnO_2 in strongly acidic solutions. *J. App. Electrochem.*, Vol. 12 (1982) pp. 109-114.
315. Davis, C.W., Dissolution of various manganese minerals, Bureau of Mines, RI 3024 (US Department of Interior, Washington, D.C., 1930) 11 pp.
316. Wyman, W.F. and Ravitz, S.F., Sulfur dioxide leaching tests on various western manganese ores, Bureau of Mines, RI 4077 (US Department of Interior, Washington, D.C., 1947) 12 pp.
317. Miller, J.D. and Wan, R.Y., Reaction kinetics for the leaching of MnO_2 by sulfur dioxide. *Hydromet.*, Vol. 10 (1983) pp. 219-242.
318. Terry, B., Specific chemical rate constants for the acid dissolution of oxides and silicates. *Hydromet.*, Vol. 11 (1983) pp. 315-344.
319. Hiskey, J.B. and Wadsworth, M.E., Electrochemical processes in the leaching of metal sulfides and oxides. In: M. Kuhn (ed.) *Process and Fundamental Considerations of Selected Hydrometallurgical Systems* (SME-AIME, Denver, Colorado, 1981) pp. 303-325.
320. Garrels, R.M. and Christ, C.L., *Solutions, Minerals and Equilibria* (Harper and Row, N.Y., 1965) 450 pp.
321. Robin, R.G., The stabilities of arsenic(V) and arsenic(III) compounds in aqueous metal extraction systems. In: K. Osseo-Asare and J.D. Miller (Eds.) *Hydrometallurgy Research, Development and Plant Practice* (The Metallurgical Society of AIME, Warrendale, 1983) pp. 291-310.
322. Linkson, P.B., Precipitation of metal sulfites from aqueous liquors, *ibid*, pp. 311-328.
323. Back, A.E., Ravitz, S.F. and Tame, K.E., Formation of Dithionate and Sulfate in the Oxidation of Sulfur Dioxide by Manganese Dioxide and Air, Bureau of Mines, RI 4931 (U.S. Department of Interior, Washington, D.C., 1952) 14 pp.
324. Buser, W. and Graf, P., Radiochemische untersuchungen festkorperversbindungen und manganiten. *Helv. Chim. Acta*, Vol. 38, No. 3 (1955) pp. 810-829.
325. James, R.O., Stiglich, P.J. and Healy, T.W., Analysis of models of adsorption of metal ions at oxide-water interfaces. *Faraday Discuss.*, Chem. Soc., Vol. 59 (1975) pp. 142-156.

326. Balistrieri, L., Brewer, P.G. and Murray, J.W., Scavenging residence times of trace metals and surface chemistry of sinking particles in deep ocean. *Deep Sea Res.*, Vol. 28A (1981) pp. 101-121.
327. Varentsov, I.M., Bakov, N.V., Dikov, Y.P., Gendler, T.S. and Giovanoli, R., Synthesis of Mn, Fe, Ni, Co oxide-hydroxide phases on manganese oxides: On a model for transition ore formation in recent basins. *Acta Mineral. Petrog.*, Szeged, Vol. 24, No. 1 (1979) pp. 63-90.
328. Schwertmann, U., The influence of aluminium on iron oxide: IX. dissolution of Al-goethites in 6M HCl. *Clay Miner.*, Vol. 19 (1984) pp. 9-19.
329. Goss, C.J., The kinetics and reaction mechanism of goethite to hematite transformation. *Mineral. Mag.*, Vol. 51 (1987) pp. 437-451.
330. Cornell, R.M., Posner, A.M. and Quirk, J.P., Crystal Morphology and dissolution of goethite. *J. Inorg. Nucl. Chem.*, Vol. 36 (1974) pp. 1937-1946.
331. Warren, I.H. and Hay, M.G., Leaching of iron oxides with aqueous solution of sulfur dioxide. *Trans. I.M.M. (London)*, Vol. 84 (1975) pp. C49-53.
332. Byerley, J.J., Rempel, G.L. and Garrido, G.F., Copper catalysed leaching of magnetite in aqueous sulfur dioxide. *Hydromet.*, Vol. 4 (1979) pp. 317-336.
333. Nicol, M.J., The non-oxidative leaching of oxides and sulfides. In: K. Osseo-Asare and J.D. Miller (eds.) *Hydrometallurgy Research Development and Plant Practice* (AIME, Warrendale, 1983) pp. 176-196.
334. Baes, C.F. and Mesmer, R.E., *Hydrolysis of Cations* (John Wiley and Sons, New York, 1976) 489 pp.
335. Crerar, D., Wood, S. and Brantley, S., Chemical controls on solubility of ore forming minerals in hydrothermal solutions. *Canadian Mineral.*, Vol. 23, No. 3 (1985) pp. 333-352.
336. Bassett, H. and Parker, W.G., The oxidation of sulfurous acid. *J. Chem. Soc.* (1951) pp. 1540-1560.

APPENDIX - ACHEMICAL COMPOSITIONS OF MANGANESE NODULES FROM SOME SELECTED
REGIONS IN PACIFIC AND INDIAN OCEANPacific Ocean (52)

Area	Associated sediment	Mn/Fe mean	Mn/Fe range	Mn	Concentration, wt %				
					Fe	Ni	Co	Cu	Ti
N. Pacific	Miopelagic clays	1.17	0.5-1.8	14.6	12.4	0.47	0.24	0.29	0.61
N. Pacific	Eupelagic clays	1.74	0.64-3.9	19.1	11.0	0.65	0.33	0.54	0.72
Equatorial Pacific	Radiolarian ooze	2.9	1.1-10.6	23.1	8.0	1.1	0.18	0.89	0.60
S. Pacific	Eupelagic clays	0.96	0.4-1.9	15.6	16.3	0.42	0.37	0.22	1.07
Seamount of Central Pacific	-	1.18	0.6-4.4	18.4	15.0	0.44	0.61	0.13	0.98
N.W. periphery of ocean	Hemipelagic muds	0.48	0.1-0.8	8.2	12.9	0.11	0.08	0.09	-
E. periphery of ocean*	Hemipelagic muds	27.6	11.6-51.0	34.8	1.49	0.15	0.01	0.08	-

* near California and S. America.

Indian Ocean (37, 49)

Area	Associated sediment	Mn/Fe mean	Mn/Fe range	Mn	Concentration, wt %				
					Fe	Ni	Co	Cu	Ti
C. Indian* basin	Siliceous ooze	1.69	1.1-1.7	17.1	10.1	0.17	0.51	0.18	-
Wharton basin	Siliceous ooze	0.85	0.8-1.7	17.6	20.6	0.44	0.17	0.33	-
S. Australian basin	Siliceous ooze	1.22	0.0-2.1	16.4	13.4	0.50	0.21	0.29	-
Somali basin and seychelles region	Pelagic clay and carbonate ooze	0.98	0.0-1.2	16.2	16.5	0.36	0.34	0.08	-
Mozambique ridge	-	1.29	1.1-1.3	14.6	11.3	0.33	0.38	0.18	-

* Range of composition (wt %), Mn 5-32, Fe 4.5-19, Ni 0.01-1.6, Co 0.05-0.54, Cu 0.05-0.95.

APPENDIX - BTHE ANALYTICAL TECHNIQUES-CALIBRATION CURVE

Experimental data used in calculation of regression equation for estimation of manganese, iron, nickel, cobalt and copper

(a) Manganese

Mn mg	absorbance at 525 nm	Mn mg	absorbance at 525 nm
0.000	0.000	0.000	0.000
0.100	0.045	0.100	0.045
0.200	0.090	0.200	0.090
0.300	0.135	0.300	0.135
0.400	0.180	0.400	0.185
0.500	0.225	0.500	0.230
		0.200	0.090
		0.400	0.180

(b) Iron

Fe μg	absorbance at 520 nm	Fe μg	absorbance at 520 nm	Fe μg	absorbance at 520 nm
0.000	0.000	0.000	0.000	0.000	0.000
0.250	0.055	0.250	0.055	0.250	0.055
0.500	0.115	0.500	0.110	0.500	0.110
0.750	0.170	0.750	0.165	0.750	0.160
1.000	0.230	1.000	0.220	1.000	0.220
1.250	0.285	1.250	0.275	1.250	0.275

(c) Nickel

Ni μg	absorbance at 325 nm	Ni μg	absorbance at 325 nm	Ni μg	absorbance at 325 nm
0.00	0.000	0.00	0.000	0.00	0.000
2.50	0.032	2.50	0.032	2.50	0.032
5.00	0.065	5.00	0.065	5.00	0.065
7.50	0.099	7.50	0.100	7.50	0.099
10.00	0.135	10.00	0.135	10.00	0.132
12.50	0.166	12.50	0.165	12.50	0.165

(d) Cobalt

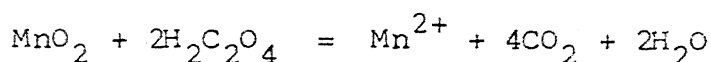
Co μg	% transmittance at 370 nm	Co μg	% transmittance at 370 nm	Co μg	% transmittance at 370 nm
0.00	100	0.00	100	0.00	100
5.00	91.5	4.00	93.5	3.00	95.0
10.00	83.0	8.00	87.0	6.00	90.0
15.00	74.5	12.00	80.5	9.00	84.5
20.00	66.5	16.00	74.0	12.00	80.0
		20.00	67.0	15.00	74.5
				18.00	70.0

(e) Copper

Cu μg	absorbance at 435 nm	Cu μg	absorbance at 435 nm	Cu μg	absorbance at 435 nm
0.00	0.000	0.00	0.000	0.00	0.000
5.00	0.042	5.00	0.042	5.00	0.042
10.00	0.085	10.00	0.085	10.00	0.085
15.00	0.130	15.00	0.125	15.00	0.127
20.00	0.170	20.00	0.170	20.00	0.170
25.00	0.218	25.00	0.212	25.00	0.218

APPENDIX - CAVERAGE OXIDATION STATE (O/Mn RATIO) IN
SYNTHETIC OXYHYDROXIDES OF MANGANESE

The chemical reaction between oxalic acid and MnO_2 is as follows



Average oxidation state of Mn is defined as

$$x = 1 + \frac{1}{2} \left[\frac{\text{Moles of manganese(IV)} \times 2}{\text{Total moles of manganese}} \right]$$

Strength of KMnO_4 solution used = 0.00996 M

Strength of oxalic acid used = 0.0394 M

For each sample the value of x was found out more than once, the details are tabulated below:

Sample description	Weight of sample used, g	Moles of manganese(IV) $\times 10^3$			Total moles* of Mn $\times 10^3$	x or [O/Mn]	wt % Mn(II)
		I	II	Average			
B-O	0.050	0.3830	0.3830	0.3830	0.4651	0.823	9.01
B-Ni(C)	0.050	0.3806	0.3806	0.3806	0.4403	1.864	6.56
B-Co(C)	0.050	0.3979	0.3954	0.3967	0.4523	1.877	6.11
B-Cu(C)	0.050	0.3756	0.3780	0.3768	0.4314	1.873	6.00
B-Ni(I)	0.050	0.3582	0.3582	0.3582	0.4404	1.813	9.02
B-Co(I)	0.050	0.3731	0.3760	0.3746	0.3698	2.025	-0.52
B-Cu(I)	0.050	0.3681	0.3656	0.3669	0.3923	1.935	2.79
V-O	0.050	0.4179	0.4154	0.4166	0.4189	1.991	~0.4
V-Ni(S)	0.050	0.4154	-	0.4154	0.4189	1.991	~0.4
V-Co(S)	0.050	0.4154	0.4154	0.4154	0.4189	1.991	~0.4
V-Cu(S)	0.050	0.4154	-	0.4154	0.4189	1.991	~0.4

* estimated by permanganate method (vide Section 4.2.1).

APPENDIX - DSURFACE AREA ESTIMATION BY EGMME RETENTION METHOD

Ethylene glycol monomethyl ether (EGMME) retention by different synthetic samples and surface area values:

Broad category	Sample description	Initial weight g	EGMME retained* $\times 10^3$ g	Surface area (m^2/g)
<u>I Birnessites</u>				
-63+53 μm size				
	B-O	0.2980	2.8	32.4
	B-Ni(C)	0.2944	3.0	35.1
	B-Co(C)	0.2947	3.3	38.6
	B-Cu(C)	0.2916	4.1	48.5
	B-Ni(I)	0.2923	5.0	59.0
	B-Co(I)	0.2958	4.1	47.8
	B-Cu(I)	0.2937	4.7	55.2
<u>II Birnessites</u>				
-210+149 μm				
	B-O	0.2938	2.2	25.8
	B-Ni(C)	0.2959	3.0	35.0
	B-Co(C)	0.2670	2.0	25.8
	B-Cu(C)	0.2940	2.1	24.8
	B-Ni(I)	0.2598	3.4	45.1
	B-Co(I)	0.2909	2.6	30.8
	B-Cu(I)	0.2916	2.5	30.6
<u>III δ-MnO₂</u>				
<53 μm				
	V-O	0.2860	12.4	149
	V-Ni(S)	0.2837	11.4	138
	V-Co(S)	0.2878	11.5	138
	V-Cu(S)	0.2825	11.3	138
<u>IV Goethites</u>				
<53 μm				
	G-O	0.3958	4.8	41.8
		0.3955	4.6	41.0 ⁺
	G-Ni(S)	0.3850	4.6	41.2
	G-Co(S)	0.3948	4.7	41.1
	G-Cu(S)	0.3966	4.8	41.7
	G-Ni(C)	0.3903	8.0	71.0
	G-Co(C)	0.3871	8.3	74.0
	G-Cu(C)	0.3855	8.6	77.0
		0.3947	8.8	77.0 ⁺

* constant value

+ repeated to check reproducibility.

APPENDIX - E

QUANTITATIVE ESTIMATION OF MICROCRYSTALLINE
DIMENSIONS IN GOETHITES

(a) Uncorrected values of peak width (B) at half height for different goethite samples

$2\theta^\circ$	(hkl)	B in degree						
		I*	II	III	IV	V	VI	VII
26.6	020	0.56	0.56	0.56	0.56	0.68	0.48	0.60
31.8	110	0.74	0.72	0.72	0.72	0.84	0.78	0.48
39.6	120	0.72	0.70	0.72	0.72	0.84	0.64	0.44
50.4	130	0.68	0.68	0.66	0.68	0.74	0.68	0.58
52.7	021	0.52	0.52	0.52	0.52	0.60	0.52	0.52
54.1	101	1.04	0.96	1.00	0.96	-	1.08	0.62
54.8	040	0.80	0.96	0.80	0.80	0.88	0.84	0.92
55.8	111	0.68	0.66	0.64	0.64	0.68	0.68	0.52
63.1	140	0.62	0.64	0.62	0.60	0.72	0.68	0.62

* I - G-O, II - G-Ni(S), III - G-Co(S), IV - G-Cu(S), V - G-Ni(C), VI - G-Co(C), VII - G-Cu(C).

(b) Peak width (b) for quartz standard (5-20 μm) were as follows

$2\theta^\circ$	b in degree
31.32	0.304
40.2	0.304
55.6	0.36
60.2	0.36
61.6	0.36

(c) The value of b ($b = 0.304^\circ$ for 2θ range 25-40 $^\circ$ and 0.36 $^\circ$ for 50-65 $^\circ$) were divided with B and corrected values of B (i.e. β) were calculated using the following equations

Equation	$\frac{b}{B}$ range
$\frac{\beta}{B} = 0.904 - 0.64(\frac{b}{B} - 0.3)$	0.30-0.35
$= 0.872 - 0.704(\frac{b}{B} - 0.35)$	0.35-0.40
$= 0.8368 - 1.04(\frac{b}{B} - 0.40)$	0.40-0.50
$= 0.7328 - 1.248(\frac{b}{B} - 0.50)$	0.50-0.60

The above equations were obtained from the correction curve given by Klug and Alexander*

- (d) The corrected values of peak width were used in calculation of MCD_{hkl} using the following equation

$$MCD_{hkl} = \frac{1.84 \times 2.2902 \times 180}{3.14 \times \beta \times \cos\theta_{hkl}}$$

The MCD_{hkl} values are listed below

(hkl)	$MCD_{hkl}, \text{ nm}$						
	I	II	III	IV	V	VI	VII
020	63.9	63.9	63.9	63.9	45.3	89.3	55.8
110	39.9	41.9	41.9	41.9	33.8	37.1	90.3
120	42.9	44.4	42.9	42.9	34.6	51.7	115.1
130	55.2	55.2	57.9	55.2	47.5	55.2	76.1
021	103.0	103.0	103.0	103.0	72.3	102.9	102.9
101	29.1	32.3	30.7	32.4	-	27.8	48.1
040	42.3	32.5	42.3	42.3	36.5	39.2	34.3
111	56.5	59.2	63.8	63.8	56.5	56.1	104.3
140	69.7	66.2	69.7	72.5	58.6	58.6	69.9

- (e) The MCD_{hkl} values were resolved in a-, b- and c-direction of unit cell using the $\cos\psi$ values given below

(hkl)	$\cos\psi$		
	a	b	c
020	0	1	0
110	0.909	0.420	0
120	0.735	0.679	0
130	0.585	0.810	0
021	0	0.518	0.854
101	0.548	0	0.834
040	0	1	0
111	0.534	0.246	0.812
140	0.477	0.881	0

* Klug, H.P., Alexander, L.E., X-ray Diffraction Procedures for Polycrystalline and Amorphous Materials, 2nd Ed., John Wiley and Sons, New York, 1974.

(f) The resolved value of MCD_{hkl} and average value of MCD_a , MCD_b and minimum value of MCD_c are tabulated below

Sample	(hkl)	020	110	120	130	021	111	140	Average* or minimum value, nm
I	MCD _a	-	36.2	31.5	32.3	-	30.2	33.2	32.7 ± 2.0
	MCD _b	63.9	16.8	29.1	44.7	53.4	13.9	61.4	59.0 ± 7.0**
	MCD _c	-	-	-	-	88.0	-	-	>88
II	MCD _a	-	38.1	32.6	32.3	-	31.6	31.6	33.2 ± 2.4
	MCD _b	63.9	17.6	30.1	44.7	53.4	14.6	58.3	59.0 ± 7.0
	MCD _c	-	-	-	-	88.0	-	-	>88
III	MCD _a	-	38.1	31.5	32.3	-	34.1	34.5	34.1 ± 2.2
	MCD _b	63.8	17.6	29.1	44.7	53.4	15.6	63.8	59.0 ± 7.0
	MCD _c	-	-	-	-	88.0	-	-	>88
IV	MCD _a	-	38.1	31.5	33.8	-	34.0	33.2	34.1 ± 2.2
	MCD _b	63.8	17.6	29.1	46.9	53.4	15.6	61.4	59.0 ± 7.0
	MCD _c	-	-	-	-	88.0	-	-	>88
V	MCD _a	-	30.7	25.4	27.8	-	30.2	28.0	28.4 ± 2.0
	MCD _b	45.3	14.2	23.4	38.4	37.4	11.3	51.6	41.0 ± 4.0
	MCD _c	-	-	-	-	62.0	-	-	>62
VI	MCD _a	-	33.7	38.0	32.2	-	29.9	28.0	32.0 ± 3.5
	MCD _b	89.3	15.6	35.1	44.7	53.3	13.8	51.6	71.0 ± 18
	MCD _c	-	-	-	-	88.0	-	-	>88
VII	MCD _a	-	82.1	84.6	44.5	-	55.7	33.3	53.9 ± 19
	MCD _b	55.8	37.9	48.4	61.7	53.3	25.7	61.6	55.0 ± 2.0
	MCD _c	-	-	-	-	87.0	-	-	>87

* broad or overlapping peaks not included in calculation

** only (020) and (021) reflection considered in calculation of average MCD_b value.

APPENDIX - FFORTTRAN IV COMPUTER PROGRAMME FOR INDEXING OF SAED SPOT PATTERN

The mathematical formulae and conditions used in the development of the programme are as follows (the program is given later at the end of this appendix).

I. Interplanar Spacings and Angles

Interplanar spacings in crystals:

$$\frac{1}{d^2} = h^2 a^{*2} + k^2 b^{*2} + l^2 c^{*2} + 2hka^*b^* \cos \gamma^* \\ + 2klb^*c^* \cos \alpha^* + 2lhc^*a^* \cos \beta^*$$

Angles between planes:

$$\cos \theta = \{h_1 h_2 a^* + k_1 k_2 b^* + l_1 l_2 c^* + (h_1 k_2 + h_2 k_1) a^* b^* \cos \gamma^* \\ + (k_1 l_2 + h_2 l_1) b^* c^* \cos \alpha^* + (l_1 h_2 + l_2 h_1) c^* a^* \cos \beta^*\} d_1 d_2$$

where

$$a^* = (bc \sin \beta)/V, \quad b^* = (ca \sin \alpha)/V, \quad c^* = (ab \sin \gamma)/V$$

$$\cos \alpha^* = (\cos \beta \cos \gamma - \cos \alpha)/(\sin \beta \sin \gamma)$$

$$\cos \beta^* = (\cos \gamma \cos \alpha - \cos \beta)/(\sin \gamma \sin \alpha)$$

$$\cos \gamma^* = (\cos \alpha \cos \beta - \cos \gamma)/(\sin \alpha \sin \beta)$$

$$V = abc(1 - \cos^2 \alpha - \cos^2 \beta - \cos^2 \gamma + 2 \cos \alpha \cos \beta \cos \gamma)^{1/2}$$

II. Zone Law: If $(h_1 k_1 l_1)$ and $(h_2 k_2 l_2)$ belong to a zone, then the plane with indices $(h_1 \pm h_2, k_1 \pm k_2, l_1 \pm l_2)$ also belongs to this zone.

III. Beam Direction: If planes $(h_1 k_1 l_1)$ and $(h_2 k_2 l_2)$ define a zone, the indices of zone axis $[uvw]$ (i.e. beam direction) are obtained from the following relationship

$$u : v : w = (k_1 l_2 - k_2 l_1) : (l_1 h_2 - l_2 h_1) : (h_1 k_2 - h_2 k_1) .$$

The program which follows was developed by the author.

```

C      THE COMPUTER PROGRAM USED FOR INDEXING THE SELECTED AREA
C      ELECTRON DIFFRACTION PATTERN
C      *****
C      SUBROUTINE REQUIRED IS ASCEND
COMMON MM
INTEGER H1,HX
DIMENSION MINAME(15),IH(300),K(300),L(300),D(300),
1 DEE(20,3),MH(20,3,300),MK(20,3,300),ML(20,3,300),
2 DD(20,3,300),PHA(20,3,300),PE(3),M(3),PE1(20),
3 PE2(20),IB1(20,200),IB2(20,200),IB3(20,200)
WRITE(50,3000)
3000  FORMAT(5X,'* DE1,DE2 and DE3 are measured D spacings',/)
WRITE(50,3010)
3010  FORMAT(5X,'* PE1 and PE2 are measured angles between
1 R1/\R2 and R1/\R3',/)
WRITE(50,3020)
3020  FORMAT(5X,'* DT1,DT2,DT3 and PH1,PH2 are calculated
1 values',/)
WRITE(50,3030)
3030  FORMAT(5X,'* B1,B2 and B3 refers to the beam direction
1 vector',/)
WRITE(50,3040)
3040  FORMAT(5X,'DIFF',5X,'DE1',5X,'DE2',5X,'DE3',7X,'PE1',
1 5X,'PE2',/)
READ(22,*) ND
READ(23,*) NM
DO 500 IX=1,ND
READ(22,*) (DEE(IX,J),J=1,3),PE1(IX),PE2(IX)
WRITE(50,1000) IX,(DEE(IX,J),J=1,3),PE1(IX),PE2(IX)
1000  FORMAT(5X,I3,2X,3F8.2,2X,2F8.1,/)
500   CONTINUE
WRITE(50,3050)
3050  FORMAT(/,3X,50(1H-),/)
DO 502 IY=1,NM
READ(23,800) MINAME,A,B,C,AL,BE,GA
800   FORMAT(1X,15A1,1X,3F7.3,3F7.2)
WRITE(50,3060)
3060  FORMAT(5X,'MND',2X,'MINERAL NAME',7X,'A',9X,'B',9X,
1 'C',6X,'ALPHA',3X,'BETA',3X,'GAMMA',/)
WRITE(50,1010) IY,MINAME,A,B,C,AL,BE,GA
1010  FORMAT(5X,I2,1X,15A1,3F10.3,3F8.2,/)
WRITE(50,3070)
3070  FORMAT(3X,75(1H-),/)
WRITE(50,3080)
3080  FORMAT(6X,'NM',1X,'ND',4X,'H1',2X,'K1',2X,'L1',
1 4X,'H2',2X,'K2',2X,'L2',4X,'H3',2X,'K3',2X,'L3',
2 5X,'DT1',5X,'DT2',5X,'DT3',3X,'PH11',3X,'PH12',
3 6X,'B1',2X,'B2',2X,'B3',/)
WRITE(50,3090)

```

```

3090  FORMAT (//)
      PI=4.0*ATAN(1.0)
      PHI=(PI/180.0)
      CAL=COS(AL*PHI)
      C2AL=CAL*CAL
      CBE=COS(BE*PHI)
      C2BE=CBE*CBE
      CGA=COS(GA*PHI)
      C2GA=CGA*CGA
      CABG=2.0*CAL*CBE*CGA
      VX1=C2AL+C2BE+C2GA
      VX2=SQRT(1.0-VX1-CABG)
      V=A*B*C*VX2
      VS=V*V
      VSI=1.0/VS
      SAL=SIN(AL*PHI)
      S2AL=SAL*SAL
      SBE=SIN(BE*PHI)
      S2BE=SBE*SBE
      SGA=SIN(GA*PHI)
      S2GA=SGA*SGA
      T11=(B*B)*(C*C)*S2AL
      T22=(A*A)*(C*C)*S2BE
      T33=(A*A)*(B*B)*S2GA
      T12=(A*B)*(C**2)*((CAL*CBE)-CGA)
      T23=(B*C)*(A**2)*((CBE*CGA)-CAL)
      T13=(A*C)*(B**2)*((CGA*CAL)-CBE)
      DO 501 IX=1,ND
      WRITE(S,*)IX,IY
      DO 112 J=1,3
      I=1
      DO 10 I1=-10,10
      DO 10 I2=-10,10
      DO 10 I3=-10,10
      H1=I1
      K1=I2
      L1=I3
      IF (ABS(H1)+ABS(K1)+ABS(L1) .EQ. 0) GO TO 10
      IF (ABS(H1)+ABS(K1)+ABS(L1) .GT. 12) GO TO 10
      TH1=T11*H1*H1
      TK1=T22*K1*K1
      TL1=T33*L1*L1
      TX1=TH1+TK1+TL1
      T1Y2=T12*H1*K1
      T2Y3=T23*K1*L1
      T1Y3=T13*H1*L1
      TY=2.0*(T1Y2+T2Y3+T1Y3)
      D11=VSI*(TX1+TY)
      IF (D11) 10,10,20
      D12=1.0/D11
      D13=SQRT(D12)
      D1=ABS(D13)
      D(I)=D1
      IF (ABS(DEE(IX,J)-D1)/D1 .GT. 0.04) GO TO 10
      IH(I)=H1

```

20

```

      K(I)=K1
      L(I)=L1
      I=I+1
10    CONTINUE
      M(J)=I-1
      MM=I-1
      CALL ASCEND(D,IH,K,L)
C      WRITE(50,2001)
C2001  FORMAT(6X,'H',6X,'K',6X,'L',8X,'D',//)
      DO 111 I=1,MM
C      WRITE(50,2002) J,I,IH(I),K(I),L(I),D(I)
C2002  FORMAT(5X,2I3,I4,5X,I4,5X,I4,8X,F12.5/)
      MH(IX,J,I)=IH(I)
      MK(IX,J,I)=K(I)
      ML(IX,J,I)=L(I)
      DD(IX,J,I)=D(I)
111    CONTINUE
112    CONTINUE
      DO 400 II=1,M(1)
      J=2
      DO 401 I=1,M(J)
      LH1=MH(IX,1,II)
      LH2=MH(IX,2,I)
      LK1=MK(IX,1,II)
      LK2=MK(IX,2,I)
      LL1=ML(IX,1,II)
      LL2=ML(IX,2,I)
      SUM1=T11*LH1*LH2+T22*LK1*LK2+T33*LL1*LL2
      SA1=T23*(LK1*LL2+LK2*LL1)
      SA2=T13*(LL1*LH2+LL2*LH1)
      SA3=T12*(LH1*LK2+LH2*LK1)
      SUM=SUM1+SA1+SA2+SA3
      PHA(IX,2,I)=DD(IX,1,II)*DD(IX,2,I)*SUM/VS
      IF (ABS(PHA(IX,2,I))-1) 11,11,401
11    PHA(IX,2,I)=ACOS(PHA(IX,2,I))/PHI
      IF (ABS(PHA(IX,2,I)-PE1(IX)) .GT. 5.0) GO TO 401
      HX=LH1+LH2
      KX=LK1+LK2
      LX=LL1+LL2
      J=3
      DO 402 IJ=1,M(J)
      LH3=MH(IX,3,IJ)
      LK3=MK(IX,3,IJ)
      LL3=ML(IX,3,IJ)
      SUM2=T11*LH1*LH3+T22*LK1*LK3+T33*LL1*LL3
      SB1=T23*(LK1*LL3+LK3*LL1)
      SB2=T13*(LL1*LH3+LL3*LH1)
      SB3=T12*(LH1*LK3+LH3*LK1)
      SUMX=SUM2+SB1+SB2+SB3
      PHA(IX,3,IJ)=DD(IX,1,II)*DD(IX,3,IJ)*SUMX/VS
      IF (ABS(PHA(IX,3,IJ))-1) 12,12,402
12    PHA(IX,3,IJ)=ACOS(PHA(IX,3,IJ))/PHI
      IF (ABS(PHA(IX,3,IJ)-PE2(IX)) .GT. 5.0) GO TO 402
      IF (HX .NE. LH3) GO TO 402
      IF (KX .NE. LK3) GO TO 402

```

```

      IF (LX .NE. LL3) GO TO 402
      IB1(IX,IJ)=LK1*LL3-LL1*LK3
      IB2(IX,IJ)=LL1*LH3-LH1*LL3
      IB3(IX,IJ)=LH1*LK3-LH3*LK1
      WRITE(5,*) IY,IX
      WRITE(50,1020) IY,IX,LH1,LK1,LL1,LH2,LK2,LL2,
     1 LH3,LK3,LL3,DD(IX,1,II),DD(IX,2,I),DD(IX,3,IJ),
     2 PHA(IX,2,I),PHA(IX,3,IJ),IB1(IX,IJ),IB2(IX,IJ),
     3 IB3(IX,IJ)
1020  FORMAT(5X,2I3,2X,3I4,2X,3I4,2X,3I4,3F8.3,2F7.2,
     1 4X,3I4)
402   CONTINUE
401   CONTINUE
400   CONTINUE
501   CONTINUE
502   CONTINUE
      STOP
      END
C *****
C SUBROUTINE ASCEND
C *****
      SUBROUTINE ASCEND(D,IH,K,L)
      COMMON MM
      DIMENSION D(1000),IH(1000),K(1000),L(1000)
      DO 10 I=2,MM
      II=I-1
      DMIN=D(II)
      DO 20 J=1,MM
      IF (DMIN .GE. D(J)) GO TO 20
      DMIN=D(J)
      II=J
20    CONTINUE
      Q=D(I-1)
      IR=IH(I-1)
      IS=K(I-1)
      IT=L(I-1)
      D(I-1)=D(II)
      IH(I-1)=IH(II)
      K(I-1)=K(II)
      L(I-1)=L(II)
      D(II)=Q
      IH(II)=IR
      K(II)=IS
      L(II)=IT
10    CONTINUE
      RETURN
      END

```

APPENDIX - GNOTE ON THE OPERATION OF SEM IN SECONDARY ELECTRON (SE)
AND BACK-SCATTERED ELECTRON (BSE) MODES

The electron-optical lens system of an SEM acts to focus a beam of electrons emitted from an electron gun into a fine probe which impinges on the surface of a target specimen. The electron-specimen interactions result in a number of distinct emission signals from which images can be derived. The different emission signals result from electrostatic interaction between the probe or incident or primary electrons and the target specimen. Some of these interactions are inelastic (e.g. secondary electron emission) whereas others are elastic (e.g. back-scattered electron emission). The energy spectrum of emitted electrons consist of three distinct regions, viz. (I) elastically scattered electrons with energies similar to those of the probe electrons (E_0); (II) multiply scattered electrons with energies in the range 50 eV to E_0 and (III) low energy electrons (i.e. <50 eV). Secondary electrons (SE) occupy group III, whilst back-scattered electron (BSE) should in principle comprise group I, but due to slight inelastic effects, a significant proportion of group II electrons are emitted as BSE.

The yield of SE (η_s) which is independent of atomic number Z of target specimen is found to vary with angle of incidence i of the electron beam according to the following relationship

$$\eta_s(i) \propto \exp A(1 - \cos i)$$

where A is a constant. Conventional scanning electron microscopy makes use of SE emission characteristics of rough surfaces, to produce images based on specimen topography. SE images can be

obtained at magnifications very much higher than those with optical microscope, whilst the incorporation of suitable X-ray microanalytical facilities (either EDAX or WDS systems) makes simultaneous compositional determination routinely possible.

BSE originate from within the target specimen and are capable of providing images based on composition (Z-contrast images) and crystal structure (electron channelling pattern). Z-contrast images are the easiest SEM/BSE images to obtain. Compared with SEM/SE mode, the resolution is better for SEM/BSE images for polished surfaces.

Atomic number or Z-contrast arises from the dependence of BSE emission coefficient (η_b) on target atomic number (Z). In specimens containing only a single phase, Z and hence η_b are constants and the BSE atomic number image therefore consists of uniform intensity with no contrast. However, in polyphase specimens, Z and hence η_b vary from phase to phase such that the BSE image contains different intensities and contrast with regions having higher Z appearing bright.

The relationship between η_b and Z has been determined experimentally. For pure elements

$$\eta_b = \frac{\ln Z}{6} - \frac{1}{4} \quad (Z \geq 10)$$

However most minerals are not pure elements and may have complex compositions. In such cases, it is necessary to amend the above equation by defining a weighted mean BSE coefficient

$$\bar{\eta}_b = \sum_{i=1}^n c_i \eta_i$$

where c_i is the concentration by weight of each element in the

mineral, η_i is element's BSE coefficient and n is the number of elements present.

To observe details in Z-contrast images some difference in \bar{Z} must be present. \bar{Z} is related with composition as follows

$$\bar{Z} = \frac{\sum (NAZ)}{\sum (NA)}$$

where N is number of atoms of each element with atomic number Z and atomic weight A ($\sum NA$ is molecular weight). Minerals which have a range of composition yield different \bar{Z} and $\bar{\eta}$ values and hence Z-contrast images of varying intensities are produced. Upto 0.01 difference in \bar{Z} can be detected in BSE, Z-contrast images.

References:

1. Hall, M.G., Metallography in the SEM, Scanning Electron Microscopy (SEM Inc., Chicago, 1981).
2. Lloyd, G.E., Atomic number and crystallographic contrast images with SEM: A review of back-scattered electron technique. Min. Mag., 51 (1987) pp. 3-19.

APPENDIX-H

FORTRAN-IV COMPUTER PROGRAM USED FOR FACTOR
ANALYSIS AND CALCULATION OF CORRELATION COEFFICIENTS

The program accepts an N by M data matrix, where N is the number of observations and M is the number of variables.

The program can be used to perform both R-mode and Q-mode factor analysis. To perform R-mode factor analysis, select ITRAN=1 and ISIM=1; for Q-mode factor analysis ITRAN=2 and ISIM=2. L specifies number of factors to be retained.

```

C      FACTOR ANALYSIS
C      *****
C      SUBROUTINES NEEDED ARE READM PRINTM SUBM MMULT MINV
C      STAND RCOEF CTHETA EIGENJ AND VARIMAX
C      *****
C      DIMENSION X(50,50),FSCORE(50,50)
C      DIMENSION A1(50,50),A2(50,50),A3(50,50)
C      MD=50
C      ND=50
C      MM=50
C
C...   READ CONTRL CARD
C
1      READ(35,*) ITRAN,ISIM,L
      IF (ITRAN.LE.0) CALL EXIT
C
C...   READ AND PRINT INPUT DATA MATRIX
C
      CALL READM(X,N,M,ND,MD)
      CALL PRINTM(X,N,M,ND,MD)
      WRITE (36,2001)
      IF (ISIM .NE. 1) GO TO 2
      CALL STAND(X,N,M,ND,MD)
      CALL PRINTM(X,N,M,ND,MD)
      WRITE (36,2008)
C
C...   TRANSEPOSE DATA MATRIX IF REQUIRED
C

```

```

2      IF (ITRAN .NE. 2) GO TO 3
      MT=M
      IF (N .GT. M) MT=N
      DO 110 I=1,MT
      DO 110 J=I,MT
      XS=X(I,J)
      X(I,J)=X(J,I)
      X(J,I)=XS
110    CONTINUE
      MT=M
      M=N
      N=MT

C
C...  CALCULATE AND PRINT SIMILARITY MATRIX
C
3      IF (ISIM .EQ. 1) CALL RCOEF(X,N,M,ND,MD,A1,MM)
      IF (ISIM .EQ. 2) CALL CTHETA(X,N,M,ND,MD,A1,MM)
      CALL PRINTM(A1,M,M,MM,MM)
      WRITE (36,2002)
      CALL EXIT

C
C...  SAVE CORRELATION MATRIX
C
      IF (ISIM .NE. 1) GO TO 4
      DO 111 I=1,M
      DO 111 J=1,M
      A3(I,J)=A1(I,J)
111    CONTINUE

C
C...  CALCULATE EIGEN VALUE AND EIGEN VECTOR
C
4      CALL EIGENJ(A1,A2,M,MM)
      SUME=0.0
      DO 100 I=1,M
      A1(I,1)=A1(I,I)
      SUME=SUME+A1(I,1)
100    CONTINUE

C
C...  CALCULATE PERCENT CONTRIBUTION OF EACH EIGEN VALUE
C
      SUMEE=0.0
      DO 101 I=1,M
      A1(I,2)=A1(I,1)*100.0/SUME
      SUMEE=SUMEE+A1(I,1)
      A1(I,3)=SUMEE*100.0/SUME
101    CONTINUE
      CALL PRINTM(A1,M,3,MM,MM)
      WRITE (36,2003)
      CALL PRINTM(A2,M,M,MM,MM)
      WRITE (36,2004)

C
C...  CAL AND PRI FACTOR LOADING
C
      DO 102 I=1,M
      DO 102 J=1,L

```

```

      A2(I,J)=A2(I,J)*SQRT(A1(J,1))
102  CONTINUE
C    CALL PRINTM(A2,M,L,MM,MM)
C    WRITE (36,2005)
      IF (ISIM.NE. 1) GO TO 5
      DO 112 I=1,M
      DO 112 J=I,M
      DET=0.0
      DO 113 K=1,L
      DET=DET+A2(I,K)*A2(J,K)
113  CONTINUE
      A1(I,J)=DET
      A1(J,I)=DET
112  CONTINUE
      CALL PRINTM(A1,M,M,MM,MM)
      WRITE (36,2010)
      CALL SUBM(A3,A1,A3,M,M,MM,MM)
      CALL PRINTM(A3,M,M,MM,MM)
      WRITE (36,2011)
C
C...  CAL AND PRINT FACTOR SCORE
C
5      DO 103 I=1,L
      DO 103 J=I,L
      DET=0.0
      DO 104 K=1,M
      DET=DET+A2(K,I)*A2(K,J)
104  CONTINUE
      A3(I,J)=DET
      A3(J,I)=DET
103  CONTINUE
      CALL MINV(A3,A1,L,MM,DET)
      CALL MMULT(A2,A1,A3,M,L,L,MM,MM,MM,MM,MM,MM)
      CALL MMULT(X,A3,FSCORE,N,M,L,ND,MD,MM,MM,ND,MD)
C    CALL PRINTM(FSCORE,N,L,ND,MD)
C    WRITE (36,2007)
C
C...  ROTATE FACTOR MATRIX
C
      CALL VARMAX(A2,M,L,MM)
C
C...  PRINT ROTATED FACTOR MATRIX
C
      CALL PRINTM(A2,M,L,MM,MM)
      WRITE (36,2006)
C
C...  CALCULATE AND PRINT VARIMAX FACTOR SCORES
C
      DO 105 I=1,L
      DO 105 J=I,L
      DET=0.0
      DO 106 K=1,M
      DET=DET+A2(K,I)*A2(K,J)
106  CONTINUE

```

```

      A3(I,J)=DET
      A3(J,I)=DET
105    CONTINUE
      CALL MINV(A3,A1,L,MM,DET)
      CALL MMULT(A2,A1,A3,M,L,L,MM,MM,MM,MM,MM,MM)
      CALL MMULT(X,A3,FSCORE,N,M,L,ND,MD,MM,MM,ND,MD)
      CALL PRINTM(FSCORE,N,L,ND,MD)
      WRITE (36,2009)
C1000  FORMAT (3I3)
2001  FORMAT (1H0,4X,'INPUT DATA MATRIX ',1X,
1 'COLUMNS=VARIABLES,ROWS=OBSERVATIONS')
2002  FORMAT (1H0,4X,'SIMILARITY MATRIX')
2003  FORMAT (1H0,4X,'COLUMN 1 = EIGENVALUES',2X,
1 'COLUMN 2=PERCENT OF TRACE',/,
2 5X,'COLUMN 3= CUMULATIVE PERCENT OF TRACE')
2004  FORMAT (1H0,4X,'PRINCIPAL AXIX MATRIX -',1X,
1 'COLUMNS =EIGENVECTORS, ROWS = VARIABLES')
2005  FORMAT (1H0,4X,'FACTOR LOADINGS-',1X,
1 'COLUMNS = FACTORS, ROWS = VARIABLES')
2006  FORMAT (1H0,4X,'ROTATED FACTOR MATRIX -',1X,
1 'COLUMNS = FACTORS, ROWS = VARIABLES')
2007  FORMAT (1H0,4X,'FACTOR SCORES -',1X,
1 'COLUMNS = FACTORS, ROWS = OBSERVATIONS')
2008  FORMAT (1H0,4X,'STANDARDIZED INPUT DATA MATRIX -',1X,
1 'COLUMNS = VARIABLES, ROWS = OBSERVATIONS')
2009  FORMAT (1H0,4X,'VARIMAX FACTOR SCORES',1X,
1 'COLUMNS = FACTORS, ROWS = OBSERVATIONS')
2010  FORMAT (1H0,4X,'REPRODUCED CORRELATION MATRIX')
2011  FORMAT (1H0,4X,'RESIDUAL CORRELATION MATRIX')
      END
C *****
C SUBROUTINE READM
C *****
      SUBROUTINE READM(A,N,M,N1,M1)
      DIMENSION A(N1,M1)
      READ(35,*) N,M
      DO 100 I=1,N
      READ(35,*) (A(I,J),J=1,M)
100    CONTINUE
      RETURN
1000  FORMAT (2I3)

      END

C *****
C SUBROUTINE PRINTM
C *****
      SUBROUTINE PRINTM(A,N,M,N1,M1)
      DIMENSION A(N1,M1)
      DO 100 IB=1,M,10
      IE=IB+9
      IF (IE-M) 2,2,1
1      IE=M
2      WRITE (36,2000) (I,I=IB,IE)

```

```

DO 101 J=1,N
WRITE (36,2001) J,(A(J,K),K=IB,IE)
101 CONTINUE
100 CONTINUE
RETURN
2000 FORMAT (1H1,1X,10I12)
2001 FORMAT (1H0,15,10F12.4)
END
C *****
C SUBROUTINE SUBM
C *****
SUBROUTINE SUBM(A,B,C,N,M,N1,M1)
DIMENSION A(N1,M1),B(N1,M1),C(N1,M1)
DO 100 I=1,N
DO 101 J=1,M
C(I,J)=A(I,J)-B(I,J)
101 CONTINUE
100 CONTINUE
END
C *****
C SUBROUTINE MMULT
C *****
SUBROUTINE MMULT(A,B,C,L,N,M,NA,MA,NB,MB,NC,MC)
DIMENSION A(NA,MA),B(NB,MB),C(NC,MC)
DO 100 I=1,L
DO 101 J=1,M
C(I,J)=0.0
DO 102 K=1,N
C(I,J)=C(I,J)+A(I,K)*B(K,J)
102 CONTINUE
101 CONTINUE
100 CONTINUE
RETURN
END
C *****
C SUBROUTINE MMINV
C *****
SUBROUTINE MINV(A,B,N,N1,DET)
DIMENSION A(N1,N1),B(N1,N1)
DO 100 I=1,N
DO 101 J=1,N
B(I,J)=0.0
101 CONTINUE
B(I,I)=1.0
100 CONTINUE
DET=1.0
DO 102 I=1,N
DIV=A(I,I)
DET=DET*DIV
DO 103 J=1,N
A(I,J)=A(I,J)/DIV
B(I,J)=B(I,J)/DIV
103 CONTINUE

```

```

DO 104 J=1,N
IF (I-J) 1,104,1
1  RATIO=A(J,I)
DO 105 K=1,N
A(J,K)=A(J,K)-RATIO*A(I,K)
B(J,K)=B(J,K)-RATIO*B(I,K)
105 CONTINUE
104 CONTINUE
102 CONTINUE
RETURN
END
C *****
C SUBROUTINE STAND
C *****
SUBROUTINE STAND(X,N,M,N1,M1)
DIMENSION X(N1,M1)
DO 100 I=1,M
SX=0.0
SXX=0.0
DO 101 J=1,N
SX=SX+X(J,I)
SXX=SXX+X(J,I)**2
101 CONTINUE
XM=SX/FLOAT(N)
SD=SQRT((SXX-SX*SX/FLOAT(N))/FLOAT(N-1))
DO 102 J=1,N
X(J,I)=(X(J,I)-XM)/SD
102 CONTINUE
100 CONTINUE
RETURN
END
C *****
C SUBROUTINE RCOEF
C *****
SUBROUTINE RCOEF(X,N,M,N1,M1,A,M2)
DIMENSION X(N1,M1),A(M2,M2)
AN=N
DO 100 I=1,M
DO 100 J=1,M
SX1=0.0
SX2=0.0
SX1X1=0.0
SX2X2=0.0
SX1X2=0.0
DO 101 K=1,N
SX1=SX1+X(K,I)
SX2=SX2+X(K,J)
SX1X1=SX1X1+X(K,I)**2
SX2X2=SX2X2+X(K,J)**2
SX1X2=SX1X2+X(K,I)*X(K,J)
101 CONTINUE
100 CONTINUE

```

```

R=(SX1X2-SX1*SX2/AN)/
1  SQRT((SX1X1-SX1*SX1/AN)*(SX2X2-SX2*SX2/AN))
A(I,J)=R
A(J,I)=R
100  CONTINUE
      RETURN
      END

C *****
C SUBROUTINE CTHETA
C *****
SUBROUTINE CTHETA(X,N,M,N1,M1,A,M2)
DIMENSION X(N1,M1),A(M2,M2)
DO 100 I=1,M
DO 100 J=1,M
SX1X1=0.0
SX2X2=0.0
SX1X2=0.0
DO 101 K=1,N
SX1X1=SX1X1+X(K,I)**2
SX2X2=SX2X2+X(K,J)**2
SX1X2=SX1X2+X(K,I)*X(K,J)
101  CONTINUE
A(I,J)=SX1X2/SQRT(SX1X1*SX2X2)
A(J,I)=A(I,J)
100  CONTINUE
      RETURN
      END

C *****
C SUBROUTINE EIGENJ
C *****
SUBROUTINE EIGENJ(A,B,N,N1)
DIMENSION A(N1,N1),B(N1,N1)
ANORM=0.0
DO 100 I=1,N
DO 101 J=1,N
IF (I-J) 2,1,2
1  B(I,J)=1.0
GO TO 101
2  B(I,J)=0.0
ANORM=ANORM+A(I,J)*A(I,J)
101  CONTINUE
100  CONTINUE
ANORM=SQRT(ANORM)
FNORM=ANORM*1.0E-09/FLOAT(N)
THR=ANORM
23  THR=THR/FLOAT(N)
3  IND=0
DO 102 I=2,N
I1=I-1
DO 103 J=1,I1
IF (ABS(A(J,I))-THR) 103,4,4

4  IND=1

```

```

      AL=-A(J,I)
      AM=(A(J,J)-A(I,I))/2.0
      AO=AL/SQRT(AL*AL+AM*AM)
      IF (AM) 5,6,6
5      AO=-AO
6      SINX=AO/SQRT(2.0*(1.0+SQRT(1.0-AO*AO)))
      SINX2=SINX*SINX
      COSX=SQRT(1.0-SINX2)
      COSX2=COSX*COSX
C      ROTATE COLUMN I AND J
      DO 104 K=1,N
      IF (K-J) 7,10,7
7      IF (K-I) 8,10,8
8      AT=A(K,J)
      A(K,J)=AT*COSX-A(K,I)*SINX
      A(K,I)=AT*SINX+A(K,I)*COSX
10     BT=B(K,J)
      B(K,J)=BT*COSX-B(K,I)*SINX
      B(K,I)=BT*SINX+B(K,I)*COSX
104    CONTINUE
      XT=2.0*A(J,I)*SINX*COSX
      AT=A(J,J)
      BT=A(I,I)
      A(J,J)=AT*COSX2+BT*SINX2-XT
      A(I,I)=AT*SINX2+BT*COSX2+XT
      A(J,I)=(AT-BT)*SINX*COSX+A(J,I)*(COSX2-SINX2)
      A(I,J)=A(J,I)
      DO 105 K=1,N
      A(J,K)=A(K,J)
      A(I,K)=A(K,I)
105    CONTINUE
103    CONTINUE
102    CONTINUE
      IF (IND) 20,20,3
20     IF (THR-FNORM) 25,25,23
25     DO 110 I=2,N
      J=I
29     IF (A(J-1,J-1)-A(J,J)) 30,110,110
30     AT=A(J-1,J-1)
      A(J-1,J-1)=A(J,J)
      A(J,J)=AT
      DO 111 K=1,N
      AT=B(K,J-1)
      B(K,J-1)=B(K,J)
      B(K,J)=AT
111    CONTINUE
      J=J-1
      IF (J-1) 110,110,29
110    CONTINUE
      RETURN
      END
C      *****
C      SUBROUTINE VARMAX
C      *****
      SUBROUTINE VARMAX(F,M,L,M1)

```

```

        DIMENSION F(M1,M1),H(100)
        WRITE (36,2001)
        SQRT2=1.0/SQRT(2.0)
        XM=M
        L1=L-1
        NIT=-1
        NCM=0
        DO 100 I=1,M
        SUMH=0.0
        DO 101 J=1,L
        SUMH=SUMH+F(I,J)**2
101      CONTINUE
        H(I)=SUMH
        DO 102 J=1,L
        F(I,J)=F(I,J)/SQRT(SUMH)
102      CONTINUE
100      CONTINUE
1      TVF=0.0
        DO 103 I=1,L
        SF1=0.0
        SF2=0.0
        DO 104 J=1,M
        SF1=SF1+F(J,I)**2
        SF2=SF2+F(J,I)**4
104      CONTINUE
        TVF=TVF+(XM*SF2-SF1*SF1)/(XM*XM)
103      CONTINUE
        IF (NIT.LT. 0) GO TO 2
        IF (ABS(TVF-TVI).GT. 0.000001) GO TO 2
        NCM=NCM+1
        IF (NCM.GE. 5) GO TO 50
2      NIT=NIT+1
        TVI=TVF
        WRITE (36,2002) NIT,TVF
        DO 105 I=1,L1
        L2=I+1
        DO 106 J=L2,L
        A=0.0
        B=0.0
        C=0.0
        D=0.0
        DO 107 K=1,M
        X=F(K,I)
        Y=F(K,J)
        U=(X+Y)*(X-Y)
        V=2.0*X*Y
        A=A+U
        B=B+V
        C=C+(U+V)*(U-V)
        D=D+2.0*U*V

107      CONTINUE

```

```

      XN=D-(2.0*A*B)/XM
      XO=C-(A*A-B*B)/XM
      XR=SQRT(XN*XN+XO*XO)
      IF (XR .LE. 0.001) GO TO 106
      COS4T=XO/XR
      COS2T=SQRT((1.0+COS4T)/2.0)
      COS1T=SQRT((1.0+COS2T)/2.0)
      SIN1T=SQRT(1.0-COS1T*COS1T)
      IF (SIN1T .LE. 0.001) GO TO 106
      IF (XN .LT. 0.0) SIN1T=-SIN1T
      DO 108 K=1,M
      X=F(K,I)
      Y=F(K,J)
      F(K,I)=X*COS1T+Y*SIN1T
      F(K,J)=Y*COS1T-X*SIN1T
108   CONTINUE
106   CONTINUE
105   CONTINUE
      GO TO 1
50    WRITE (36,2004)
      WRITE (36,2001)
      DO 110 I=1,M
      SUMH=0.0
      DO 111 J=1,L
      F(I,J)=F(I,J)*SQRT(H(I))
      SUMH=SUMH+F(I,J)**2
111   CONTINUE
      D=H(I)-SUMH
      WRITE (36,2003) I,H(I),SUMH,D
110   CONTINUE
      WRITE (36,2005)
      RETURN
2001  FORMAT (1H1)
2002  FORMAT (10X,15,3X,F15.7)
2003  FORMAT (1X,15,3F15.7,/)
2004  FORMAT (1H0,4X,'NUMBER OF VARIMAX ITERATIONS',1X,
1      'AND VARIANCE AT EACH STEP')
2005  FORMAT (1H0,4X,'COLUMN 1 = INITIAL COMMUNALITY',2X,
1      'COLUMN 2 = COMMUNALITY AFTER ROTATION',/,
2      5X,'COLUMN 3 = DIFFERENCE')
      END

```

REFERENCE

Davis,C.J., Statistics and Data Analysis in Geology

(John Wiley and Sons ,New York,1973) pp. 519-524

APPENDIX-I

FORTRAN-IV PROGRAM FOR MULTIPLE REGRESSION ANALYSIS

The program accepts an N by M data matrix, where N is the number of observations and M is the number of variables.

Variabele 1 is the dependent variable and 2 through M are independent.

```

C      MULTIPLE REGRESSION ANALYSIS
C      *****
C      SUBROUTINE REQUIRED ARE PRINTM, READM AND SLE . NOTE
C      THAT SUBROUTINE PRINTM AND READM ARE GIVEN IN THE
C      FACTOR ANALYSIS PROGRAM (VIDE APPENDIX-H)
C      *****
C      DIMENSION X(100,20),D(100,3),A(20,20),B(20)
C      ND=100
C      MD=20
C      NM=20
C
C...   READ AND PRINT DATA MATRIX
C
C      CALL READM(X,N,M,ND,MD)
C      CALL PRINTM(X,N,M,ND,MD)
C      WRITE (21,2005)
C
C...   ZERO SLE MATRIX AND OTHERS
C
C      DO 100 I=1,M
C      B(I)=0.0
C      DO 100 J=1,M
C      A(I,J)=0.0
100    CONTINUE
C
C...   CALCULATE SLE MATRIX
C
C      DO 101 I=1,N
C      Y=X(I,1)
C      X(I,1)=1.0
C      DO 102 J=1,M
C      B(J)=B(J)+X(I,J)*Y
C      DO 102 K=1,M
C      A(J,K)=A(J,K)+X(I,J)*X(I,K)

```

```

102    CONTINUE
      X(I,1)=Y
101    CONTINUE
C
C...   SOLVE SLE
C
      CALL SLE(A,B,M,MM,1.0E-08)
C
C...   CALCULATE ESTIMATED VALUE AND DEVIATION
C
      DO 103 I=1,N
        D(I,1)=X(I,1)
        D(I,2)=B(1)
        DO 104 J=2,M
          D(I,2)=D(I,2)+B(J)*X(I,J)
104    CONTINUE
        D(I,3)=D(I,1)-D(I,2)
103    CONTINUE
C
C...   PRINT Y,ESTIMATED Y,DEVIATION
C
      CALL PRINTM(D,N,3,ND,3)
      WRITE(22,2006)
C
C...   PRINT REGRESSION COEFFICIENTS
C
      CALL PRINTM(B,M,1,MM,1)
C
C...   CALCULATE ERROR MEASURES
C
      SY=0.0
      SYY=0.0
      SYC=0.0
      SYYC=0.0
      DO 105 I=1,N
        SY=SY+D(I,1)
        SYY=SYY+D(I,1)**2
        SYC=SYC+D(I,2)
        SYYC=SYYC+D(I,2)**2
105    CONTINUE
      SST=SYY-SY*SY/FLOAT(N)
      SSR=SYYC-SYC*SYC/FLOAT(N)
      SSD=SST-SSR
      NDF1=M-1
      AMSR=SSR/FLOAT(NDF1)
      NDF2=N-M
      AMSD=SSD/FLOAT(NDF2)
      R2=SSR/SST
      R=SQRT(R2)
      F=AMSR/AMSD
      NDF3=N-1
C
C...   PRINT ERROR MEASURES

```

```

C      WRITE(21,2000)
      WRITE(21,2001) SSR,NDF1,AMSR,F
      WRITE(21,2002) SSD,NDF2,AMSD
      WRITE(21,2003) SST,NDF3
      WRITE(21,2004) R2,R
      CALL EXIT
2000   FORMAT(2X,'SOURCE OF',13X,'SUM OF DEGREE OF MEAN'
1       ,/,1X,'VARIATION',13X,'SQUARES FREEDOM SQUARES
2       F-TEST',/,1X,60(1H-))
2001   FORMAT(1X,'REGRESSION',10X,F10.2,18,2X,F10.2,/,
1       51X,F10.4)
2002   FORMAT(1X,'DEVIATION',11X,F10.2,18,2X,F10.2)
2003   FORMAT(2X,'TOTAL VARIATION',5X,F10.2,18)
2004   FORMAT('GOODNESS OF FIT = ',F10.4,/,
1       'CORRELATION COEFFICIENT = ',F10.4)
2005   FORMAT(1H0,4X,'INPUT DATA MATRIX -',1X,
1       'COLUMNS=VARIABLES, ROWS=OBSERVATION')
2006   FORMAT(1H0,4X,'COLUMN 1 = Y, COLUMN 2 =
1       ESTIMATED Y',1X,'COLUMN 3 = DEVIATION')
2007   FORMAT(1H0,4X,'REGRESSION COEFFICIENTS',3X,
1       '1 = CONSTANT TERM')
      END
C      *****
C      SLE
C      *****
      SUBROUTINE SLE(A,B,N,N1,ZERO)
      DIMENSION A(N1,N1),B(N1)
      DO 100 I=1,N
      DIV=A(I,1)
      IF (ABS(DIV)-ZERO) 1,1,1
1      DO 101 J=1,N
      A(I,J)=A(I,J)/DIV
101     CONTINUE
      B(I)=B(I)/DIV
      DO 102 J=1,N
      IF (I-J) 2,102,2
2      RATIO=A(J,I)
      DO 103 K=1,N
      A(J,K)=A(J,K)-RATIO*A(I,K)
103     CONTINUE
      B(J)=B(J)-RATIO*B(I)
102     CONTINUE
100     CONTINUE
      99     RETURN
      *99    CALL EXIT
      END

```

REFERENCE

 Davis,C.J., Statistics and Data Analysis in Geology
 (John Wiley and Sons, New York,1973) pp.415-417

APPENDIX - J

LIST OF MULTIPLY INDEXED SELECTED AREA ELECTRON
DIFFRACTION PATTERNS

Details of diffraction patterns					Minerals indexed*	Remark**
d ₁ A°	d ₂ A°	d ₃ A°	φ ₁ degree	φ ₂ degree		
2.51	2.33	1.41	64.0	33.5	1, 2, 3, 7, 8, 11	0
3.42	3.38	2.52	95.0	48.0	3, 9	0
2.68	2.70	1.91	90.0	45.0	11, 12	0
2.56	2.56	2.45	115.0	57.5	4, 6, 13	0
1.85	1.52	1.22	93.5	51.5	2, 3, 5, 6, 8, 9, 10, 11, 12	0
3.42	3.38	2.49	94.5	47.0	6, 15	0
5.85	1.75	1.65	83.0	67.0	1, 3, 4, 5	0
4.24	4.11	2.47	64.0	32.0	1, 2, 7	0
4.48	4.09	4.14	119.0	65.0	7, 11	1
3.98	1.58	1.40	81.5	60.0	1, 3, 10, 11	0
4.49	3.39	2.24	62.0	35.0	3, 7	2

- * The minerals corresponding to different numbers are as follows:
- | | |
|--|--------------------------------|
| 1. Mordenite (ASTM 6-239), | 2. Phillipsite (ASTM 12-195), |
| 3. Labradorite (ASTM 18-1202), | 4. Orthoclase (ASTM 19-931), |
| 5. Sanidine (ASTM 14-164), | 6. α-quartz (ASTM 5-490), |
| 7. Montmorillonite-chlorite (ASTM 12-237), | |
| 8. Prehnite (ASTM 19-1227), | 9. Kaolinite (ASTM 14-164), |
| 10. Pyrophyllite (ASTM 12-203), | 11. Birnessite (ASTM 23-1046), |
| 12. Todorokite (ASTM 13-164), | 13. Nsutite (ASTM 17-510), |
| 14. Goethite (ASTM 17-536), | 15. Manganite (ASTM 13-157). |

** Observed in: 0 - as received sample
1 - residue after removal of only manganese
2 - siliceous residue.

APPENDIX - K

ELEMENTAL COMPOSITION OF NODULES FROM DIFFERENT
REGIONS IN CENTRAL INDIAN BASIN* (49)

The chemical compositions used in the calculation of correlation coefficient matrix in Table VI.3 are given below:

S. No.	Element, wt %					Mn/Fe ratio
	Mn	Fe	Ni	Co	Cu	
1	11	19.9	0.1	0.16	0.09	0.55
2	9	12.8	0.34	0.12	0.26	0.70
3	20	7.6	0.29	0.10	0.10	2.63
4	20	16.5	0.10	0.14	0.5	1.21
5	10	13.6	0.69	0.20	0.35	0.74
6	17	11.8	0.34	0.13	0.43	1.44
7	32	4.8	1.5	0.14	0.26	6.67
8	17	9.5	0.54	0.19	0.31	1.79
9	31	6.0	0.60	0.18	1.6	5.17
10	8	15.8	0.2	0.9	0.23	0.51
11	24	12.4	0.22	0.20	0.22	1.94
12	22	11.7	0.73	0.10	0.73	1.88
13	12	4.5	1.4	0.10	1.4	2.66
14	32	7.8	1.0	0.12	0.95	4.10
15	90	5.6	0.27	0.19	0.96	16.1
16	19	12.3	0.89	0.17	0.59	1.54
17	15	11.2	1.1	0.06	0.27	1.33
18	20	6.3	0.46	0.17	1.6	3.17
19	14	9.2	1.2	0.10	1.1	1.52
20	22	5.4	1.2	0.09	1.3	4.07
21	22	7.1	1.4	0.24	1.6	3.09
22	14	5.2	1.5	0.10	1.6	2.69
23	26	5.8	1.5	0.32	0.6	4.48
24	27	13.0	0.87	0.54	0.46	2.08
25	19	10.6	0.62	0.15	0.11	1.79
26	11	17.9	0.33	0.10	0.49	0.62
27	17	4.7	1.5	0.22	0.28	3.62
28	5	8.1	0.74	0.10	0.29	0.61
29	13	9.9	0.38	0.12	0.10	1.31
30	12	5.6	0.29	0.22	0.4	2.14
31	12	13.0	0.44	0.16	0.39	0.92
32	10	11.2	0.60	0.18	0.13	0.89
33	18	8.2	0.4	0.08	0.18	2.20
34	16	14.0	0.54	0.21	0.40	1.14
35	8	16.4	0.47	0.14	0.05	0.49
36	7	12.1	0.47	0.10	0.12	0.578
37	15	6.2	0.01	0.05	0.06	2.41

* Average depth 4900 metre.

APPENDIX - LINTERACTION OF HYDROUS MANGANESE(IV) OXIDES WITH
Ni, Co AND Cu IONS IN SOLUTION

The chemistry of transition metal ions interaction with hydrous manganese oxides is a complex topic in itself. The chemistry of metal adsorption on oxides has been reviewed by several workers (1-4). The objective here is to present some salient features on the subject with special emphasis on Ni, Co and Cu and oxides of interest.

Marti (5) and Wadsley (6) presented evidence for ion exchange in oxyhydroxides of manganese. Buser and Graf (7) have noted that in layered structure manganese oxides, consisting of well ordered main lattice, regularly alternating with disordered interstitial lattice (e.g. birnessite, buserite), the ions in interstitial lattice exchange quickly compared to Mn(IV) ions in the main lattice. Jeffries and Stumm (8) studied the adsorption of Ca, Zn and Cu on buserite and found that the adsorption data for Cu did not agree with a simple 1:1 (Cu:H) exchange model of adsorption, indicating 1:2 surface exchange and/or specific adsorption. Egorov (9) stressed that ion exchange does not exclude chemisorption interaction, and the primary sorption implies the effect of completing the solid phase by sorbed ions and its structural incorporation in the sorbent. Other workers (10) have also emphasized on the important role of sorbed cation penetration into the sorbent structure.

It has been found by some investigators that the sorption of heavy metal ions on oxides, particularly those subjected to

hydrolysis, increases markedly within a narrow pH range (2, 10-12). At relatively low pH's the phenomena of sorption are regarded as ion exchange between H^+ from the sorbent OH-group and sorbed ion, and in alkaline pH's hydrolysis is considered to be the main sorption factor. Varentsov et al. (2) and McKenzie (4, 13) have noted that large number of ion exchange and molecular sorption models (e.g. surface coordination model (1), coordination-coprecipitation-sorption model (14), surface complexation model (11), site binding model (15)) are generally found inadequate to explain the adsorption of transition metal ions on hydrous manganese oxides. Elements like Ni, Co and Cu interact more strongly with manganese oxides compared with oxyhydroxide of iron and significantly narrow pH range in which adsorption increases from 0-100% is not observed for manganese oxides (4).

Ni, Co and Cu are more strongly adsorbed on manganese dioxide compared to alkali metals e.g. Li, Na, K (16). The adsorption of Ni, Co and Cu take place even at pH near isoelectric point (16). McKenzie (17, 18) have significantly advanced the idea of heavy metals sorption by hydrous manganese dioxide. He (17, 18) has shown that the sorption of Co, Cu and Ni by hydrous manganese oxide from chloride solutions at pH ~ 5 is a multistage process which involve (i) rapid sorption of metal ions ($Cu > Co > Ni$) accompanied by displacement of exchangeable ions H^+ , K^+ and Mn^{2+} from the surface, (ii) oxidation of element sorbed on the surface e.g. $Co(II) \rightarrow Co(III)$ by $Mn(III)$. The possibility of these reactions is attributed to the differences in the magnitude of crystal field stabilization energy for these elements (17, 18). Burns (19) proposed that adsorption would most likely occur in the vicinity

of essential and defect vacancies in the $\delta\text{-MnO}_2$ lattice or by replacement of interstitial Na^+ and Mn^{2+} .

During adsorption of Ni, Co and Cu on 10 \AA manganite (i.e. busserite), birnessite or $\delta\text{-MnO}_2$, large amount of Mn^{2+} is released in Co sorption compared to Ni and Cu sorption (17, 20). Loganathan and Bureau (20) and McKenzie (17) proposed that the reason for large release of Mn by Co compared to that by other ions might be due to substitution of solution Co^{2+} for structural Mn(III) coupled with an electron transfer step to give Co(III) in the structure and Mn^{2+} in solution. According to Murray (21) this interpretation is not completely satisfactory because of large discrepancy of ionic radius between octahedrally coordinated low spin Co^{3+} (0.525 \AA) and Mn^{2+} (0.80 \AA) and Mn^{3+} (0.65 \AA). Burns and Burns (22) contend that close agreement between ionic radius of Co^{3+} and Mn^{4+} (0.54 \AA) suggest that some cobalt substitute for Mn^{4+} in edge shared (MnO_6) octahedra. XPS measurement for cobalt adsorbed on $\delta\text{-MnO}_2$ has provided experimental evidence for oxidation of Co(II) to Co(III) (23). Using the sorption model developed by James and Healy (24) (i.e. $\Delta G_{\text{ads}} = \Delta G_{\text{chemical}} + \Delta G_{\text{columbic}} + \Delta G_{\text{solvation}}$) and others (15), Murray and Dillard (23) contended that Co(II) cannot be oxidized by O_2 to Co(III) in bulk solution, but the oxidation can proceed in the presence of strong electrical field at the MnO_2 -solution interface. Ni(II) however cannot be oxidized at the interface except at very large concentration of Ni in the solution (23). Further XPS studies (25) for Co sorbed on sodium birnessite ($\text{Na}_4\text{Mn}_{13}\text{O}_{27} \cdot 9\text{H}_2\text{O}$) has unveiled that Mn(IV) serves as the oxidizing agent for the formation of Co(III) on birnessite surface and oxidation of Co adsorbed on birnessite is not favoured above pH 8.

Hem (26) has suggested that coprecipitation process in which the necessary ions are incorporated in the growing crystal lattice may be more realistic situation for natural processes.

Giovanoli (27) has explained that not only the interaction of metal ions with hydrous manganese dioxide is far from being just a sorption/desorption at the surface, but even a simple exchange (in the sense of zeolitic exchange reaction) is not an appropriate term since a lattice rearrangement may be involved. Sorption isotherms can therefore be only part of the truth i.e. they are a formal representation of a chemical reaction that goes much deeper into the bulk phase than hitherto assumed (27).

References:

1. Stumm, W., Hohl, H. and Dalang, F., *Croat. Chem. Acta*, 48(4) (1976) 491-504.
2. Varentsov, I.M., Bakov, N.Y., Dikov, Y.P., Gendler, T.S. and Giovanoli, R., *Acta Mineral. Petrog. Szeged*, 24(1) (1979) 63-90.
3. Turner, D.R. and Whitfield, M., *Ecol. Bull. (Stockholm)* 35 (1983) 9-37.
4. McKenzie, R.M., *Aust. J. Soil Res.*, 18 (1980) 61-73.
5. Marti, W., Ph.D. Thesis, Univ. Berne, 1944 (Unpublished).
6. Wadsley, A.D., *J. Am. Chem. Soc.*, 72 (1950) 1781-1784.
7. Buser, W. and Graf, P., *Helv. Chim. Acta*, 38(3) (1955) 810-829.
8. Jeffries, D.S. and Stumm, W., *Can. Miner.*, 14 (1976) 16-22.
9. Egorov, J.V., *Statics of Microelement Sorption by Oxyhydrate*, M., Atomizdat (in Russian) cited in ref. 2.
10. Anderson, B.J., Jenne, E.A. and Chato, T.T., *Geochim. Cosmochim. Acta*, 37(3) (1973) 611-622.
11. James, R.O., Stiglich, P.J. and Healy, T.W., *Far. Discuss. Chem. Soc.*, 59 (1975) 142-156.

12. Tewari, P.H., Campbell, A.B. and Lee, W., *Can. J. Chem.*, 50 (1972) 1642-1648.
13. Novikov, A.I., Shaffert, A.A. and Yakubova, N.S., In: *Coprecipitation by Hydroxides*, Vol. 2, Published by Tajik State Univ., Dushanbe, USSR, 1977, 81-86 (in Russian) cited in ref. 2.
14. Davis, J.A., James, R.O. and Leckie, J.O., *J. Coll. Interf. Sci.*, 63 (1978) 480-499.
15. McKenzie, R.M., *Aust. J. Soil Res.*, 19 (1981).
16. Murray, D.J., Healy, T.W. and Fuerstenau, D.W., *Adv. Chem. Ser.*, 78 (1968) 74-81.
17. McKenzie, R.M., *Aust. J. Soil Res.*, 8 (1970) 97-106.
18. McKenzie, R.M., *Geoderma*, 8 (1972) 29-35.
19. Burns, R.G., *Geochim. Cosmochim. Acta*, 40(1) (1976) 95-102.
20. Loganathan, P. and Burau, R.G., *Geochim. Cosmochim. Acta*, 37 (1973) 1277-1293.
21. Murray, J.W., *Geochim. Cosmochim. Acta*, 39 (1975) 635-647.
22. Burns, R.G. and Burns, V.M., In: G.P. Glasby (ed.) *Marine Manganese Deposits* (Elsevier, Amsterdam, 1977) 185-248.
23. Murray, J.W. and Dilard, J.G., *Geochim. Cosmochim. Acta*, 43 (1979) 781-787.
24. James, R.O. and Healy, T.W., *J. Coll. Interf. Sci.*, 40 (1972) 6581.
25. Crowther, D.L., Dilard, J.G. and Murray, J.W., *Geochim. Cosmochim. Acta*, 47 (1983) 1399-1403.
26. Hem, J.D., *Chem. Geol.*, 21 (1978) 199-218.
27. Giovanoli, R., In: I.M. Varentsov and G. Grasselly (eds.) *Geology and Geochemistry of Manganese*, Vol. 1 (Akademiai Kiado, Budapest, 1980) 159-202.

APPENDIX - M

CRYSTAL FIELD THEORY

Crystal field theory is concerned with the chemical bonding characteristics of those atoms having varying number of d (or f) electrons namely the transition metals (or the lanthanides). The theory has been used with particular success in the qualitative and quantitative interpretation of the chemical behaviour of first transition series from Sc to Cu (electronic configuration $(1s)^2 (2s)^2 (2p)^6 (3s)^2 (3p)^6 (3d)^{10-n} (4s)^1 \text{ or } 2$). Brief description of crystal field theory which is presented in this appendix has been taken from reference (1-5) and is confined to the elements of the first transition series.

In the absence of magnetic and electric fields, the five 3d orbitals of an isolated transition metal ion have the same energy, that is, they are five fold degenerate but different spatial orientations. Lobes of d_{z^2} and $d_{x^2-y^2}$ orbitals (the e_g group, doubly degenerate levels) projects along the Cartesian axes, whereas the lobes of d_{xy} , d_{xz} and d_{yz} orbitals (the t_{2g} group, triply degenerate levels) are directed between these axes. The five d orbitals, which are degenerate and equal in energy in the gaseous metal ions becomes differentiated, due to their asymmetric nature, in the presence of the electrostatic field of ligands (i.e. the crystal field). In particular those orbitals lying in the direction of the ligands are raised in energy with respect to those lying away from the ligands. By preferential filling of the low lying levels, the d electron can stabilize the system as compared to the case of random filling of

the d orbitals. The gain in bonding energy achieved in this way may be called crystal field stabilization energy (CFSE).

Typically when a transition metal ion is in octahedral co-ordination in a structure, the effect of six ligands situated along the Cartesian axes is to repel electrons in e_g orbitals to a greater extent than the electrons in t_{2g} orbitals. The octahedral crystal field splitting parameter $10 Dq$ is the induced energy separation between the t_{2g} and e_g orbital groups. The energy level of the t_{2g} group is lowered by $4 Dq_{oct}/\text{electron}$ and e_g group raised by $6 Dq_{oct}/\text{electron}$ relative to the energy of unresolved 3d orbitals. The CFSE represent the sum of these two factors. Relative to the unsplit configuration the energy of split $t_{2g}^m . e_g^n$ configuration is $m \times (-4 Dq_{oct}) + n \times (6 Dq_{oct})$. This sum is the octahedral crystal field stabilization energy. For tetrahedral co-ordination the energy levels are exactly reversed. The CFSE for octahedral complex is always greater than that for tetrahedral complexes for the same metal and ligand ($Dq_{tet} = - 4/9 Dq_{oct}$). The magnitude of $10 Dq$ parameter depends on the valence of the ion, nature and type ligand, interatomic distance, and symmetry of co-ordinated ligand. Most transition metal ions occur in six co-ordinate sites in oxides and silicates and as hexahydrated ions $M(H_2O)_6^{n+}$ in solution.

Ions may have either high spin configurations in which electrons with spin aligned occupy singly as many t_{2g} and e_g orbitals as possible or low spin configuration in which electrons fill the t_{2g} orbitals. Favourable exchange interactions, reduced interelectronic repulsion and unnecessary pairing energies of two electrons in one orbital contribute to the stability of high spin state. Low spin state leads to a substantial increase in CFSE.

Values of CFSE for ions in octahedral field are summarized in Table M.1. Apart from ions in d^6 configuration (e.g. Co^{3+}) all transition metal ions exist in high spin state in oxide structure at pressure existing in earth's crust. The CFSE values listed in Table M.1 illustrate that ions in high spin state and with configurations other than $3d^0$, $3d^5$ or $3d^{10}$ will be stabilized by octahedral field relative to a spherical field. Mn^{2+} and Fe^{3+} have zero CFSE in high spin state. The ions with high spin d^3 and d^8 structure (i.e. Ni^{2+} , Cr^{3+}) and spin paired or low spin d^6 structure (i.e. Co^{3+}) have very high CFSE in octahedral co-ordination.

If the d electrons are symmetrically arranged with respect to an octahedral ligand field (for example in high spin d^3 , d^5 , d^8 , d^{10} and low spin d^6 configurations) they will repel all six ligands equally and a completely regular octahedral structure will be formed. For unsymmetrical arrangement of d electron (high spin d^4 and d^9 configurations), the Jahn-Teller theorem states that uneven distribution of electrons in e_g orbitals should spontaneously distort the octahedral environments, thereby attaining increased electronic stability in the low symmetry sites. Ions like Cu^{2+} (d^9) and Mn^{3+} (d^4) show Jahn-Teller distortion in octahedral field and form a tetragonally distorted octahedral structure. In low symmetry co-ordination sites, the simple CFSE parameter loses some of its significance since more than one energy separation between 3d orbital energy levels must be considered.

The variations in lattice energy of oxides, hydration energy and ionic radii of transition metals ion with electronic configurations has been successfully explained in terms of crystal field effects. The value of the splitting parameter ($10 Dq$) has been

Table M.1: Electronic configurations and crystal field stabilization energies of transition metal ions in octahedral co-ordination

Electronic configuration	Ion*	High-spin state			Low-spin state		
		Configuration of 3d electron t_{2g} e_g	Unpaired elec- trons	CFSE in 10 Dq	Configuration of 3d electron t_{2g} e_g	Unpaired elec- trons	CFSE in 10 Dq
(Ar) 3d ⁰	Ca ²⁺ , Sc ³⁺ , Ti ⁴⁺		0	0		0	0
(Ar) 3d ¹	Ti ³⁺	↑	1	4	↑	1	4
(Ar) 3d ²	Ti ²⁺ , V ³⁺	↑ ↑	2	8	↑ ↑	2	8
(Ar) 3d ³	V ²⁺ , Cr ³⁺ , <u>Mn</u> ⁴⁺	↑ ↑ ↑	3	6	↑ ↑ ↑	3	6
(Ar) 3d ⁴	Cr ²⁺ , <u>Mn</u> ³⁺	↑ ↑ ↑ ↑	4	6	↑ ↓ ↑ ↑	2	12
(Ar) 3d ⁵	<u>Mn</u> ²⁺ , <u>Fe</u> ³⁺	↑ ↑ ↑ ↑ ↑	5	0	↑ ↓ ↑ ↓ ↑	1	20
(Ar) 3d ⁶	Fe ²⁺ , <u>Co</u> ³⁺ , Ni ⁴⁺	↑ ↓ ↑ ↑ ↑	4	4	↑ ↓ ↑ ↓ ↑	0	24
(Ar) 3d ⁷	<u>Co</u> ²⁺ , Ni ³⁺	↑ ↓ ↑ ↑ ↑	3	8	↑ ↓ ↑ ↓ ↑	1	18
(Ar) 3d ⁸	<u>Ni</u> ²⁺	↑ ↓ ↑ ↑ ↑	2	6	↑ ↓ ↑ ↓ ↑	2	12
(Ar) 3d ⁹	<u>Cu</u> ²⁺	↑ ↓ ↑ ↑ ↑	1	6	↑ ↓ ↑ ↓ ↑	1	6
(Ar) 3d ¹⁰	Zn ²⁺ , Ga ³⁺ , Ge ⁴⁺	↑ ↓ ↑ ↓ ↑	0	0	↑ ↓ ↑ ↓ ↑	0	0

(Ar) - Configuration of argon: $1s^2 2s^2 2p^6 3s^2 3p^6$

* Position of ions of interest are underlined.

estimated from optical adsorption spectroscopy* of aqueous solutions of transition metal ions and of glasses doped with these elements. Dunitz and Orgel (6) and McClure (7) give value of 10 Dq parameter for oxide structures and from these they calculated the octahedral CFSE for a number of transition element ions.

The attraction of metal for the ligands and mutual repulsion of ligands bring in energies of the order of 500-1500 Kcal/mole. Crystal field effects are of the order of 10-50 Kcal. It is obvious that other factors determining bond strengths will be much more important than CFSE in fixing co-ordination number and geometry. Nevertheless, in many cases these other factors are so nearly balanced that crystal field effects will provide the small, extra weight needed to tip the scales in one direction or the other. It is to be noted that at room temperature 1.4 Kcal is one power of a ten in a rate or equilibrium constant. Hence, CFSE while small compared to bond energies, are clearly large enough to be chemically significant.

Basolo and Pearson (1) have used the crystal field theory to explain the bimolecular substitution reactions of octahedral complex ions in solution. The processes are believed to proceed through a seven co-ordinate transition state possessing the configuration of a pentagonal bipyramid. The difference, ΔE_a (crystal field activation energy (CFAE)), between the CFSE of an ion in the six co-ordinate and seven co-ordinate states may be regarded as a contribution to the total activation energy, E_a . A large positive value of ΔE_a results in a slow reaction, since the rate constant for a bimolecular

* The frequency ν of the radiation that is adsorbed is related to the splitting parameter by $\nu = Dq/h$, where h is Planck's constant.

Table M.2: Crystal field activation energies (in Dq) for the substitution mechanism: octahedral \rightarrow pentagonal bipyramid symmetry (1)

Electronic configuration	Ion *	High-spin state			Low-spin state		
		Octahedral CFSE	Pentagonal bipyramid CFSE	ΔE_a^+	Octahedral CFSE	Pentagonal bipyramid CFSE	ΔE_a
(Ar) 3d ¹	Ti ³⁺	0.40	0.528	-0.128	0.40	0.528	-0.128
(Ar) 3d ²	V ³⁺	0.80	1.056	-0.256	0.80	1.056	-0.256
(Ar) 3d ³	Cr ³⁺ , <u>Mn</u> ⁴⁺	1.20	0.774	<u>0.426</u>	1.20	0.774	0.426
(Ar) 3d ⁴	Cr ²⁺ , <u>Mn</u> ³⁺	0.60	0.493	<u>0.107</u>	1.60	1.302	0.298
(Ar) 3d ⁵	<u>Mn</u> ²⁺ , <u>Fe</u> ³⁺	0	0	<u>0</u>	2.00	1.830	0.170
(Ar) 3d ⁶	Fe ²⁺ , <u>Co</u> ³⁺	0.40	0.528	-0.127	2.40	1.548	<u>0.852</u>
(Ar) 3d ⁷	<u>Co</u> ²⁺ , Ni ³⁺	0.80	1.056	<u>-0.256</u>	1.80	1.266	0.534
(Ar) 3d ⁸	<u>Ni</u> ²⁺	1.20	0.774	<u>0.426</u>	1.20	0.774	0.462
(Ar) 3d ⁹	<u>Cu</u> ²⁺	0.60	0.493	<u>0.107</u>	0.90	0.493	0.107

* Underline means relevant to this investigation

+ Negative values may be taken as zero.

reaction is related to the activation energy by $k = A \exp(-E_a/RT)$. Crystal field stabilization energies and activation energies for ions with different d^n configurations in octahedral and pentagonal bipyramid co-ordination sites are summarized in Table M.2. The CFAE values in Table M.2 show that transition metal ions with d^3 , d^8 and low spin d^6 configurations are the ones most affected as far as CFSE is concerned by the formation of seven co-ordinate transition state. Activation energies are predicted to be high in reactions involving Ni^{2+} and Co^{3+} ions, with the result that rates of substitution reactions involving these ions will be low.

Substitution reactions involving transition metal ions in silicates and oxyhydroxides of manganese and iron probably bear resemblances to bimolecular reactions of octahedral ions in solution. By analogy, Ni^{2+} and Co^{3+} ions will be more resistant for substitution reaction. The experimental results on the leaching of ions from silicates have been found to be in agreement with the prediction of the crystal field theory (2).

References:

1. Basolo, F. and Pearson, R.G., Mechanisms of Inorganic Reactions (John Wiley and Sons, Inc., New York, 1967).
2. Burns, R.G., Mineralogical Applications of Crystal Field Theory (Cambridge University Press, 1970).
3. Henderson, P., Inorganic Geochemistry (Pergamon Press, Oxford, 1982).
4. Crerar, D., Wood, S., Brantley, S. and Bocarsly, A., Can. Mineral., Vol. 23 (1985) pp. 333-352.
5. Lee, J.D., A New Concise Inorganic Chemistry, Third Edition (The English Language Book Society and Van Nostrand Reinhold (UK) Co. Ltd., London, 1984) pp. 420-442.
6. Dunitz, J.D. and Orgel, L.E., J. Phys. Chem. Solids, Vol. 3 (1957) pp. 318-323.
7. McClure, D.S., J. Phys. Chem. Solids, Vol. 3 (1957) pp. 311-317.

APPENDIX - N

FREE ENERGY DATA

ΔG_f° , 298.15 K (Kcal*/mole) values for selected compounds and ionic species

Compound/ ionic species	State	ΔG_f° ($\frac{\text{Kcal}}{\text{mole}}$)	Ref.	Compound/ ionic species	State	ΔG_f° ($\frac{\text{Kcal}}{\text{mole}}$)	Ref.
NiO	(c)	-50.6	1	Ni ²⁺	(aq)	10.9	1
Ni ₂ O ₃ ·H ₂ O	(c)	-169.96	2	Co ²⁺	(aq)	13.0	1
Ni ₃ O ₄	(c)	-170.15	3	Co ³⁺	(aq)	28.9	2
Ni(OH) ₂	(c)	-160.9	1	Cu ²⁺	(aq)	15.7	1
Ni(OH) ₃	(c)	-129.5	2	Cu ⁺	(aq)	11.9	3
CoO	(c)	-51.20	1	Mn ²⁺	(aq)	-54.5	1
Co ₃ O ₄	(c)	-185.0	3	Mn ³⁺	(aq)	-19.6	2
Co(OH) ₂	(c)	-109.5	1	Fe ³⁺	(aq)	-4.02	4
Co(OH) ₃	(c)	-142.6	2	Fe ²⁺	(aq)	-18.85	4
CuO	(c)	-30.57	1	H ₂ O	(l)	-56.69	1
Cu(OH) ₂	(c)	-85.82	1	H ⁺	(aq)	0.0	1
MnO	(c)	-86.74	1	OH ⁻	(aq)	-37.59	2
δ-MnO ₂	(c)	-108.3	3	H ₂ SO ₄	(aq)	-177.34	2
Mn ₂ O ₃	(c)	-210.6	3	HSO ₄ ⁻	(aq)	-179.94	2
Mn ₃ O ₄	(c)	-306.7	3	SO ₄ ²⁻	(aq)	-177.97	2
Mn(OH) ₂	(c)	-147.0	1	SO ₂	(g)	-71.75	5
Mn(OH) ₃	(c)	-181.0	2	SO ₂	(aq)	-71.87	5
α-FeOOH**	(c)	-115.28	4	HSO ₃ ⁻	(aq)	-126.2	5
α-FeOOH**	(c)	-116.38	4	SO ₃ ²⁻	(aq)	-116.3	5

* 1 Kcal = 4.184 kJ

** Value depends on crystallinity

References:

1. Robin, R.G., In: K. Osseo-Asare and J.D. Miller (eds) Hydro-metallurgy Research Development and Plant Practice (AIME, Warrendale, 1982) p. 308.
2. Garrels, R.M. and Christ, C.L., Solutions, Minerals and Equilibria (Harper and Row, N.Y., 1965).
3. Hem, J.D., Chem. Geol., Vol. 21 (1978) pp. 199-218.
4. Murray, J.W., In: R.G. Burn (ed.) Marine Minerals (Mineralogical Society of America, 1979) p. 65.
5. Linkson, P.B., Ref. 1, p.317.

APPENDIX - O

LEACHING DATA FOR OXYHYDROXIDE OF MANGANESE

I. SULFURIC ACID

Leaching conditions: H_2SO_4 concentration - 1.0 N, temperature - $50^\circ C$, amount of solid used - 0.5 g, volume of acid used - 250 ml, stirring speed - 900 r.p.m., particle size of solid - $-63 + 53 \mu m$.

A. Birnessite samples (Figures VII.7 and VII.8(b), Table VII.6)

Time minutes	Mn					R			
	Mole/L	Mole/	F_{Mn}	$F_{Mn(II)}$	$NF_{Mn(II)}$	Mole/L	Mole/	F_R	NF_R
	$\times 10^4$	cm^2 $\times 10^6$	$\times 10^2$	$\times 10^2$	$g.m^{-2}$ $\times 10^3$	$\times 10^5$	cm^2 $\times 10^6$	$\times 10^2$	$g.m^{-2}$ $\times 10^3$
1	2	3	4	5	6	7	8	9	10

B-O

5	14.2	12.1	7.9	45.1	13.9	-	-	-	-
20	14.3	12.1	8.0	45.3	14.0	-	-	-	-
40	14.4	12.2	8.0	45.6	14.1	-	-	-	-
60	14.5	12.3	8.1	45.8	14.1	-	-	-	-
80	14.5	12.3	8.1	45.8	14.1	-	-	-	-
100	14.5	12.3	8.1	45.8	14.1	-	-	-	-

B-Ni(C)

5	8.7	12.4	5.1	37.7	10.7	17.6	2.5	20.8	5.9
20	8.7	12.4	5.1	37.7	10.7	24.5	3.5	29.1	8.3
40	8.7	12.4	5.1	37.7	10.7	29.7	4.2	35.2	10.0
60	8.7	12.4	5.1	37.7	10.7	30.4	4.3	36.0	10.3
80	8.7	12.4	5.1	37.7	10.7	-	-	-	-
100	8.7	12.4	5.1	37.7	10.7	31.5	4.5	37.3	10.6

B-Co(C)

5	-	-	-	-	-	6.9	0.9	8.0	2.1
20	8.0	10.4	4.6	34.9	9.0	6.9	1.1	10.3	2.7
40	8.0	10.4	4.6	34.9	9.0	-	-	-	-
60	8.0	10.4	4.6	34.9	9.0	9.8	1.3	11.4	3.0
80	8.0	10.4	4.6	34.9	9.0	-	-	-	-
100	8.0	10.4	4.6	34.9	9.0	11.8	1.5	13.7	3.6

1	2	3	4	5	6	7	8	9	10
<u>B-Cu(C)</u>									
5	9.9	10.2	5.9	47.2	9.7	44.0	4.5	50.6	10.4
20	10.4	10.7	6.2	49.4	10.2	48.3	5.0	55.6	11.4
40	10.4	10.7	6.2	49.4	10.2	49.1	5.1	56.5	11.7
60	10.4	10.7	6.2	49.4	10.2	51.0	5.3	58.7	12.1
80	10.4	10.7	6.2	49.4	10.2	53.1	5.5	61.1	12.6
100	10.6	10.9	6.3	50.1	10.2	55.0	5.7	63.3	13.1
<u>B-Ni(I)</u>									
5	7.9	6.7	4.6	25.1	4.3	30.1	2.6	8.9	1.5
20	9.9	8.4	5.8	31.4	5.3	38.7	3.3	11.4	1.9
40	10.4	8.8	6.1	32.9	5.6	46.5	3.9	13.7	2.3
60	11.1	9.4	6.4	35.1	6.0	51.6	4.4	15.2	2.6
80	-	-	-	-	-	56.8	4.8	16.7	2.8
100	11.9	10.1	6.9	37.7	6.4	62.0	5.3	18.3	3.1
<u>B-Co(I)</u>									
5	8.2	8.6	5.7	-	-	15.4	1.6	2.9	0.6
20	8.7	9.1	6.0	-	-	17.7	1.9	3.3	0.7
40	8.7	9.1	6.0	-	-	18.0	1.9	3.4	0.7
60	8.8	9.2	6.1	-	-	18.3	1.9	3.5	0.7
80	-	-	-	-	-	18.3	1.9	3.5	0.7
100	8.7	9.1	6.0	-	-	18.3	1.9	3.5	0.7
<u>B-Cu(I)</u>									
5	4.0	3.6	2.6	40.4	7.3	139.4	12.6	30.8	5.6
20	5.0	4.5	3.3	50.6	9.2	196.4	17.8	43.3	7.8
40	5.2	4.7	3.4	52.7	9.5	216.0	19.6	47.7	8.6
60	5.2	4.7	3.5	53.4	9.7	255.3	23.1	56.3	10.2
80	-	-	-	-	-	274.9	24.9	60.7	11.0
100	5.4	4.9	3.7	55.7	10.1	294.6	26.7	65.0	11.8

B. $\delta\text{-MnO}_2$ samples (Figure VII.8(a), Table VII.6)

Time minutes	Mn			R	
	F_{Mn}	Mole/L	Mole/cm ²	F_{R}	NF_{R}
	$\times 10^2$	$\times 10^5$	$\times 10^7$	$\times 10^2$	$\text{g.m}^{-2} \times 10^3$
1	2	3	4	5	6

V-O

5	0.24	-	-	-	-
100	0.24	-	-	-	-

	1	2	3	4	5	6
<u>V-Ni(S)</u>						
5		0.14	5.3	1.9	12.9	0.9
20		-	6.5	2.4	16.2	1.2
40		-	8.1	2.9	20.0	1.5
60		-	-	-	-	-
80		-	10.8	3.9	27.3	2.0
100		0.14	12.9	4.7	32.5	2.4
<u>V-Co(S)</u>						
5		0.14	0.0	0.0	0.0	0.0
20		-	0.0	0.0	0.0	0.0
40		-	0.0	0.0	0.0	0.0
60		-	0.0	0.0	0.0	0.0
80		-	0.0	0.0	0.0	0.0
100		0.14	0.0	0.0	0.0	0.0
<u>V-Cu(S)</u>						
5		<0.14	8.2	3.0	21.8	1.6
20		-	9.8	3.6	26.0	1.9
40		-	11.8	4.3	31.3	2.3
60		-	13.7	5.0	36.4	2.6
80		-	15.7	5.7	41.6	3.0
100		<0.14	17.7	6.4	46.8	3.4

II. SULFUROUS ACID

Leaching conditions: H_2SO_3 concentration - 0.2 g SO_2 /100 ml H_2O , temperature - 20°C , amount of solid used - 0.25 g, volume of acid - 250 ml, stirring speed - 900 r.p.m., particle size of solid - $-210 + 149 \mu\text{m}$

A. Birnessite samples (Figures VII.11 and VII.12, Table VII.6)

Time minutes	Mn				R				[Mn]/[R] mole ratio in solu- tion
	Mole/L	Mole/	F_{Mn}	NF_{Mn}	Mole/L	Mole/	F_{R}	NF_{R}	
	$\times 10^4$	cm^2 $\times 10^5$	$\times 10^2$	g.m^{-2} $\times 10^3$	$\times 10^4$	cm^2 $\times 10^5$	$\times 10^2$	g.m^{-2} $\times 10^3$	
1	2	3	4	5	6	7	8	9	10

B-O

0.5	48.6	18.8	54.3	-	-	-	-	-	-
-----	------	------	------	---	---	---	---	---	---

1	2	3	4	5	6	7	8	9	10
1.4	68.7	26.6	76.9	-	-	-	-	-	-
3.0	87.0	33.7	94.8	-	-	-	-	-	-
5.0	89.1	34.5	99.6	-	-	-	-	-	-
10.0	89.3	34.6	99.7	-	-	-	-	-	-
<u>B-Ni(C)</u> ([Mn]/[Ni]) _{solid} - 20.1									
0.5	21.8	6.2	25.8	73.7	1.3	0.37	30.8	8.8	16.9
1.8	44.4	12.6	52.5	15.0	2.4	0.69	57.8	16.5	18.3
3.0	58.9	16.8	69.5	19.9	3.2	0.91	77.0	22.0	18.4
5.0	74.5	21.3	87.9	25.1	3.8	1.09	90.9	25.9	19.5
10.0	76.9	22.0	90.8	25.9	4.1	1.18	98.6	28.2	18.6
<u>B-Co(C)</u> ([Mn]/[Co]) _{solid} - 20.4									
0.6	40.4	15.6	46.5	18.0	2.3	0.88	52.9	20.5	17.9
1.9	65.9	25.5	80.0	31.0	3.7	1.45	87.4	33.9	17.7
3.0	76.9	29.8	88.3	34.2	3.9	1.52	92.0	35.7	19.6
5.0	83.0	32.2	95.4	37.0	4.1	1.60	96.6	37.4	20.2
10.0	85.0	32.9	97.7	37.9	4.2	1.63	98.9	38.3	20.2
<u>B-Cu(C)</u> ([Mn]/[Cu]) _{solid} - 19.9									
0.6	24.3	9.9	29.3	11.9	1.1	0.46	26.5	10.7	21.3
1.5	40.5	16.5	48.8	19.8	2.1	0.85	48.5	19.7	19.5
3.3	60.7	24.7	73.2	29.8	3.1	1.28	73.1	29.8	19.3
5.0	76.9	31.3	92.7	37.7	3.7	1.50	86.0	35.0	20.8
10.0	82.9	33.7	100.0	40.7	4.3	1.74	99.7	40.5	19.4
<u>B-Ni(I)</u> ([Mn]/[Ni]) _{solid} - 5.1									
0.6	34.4	7.6	40.6	9.0	6.3	1.40	37.9	8.4	5.4
1.4	53.8	11.9	63.5	14.1	10.7	2.37	64.2	14.2	5.0
3.0	62.7	13.9	74.1	16.4	14.2	3.15	84.9	18.8	4.4
5.0	72.8	16.1	86.0	19.1	16.1	3.57	96.6	21.4	4.5
-	-	-	-	-	-	-	-	-	-
<u>B-Co(I)</u> ([Mn]/[Co]) _{solid} - 2.7									
0.7	25.1	8.2	35.2	11.4	9.8	3.19	37.8	12.3	2.6
1.5	34.3	11.1	48.9	15.9	15.2	4.94	58.6	19.0	2.3
3.4	51.8	16.8	72.8	23.6	21.6	7.00	83.1	26.9	2.4
5.1	63.9	20.7	89.9	29.2	24.5	7.96	94.5	30.7	2.6
10.0	71.8	23.3	101.0	32.7	26.0	8.44	100.1	32.5	2.7
<u>B-Cu(I)</u> ([Mn]/[Cu]) _{solid} - 3.4									
0.5	34.4	11.2	45.6	14.9	11.6	3.78	51.6	16.8	3.0
1.5	56.7	18.5	75.2	24.6	17.7	5.78	78.7	25.7	3.2
3.1	64.8	21.2	85.9	28.1	20.6	6.73	91.8	30.0	3.1
5.1	72.8	23.8	96.6	31.6	21.6	7.06	96.2	31.4	3.3
10.0	74.9	24.5	99.3	32.5	22.2	7.26	98.9	32.5	3.4

B. δ -MnO₂ samples (Figure VII.13, Table VII.6)

	1	2	3	4	5	6	7	8	9	10
<u>V-O</u>										
0.5	64.6	4.3	80.3	5.4	-	-	-	-	-	-
1.3	74.9	5.0	92.9	6.2	-	-	-	-	-	-
3.0	76.8	5.2	95.4	6.4	-	-	-	-	-	-
5.0	80.8	5.4	100.3	6.7	-	-	-	-	-	-
<u>V-Ni(S)</u> ([Mn]/[Ni]) _{solid}										
0.5	64.6	4.7	80.3	5.8	1.6	0.12	78.9	5.7		40.3
1.3	74.9	5.4	92.9	6.7	1.8	0.13	89.9	6.5		41.1
3.0	76.8	5.6	95.4	6.9	1.9	0.14	94.0	6.8		40.0
5.0	80.8	5.9	100.3	7.3	2.0	0.15	100.0	7.2		40.0
<u>V-Co(S)</u> ([Mn]/[Co]) _{solid} - 40.9										
0.5	64.6	4.7	80.3	5.8	1.4	0.10	69.3	5.0		47.1
1.3	74.9	5.4	92.9	6.7	1.6	0.12	81.7	5.9		46.2
3.0	76.8	5.6	95.4	6.9	1.7	0.13	88.2	6.4		44.1
5.0	80.1	5.8	99.5	7.2	2.0	0.15	102.0	7.4		40.4
<u>V-Cu(S)</u> ([Mn]/[Cu]) _{solid} - 42.4										
0.5	64.6	4.7	80.2	5.8	1.2	0.08	61.4	4.5		55.6
1.3	74.9	5.4	92.9	6.7	1.4	0.10	72.8	5.3		54.6
3.0	76.1	5.5	94.5	6.9	1.6	0.11	83.2	6.0		48.4
5.0	80.1	5.8	99.5	7.2	1.9	0.14	99.8	7.2		42.6

APPENDIX - P

LEACHING DATA FOR GOETHITES

I. SULFURIC ACID

Leaching conditions: H_2SO_4 concentration - 1.0 N, temperature - 50°C , amount of solid used - 0.5 g, volume of acid used - 250 ml, stirring speed - 900 r.p.m., particle size of solid - $<53\ \mu\text{m}$
(Figures VIII.5 and VIII.7, Table VIII.6)

Time minutes	Fe				R				MCR*
	Mole/L $\times 10^4$	Mole/ cm^2 $\times 10^6$	F_{Fe} $\times 10^2$	NF_{Fe} g.m^{-2}	Mole/L $\times 10^4$	Mole/ cm^2 $\times 10^7$	F_{R} $\times 10^2$	NF_{R} g.m^{-2} $\times 10^3$	
1	2	3	4	5	6	7	8	9	10
<u>G-O</u>									
5	18.4	23.0	8.7	2.1	-	-	-	-	-
20	19.7	24.7	9.3	2.2	-	-	-	-	-
40	20.6	25.8	9.8	2.4	-	-	-	-	-
60	-	-	-	-	-	-	-	-	-
80	21.2	26.5	10.1	2.4	-	-	-	-	-
100	21.7	27.2	10.3	2.5	-	-	-	-	-
<u>G-Ni(C)</u> ($[\text{Fe}]/[\text{Ni}]$) _{solid} ~ 25									
5	38.8	28.4	20.6	2.9	4.26	31.2	53.3	7.5	9.1
20	40.9	30.0	21.6	3.0	4.65	34.1	58.1	8.2	8.8
40	41.6	30.5	22.1	3.1	4.72	34.6	59.1	8.3	8.8
60	42.5	31.1	22.6	3.2	4.77	34.9	59.8	8.4	8.9
80	-	-	-	-	-	-	-	-	-
100	45.4	33.2	23.8	3.6	4.85	35.5	60.7	8.5	9.3
<u>G-Co(C)</u> ($[\text{Fe}]/[\text{Co}]$) _{solid} ~ 26									
5	39.7	27.8	20.8	2.8	1.95	13.7	24.7	3.3	20.4
20	41.3	29.0	21.7	2.9	2.05	14.4	26.0	3.5	20.2
40	42.3	29.7	22.2	3.0	2.12	14.9	26.8	3.6	20.0
60	43.4	30.5	22.7	3.1	2.13	15.0	27.0	3.7	20.4
80	-	-	-	-	2.15	15.1	27.2	3.7	-
100	45.4	31.9	23.8	3.2	2.18	15.3	27.5	3.7	20.8

* MCR - Molar concentration ratio ($C_{\text{Fe}}/C_{\text{R}}$) in leach liquor.

1	2	3	4	5	6	7	8	9	10
<u>G-Cu(C)</u> ($[\text{Fe}]/[\text{Cu}]$) _{solid} ~ 28									
5	58.5	39.5	28.9	3.8	1.05	7.1	14.6	1.9	55.7
20	60.6	40.9	30.0	3.9	1.11	7.5	15.5	2.0	54.6
40	61.9	41.8	30.7	4.0	1.15	7.7	16.1	2.1	53.8
60	62.6	42.3	31.0	4.0	-	-	-	-	-
80	62.6	42.3	31.0	4.0	1.18	7.8	16.4	2.1	53.0
100	62.6	42.3	31.0	4.0	1.18	7.8	16.4	2.1	53.0
<u>G-Ni(S)</u> ($[\text{Fe}]/[\text{Ni}]$) _{solid} ~ 78									
5	18.1	22.7	8.8	2.1	1.81	22.6	68.7	16.6	10.0
20	19.2	24.1	9.4	2.2	1.88	23.6	72.0	17.4	10.2
40	-	-	-	-	2.01	25.2	76.8	18.5	-
60	20.2	25.3	9.7	2.3	2.07	25.9	78.8	18.9	9.8
80	-	-	-	-	2.07	25.9	78.8	18.9	-
100	21.0	26.3	10.2	2.5	2.10	26.3	79.9	19.2	10.0
<u>G-Co(S)</u> ($[\text{Fe}]/[\text{Co}]$) _{solid} ~ 87									
5	18.1	22.7	8.8	2.1	1.82	22.8	77.0	18.6	9.9
20	18.9	23.7	9.2	2.2	1.92	24.7	83.3	20.1	9.6
40	20.6	25.8	9.9	2.4	2.05	25.7	86.6	20.8	10.0
60	-	-	-	-	2.12	26.7	89.4	21.5	-
80	21.5	26.9	10.2	2.5	2.17	27.2	91.7	22.1	9.9
100	22.1	27.6	10.3	2.5	2.17	27.2	92.0	22.2	10.1
<u>G-Cu(S)</u> ($[\text{Fe}]/[\text{Cu}]$) _{solid} ~ 52									
5	17.9	22.4	8.7	2.1	3.04	38.1	76.7	18.5	5.9
20	18.8	23.6	9.1	2.2	3.19	40.0	80.2	19.3	5.9
40	20.0	25.1	9.8	2.4	3.24	40.6	81.7	19.7	6.1
60	-	-	-	-	3.30	41.3	83.2	20.1	-
80	20.6	25.8	10.1	2.4	3.34	41.8	84.2	20.3	6.2
100	21.1	26.4	10.3	2.5	3.41	42.6	85.9	20.6	6.2

II. SULFUROUS ACID

Leaching conditions: H_2SO_3 concentration - 1.5 g SO_2 /100 ml H_2O ,
temperature - 20°C, pH - 1.5, amount of solid used - 0.25 g, volume
of acid - 250 ml, stirring speed - 900 r.p.m., particle size of
solid - <53 μm

(Figures VIII.6 and VIII.8, Table VIII.6)

Time minutes	Fe				R				MCR
	Mole/L	Mole/	F_{Fe}	NF_{Fe}	Mole/L	Mole/	F_R	NF_R	
	$\times 10^4$	cm^2 $\times 10^6$	$\times 10^2$	$\times 10^4$	$\times 10^5$	cm^2 $\times 10^7$	$\times 10^2$	g.m^{-2} $\times 10^3$	
1	2	3	4	5	6	7	8	9	10

G-O

1.0	1.7	4.1	1.6	3.9	-	-	-	-	-
3.0	2.0	5.1	2.0	4.8	-	-	-	-	-
5.0	3.1	7.8	3.0	7.2	-	-	-	-	-
8.2	4.1	10.2	3.9	9.4	-	-	-	-	-
12.3	5.7	14.2	5.5	13.3	-	-	-	-	-
16.4	-	-	-	-	-	-	-	-	-
20.0	8.2	20.1	7.8	18.8	-	-	-	-	-

G-Ni(C) ($[Fe]/[Ni]_{\text{solid}} \sim 25$)

1.0	1.2	1.7	1.2	1.7	5.3	7.7	13.2	1.9	2.3
3.0	2.5	3.7	2.5	3.5	6.5	9.5	16.2	2.3	3.8
5.0	3.3	4.8	3.3	4.7	8.0	11.7	20.0	2.8	4.1
8.0	5.0	7.3	5.0	7.0	9.3	13.6	23.3	3.3	5.4
12.0	7.3	10.7	7.4	10.4	12.3	17.9	30.7	4.3	5.9
16.1	-	-	-	-	15.1	22.1	37.8	5.3	-
20.0	12.4	18.1	12.5	17.6	17.4	25.5	43.6	6.1	7.3

G-Co(C) ($[Fe]/[Co]_{\text{solid}} \sim 25$)

2.0	2.8	3.9	2.8	3.7	2.4	3.4	6.2	0.8	11.7
4.0	3.9	5.5	3.9	5.3	2.9	4.1	7.4	1.0	13.4
6.5	6.0	8.4	5.9	7.8	3.7	5.1	9.3	1.3	16.2
8.0	7.4	10.5	7.4	10.0	4.1	5.8	10.4	1.4	18.0
12.0	10.8	15.2	10.7	14.5	5.9	8.2	14.9	2.0	18.3
16.0	11.8	16.5	11.7	15.8	6.8	9.6	17.3	2.3	17.4
20.0	14.1	19.8	14.0	18.9	7.3	10.3	18.5	2.5	19.3

G-Cu(C) ($[Fe]/[Cu]_{\text{solid}} \sim 28$)

1.0	2.8	3.8	2.8	3.6	0.9	1.3	2.6	0.3	31.1
3.2	4.0	5.4	4.0	5.2	1.1	1.5	3.2	0.4	36.4
5.0	5.2	7.0	5.2	6.8	1.3	1.7	3.7	0.5	40.0
9.0	6.0	8.1	6.0	7.7	1.6	2.1	4.4	0.6	37.5
12.2	7.2	9.7	7.3	9.5	1.9	2.6	5.3	0.7	37.9
16.0	-	-	-	-	2.2	3.0	6.1	0.8	-
20.0	12.8	17.2	12.9	16.8	2.5	3.4	7.0	0.9	51.2

1	2	3	4	5	6	7	8	9	10
<u>G-Ni(S)</u> ($[\text{Fe}]/[\text{Ni}]$) _{solid} ~ 78									
1.0	0.6	1.5	0.6	1.4	3.9	9.7	29.6	7.1	1.5
3.4	1.2	3.1	1.2	2.9	4.5	11.3	34.5	8.3	2.7
5.2	1.8	4.6	1.8	4.3	5.2	12.9	39.4	9.5	3.5
8.0	2.8	6.9	2.7	6.5	6.5	16.2	49.2	11.9	4.3
12.0	3.9	9.7	3.8	9.2	7.7	19.4	59.1	14.2	5.1
16.0	-	-	-	-	-	-	-	-	-
20.0	6.3	15.8	6.1	14.7	9.8	24.6	75.0	18.1	6.4
<u>G-Co(S)</u> ($[\text{Fe}]/[\text{Co}]$) _{solid} ~ 87									
2.4	1.1	2.8	1.1	2.7	7.4	18.6	63.3	15.3	1.5
4.5	1.7	4.2	1.6	3.9	7.9	20.0	68.0	16.4	2.2
6.0	2.4	6.0	2.3	5.5	8.1	20.4	69.3	16.7	3.0
8.3	3.3	8.2	3.2	7.7	8.9	22.3	75.8	18.3	3.7
12.0	4.8	11.9	4.7	11.3	9.3	23.3	79.1	19.1	5.2
16.0	5.1	12.8	4.9	11.8	9.3	23.3	79.1	19.1	5.5
20.0	5.9	14.7	5.7	13.7	9.3	23.3	79.1	19.1	6.3
<u>G-Cu(S)</u> ($[\text{Fe}]/[\text{Cu}]$) _{solid} ~ 52									
1.0	1.4	3.6	1.4	3.4	10.6	26.6	53.5	12.9	1.3
3.0	2.0	4.9	1.9	4.6	11.8	29.6	59.4	14.3	1.7
5.3	2.7	6.6	2.6	6.2	12.6	31.6	63.7	15.3	2.1
8.2	3.9	9.7	3.8	9.2	13.0	32.5	65.4	15.8	3.0
12.0	5.3	13.3	5.2	12.5	13.2	33.1	66.6	16.1	4.0
16.2	-	-	-	-	13.4	33.5	67.4	16.2	-
20.0	7.3	18.3	7.1	17.1	13.4	33.5	67.4	16.2	5.4